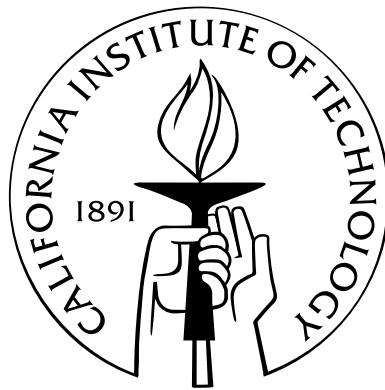


Effects of Damping and Reynolds Number on Vortex-Induced Vibrations

Thesis by
Joseph Thomas Klamo

In Partial Fulfillment of the Requirements
for the Degree of
Doctor of Philosophy



California Institute of Technology
Pasadena, California

2007

(Defended 29 September 2006)

© 2007

Joseph Thomas Klamo

All Rights Reserved

This thesis is dedicated to my parents, Mary and Thomas

Acknowledgements

This work would not have been possible without the guidance and support of my three “advisors.” Simply put, Tony Leonard was a great advisor. He gave me the freedom to explore what I was interested in, yet somehow kept me on a path of scientific discovery. His door was always open, literally, for me to stop in and toss an idea around. My second advisor, Mory Gharib, gave me complete control of the water tunnel, and the whole Noah lab for that matter, allowing me to run my experiments whenever I wanted. He also would never hesitate to help me find an odd piece of equipment I needed, even if it meant digging through long-ago-forgotten equipment stockrooms. My final advisor, Anatol Roshko, sacrificed an enormous amount of his time, giving me advice and direction. He even let me take up his time at home in Altadena, going over a presentation with me the day before I left for the conference.

I am also very grateful to the other two members of my committee, Profs. Dave Goodwin and Chris Brennen. Dave was an enormous help with the design of the variable magnetic eddy-current damping system, which was critical to this work. Chris provided invaluable insight by pointing out various unwanted effects that could creep into my experiments and ways to verify that they were minimized.

It would have been impossible for me to run all my various tests without the constant fabrication by Joe Haggarty and the machinists in the Aero machine shop of the necessary parts for my ever changing test apparatus. And whenever I busted one of my glass cylinders, or simply needed one modified, I made my way over to the glass-blowing shop to see Rick Gerhart.

I was lucky enough to be able to spend my first two years in the Noah Lab with Dr. Tait Pottebaum. Besides having lengthy discussions about how to improve college football, he taught me countless useful things regarding experimental techniques. He inspired the six-degree-of-freedom support stand for the LVDT as well as always reminding me to “use

slots, not holes.” The number of times this came in handy, I lost count of a long time ago. Then there are all the other graduate students in the Gharib research group that helped me out at various stages along the way. I would especially like to thank a few who have been down in the basement of Guggenheim as long as I have. Emilio Graff gave me the most important thing an experimentalist could have, a *complete* set of Allen wrenches. Dr. John Dabiri provided insight and advice on all the flow visualization. Finally, getting the old tow tank working again in order to calibrate the velocity meters would not have been possible without the help from Dr. Michele Milano.

Of course there was SOPS and all the people of Thomas that made my graduate experience so enjoyable. The social hours, intramural sports teams, and lunches from Ernie are all a side of graduate school that most students, who aren’t lucky enough to be surrounded by such extraordinary people, don’t get to experience. Kristo Kriechbaum always made his house available for a gathering. Alex “The Greek” Taflanidis ran our championship soccer team and let me play goalie, even though I didn’t know the rules. Kunihiko “Toyota” Taira, regardless of the fact that he actually believes CFD results, always had interesting suggestions regarding my research and we battled through the upper level aeronautics courses together. Then there was the much older, yet newer, grad student Michael “Fox” Wolf, who was always willing to talk about Luke Walton, Chris Mihm, and the rest of the Lakers. And the always hungry Nick Hudson who was constantly trying to buy my lunch off me. And even though not an official member of SOPS, the cornish game hen stuffed with apples and wrapped in bacon that Matt Dicken cooked once should give him life-time membership. Finally, everyone in SOPS was lucky to have Tim Chung as SOPS president. He was always trying to make SOPS and Thomas a better place.

I have had some great roommates over the years. Samantha Daly, besides being a great friend, found the house that I would eventually live in for my entire graduate career and was a great roommate while we lived there together. My other roommates Craig Kalenze, Tamer Elsayed, and Anna Olsen are all unbelievable people for being able to put up with me in a confined space for extended periods of time. Finally, there is Moh El-Naggar, who thought I was joking when I told him that we were going “to spend the rest of our (graduate school) lives together.” He has been a great roommate, a great help in my everyday life, and, most importantly, a great friend.

I would not have gotten to where I am now without the constant support and help

from my loving parents. They somehow instilled in me the importance of knowledge, at a young age when I did not appreciate all the opportunities I would have because of it. I was lucky enough to spend four years of grad school with my sister, Sara. She looked out for me during my first year and made sure I survived. After that we had time to do more important things like eat potato tacos on Friday, watch Michigan football games on Saturdays, and eat fried ice cream at Dona Maria's whenever their freezer was not broken. My sister Rachel visited often, went to two unbelievable Rose Bowls games with me, and would always be willing to chat with me. And my little brother Ben visited me during his spring break in college, and even though he was harassed by a quick-chop seller at Paseo Colorado, he did not hold it personally against me.

Finally, there is the person who has caused me to laugh, smile, and enjoy life more than everyone else combined, my fiancé Jennifer Ruglovsky. She reaffirmed for me that it is all right to be extremely passionate about things you really care about, even if others around you find those same things unimportant. More than anything, her endless love for me got me through the difficult parts of this process and has made me want to be her best friend, Steelers football fan, and soul mate for the rest of my life. I am excited to start the next part of our life together. You are the reason I dream at night. I love you.

Abstract

Vortex-induced vibrations (VIV) have been studied experimentally with emphasis put on damping and Reynolds number effects. Our system is an elastically-mounted rigid circular cylinder, free to oscillate only transverse to the flow direction, with very low inherent damping. We are able to prescribe the mass, m , damping, b , and stiffness, k , of the system over a wide range of values of interest. Unlike most studies of VIV, where the damping cannot be controlled, we are able to impose our system damping through the use of a custom-made variable magnetic eddy-current damping system. This control has allowed us to explore various damping effects on VIV behavior.

Although some results and ideas are discussed in the traditional nondimensional formulation, special emphasis is put on a different formulation of nondimensional parameters, known as the effective stiffness formulation. The advantages of this formulation over the traditional one are explained, and an important parameter, the effective stiffness, k_{eff}^* , is introduced. Through the use of this new formulation, the amplitude, A^* , and frequency, f^* , response are only a function of three parameters, damping, b^* , Reynolds number, Re , and effective stiffness, k_{eff}^* , instead of four when using the traditional formulation.

We show the effects that damping and Reynolds number each have on the amplitude and frequency response profiles, respectively. This allows us to make the interesting observation that, in general, damping and Reynolds number have similar effects on the response profiles. That is, a decrease in damping has similar effects that an increase in the Reynolds number has. The similarity between damping and Reynolds number effects is highlighted by showing how the large-amplitude portion of the response profile can be eliminated by either increasing the damping or decreasing the Reynolds number. We also show that numerous unique combinations of damping and Reynolds number values exist that produce a similar amplitude response profile for each system.

The maximum amplitude, A_{Max}^* , of our system has been studied in detail. Using the

effective stiffness formulation, we are able to theoretically show that maximum amplitudes should be functions of both damping and Reynolds number. We also define maximum amplitudes in the case of zero damping as limiting amplitudes, A_{Lim}^* , and show that they are only a function of Reynolds number. Using the effective stiffness parameter, we experimentally find that maximum amplitudes occur at roughly the same effective stiffness value, $k_{\text{eff}}^*|_{A_{\text{Max}}^*}$, for all the systems studied. This allows us to create constant-Reynolds-number curves of maximum amplitude over a large range of damping values, which we call a “generalized” Griffin plot. Extrapolating these results to zero damping, we are able to experimentally determine our limiting amplitude dependence on Reynolds number over the range $200 \lesssim \text{Re} \lesssim 5050$. By examining the wake structure of these maximum amplitude points we note that the wake for an oscillating cylinder is close to two dimensional at $\text{Re} \approx 200$ but is strongly three dimensional by $\text{Re} \approx 525$. We also note that up to $\text{Re} \approx 1000$, the wake structure of A_{Max}^* contains two single vortices shed per cycle (2S), even though the existence of the large-amplitude, upper branch and the location of the maximum amplitude in the Williamson-Roshko (WR) plane both suggest a wake structure involving two pairs of vortices shed per cycle (2P). However, above $\text{Re} \approx 2600$ we do observe the expected 2P wake structure of A_{Max}^* .

Discontinuities in the amplitude response profile are also investigated, which happen to occur in hysteresis regions. The discontinuity between the initial branch and the large-amplitude, upper branch portion of the response is studied in two ways. First, the time-averaged behavior is examined in an attempt to understand what controls the hysteresis as well as any damping and Reynolds number effects. We find that as tunnel velocity is increased, the system jumps upward, past the 2S/2P dividing curve of the WR-plane, and well inside the 2P wake structure region. However, as tunnel velocity is decreased, the system jump downward is controlled directly by the 2S/2P dividing curve. We showed the effects that damping has on this region, for both directions of tunnel velocity changes, and how sufficient damping eliminates the large-amplitude portion of the response curve. This region was also examined by tracking the transient behavior as the system underwent this discontinuous change in amplitude. The transient behavior was induced either by changes in the tunnel velocity or system damping. We note that for tunnel velocity changes, the system will always quickly move from a small- to a large-amplitude response. However, the system will not always move from a large- to a small-amplitude response, and instead

will sometimes stay in a “steady” transient condition. On the other hand, for damping changes, the reverse holds, the system will always quickly move from a large- to a small-amplitude response but will not always move from a small- to a large-amplitude response and instead will find a “steady” transient condition. We also find a new discontinuity hysteresis region that involves a jump between the lower branch and the desynchronized region. This hysteresis appears to be a low Reynolds number effect and is only seen in systems with $\text{Re} \lesssim \mathcal{O}(10^3)$.

Table of Contents

Acknowledgements	iv
Abstract	vii
Table of Contents	x
List of Figures	xiv
List of Tables	xxiv
List of Symbols	xxv
1 Introduction	1
1.1 Importance	1
1.2 Previous Work: One-Degree-of-Freedom Free-Vibrations of Rigid Circular Cylinders	2
1.3 Connection to One-Degree-of-Freedom Forced-Vibrations of Cylinders	6
1.4 Connection to Two-Degree-of-Freedom Free-, Forced-, and Simulated-Vibrations of Cylinders	8
1.5 Thesis Layout	11
2 Theory and Parameters	12
2.1 Chapter Overview	12
2.2 Bluff-Body Flows	12
2.3 Stationary Cylinder Considerations	13
2.4 Oscillating Cylinder Wake Structure	16
2.5 Governing Equation	16

2.6	Various Vortex-Induced Vibration Response Models	19
2.7	Traditional Formulation	20
2.8	Effective Stiffness Formulation	23
2.9	Formulation Comparison	25
2.10	Effective Stiffness Parameter	25
2.11	Comments on the Effective Stiffness Parameter	27
3	Experimental Setup and Test Procedures	29
3.1	Chapter Overview	29
3.2	Noah Water Tunnel	30
3.3	Traversing Plate with Adjustable Mass and Elasticity	34
3.4	Variable Magnetic Eddy-Current Damping System	36
3.5	Cylinder Models and Mounting Collars	38
3.6	Linear Variable Displacement Transducer	41
3.7	Digital Particle Image Velocimetry	42
3.8	Dye Flow Visualization	43
3.9	General Test Procedure	46
3.10	Parameter Values	46
3.11	Data Reduction Methodology	47
3.12	Cylinder End Effects and Boundary Layer Effects	48
3.13	Starting Method Dependence	51
4	Basic Results	54
4.1	Chapter Overview	54
4.2	General Characteristics of Amplitude and Frequency Responses	55
4.3	Formulation Comparison of Response Profiles	57
4.4	Time-Varying Motion	63
4.5	General Wake Structure	66
4.6	System Singularities	77
4.7	Damping Effects on the Amplitude Response Profile	81
4.8	Damping Effects on the Frequency Response Profile	84
4.9	Reynolds Number Effects on the Amplitude Response Profile	84
4.10	Reynolds Number Effects on the Frequency Response Profile	88

4.11	Practical Application	89
5	Maximum and Limiting Amplitudes	92
5.1	Chapter Overview	92
5.2	Background	92
5.3	Theoretical Development	100
5.4	Experimental Procedure	102
5.5	Generalized Griffin plot	103
5.6	Extending the Reynolds Number Range	108
5.7	Limiting Amplitudes	111
5.8	Comparison with Previous Work	112
5.9	Flow Visualization	116
5.10	Heavily Damped Systems	121
6	Discontinuities: Hysteretic Regions and Transient Behavior	125
6.1	Chapter Overview	125
6.2	Background	125
6.3	Hysteresis Between Initial Branch and Upper Branch	127
6.4	Transition Between Upper Branch and Lower Branch	130
6.5	Hysteresis Between Lower Branch and Desynchronized Region	134
6.6	Velocity-Induced Transients	136
6.7	Damping-Induced Transients	144
6.8	Comparison of Velocity- and Damping-Induced Transients	149
7	Summary and Future Considerations	151
7.1	Summary of Basic Results	151
7.2	Summary of Maximum and Limiting Amplitudes	154
7.3	Summary of Discontinuities	155
7.4	Future Considerations	156
Appendix A: Detailed Overview of the Data Reduction Process and Filtering Scheme		159

Appendix B: Damping Theory and System Damping Determination for Free-Vibration Natural Decay	164
Appendix C: Variable Magnetic Eddy-Current Damping System Theory	168
Appendix D: Top 10% Average Amplitude Adjustment Factor Calculations	171

List of Figures

2.1	Strouhal number, St , dependence on Reynolds number, Re . Figure and references from Norberg (2001).	14
2.2	Root-mean-square fluctuating lift coefficient, C_L' for a stationary circular cylinder as a function of Reynolds number, Re . Figure and references from Norberg (2001).	15
2.3	Full Williamson-Roshko plane mapping of the various possible wake structures behind the forced oscillations of a circular cylinder. Figure and parameter definitions from Williamson and Roshko (1988).	17
2.4	Detailed Williamson-Roshko plane mapping of the 2S and 2P wake structures behind the forced oscillations of a circular cylinder. Figure and parameter definitions from Williamson and Roshko (1988).	18
2.5	Canonical arrangement for the study of vortex-induced vibrations (VIV). . .	18
3.1	General layout of the Noah Water Tunnel. The settling chamber is visible on the left with the contraction in the middle and the test section on the far right. Visible in front of the test section is the water tunnel motor controller. . . .	31
3.2	Detailed view of the Noah Water Tunnel test section. Flow is from left to right in this view.	31
3.3	Transient response of the tunnel velocity in the test section caused by an extreme “impulsive” tunnel velocity change, from an initial velocity of 3.33 cm/s to a final velocity of 35 cm/s, recorded using a Nixon Streamflo velocity meter.	32
3.4	Power spectrum of frequencies in the test section caused by an extreme “impulsive” tunnel velocity change.	33
3.5	Transient settling time for regular operating “impulsive” tunnel velocity changes of 0.50 cm/s	34

3.6	General overview of the traversing plate with multiple stainless steel plates attached, for varying the system mass, and multiple springs attached, for varying the system elasticity. Also visible are the LVDT (on the left) and the VMEC damping system (on the right) as well as a test cylinder, suspended downward into the test section.	35
3.7	General overview of the variable magnetic eddy-current (VMEC) damping system. Shown are the three top electromagnets and the copper conducting plate attached to the traversing plate. The three bottom electromagnets, located underneath the conducting plate, are not visible.	37
3.8	Available range of imposed magnetic damping values, b_{mag} , possible using the VMEC damping system as functions of supplied current, i_{sup} , and copper conductive plate thickness.	39
3.9	Sample of free-vibration decay curves showing the linear relationship between the logarithm of amplitude against time for ideal viscous damping.	39
3.10	View of the four basic circular cylinders used for this study.	40
3.11	View of the three collars for the hollow cylinders, used to attach them to the traversing plate, and the collarless solid cylinder.	40
3.12	View of the setup for the LVDT system showing the six-degree-of-freedom mounting stand along with the attachment point to the traversing plate.	42
3.13	Detailed view of the dye-injection ports on the 38 mm diameter circular cylinder used for flow visualization.	44
3.14	General overview of the cylinder component of the flow visualization setup showing the flexible tubing, adjustable collar, and hollow circular cylinder with injection ports.	45
3.15	Overall view of the complete flow visualization setup. The two large beakers held the food coloring mixtures at a sufficient height to allow gravity to drive the flow of dye. The two dials used to adjust the flow can also be seen (light blue circular knobs).	45
3.16	Amplitude response profile dependence on the gap distance, G/D , between the end of the cylinder and bottom of the test section.	50
3.17	Frequency response profile dependence on the gap distance, G/D , between the end of the cylinder and bottom of the test section.	50

3.18	Amplitude response profile dependence on various starting method techniques for SM01 and SM02.	53
3.19	Frequency response profile dependence on various starting method techniques for SM01 and SM02.	53
4.1	Two distinct amplitude response profiles, shown in the traditional formulation plotted against the reduced velocity, U_R , for systems experiencing VIV. Arrows mark a point in each run where time-varying motions will be investigated in Section 4.4.	56
4.2	Corresponding frequency response profiles for Figure 4.1, shown in the traditional formulation plotted against the reduced velocity, U_R	56
4.3	Two distinct amplitude responses profiles, shown in the effective stiffness formulation plotted against the negative effective stiffness, $-k_{\text{eff}}^*$, for systems experiencing VIV. Arrows mark a point in each run where time-varying motions will be investigated in Section 4.4.	58
4.4	Corresponding frequency responses profiles for Figure 4.3, shown in the effective stiffness formulation plotted against the negative effective stiffness, $-k_{\text{eff}}^*$	58
4.5	Maximum amplitude, A_{Max}^* , of various system configurations plotted against effective stiffness, k_{eff}^* . Note that the maximum amplitude point for each configuration always occurs around $k_{\text{eff}}^* _{A_{\text{Max}}^*} \approx 2.5$. Damping and Reynolds number values for each run can be found in Table 5.1.	60
4.6	Frequency response in the traditional formulation displayed over the entire range of interest which causes the response profile to appear to be “locked-in” to the system natural frequency.	62
4.7	Same frequency response as Figure 4.6 but now only displayed over a small range near the system natural frequency.	62
4.8	Amplitude fluctuations per cycle of a low Reynolds number, high mass system (Run02(a)) viewed over approximately 400 cycles.	64
4.9	Same amplitude fluctuations per cycle as shown in Figure 4.8 but now displayed over a much smaller amplitude range, 0.014 units, in order to show the cycle-by-cycle fluctuations clearly.	64

4.10	Frequency fluctuations per cycle of a low Reynolds number, high mass system (Run02(a)) viewed over approximately 400 cycles. The fluctuations are below our measurement resolution, causing the response to alternate between our two minimum resolved frequencies.	65
4.11	Amplitude fluctuations per cycle of a high Reynolds number, light mass system (Run04(a)) viewed over approximately 250 cycles.	67
4.12	Frequency fluctuations per cycle of a high Reynolds number, light mass system (Run04(a)) viewed over approximately 250 cycles.	67
4.13	Amplitude cycle-by-cycle histogram results for four runs, approx 1000 cycles, of a high Reynolds number, light mass system (Run04(a)).	68
4.14	Frequency cycle-by-cycle histogram results for four runs, approx 1000 cycles, of a high Reynolds number, light mass system (Run04(a)).	68
4.15	Locations in the amplitude response profile where the wake structure was investigated using DPIV.	69
4.16	Wake structure of the initial branch (case 1).	70
4.17	Wake structure of the beginning of the upper branch (case 2).	71
4.18	Wake structure of the middle of the upper branch (case 3).	72
4.19	Wake structure of the end of the upper branch (case 4).	73
4.20	Wake structure of the beginning of the lower branch (case 5).	74
4.21	Wake structure of the end of the upper branch (case 6).	75
4.22	Flow visualization of the wake during an individual cycle in the middle part of the upper branch (case 3) showing a structure resembling a 2S wake. . . .	76
4.23	Flow visualization of the wake during an individual cycle of the middle of the upper branch (case 3) showing a structure resembling a classic 2P wake. . . .	76
4.24	Schematic showing allowable system states for two limiting structural parameter cases, a zero mass and zero stiffness system.	79
4.25	Sample of Sequence 03 amplitude response profiles in the traditional formulation showing the two effects that cause the scaling down of the lower branch as damping is increased. Damping values for each run can be found in Table 5.1.	82

4.26 Same results as Figure 4.25 showing the effects that damping has on the amplitude response profiles, but now displayed in the effective stiffness formulation plotted against negative effective stiffness, $-k_{\text{eff}}^*$. Damping values for each run can be found in Table 5.1. 83

4.27 Effects of damping on the frequency response profiles of the upper branch systems of Sequence 03 in the effective stiffness formulation. Solid lines represent increasing tunnel velocities; dashed lines represent decreasing tunnel velocities; f_{St} : stationary cylinder Strouhal frequency; f_N : system natural frequency in air. Damping values for each run can be found in Table 5.1. 85

4.28 Schematic showing the general trends of damping effects on the frequency response profiles for upper branch systems. 86

4.29 Elimination of the upper branch portion of the amplitude response profile through an increase in damping for $\text{Re}|A_{\text{Max}}^*| \approx 1000$ 87

4.30 Elimination of the upper branch portion of the amplitude response profile through a decrease in Reynolds number for $b^*|A_{\text{Max}}^*| \approx 0.13$ 87

4.31 Three distinct systems, each with a different damping and Reynolds number value, but by appropriate combinations of them, the amplitude response profiles of the three systems are nearly the same. 88

4.32 Effects of Reynolds number on the frequency response profiles of upper branch systems in the effective stiffness formulation. f_{St} : stationary cylinder Strouhal frequency; f_N : system natural frequency in air. 89

4.33 Effects of damping on the frequency response profiles of the upper branch systems of Sequence 04 in the effective stiffness formulation. Solid lines represent increasing tunnel velocities; dashed lines represent decreasing tunnel velocities; f_{St} : stationary cylinder Strouhal frequency; f_N : system natural frequency in air. Damping values for each run can be found in Table 5.1. 90

5.1 A typical “Griffin plot” in log-log form showing the proposed maximum amplitude, A_{Max}^* , dependence on a “mass-damping” parameter, in this case S_G . Curve fit given by Equation (5.7) with $\mathcal{A} = 0.385$ and $\mathcal{B} = 0.12$. Figure from Skop and Balasubramanian (1997). 98

5.2 A typical “Griffin plot” but in linear-log form to accentuate the large amount of scatter that exists in the compiled data. Curve fit given by Equation (5.7) with $\mathcal{A} = 0.385$ and $\mathcal{B} = 0.12$. Figure from Williamson and Govardhan (2004). 99

5.3 A “Griffin plot” modified by Williamson and Govardhan to show only similar geometries in order to reduce the scatter in the reported data. Figure from Williamson and Govardhan (2004). (Note that “lower branch” data has been removed for simplicity.) 100

5.4 Select runs showing Sequence 01 response amplitude, A^* , dependence on the effective stiffness, k_{eff}^* , for various damping values 105

5.5 Select runs showing Sequence 02 response amplitude, A^* , dependence on the effective stiffness, k_{eff}^* , for various damping values 105

5.6 Select runs showing Sequence 03 response amplitude, A^* , dependence on the effective stiffness, k_{eff}^* , for various damping values 106

5.7 Select runs showing Sequence 04 response amplitude, A^* , dependence on the effective stiffness, k_{eff}^* , for various damping values 106

5.8 New “Generalized” Griffin plot showing maximum amplitude, A_{Max}^* , dependence on damping, b^* , and Reynolds number, Re 107

5.9 Detailed view of the “Generalized” Griffin plot for low damping, $b^* < 0.75$, and various Reynolds numbers, $100 \lesssim \text{Re} \lesssim 5050$ 110

5.10 Reynolds number effects on limiting amplitudes, A_{Lim}^* , over the range $200 \lesssim \text{Re} \lesssim 5050$ for our data extrapolated to zero damping. 113

5.11 Reynolds number effects on maximum amplitudes, A_{Max}^* , with small, but finite, damping values. For these cases, A_{Max}^* should approximate A_{Lim}^* fairly well since $b^* < 0.10$. Experimental data compiled by Williamson and Govardhan (2004). 113

5.12 Flow visualization showing the nearly two-dimensional flow around an oscillating cylinder at its maximum amplitude, $A_{\text{Max}}^* \approx 0.35$, for $\text{Re} \approx 200$ 118

5.13 Flow visualization showing the three dimensionality of the flow around an oscillating cylinder at its maximum amplitude, $A_{\text{Max}}^* \approx 0.55$, for $\text{Re} \approx 525$ 118

5.14 Flow visualization showing a 2S wake structure for an oscillating cylinder at its maximum amplitude, $A_{\text{Max}}^* \approx 0.61$, for $\text{Re} \approx 1000$ 120

5.15	Flow visualization showing a 2P wake structure for an oscillating cylinder at its maximum amplitude, $A_{\text{Max}}^* \approx 0.73$, for $\text{Re} = 2600$	120
5.16	Flow visualization showing a 2S wake structure for an oscillating cylinder at its maximum amplitude, $A_{\text{Max}}^* \approx 0.35$, for $\text{Re} = 200$	122
5.17	Flow visualization showing a 2P wake structure for an oscillating cylinder at its maximum amplitude, $A_{\text{Max}}^* \approx 0.78$, for $\text{Re} = 5050$	122
5.18	Select runs from Sequence 02 showing the changes to the amplitude response profile for heavily damped systems, $b^* _{A_{\text{Max}}^*} > 1.75$, along with lightly damped systems for reference. Damping values for each run can be found in Table 5.1.	124
5.19	Select runs from Sequence 04 showing the changes to the amplitude response profile for heavily damped systems, $b^* _{A_{\text{Max}}^*} > 1.75$, along with lightly damped systems for reference. Damping values for each run can be found in Table 5.1.	124
6.1	Erosion of the upper branch for Sequence 03. Solid lines represent increasing tunnel velocities and dashed lines represent decreasing tunnel velocities. Damping values for each run can be found in Table 5.1.	127
6.2	Amplitude response downward jump from the upper branch to initial branch for decreasing U_R along with its dependence on the WR-plane 2S/2P dividing curve. Shown are selected runs from Sequence 02 – Sequence 04; the damping values for each run can be found in Table 5.1.	129
6.3	Amplitude response upward jump from the initial branch to upper branch for increasing U_R along with the WR-plane 2S/2P dividing curve displayed for reference. Shown are selected runs from Sequence 02 – Sequence 04; the damping values for each run can be found in Table 5.1.	129
6.4	Transition region between the upper branch and lower branch, highlighted by the gray ellipse, shown in the traditional formulation.	130
6.5	Transition region between the upper branch and lower branch, highlighted by the gray ellipse, shown in the effective stiffness formulation.	131
6.6	Cycle-by-cycle amplitude results from four tests of Run04(a) in the transition region between the upper and lower branch.	132
6.7	The corresponding cycle-by-cycle frequency results from four tests of Run04(a) in the transition region between the upper and lower branch.	132

6.8	Cycle-by-cycle amplitude results from the four tests in Figure 6.6 shown in a single histogram.	133
6.9	Cycle-by-cycle frequency results from the four tests in Figure 6.7 shown in a histogram.	134
6.10	Amplitude response profiles for Sequence 01 showing the lower branch to desynchronized state hysteresis. Solid lines and white data points show increasing tunnel velocities and dashed lines and colored data points show decreasing tunnel velocities. Damping values for each run can be found in Table 5.1.	135
6.11	Test methodology for transient behavior (TB) tests involving velocity- and damping-induced transients on TB01 configuration.	138
6.12	Test methodology for transient behavior (TB) tests involving velocity- and damping-induced transient on TB02 configuration.	138
6.13	Time traces of TB01(ID) amplitudes through the discontinuous region for increasing (left) and decreasing (right) tunnel velocities; blue data: $U_R = 0.816$, red data: $U_R = 0.834$, and green data: $U_R = 0.852$; $-$: steady-state, \circ : transient.	140
6.14	Frequency-amplitude mapping of TB01(ID) through the discontinuous region for increasing (left) and decreasing (right) tunnel velocities; blue data: $U_R = 0.816$, red data: $U_R = 0.834$, and green data: $U_R = 0.852$; \square : steady-state, \circ : transient. Also shown is the WR-plane 2S/2P dividing curve.	140
6.15	Time traces of TB02(ID) amplitudes through the discontinuous region for increasing (left) and decreasing (right) tunnel velocities; purple data: $U_R = 0.630$, blue data: $U_R = 0.654$, red data: $U_R = 0.678$, and green data: $U_R = 0.702$; $-$: steady-state, \circ : transient.	142
6.16	Frequency-amplitude mapping of TB02(ID) through the discontinuous region for increasing (left) and decreasing (right) tunnel velocities; purple data: $U_R = 0.630$, blue data: $U_R = 0.654$, red data: $U_R = 0.678$, and green data: $U_R = 0.702$; \square : steady-state, \circ : transient. Also shown is the WR-plane 2S/2P dividing curve.	142

6.17	Time traces of TB01 amplitudes through the discontinuous region involving damping decreases (left) and increases (right) at $U_R = 0.852$; blue data: low damping (LD) state, red data: high damping (HD) state; $-$: steady-state, \circ : transient.	146
6.18	Frequency-amplitude mapping of TB01 through the discontinuous region involving damping decreases (left) and increases (right) at $U_R = 0.852$; blue data: low damping (LD) state, red data: high damping (HD) state; \square : steady-state, \circ : transient. Also shown is the WR-plane 2S/2P dividing curve.	146
6.19	Time traces of TB02 amplitudes through the discontinuous region involving damping decreases (left) and increases (right) at either $U_R = 0.702$ (top and middle plots) or $U_R = 0.736$ (bottom plots); blue data: low damping (LD) state, purple data: “marginally stable” low damping state, green data: expected low damping state, red data: high damping (HD) state; $-$: steady state, \circ : transient.	148
6.20	Frequency-amplitude mapping of TB02 through the discontinuous region involving damping decreases (left) and increases (right) at $U_R = 0.702$ or $U_R = 0.736$; blue data: low damping (LD) state, purple data: “marginally stable” low damping state, green data: expected low damping state, red data: high damping (HD) state; \square : steady-state, \circ : transient. Also shown is the WR-plane 2S/2P dividing curve.	148
A.1	Noisy measured signal data (green data) along with the “fitted” ideal power spectrum (black data) and the Wiener filtered results (red data). Note that for frequencies below about 1 Hz, the measured noisy signal and the filtered results coincide.	161
A.2	Comparison of the optimal Wiener filter to a simple high frequency truncation filter. The measured noisy signal (green data) is shown along with the truncation filter results (blue data) and Wiener filter results (red data).	163
B.1	Least-squares linear curve fit to the amplitudes of a free-vibration natural decay test undergoing a large number of oscillations. The actual amplitude (blue data) deviates very little from the linear curve fit (green line) and only noticeably at the beginning and end of the time trace.	167

B.2	Least-squares exponentially decaying sine wave curve fit to the full displacement time trace of a free-vibration natural decay test undergoing a limited number of oscillations. The actual displacement (yellow data) deviates very little from the curve fit (red data).	167
D.1	Differences in maximum amplitudes, A_{Max}^* , determined by averaging every cycle (full average value) and by averaging the largest 10% amplitude cycles (top 10% average value).	172
D.2	Increasing percent difference between the top 10% average value and full average value methods as a function of Reynolds number. Dashed line is least-squares linear curve fit, for $\text{Re} < 10^4$, and constant value approximation, for $\text{Re} > 10^4$	172

List of Tables

3.1	Characteristics of the circular cylinders used in this study.	41
3.2	Various fixed system parameters for each test configuration.	47
3.3	System configurations used for the gap distance (GD) tests. All GD test configurations had $D = 10$ mm, $m = 1.930$ kg, and $k = 205$ N/m.	48
3.4	Reynolds number and nondimensional laminar boundary layer thickness at various tunnel velocities using two different characteristic lengths, downstream distance from the beginning of the test section to the cylinder, $x = 50.5$ cm, and diameter of cylinder, $D = 10$ mm.	49
3.5	System configurations used for the starting method (SM) tests.	51
4.1	System configurations used to compare the traditional and effective stiffness formulations.	55
4.2	Comparison between two predictive relationships for $U _{A_{\text{Max}}^*}$. Note that all $U _{A_{\text{Max}}^*}$ values are given in cm/s.	91
5.1	Imposed system damping values for sequences with moderate Reynolds number $525 \lesssim \text{Re} _{A_{\text{Max}}^*} \lesssim 2600$	104
5.2	Imposed system damping values for sequences with $\text{Re} _{A_{\text{Max}}^*} < 500$	109
5.3	Imposed system damping values for sequences with $\text{Re} _{A_{\text{Max}}^*} > 10^3$	109
6.1	System configurations for the transient behavior (TB) tests	136
6.2	Imposed system damping values for damping-induced transient tests	137

List of Symbols

Roman symbols

A	oscillation amplitude
A_{Max}	maximum amplitude
A^*	nondimensional oscillation amplitude
A_{Max}^*	nondimensional maximum amplitude
A_{Lim}^*	nondimensional limiting amplitude
\mathcal{A}	curve-fitting constant
a	characteristic area
B	magnetic field strength
\mathcal{B}	curve-fitting constant
b	total system damping
b_{mag}	imposed magnetic damping
b^*	nondimensional damping
$b^* _{A_{\text{Max}}^*}$	nondimensional damping at maximum amplitude
C_a	added mass coefficient
C_D	drag coefficient
C_L	lift coefficient
$C_{L,o}$	amplitude of sinusoidal lift
$C_{L'}$	fluctuating lift coefficient
\mathcal{C}	curve-fitting constant
D	cylinder diameter
F	force
F_L	lift force
$F_{L,o}$	amplitude of sinusoidal lift force

F_L'	root-mean-square lift fluctuations
f	oscillation frequency
f_N	system natural frequency in air
f_{shed}	observed fixed cylinder shedding frequency
f_{St}	predicted fixed cylinder shedding frequency
f^*	nondimensional oscillation frequency
f_{tr}^*	traditional nondimensional oscillation frequency
$f^* _{A_{Max}^*}$	nondimensional oscillation frequency at maximum amplitude
G	gap distance between cylinder and bottom of test section
i	imaginary number
i_{sup}	supplied current to electromagnets
i_{eddy}	local eddy current
k	total system elasticity (stiffness)
k_{rel}	relative permeability
k^*	nondimensional elasticity (stiffness)
k_{eff}^*	effective stiffness parameter
$k_{eff}^* _{A_{Max}^*}$	effective stiffness at maximum amplitude
L	wetted cylinder length
L_{total}	total cylinder length
ℓ	characteristic length scale
ℓ_c	spanwise segment length
m	total system mass
m^*	nondimensional mass
m_{tr}^*	traditional nondimensional mass
m_{crit}^*	critical nondimensional mass
n	turn density (loops per unit length)
R	material resistance
Re	Reynolds number
Re_x	Reynolds number based on length scale x
$Re _{A_{Max}^*}$	Reynolds number at maximum amplitude
S_G	common mass-damping parameter

St	Strouhal number
t	time
t^*	nondimensional time
U	free-stream fluid velocity
U_R	traditional nondimensional velocity (reduced velocity)
$U _{A_{\text{Max}}^*}$	fluid velocity at maximum amplitude
V	measured LVDT voltage
V_{induced}	induced voltage
v	oscillation velocity of the conducting plate
w	width (non-oscillating direction) of the conducting plate
x	downstream distance length scale
Y^*	nondimensional displacement
\dot{Y}^*	nondimensional velocity
\ddot{Y}^*	nondimensional acceleration
y	displacement
\dot{y}	velocity
\ddot{y}	acceleration

Greek symbols

α	VIV response model fitting parameter
β	VIV response model fitting parameter
γ	VIV response model fitting parameter
ζ	traditional nondimensional damping
δ	laminar, flat-plate boundary layer thickness
λ	time eigenvalues
μ	fluid dynamic viscosity
μ_o	permeability of vacuum
ν	fluid kinematic viscosity
ρ	fluid density
ω	oscillation angular frequency
ω_d	angular frequency of forcing (driving frequency)
ω_N	system natural angular frequency in air

ω^*	nondimensional oscillation angular frequency
ω_{tr}^*	traditional nondimensional oscillation angular frequency
$\omega^* _{A_{Max}^*}$	nondimensional oscillation angular frequency at maximum amplitude
ω_{St}	predicted fixed cylinder shedding angular frequency
τ	traditional nondimensional time

Chapter 1

Introduction

1.1 Importance

The potential destructive forces that can result from the interaction between a moving fluid and a structure were spectacularly displayed in 1940 with the collapse of the Tacoma Narrows Bridge. This collapse resulted from a complicated fluid-structure interaction between the gusting wind and massive bridge. This interaction caused the bridge to undergo complex oscillations that eventually reached a severe enough magnitude to cause the dramatic collapse of the bridge.

As a fluid moves past a bluff, non-streamlined, body, the fluid detaches from the body and an unsteady wake is created. This causes vortices to detach and shed from alternate sides of the body and be convected downstream by the flow. These shedding vortices produce periodic forces on the body and, in many cases, these forces are strong enough to start the body into oscillatory motion. Such behavior is known as vortex-induced vibrations (VIV). Since most objects are not streamlined, an enormous number of structures are susceptible to VIV. Some of these susceptible structures include bridges, smokestacks, underwater and hanging cables, towed objects, and off-shore platforms.

The understanding of VIV is critical in order to safely design many common engineering structures. Yet, for all the work that has been done in the past half century, many fundamental fluid mechanics and basic engineering questions remain unanswered. This fact was reinforced when, in January 2002, a tall circular steel support structure, that was part of the Vertigo thrill ride at Cedar Point, suddenly collapsed. After an investigation, the cause of the collapse was deemed to be due to a vortex-shedding phenomenon. Clearly, there is much that still needs to be learned regarding VIV.

1.2 Previous Work: One-Degree-of-Freedom Free-Vibrations of Rigid Circular Cylinders

There has been an enormous amount of research done on VIV during the past fifty years. Much of this work is documented in the comprehensive reviews of Sarpkaya (1979, 2004), Griffin and Ramberg (1982), Bearman (1984), Parkinson (1989), and Williamson and Govardhan (2004). The majority of the work has involved two different approaches to the problem, free- and forced-vibration studies. Free-vibration studies themselves have involved both experimental and computational investigations of one- and two-degree-of-freedom motion on rigid, flexible, pivoted, and cantilevered cylinders. The most popular geometry for experiments is the rigid circular cylinder with only one-degree-of-freedom motion (transverse to the flow direction). However, for simulations, there is not such a preferred configuration and one can find both one- and two-degree-of-freedom motion on both rigid and flexible cylinders. Comparably, forced-oscillation studies are much less diverse, most of them involve the experimental investigation of constant amplitude and frequency movement of a rigid cylinder undergoing one-degree-of-freedom motion.

Since this thesis only involves the canonical geometry for VIV (one-degree-of-freedom, rigid circular cylinder), we will mainly discuss previous work involving this type of configuration. Furthermore, since this geometry still involves an enormous amount of literature, we will concentrate on previous work that involved understanding the amplitude and frequency responses, the wake structures, and the damping and Reynolds number effects. In the next two sections however, we will briefly discuss one-degree-of-freedom forced-vibration experiments and then two-degree-of-freedom free- and forced-vibration studies. This is done so that we can discuss how, if at all, our results and conclusions from the restrictive one-degree-of-freedom, free-vibration, rigid circular cylinder case can be generalized and applied to these two other VIV configurations. Therefore, previous work using these two configurations will be presented along with a brief discuss of the relationship and coupling to one-degree-of-freedom, free-vibrations, of rigid circular cylinders.

For free-vibrations, at least two types of system response are possible for VIV, as reported by Khalak and Williamson (1997b). One of these involves a small-amplitude, two-branch response and is believed to correspond to high “mass-damping”. Mass-damping refers to the historical practice of combining the system mass and damping into a single

parameter. These branches were labeled as the “initial” and the “lower” branch (using the terminology of Khalak and Williamson). This type of response is similar to what Feng (1968), and many other early researchers, observed. These early investigations involved systems that used air as the working fluid and had a nondimensional mass of $\mathcal{O}(10^2)$. The large system mass meant that the mass-damping parameter was always large, regardless of the damping. A defining characteristic of this type of response is that the frequency at which vortices are shed from the cylinder abandons the Strouhal relationship (see Section 2.3) and instead “closely” matches the natural frequency of the system. In the past, this phenomenon has been called various things including “lock-in,” “synchronization,” and “self-excited oscillations.” It is worth mentioning here that in this thesis, these terms will each have their own meaning. “Lock-in” will refer to when the shedding frequency breaks from the Strouhal relationship *and* matches the natural frequency of the system. “Synchronization,” on the other hand, will only mean that the shedding frequency has broken from the Strouhal relationship but is matched to a particular frequency that is not necessarily the natural frequency. Therefore, lock-in is a special case of synchronization. Finally, although the exact phrase “self-excited oscillations” will not be used, similar terms such as free-vibrations, and the more general term vortex-induced vibrations (VIV), will refer to a fluid driven oscillating system, regardless of the shedding frequency.

The second type of reported response is a large-amplitude, three-branch response that was believed to result from low mass-damping. These three branches were labeled the “initial,” “upper,” and “lower” branches, also by Khalak and Williamson (1997b). This type of response has been seen more recently in systems that used water as their working fluid, so that the nondimensional mass was $\mathcal{O}(10)$, and had extremely low inherent damping. This allowed for a very small mass-damping parameter. Much of the current work on VIV has centered around systems with low mass and damping and the resultant interesting behavior. Besides the large-amplitude, three-branch response, one interesting behavior these types of systems exhibit is a much wider response range, or range of flow velocities that cause a response. Griffin and Ramberg (1982) noted the widening of the response region for these small mass type systems. Work done with high mass-damping, small-amplitude response systems resulted in the belief that substantial amplitudes could only result from lock-in. However, this is not the case with low mass-damping system. Therefore, another interesting behavior that they display is that only synchronization is needed for substantial amplitudes.

In Govardhan and Williamson (2000), they showed the departure that the frequency could take from classic lock-in while still producing large-amplitude oscillations. In order to clearly show this however, they needed a small nondimensional mass of $\mathcal{O}(1)$, which explained why early investigators only saw lock-in behavior.

The characteristics of the wake behind an oscillating cylinder were studied in detail by various investigators. Early work was restricted to the small-amplitude, two-branch response system. The velocity fluctuations in the near wake as well as the phase angle between the displacement and velocity fluctuations were measured by Griffin (1972). Lift coefficients, energy transfer, and flow visualization photographs of the wake were presented in Griffin et al. (1973). Brika and Laneville (1993) showed the wake structure of the initial and lower branches using smoke visualization. We mention their work in this section even though they used a flexible, free-vibrating cable. Later work, with smaller mass-damping valued systems, explored the wake for a large-amplitude, three-branch response system. Khalak and Williamson (1999) measured lift and drag coefficients over the entire response region and did hydrogen bubble flow visualization. The wake structure behind large-amplitude, three-branch systems and small-amplitude, two-branch systems was carried out in detail by Govardhan and Williamson (2000). They found (using the terminology of Williamson and Roshko (1988)) that the wake structure of the initial branch had two single vortices shed per cycle (2S) while the wake structure of upper and lower branches both had two pairs of vortices shed per cycle (2P).

Some early studies of VIV explored the effects of damping on the response behavior of the system. For instance, Vickery and Watkins (1964) reported peak amplitudes in air and water against a mass-damping parameter and Scruton (1965) plotted the amplitude response profile for three different damping values. The most extensive damping study may have been by Feng (1968) who explored the effects of damping on both the amplitude and frequency response profiles for five different damping values. Feng used an electromagnetic eddy-current damper designed by Smith (1962) to impose controlled damping values on his system. However, Feng's system had high mass-damping (due to the large m^* since his working fluid was air) and was constrained to the small-amplitude, two-branch response behavior. Due to this, he was only able to look at what effect a threefold increase in damping had on a low-amplitude response profile.

More recent studies of damping effects on VIV have been largely directed toward low

values of system mass and damping and the high amplitudes that they allow. Over the past twenty-five years, the mass-damping parameter has replaced the actual system damping value as the parameter that is reported in damping studies. Unfortunately, most studies involving mass-damping effects have only looked at the maximum amplitude response point of the system. A few studies have investigated the entire response behavior. For example, Khalak and Williamson (1997a) have full amplitude response curves of three different system masses, each exposed to four different damping values. However, as in the past, the range of damping values they spanned was small and a change in system response was not seen, other than a slight decrease in the maximum amplitude. Another recent study was by Hover et al. (1997) who used a force-feedback controlled oscillation apparatus and reported total lift coefficient, phase angle, and amplitude response. Although they spanned a much larger range of damping values than previous investigators, the amplitude response profile remained a large-amplitude type response with slight changes until the highest damped case, which resulted in almost no response.

Even though it is perhaps the most important nondimensional number in fluid mechanics, most early studies of VIV did not emphasize Reynolds number. While most researchers did make reference to the Reynolds number of their experiments, they usually only gave a range of Reynolds numbers corresponding to when amplitudes occurred. Recently however, Reynolds number has begun to be recognized as an extremely important parameter in VIV. Consequently, research has begun to look directly at Reynolds number effects. Anagnostopoulos and Bearman (1992) explored VIV at low Reynolds number, $Re \approx 100$, and compared this to higher Reynolds number experiments. Ryan et al. (2005) simulated Reynolds number effects associated with the “critical mass” defined by Govardhan and Williamson (2002). And the importance of the Reynolds number on the maximum amplitude was pointed out by Klamo et al. (2005).

Finally, we briefly mention a different approach to the study of VIV, working on methods to suppress them. Much of this work is summarized in the review by Zdravkovich (1981) and books by Blevins (1994) and Sumer and Fredsoe (1997). Designing a structure that will not be excited by any of the flow velocities it experiences while in service is not always possible. Nor is it always possible to have a large enough structural damping to keep the excited oscillations small. Therefore, various devices that are added to the structure to interfere with the shedding vortices have been studied. Although this list is not inclusive,

we briefly mention three different suppression devices. Long splitter plates, long enough to extend past the vortex formation region, were studied by Roshko (1954), Apelt et al. (1973), Sallet (1970), and Stansby and Pinchbeck (1986). Helical strakes, originally proposed by Scruton and Walshe (1957), were investigated by Woodgate and Maybrey (1959), Cowdrey and Lawes (1959), Jones and Lamb (1992), and Branković (2004). Finally, helical wires were studied by Chyu and Rockwell (2002) and Hover et al. (2001). Although this is an important part of studying VIV, suppression strategies will not be discussed in this thesis.

1.3 Connection to One-Degree-of-Freedom Forced-Vibrations of Cylinders

The main emphasis of most forced-vibration studies is to measure the fluctuating lift and drag forces, vortex shedding frequencies, and phase difference between the motion and forces. Also, the wake is usually observed to look for recognizable structures. Some of the first work done with forced-vibrations was conducted by Bishop and Hassan (1964) in which they measured the fluctuating lift and drag forces. They also noted that when the frequency of the forced oscillations was close to the Strouhal frequency, the wake and cylinder frequencies became “synchronized.” This synchronization lasted over a large range of oscillation frequencies and they termed it the “range of synchronization.” They also noticed that their system exhibited hysteresis. Other early experiments also measured the lift coefficient and phase angle (Protos et al., 1968; Toebes, 1969; Stansby, 1976). Sarpkaya (1977, 1978) did extensive measurements of the transverse force coefficient and separated it into an inertial component, in-phase with the cylinder acceleration, and a drag component, in-phase with the cylinder velocity.

More recent experiments have focused on collecting force measurements over a wide Reynolds number range, predicting free-vibrations behavior from forced-vibration results, and looking at wake transitions. Sarpkaya (2004) continued his earlier forced-vibration studies but spanned a much larger Reynolds number range as well as specifically looking for Reynolds number effects. Low Reynolds number forced-vibration experiments were carried out by Koopmann (1967) and Griffin (1971). Both Staubli (1983) and Sarpkaya (1978) used forced-vibration force measurements to predict free-vibration VIV behavior. Moe and Wu (1990) compared forced-vibration results to free-vibration results for both one- and

two-degree-of-freedom motion. Forces and phase angles from free- and forced-vibration tests were compared under identical conditions in Morse and Williamson (2006). Carberry et al. (2001, 2003, 2005) studied the transitions in the wake as the system changes from a “low-frequency state” to a “high-frequency state.” By studying these transitions, they discovered a self-excited change from a low-frequency state to a high-frequency state but never the reverse. They also discovered an “intermediate state” that has certain features similar with each of the other two states.

Finally, at the merging point between free- and forced-vibration experiments, Hover et al. (1997, 1998) used a force-feedback testing apparatus. Their system involved measuring the instantaneous forces on an oscillating cylinder, using these results in a numerical simulation of an equivalent mass-damper-spring system, and then finally driving the cylinder to the position predicted by the simulation. The process was then repeated for a long enough time to allow for a large number of oscillation cycles to be completed. Besides showing the resultant amplitude, frequency, force coefficients, and phase angles, they also produced a plot showing excitation contours (which shows the direction of energy transfer between the cylinder and fluid stream).

An important question involves how much of the results from forced-vibration tests can be applied to free-vibrations and thus predict naturally occurring VIV. The differences between free- and forced-vibrations are numerous. Free-vibration tests almost always involve generating the response profile by spanning all tunnel velocities of interest, which means that each point is at a *different* Reynolds number. On the other hand, forced-vibration tests look at the response profile by varying the amplitude and frequency of oscillation at a constant tunnel velocity, and thus a *constant* Reynolds number. Also, free-vibration tests are driven by a coupling between the wake and body motion, each affecting the other, and therefore the response depends not only on the present state but also on *past* states. The resultant motion varies in both amplitude and frequency over time. Forced-vibration tests involve driving the cylinder at a predetermined constant amplitude and frequency with no possibility for the wake to affect the motion. The cases are clearly not the same, therefore the important question is what, if anything, can one obtain from a forced-vibration test that can be applied to predict free-vibration behavior.

If the system parameters are such that the amplitude and frequency fluctuations are small, and thus the motion is well approximated by a constant amplitude and frequency

sine wave, then the measured forces from a forced-vibration test will compare reasonably well to results from a free-vibration test. This will be true as long as the tests match the Reynolds number and geometry arrangement, among other things. However, these limitations greatly restrict when such a strategy can be used. For instance, “beating” is usually observed at the initial onset of the response for all systems and certain systems have amplitude variations throughout their response range of around 10 percent. Using force measurements from constant amplitude and frequency forced-vibration experiments will not be able to reproduce such complicated motions.

In an attempt to reproduce large fluctuating motions more accurately, Morse and Williamson (2006) split the continuous response from a free-vibration test into two separate response behaviors, one that had response characteristics of the upper branch and the other had lower branch response characteristics. They then noted that they could produce similar force and phase angle results by conducting two *separate* forced experiments, one at each of the average amplitude and frequency values of the upper and lower branches. While this result suggests an interesting way to attempt to use forced-vibration experiment data in regions that display variations between two dominant states, there are still problems. First, one does not know when the free-vibration response would move from one state toward the other. And second, as the free-vibrations system moves between states, one does not have any force or phase angle information for these transients. Even if one attempted to perform a time-varying amplitude and frequency forced-vibration test, the results could very likely not be applicable to free-vibrations. In free-vibrations, there is a coupling between the cylinder motion and the wake. Slight changes to the cylinder motion will cause changes to the wake, which in turn alters the motion of the cylinder. However, in forced-vibration tests, the cylinder affects the wake but the wake cannot affect the cylinder. Any changes in the wake have no influence on the motion.

1.4 Connection to Two-Degree-of-Freedom Free-, Forced-, and Simulated-Vibrations of Cylinders

Since most naturally occurring VIV involves a two-degree-of-freedom geometry, there has been an extensive amount of experimental work done involving such systems. Moe and Wu (1990) and Sarpkaya (1995) each did free-vibration studies on unmatched masses and natural

frequencies in the two directions of freedom. Jauvtis and Williamson (2003, 2004) did free-vibrations studies on a pendulum system, which allowed for matched masses and natural frequencies in the two directions of freedom. Vandiver and Jong (1987) and Vandiver (1993) have carried out field and laboratory tests of cable dynamics. Tests on a flexible cylinder exposed to vertically sheared flows were conducted by Marcollo and Hinwood (2006). Work at high Reynolds number, using various arrangements, including a two-degree-of-freedom pinned beam, has been carried out by Triantafyllou et al. (2003). There has even been two-degree-of-freedom forced-oscillations, carried out by Jeon and Gharib (2001) where they restricted the motion to be a figure-eight pattern.

There is an enormous body of computational work involving VIV, much of it involving two-degree-of-freedom vibrations. However, due to the limitations that a direct numerical simulation (DNS) puts on Reynolds number, almost all of these are for systems with $Re \approx \mathcal{O}(10^2)$. Blackburn and Karniadakis (1993) and Blackburn and Henderson (1996) simulated both free- and forced-vibrations in two dimensions using a 2D DNS code. Mittal and Kumar (1999) did similar studies while Newman and Karniadakis (1996, 1997) explored two-degree-of-freedom flexible cables using a 3D DNS code. Zhou et al. (1999) used a 2D vortex-in-cell (VIC) code to simulate their two-degree-of-freedom system. Finally, Singh and Mittal (2005) spanned a wide range of low Reynolds numbers using a 2D DNS code. In order to simulate higher Reynolds numbers, some researchers have used RANS methods, such as Guilmineau and Queutey (2004), and LES methods, such as Zhang and Dalton (1996) or Al-Jamal and Dalton (2004).

Due to the extra degree of freedom, two-degree-of-freedom VIV motion has the potential to be governed by a much larger number of important parameters. The complicated two-dimensional motion that two-degree-of-freedom systems can take compared to the straight-line motion of a one-degree-of-freedom system is another difficulty. These are some of the reasons why many investigations of VIV have used the most basic system, a one-degree-of-freedom rigid cylinder. It is hoped that what has been learned from such idealized situations can be extended to the more complicated two-degree-of-freedom arrangements. However, because of these extra complications, there is a possibility that only some of the results from one-degree-of-freedom tests can be applied to the more realistic, two-degree-of-freedom situations.

Because there is a large amount of variability in the predicted amplitudes of even one-

degree-of-freedom simulations, we will not attempt to include simulation results in our discussion. There is another reason as well that is worth noting. We attempt to determine if, or under what conditions, we can use one-degree-of-freedom results to predict naturally occurring two-degree-of-freedom VIV. For this prediction to succeed, the Reynolds numbers of the two situations must be matched. However, naturally occurring VIV usually involves Reynolds numbers that are orders of magnitude higher than the low Reynolds numbers that simulations are capable of, making the simulation results very limited for predictive purposes.

Due to the complicated non-linear behavior of the fluid system, the motions in each direction of a two-degree-of-freedom system are not independent of each other. The past motion of the cylinder will affect the nature of the flow around the cylinder, including the separation points, correlation length, and pressure distribution, which will in turn affect the motion of the cylinder (Moe and Wu, 1990). Therefore, we must determine under what conditions two-degree-of-freedom systems have *similar* behavior to the idealized one-degree-of-freedom systems. It appears that if the system natural frequencies are matched in each direction, then the resultant transverse component of the two-degree-of-freedom motion is very similar to the one-degree-of-freedom results. In fact, Jauvtis and Williamson (2004) also matched the mass ratios in each direction and found almost identical transverse component behavior when compared to one-degree-of-freedom results. This included seeing the same distinct branches and corresponding wake structures, down to a mass ratio as low as $m_{tr}^* \approx 6$. When Sarpkaya (1995) only matched the natural frequencies, he saw about a 20 percent increase in maximum amplitude and response range. Triantafyllou et al. (2003) ran one- and two-degree-of-freedom tests on the same system at high Reynolds number and observed the same response trends in both cases. However, when the natural frequencies are not matched (Moe and Wu, 1990; Sarpkaya, 1995), the distinct response branches are no longer seen and the maximum amplitude occurs at a much higher reduced velocity value. Also, even for cases with matched masses and natural frequencies, if the nondimensional mass drops below $m_{tr}^* \approx 6$, then new branches and wake states exist and the response region around the large amplitude portion is fundamentally different. Finally, the wake dynamics behind flexible cylinders is different enough such that results from one-degree-of-freedom tests cannot be used as pointed out by Vandiver and Jong (1987) and Marcollo and Hinwood (2006).

1.5 Thesis Layout

Chapter 2 first covers the basic topics associated with bluff-body separated flow, for both stationary and oscillating cylinders. In the second part of the chapter, we introduce and discuss how the relevant parameters for an oscillating cylinder are nondimensionalized in two different formulations.

Chapter 3 begins by explaining the experimental setup of our VIV system. The middle part of the chapter describes the various pieces of equipment that were used to acquire our results. The final part of Chapter 3 covers different exploratory tests that were done to ensure that unwanted effects were not distorting our results.

Chapter 4 is a general chapter that covers a broad range of VIV behavior. A sample of some basic results are presented so that different parameter formulations can be compared. Next, the complex time-varying motion of a VIV system is highlighted by examining both the amplitude and frequency responses as well as the wake structure. We also look at limiting structural parameters, the system singularities they cause, and the interesting behavior that results. Finally, we show and discuss the interesting fact that damping and Reynolds number have similar effects on the amplitude and frequency response profiles of our system.

Chapter 5 deals specifically with understanding the maximum amplitude that a VIV system can have. Previous work on the subject is discussed, followed by theoretical predictions, and then current results are presented. Next, the idea of limiting amplitudes, as damping tends toward zero, are discussed. Finally, some of our results are further explored with flow visualization.

Chapter 6 deals with exploring the individual cycle-by-cycle motions of a VIV system and the interesting discontinuous behavior that it allows one to observe. The first part of the chapter looks at two different hysteresis regions and explores how damping and Reynolds number affect their existence. The second part of the chapter deals with purely transient VIV behavior induced by either changing the flow velocity or system damping.

Chapter 7 is the final chapter and is a summary of the important results presented in this thesis along with recommendations for future work.

Chapter 2

Theory and Parameters

2.1 Chapter Overview

In this chapter we develop some of the mathematical theories governing VIV as well as introduce all the relevant parameters. We start in Section 2.2 by describing the characteristics of bluff-body flows and one parameter that control such flows, the Reynolds number. We discuss the connection with a stationary cylinder and introduce two more important parameters, the Strouhal number and lift coefficient, in Section 2.3. In Section 2.4 we describe the various wake structures behind an oscillating cylinder. We then move into our specific problem formulation and develop our governing equation of motion in Section 2.5. We briefly discuss two common models used to predict VIV behavior in Section 2.6. Next, we define the parameters that have traditionally been used to study VIV in Section 2.7, and the parameters we prefer to use in Section 2.8. In Section 2.9 we connect these two formulations. Finally, in Section 2.10 we introduce a new parameter, the effective stiffness, that appears in our formulation, and discuss this parameter in Section 2.11.

2.2 Bluff-Body Flows

A bluff body is any non-streamlined shape. Since few objects are actually streamlined, with the exception of airfoils at modest angles of attack, almost all objects are bluff bodies. One of the consequences of being a bluff body is that, above a certain Reynolds number, a low-pressure region develops behind them due to the flow separating as it moves around the body. This type of behavior is controlled by the Reynolds number, which is perhaps the most important parameter in fluid mechanics.

The Reynolds number, Re , is a measure of the inertial effects to the viscous effects of the fluid. The Reynolds number is defined as

$$Re = \frac{\rho \ell U}{\mu}, \quad (2.1)$$

where ρ and μ are the fluid density and dynamic viscosity, ℓ is the characteristic length scale of the flow, and U is the fluid velocity. One of the reasons that the Reynolds number is so important is that its value determines the type of flow around a bluff body.

For a stationary circular cylinder, there is a stagnation line at the leading face of the cylinder for all Reynolds number. However, the behavior of the boundary layers wrapping around both sides of the cylinder depends on the value of the Reynolds numbers (Taneda, 1956). For $Re \lesssim 5$ these boundary layers remain attached and meet at the back edge of the cylinder, forming a second stagnation point. For higher Reynolds number, these boundary layers will separate and the vorticity in the free shear layers produced from their separation rolls up into vortices and is convected downstream in the wake. For $5 \lesssim Re \lesssim 40$ these vortices are steady and the wake is symmetric. For $40 \lesssim Re \lesssim 180$ the wake becomes unstable, remains two dimensional, and the classical Kármán vortex street is formed where vortices are periodically shed from alternating sides of the cylinder. For $180 \lesssim Re \lesssim 1000$ the stationary cylinder wake becomes three dimensional (Williamson and Roshko, 1988). For $Re \gtrsim 1000$ the shear layers are turbulent. The actual Reynolds number that these various transitions occur at can be affected by the aspect ratio of the cylinder (Norberg, 1994).

2.3 Stationary Cylinder Considerations

There has been a great deal of work done on measuring various parameters of a stationary cylinder. Two of the most important ones are the frequency at which vortices are shed into the wake and the fluctuating lift coefficient.

Strouhal, while studying the Aeolian tones produced by wind passing over a wire, developed a nondimensional parameter relating the observed vortex shedding frequency, flow velocity, and wire diameter. This nondimensional frequency at which the vortices are shed

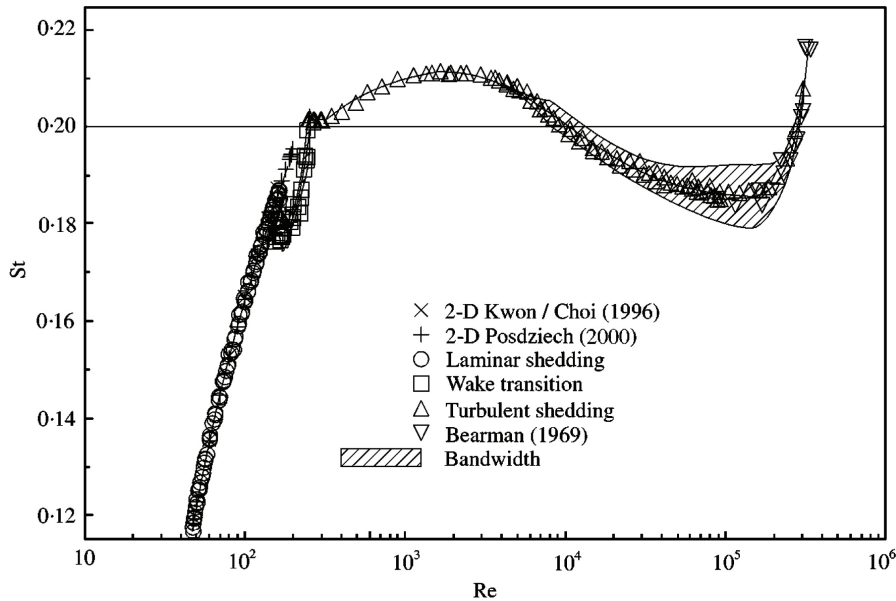


Figure 2.1: Strouhal number, St , dependence on Reynolds number, Re . Figure and references from Norberg (2001).

into the wake is known as the Strouhal number

$$St = f_{shed} \frac{D}{U}, \quad (2.2)$$

and is obtained by nondimensionalizing the *observed* vortex shedding frequency, f_{shed} , with the cylinder diameter, D , and free-stream velocity, U . The Strouhal number dependence on Reynolds number has been investigated (Norberg, 2001) and can be seen in Figure 2.1. In this thesis, when the Strouhal number relationship, Equation (2.2), is used to *estimate* the vortex shedding frequency, then this resultant calculated shedding frequency will be denoted as f_{St} . Although at times the Strouhal frequency is used by some to characterize the vortex shedding frequency of both stationary and oscillating cylinders, we restrict the use of the term Strouhal frequency to refer to the shedding frequency of *only* a stationary cylinder.

A stationary cylinder, or similar bluff object, will experience a force due to its interaction with the fluid moving past it. This force can be decomposed into two orthogonal components, one in the direction of the flow path, called the drag force, and one transverse to the

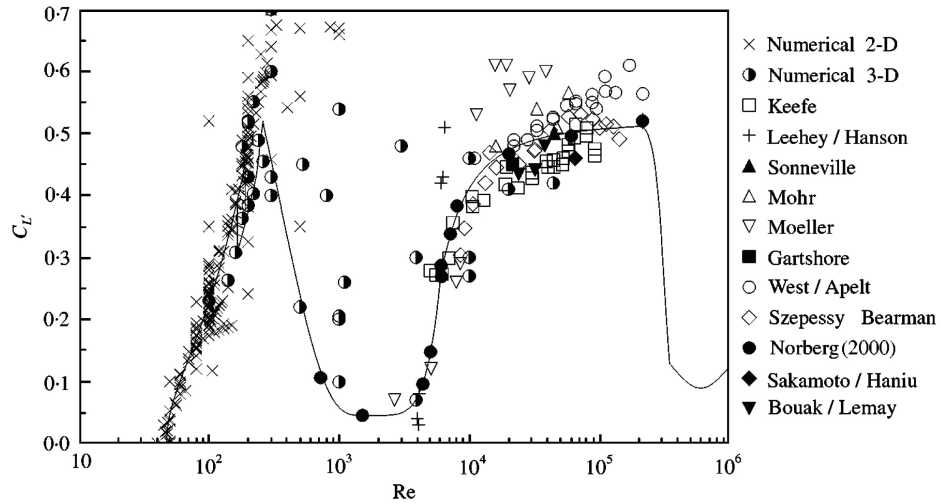


Figure 2.2: Root-mean-square fluctuating lift coefficient, C_L' for a stationary circular cylinder as a function of Reynolds number, Re . Figure and references from Norberg (2001).

flow path, called the lift force. This leads to an important parameter, the nondimensional lift force, known as the lift coefficient,

$$C_L = \frac{F_L}{\frac{1}{2}\rho a U^2}, \quad (2.3)$$

and is obtained by nondimensionalizing the lift force, F_L , with the fluid density, ρ , characteristic area of the body, a , and free-stream fluid velocity, U . This is a general definition that is used for any body shape.

For a stationary circular cylinder, even though there is periodic shedding from alternating sides of the body, due to symmetry, the time-averaged lift coefficient is zero. Instead, the fluctuating lift is of interest. Like the Strouhal number, this fluctuating lift also shows a dependence on Reynolds number. Norberg (2001) experimentally measured this fluctuating lift on a circular cylinder and his results are shown in Figure 2.2. This fluctuating lift coefficient is defined as

$$C_L' = \frac{2F_L'}{\rho D \ell_c U^2}, \quad (2.4)$$

where F_L' is the root-mean-square lift fluctuations which act on a cylinder with diameter D and spanwise segment of length ℓ_c . The other parameters were defined in Equation (2.3).

2.4 Oscillating Cylinder Wake Structure

For a stationary cylinder with $\text{Re} \gtrsim 40$, the wake takes on only one general structure, the classic von Kármán vortex street. This involves the shedding of opposite signed vortices from alternating sides of the body into the wake. These structures are convected downstream by the flow and eventually are dissipated away. The three dimensionality and stability of this wake structure are controlled by the Reynolds number. However, if the body is now allowed to oscillate transverse to the flow direction, various other structures in the wake are possible. These various wake structures were investigated and reported by Williamson and Roshko (1988). In that work, they present a map of the amplitude and frequency space for the forced oscillations of a cylinder and show the wake structure that is present for a given oscillation amplitude and frequency at the Reynolds number they investigated. The wake structures are labeled based on the number of vortices shed per cycle. For example, a 2S wake structure involves two single vortices shed per cycle and a 2P wake structure involves two pair of vortices (four total vortices) shed per cycle. There can be combinations of these single and pair vortices, for example S+P, which involves a single and a pair of vortices shed per cycle. The map that Williamson and Roshko produced has become known as the Williamson-Roshko plane (WR-plane, henceforth). The full plane space can be seen in Figure 2.3 and a detailed view of the 2S and 2P regions, which, as we will see, are important in VIV, can be seen in Figure 2.4.

2.5 Governing Equation

The canonical arrangement for the study of VIV has been the elastically-mounted, rigid circular cylinder in cross-flow that is restricted to motion only in the transverse direction. Consider such a system, as shown in Figure 2.5, with the structural side characterized with mass, m , damping, b , and elasticity, k . The fluid side of the system is characterized by the free-stream fluid velocity, U , and fluid properties of density, ρ , and dynamic viscosity, μ . The characteristic length scale for the system is the cylinder diameter, D .

The system shown in Figure 2.5 is a classical forced mass, damper, spring system with the fluid supplying the forcing term. Such a system has a well-known governing equation of motion given by

$$m\ddot{y} + b\dot{y} + ky = F_L, \quad (2.5)$$

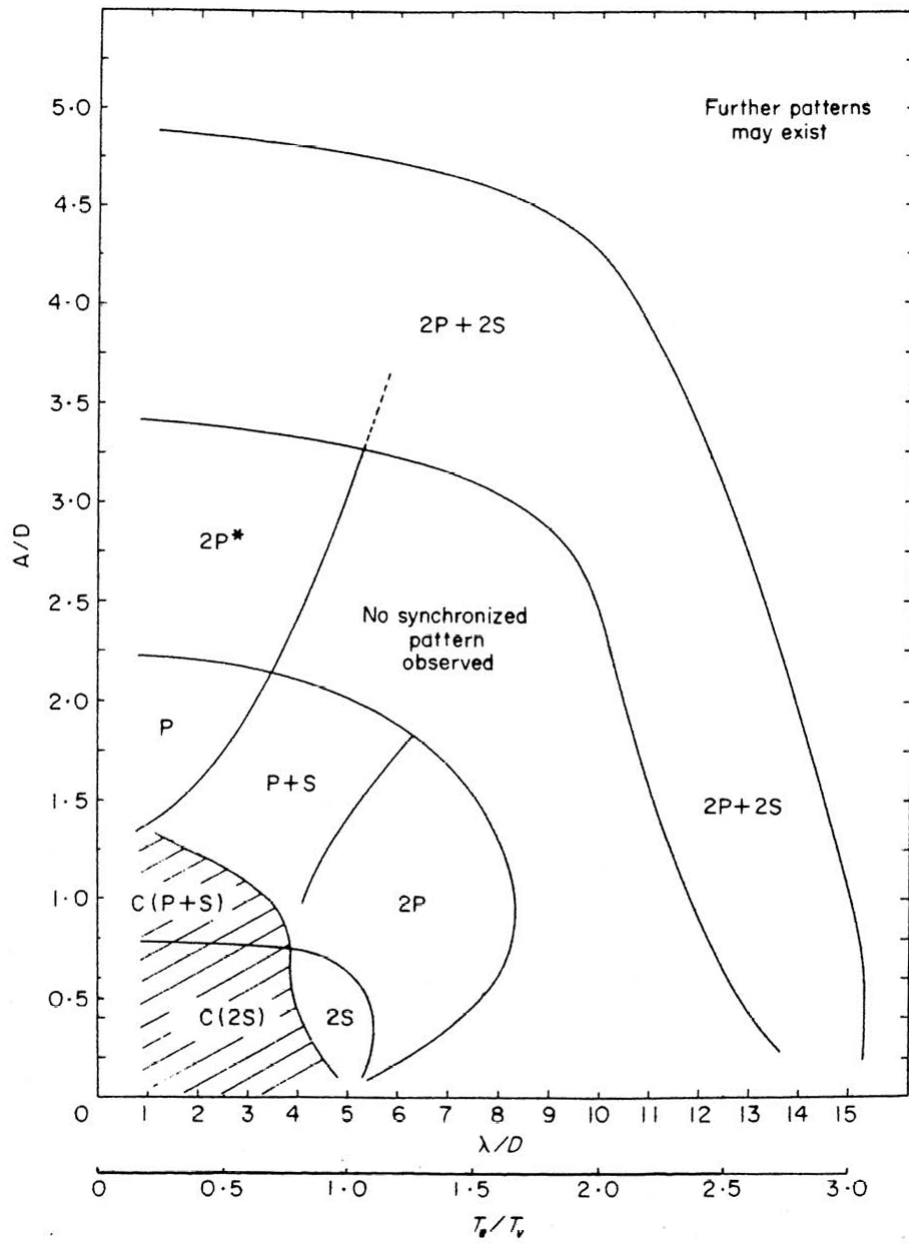


Figure 2.3: Full Williamson-Roshko plane mapping of the various possible wake structures behind the forced oscillations of a circular cylinder. Figure and parameter definitions from Williamson and Roshko (1988).

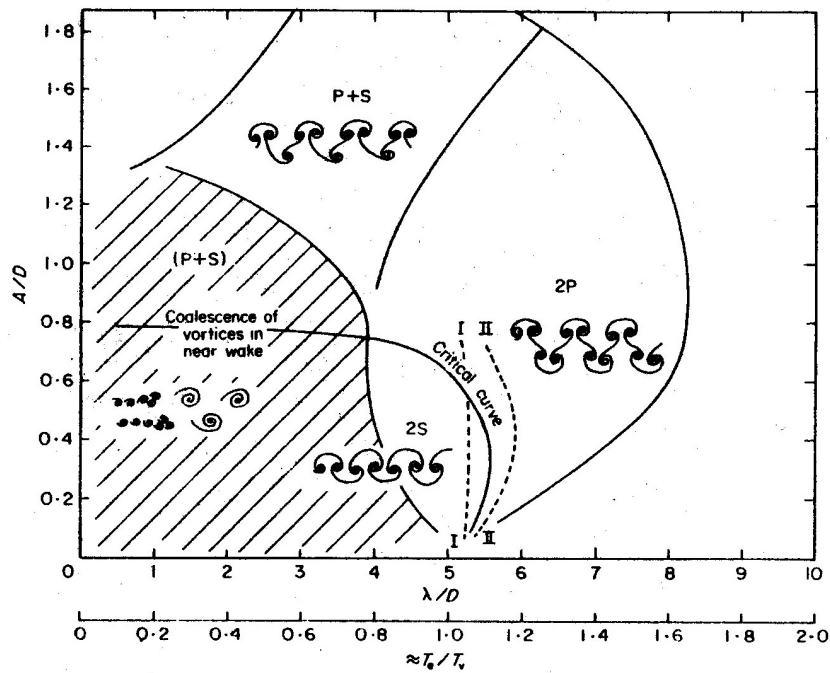


Figure 2.4: Detailed Williamson-Roshko plane mapping of the 2S and 2P wake structures behind the forced oscillations of a circular cylinder. Figure and parameter definitions from Williamson and Roshko (1988).

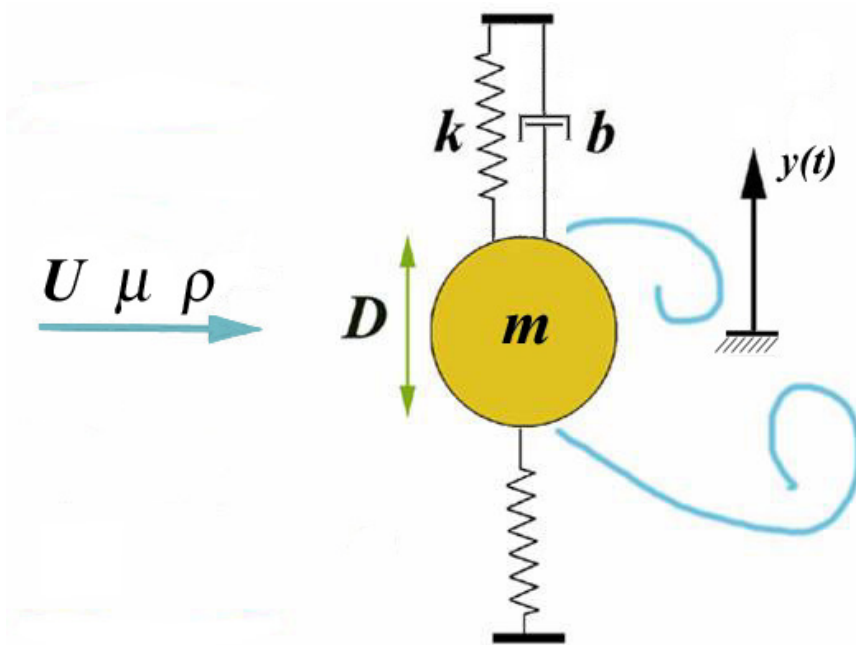


Figure 2.5: Canonical arrangement for the study of vortex-induced vibrations (VIV).

where y , \dot{y} , and \ddot{y} are the displacement, velocity, and acceleration in the cross-flow direction and all the parameters are currently dimensional. The fluid forcing term is labeled F_L since only the lift component of the fluid force contributes to the motion. Using the definition of the lift coefficient, Equation (2.3) in Section 2.3, one can rewrite Equation (2.5) as

$$m\ddot{y} + b\dot{y} + ky = \frac{1}{2}\rho a U^2 C_L . \quad (2.6)$$

Various nondimensional groups have been used in previous studies to nondimensionalize the equation and those groups will be discussed in Sections 2.7 and 2.8.

2.6 Various Vortex-Induced Vibration Response Models

At the core of modeling VIV, one must determine a relationship between the time-varying lift coefficient, $C_L(t^*)$, and its dependence on various parameters, such as Reynolds number, Re , cylinder displacement, Y^* , velocity, \dot{Y}^* , and acceleration, \ddot{Y}^* . This relationship could then be combined with the governing equation of motion, Equation (2.6), to solve for the amplitude and frequency behavior of the system. However, the dependence of the lift coefficient on these parameters is quite complex and the functional relationships are unknown. Many researchers have attempted to reproduce VIV behavior by using various simplified lift coefficient models. We discuss two of the most commonly used models.

One type of simplified model is the amplitude-dependent lift model described by Blevins (1994). This model involves a sinusoidal form for the time-varying lift coefficient so that

$$C_L(t^*) = C_{L,o} \sin(\omega_{St} t^*) , \quad (2.7)$$

where $C_{L,o}$ is the amplitude of the sinusoidal lift, the frequency of forcing is at the Strouhal frequency, $\omega_{St} = 2\pi f_{St}$, and t^* is the nondimensional time. The cylinder amplitude dependence is captured in the lift amplitude term through a relationship of the form

$$C_{L,o} = \alpha + \beta A^* + \gamma A^{*2} , \quad (2.8)$$

where α , β , and γ are fitting parameters and A^* is the nondimensional cylinder oscillation amplitude in the cross-flow direction. Although with an appropriate choice of α , β , and γ

the model can capture the experimentally seen behavior, as tunnel velocity is continually increased, of initially increasing lift followed by a decrease back down to zero near the resonant condition, there are still many problems with the model. The first is that the frequency cannot be modeled as a constant value if one hopes to capture the full range of behavior. The oscillation frequency varies throughout the response range and the extent of its deviation from the natural frequency is controlled by the nondimensional mass of the system. Also, the parameters α , β , and γ need to at least be functions of Reynolds number, and likely more parameters as well.

The second type of model is the wake-oscillator model in which one usually uses a van der Pol type equation for $C_L(t^*)$ that has correct limit-cycle behavior for the fluid force of a stationary cylinder. The affinity for the van der Pol type equation results from the fact that it describes self-sustaining oscillations in which small oscillations fed energy into the system and large oscillations remove it, both of which are believed necessary in a model trying to accurately predict VIV. One of the most comprehensive of such models was constructed by Skop and Balasubramanian (1997). Their improvements to previous models involved adding an additional damping term to the fluid force model. This allowed them to obtain reasonable results in the limiting case of structural damping. However, all models of this type are problematic for low mass because in the limiting case of zero mass, the fluid force is identically zero for all time, but cylinder motions of substantial amplitudes still occur. Another problem with these types of models is that the constants appearing in the van der Pol equation depend on the actual system parameters, instead of only depending on the flow.

2.7 Traditional Formulation

Early studies of VIV involved nondimensionalizing the various parameters independently of each other and not necessarily in a consistent manner. We will refer to these resultant nondimensional parameters as the traditional parameters. The system mass, m , was nondimensionalized using the physical concept of the displaced fluid mass. This made the nondimensional mass term

$$m_{tr}^* = \frac{m}{\frac{\pi}{4}\rho LD^2}, \quad (2.9)$$

where L is the wetted length of cylinder and the other parameters have been previously defined.

The system damping, b , was nondimensionalized using the approach that is taken in classical forced vibrations analysis. In such an analysis, the system value $2\sqrt{mk}$ compared to b controls the type of system response and is thus termed the “critical” damping value (since it has units of damping). The damping is then nondimensionalized using this critical damping term. This approach was applied to the traditional formulation parameters and meant that the nondimensional damping term was given by

$$\zeta = \frac{b}{2\sqrt{mk}} = \frac{b}{2m\omega_N}, \quad (2.10)$$

where $\omega_N = \sqrt{k/m}$ is the natural angular frequency of the system in air. It is interesting to note that even the same symbol, ζ , that is used in classic vibration analysis, was used in the traditional formulation.

The elasticity, k , of the system was not explicitly nondimensionalized in this traditional approach. Instead, the free-stream tunnel velocity was nondimensionalized in a manner that was convenient for conducting experiments (since tests were carried out by spanning tunnel velocities of interest, this allowed the direct nondimensionalization of those velocities). This lead to the creation of a parameter called the reduced velocity, U_R , defined as

$$U_R = \frac{U}{\omega_N D}. \quad (2.11)$$

Although these three nondimensional groups have been presented as ad hoc parameters, some of the rational for there use can be seen by defining a nondimensional position and time as

$$Y^* = \frac{y}{D}, \quad (2.12)$$

$$\tau = \omega_N t. \quad (2.13)$$

Using this scaling for time results in the time derivatives being nondimensionalized as

$$\frac{d}{dt} = \left(\frac{d}{d\tau}\right) \left(\frac{d\tau}{dt}\right) = \omega_N \frac{d}{d\tau}, \quad (2.14)$$

by making use of the chain rule of differentiation. By substituting Equation (2.12) and Equation (2.14) into Equation (2.6) one gets

$$mD\omega_N^2\ddot{Y}^* + bD\omega_N\dot{Y}^* + kDY^* = \frac{1}{2}\rho LDU^2C_L, \quad (2.15)$$

where the time derivatives, $(\dot{})$, are now in terms of the nondimensional time, τ , and the characteristic area, a , is the wetted area of the circular cylinder, the product of diameter, D , and wetted length, L . By reorganizing terms and noting that $\omega_N = \sqrt{k/m}$, one can obtain

$$\ddot{Y}^* + \frac{b}{m\omega_N}\dot{Y}^* + Y^* = C_L \left(\frac{\frac{1}{2}\rho LD^2}{m} \right) \left(\frac{U}{\omega_N D} \right)^2, \quad (2.16)$$

where the previously defined terms in Equation (2.9), (2.10), and (2.11) can be seen. By noting these previously defined terms, one can rewrite Equation (2.16) in these traditional parameter groups

$$\ddot{Y}^* + 2\zeta\dot{Y}^* + Y^* = \frac{2}{\pi} \frac{U_R^2}{m_{tr}^*} C_L, \quad (2.17)$$

where the $2/\pi$ factor must be introduced because of the incompatible definition of m_{tr}^* previously.

The response parameters in the traditional formulation follow logically from the previous scaling of time and space. In a consistent manner to how the position was nondimensionalized in Equation (2.12), the nondimensional amplitude response is

$$A^* = \frac{A}{D}, \quad (2.18)$$

where A is the amplitude of the system oscillations. Since time was nondimensionalized with the system natural frequency in Equation (2.13), the nondimensional frequency response of the system is

$$f_{tr}^* = \frac{f}{f_N}, \quad (2.19)$$

where f_N is the system natural frequency and $\omega_N = 2\pi f_N$.

This formulation gives the governing equation of motion in terms of the traditional parameters of m_{tr}^* , ζ , and U_R . A problem with the traditional formulation is that the characteristic length and time scales lack any connection to the fluid side of the system. The parameters of time, frequency, damping, and even the fluid velocity, are nondimen-

sionalized with the structural system properties of mass and elasticity. This also causes the nondimensional parameters to break down and become undefined in the case of limiting structural parameters such as no mass or elasticity. This will be discussed more in detail in Section 4.6.

2.8 Effective Stiffness Formulation

Instead of using the structural system natural frequency to scale time, we prefer to use a fluid mechanics approach in a manner consistent with the Strouhal frequency, St (see Section 2.3). This means that we nondimensionalize time by

$$t^* = t \frac{U}{D}, \quad (2.20)$$

using a fluid time scale. Identical to the traditional formulation, Equation (2.12), we use the characteristic length scale D to nondimensionalize position

$$Y^* = \frac{y}{D}. \quad (2.21)$$

By taking such an approach, the time derivative is scaled by

$$\frac{d}{dt} = \left(\frac{d}{dt^*} \right) \left(\frac{dt^*}{dt} \right) = \left(\frac{U}{D} \right) \frac{d}{dt^*}, \quad (2.22)$$

so that only the fluid velocity and characteristic length scale are needed, there is no connection to the structural mass-damper-spring system. In essence, the time scale of our problem is the fluid time scale, not the structural oscillation time scale. By following Shiels (1998) or Gharib (1999) and substituting Equation (2.21) and Equation (2.22) into Equation (2.6) one gets

$$mD \left(\frac{U}{D} \right)^2 \ddot{Y}^* + bD \frac{U}{D} \dot{Y}^* + kDY^* = \frac{1}{2} \rho LDU^2 C_L, \quad (2.23)$$

where the time derivatives, $(\dot{})$, are now in terms of the nondimensional time, t^* , and the characteristic area, a , is again the wetted area of the circular cylinder. By simplifying terms and dividing by the necessary right-hand-side terms so that only C_L remains, one gets

$$\frac{m}{\frac{1}{2} \rho LD^2} \ddot{Y}^* + \frac{b}{\frac{1}{2} \rho LDU} \dot{Y}^* + \frac{k}{\frac{1}{2} \rho LU^2} Y^* = C_L, \quad (2.24)$$

where each of the terms is a nondimensional group. Logically naming each nondimensional group allows one to rewrite Equation (2.24) in these parameter groups

$$m^* \ddot{Y}^* + b^* \dot{Y}^* + k^* Y^* = C_L, \quad (2.25)$$

where all the parameter groups are purely mathematically derived groups. For clarity, these groups are restated. The nondimensional mass, m^* , is

$$m^* = \frac{m}{\frac{1}{2}\rho L D^2}, \quad (2.26)$$

the nondimensional damping, b^* , is

$$b^* = \frac{b}{\frac{1}{2}\rho L D U}, \quad (2.27)$$

and the nondimensional elasticity, k^* , is

$$k^* = \frac{k}{\frac{1}{2}\rho L U^2}, \quad (2.28)$$

and it should be noted again that only the fluid velocity, U , and density, ρ , and characteristic length scale of the flow, D , are needed to nondimensionalize all quantities. Our lift coefficient is defined in a consistent manner to Equation (2.3) such that

$$C_L(t^*) = \frac{F_L(t^*)}{\frac{1}{2}\rho L D U^2}. \quad (2.29)$$

Of particular interest is the response of the system, characterized by the nondimensional amplitude, A^* , and frequency, ω^* , which we define as

$$A^* = \frac{A}{D}, \quad (2.30)$$

and

$$\omega^* = \omega \frac{D}{U}, \quad (2.31)$$

where we have maintained our consistent nondimensionalization so that only the tunnel velocity, U , and characteristic length, D , are used.

2.9 Formulation Comparison

It should be noted that the two formulations, traditional and effective stiffness, are not incompatible. In fact, one can go between the various parameters in the following manner

$$m^* = \frac{\pi}{2} m_{tr}^*, \quad (2.32)$$

$$b^* = \left(\frac{\pi}{U_R} \right) m_{tr}^* \zeta, \quad (2.33)$$

$$k^* = \left(\frac{\pi}{2} \right) \frac{m_{tr}^*}{U_R^2}. \quad (2.34)$$

The mass and damping are obviously very important parameters in VIV systems. However, there has been much debate over the past quarter century, as pointed out by Sarpkaya (2004), regarding whether they each act independently, or in combination, in the form of a “mass-damping” parameter, $m^* \zeta$. This question appears to be answered by looking at the parameter formulation comparison. The mass term acts independently. However, the individual damping term, ζ , in the traditional formulation is simply poorly nondimensionalized since it needs to be combined with the mass to be meaningful in this problem. This can be seen by noting what the equivalent parameter to our b^* is in terms of the traditional formulation parameters. Our b^* term requires both the mass, m_{tr}^* , and damping, ζ , as well as the additional factor of $1/U_R$ when written in terms of traditional formulation parameters.

Another important difference between the damping terms is that the traditional formulation damping term, ζ , is a constant for a given system but the effective stiffness formulation damping term, b^* , varies for a given system during a test. This is because all of our tests will involve spanning the fluid velocities of interest and b^* contains the fluid velocity whereas ζ only contains structural parameters of the system. Therefore, to establish a damping value for a given system when using the effective stiffness formulation, we will use $b^*|_{A_{\text{Max}}^*}$, the system damping value at the maximum amplitude.

2.10 Effective Stiffness Parameter

Although the full behavior of VIV cannot be accurately captured using a constant amplitude and frequency sinusoidal forcing term, the behavior of a single test point experiencing sufficient amplitude, can be reasonably approximated by just such a forcing term. If we

make this assumption for the lift coefficient, C_L , we have

$$C_L = C_{L,o} e^{i\omega^* t^*}, \quad (2.35)$$

and we would expect resultant sinusoidal motion of the form

$$Y^* = A^* e^{i\omega^* t^*}. \quad (2.36)$$

Upon substitution of Equation (2.35) and Equation (2.36) into the nondimensional equation of motion Equation (2.25) one obtains

$$(-m^* \omega^{*2} + i\omega^* b^* + k^*) A^* = C_{L,o}, \quad (2.37)$$

where one can see that two real terms and one imaginary term exist. If we group real and imaginary terms separately,

$$\left([-m^* \omega^{*2} + k^*] + i[\omega^* b^*] \right) A^* = C_{L,o}, \quad (2.38)$$

we see that the real part of the equation, the mass and elasticity of the system, could be combined into a single parameter. We call this parameter the effective stiffness, k_{eff}^* , of the system, that is,

$$k_{\text{eff}}^* = -m^* \omega^{*2} + k^*. \quad (2.39)$$

The name of the parameter comes from the fact that the dimensional equivalent of the parameter would have units of stiffness, hence effective stiffness.

This led to the proposal by Shiels et al. (2001) that for an undamped system ($b = 0$), the motion of the system is simply controlled by

$$k_{\text{eff}}^* A^* = C_{L,o}, \quad (2.40)$$

and the idea was also extended to a system with damping, so that the motion of the system is then controlled by

$$(k_{\text{eff}}^* + i\omega^* b^*) A^* = C_{L,o}. \quad (2.41)$$

It should be noted that this is a mathematical construct and is not guaranteed to be

a useful parameter. An assumption was made about the sinusoidal lift coefficient which allowed the parameters to be grouped into the real and imaginary terms that govern the motion. Mathematically speaking, in terms of phase, grouping the real (in-phase) terms as a single entity, separate from the imaginary (out-of-phase) terms, makes sense. In a physical sense, one might argue that since the mass and elasticity of the system are in phase, the fluid system cannot tell whether it is forcing a massive, very stiff system or a lightweight system, with soft springs. However, until this parameter is used to unify actual experimental data, its usefulness is uncertain.

2.11 Comments on the Effective Stiffness Parameter

At first it may appear that one does not have enough control over the effective stiffness parameter in order to make sure that all the values of interest are spanned. In most experiments, the traditional parameter that most results are plotted against is the reduced velocity, U_R . It is easy to see the direct linear connection between actual tunnel velocity and reduced velocity. In order to span the U_R space, one only needs to span the available tunnel velocities. However, that same result holds for the effective stiffness parameter; all values of interest can be spanned by simply spanning the available tunnel velocities. To understand this, it is helpful to write the effective stiffness in a different form

$$k_{\text{eff}}^* = \frac{1}{U^2} \left(-\omega^2 D^2 m^* + \frac{2k}{\rho L} \right), \quad (2.42)$$

which highlights the connection between the effective stiffness and tunnel velocity. Because D , m^* , k , ρ , and L are constant during an experiment and ω is bounded, changes in the effective stiffness are strongly connected to changes in the tunnel velocity. Therefore, in general, as the tunnel velocity is increased, the value of the effective stiffness will decrease. As long as a wide enough range of tunnel velocities are spanned, the necessary range of effective stiffness values will be covered.

The application of the effective stiffness parameter involves knowing the value of the elasticity of your system quite accurately. However, measuring the system elasticity, or each spring stiffness directly, with the necessary accuracy, is quite complicated. Instead, our experimental configuration allows for a simple, direct, and accurate measure of the

natural frequency of the system in air. Therefore, it is advantageous to write Equation (2.39) in a form involving the natural frequency of the system instead of the elasticity. This can be done by factoring out the nondimensional mass, m^* , and noting that $\omega_N^2 = k/m$, to write

$$k_{\text{eff}}^* = m^* \left(\omega_N^{*2} - \omega^{*2} \right), \quad (2.43)$$

which eliminates the need to know the elasticity directly. The form of Equation (2.43) also highlights the importance of being able to accurately measure frequencies as well as the influence that mass has on the effective stiffness value. There is a region of the response curve, near the maximum amplitude point, where the system oscillation frequency passes through the system natural frequency. Therefore, there exists a response region of interest, due to its proximity to the maximum amplitude location, where the two frequencies are extremely close and an accurate measurement of both frequencies is necessary. The nondimensional mass of the system will effect just how close the system remains near the natural frequency during the majority of its response behavior (Govardhan and Williamson, 2002). The nondimensional mass will also directly effect the effective stiffness, as can be seen in Equation (2.43). The value of the difference between the natural and oscillation frequencies is scaled by the nondimensional mass. Therefore, the slight error in the measurement of either frequency is exaggerated by the value of the mass. Therefore, from the point of getting extremely accurate effective stiffness values, one prefers a system with a low natural frequency (so that the oscillation and natural frequencies can be measured very accurately) and a small nondimensional mass (so that any error in the frequency difference is scaled by as small a quantity as possible).

Chapter 3

Experimental Setup and Test Procedures

3.1 Chapter Overview

In this chapter we discuss the experimental test facility and laboratory equipment used. We also show and comment on results from studies that explored the boundary layer influence, cylinder end effects, and starting method of cylinder oscillation dependence. All experimental work was performed in the Noah water tunnel, described in Section 3.2, which is located in the Guggenheim building of the Graduate Aeronautics Laboratory at the California Institute of Technology (GALCIT). The main experimental setup was positioned on top of the test section of the water tunnel and consisted of a traversing plate mounted on air bearings with adjustable mass and elasticity, described in Section 3.3, and adjustable damping provided by a variable magnetic eddy-current (VMEC) damping system, described in Section 3.4. In Section 3.5 we describe the various circular cylinders that were attached to the traversing plate and suspended downward into the test section. Various data and visualization recording equipment was used to collect and store the results from each test. In Section 3.6 we describe the methodology and arrangement of a linear variable displacement transducer (LVDT). Two different flow diagnostic tools were used for various portions of this study, digital particle image velocimetry (DPIV), described in Section 3.7, and dye flow visualization, in Section 3.8. Next, our general test procedure is explained in Section 3.9, and in Section 3.10 we give the parameter values of all the system configurations we used. In Section 3.11 we briefly describe how we obtained our amplitude and frequency results from the LVDT. Finally, we validate our experimental setup and test methodology by looking

for any cylinder end effects and boundary layer effects in Section 3.12 and any dependence on the starting method of the cylinder motion in Section 3.13.

3.2 Noah Water Tunnel

The Noah water tunnel is a low-velocity, free-surface water tunnel facility and can be seen in Figure 3.1. The water tunnel consists of a large settling chamber with two sections of honeycomb, two metal grids, and four screens of increasing fineness. This is followed by the contraction section of the tunnel which has a ratio of approximately 9 to 1. The test section is 45.75 cm (18 inches) wide, 60 cm (22 inches) deep and 150 cm (60 inches) long. The test section is made of glass and allows for the flow to be viewed from either side, as well as the bottom. The test section can be seen in detail in Figure 3.2.

The Noah water tunnel settling chamber includes four custom-made screens. The screen frames were rectangular in shape measuring 1.85 m (6.1 ft) across and 0.61 m (2.0 ft) tall. They were made of PVC and had a beveled edge around the outside that allowed them to be set into grooves in the walls of the water tunnel. The screens were made of stainless steel wire mesh and were aligned in the tunnel to have increasing mesh fineness (24 x 24 mesh first, then 28 x 28 mesh, then 32 x 32 mesh, and finally 36 x 36 mesh) in order to destroy successively smaller structures in the flow. For this wire mesh, the mesh number referred to the number of stainless steel wires per inch. The screens were made with a small enough diameter wire so that the Reynolds number, based on mesh wire diameter, for the fastest flow of the tunnel, would not be above about 30. This ensured that vortex shedding around the wires would be avoided.

The tunnel has a minimum velocity of 3.33 cm/s and a maximum velocity of approximately 50 cm/s. The test section was visually unsteady, the appearance of standing waves were visible in the test section, during high velocities ($U \gtrsim 35$ cm/s) and consequently no tests were performed at velocities above this. For the velocities used in this study, the free-stream turbulence level on the centerline was below 0.5 percent. A LabView program controlled the voltage supplied to the motor as well as when that voltage was changed and when cylinder oscillation data was recorded. The test section velocity was calibrated using DPIV that was performed without any cylinder in the test section. By determining the planar velocity vectors, we not only obtained a calibration curve but verified the uniformity



Figure 3.1: General layout of the Noah Water Tunnel. The settling chamber is visible on the left with the contraction in the middle and the test section on the far right. Visible in front of the test section is the water tunnel motor controller.



Figure 3.2: Detailed view of the Noah Water Tunnel test section. Flow is from left to right in this view.

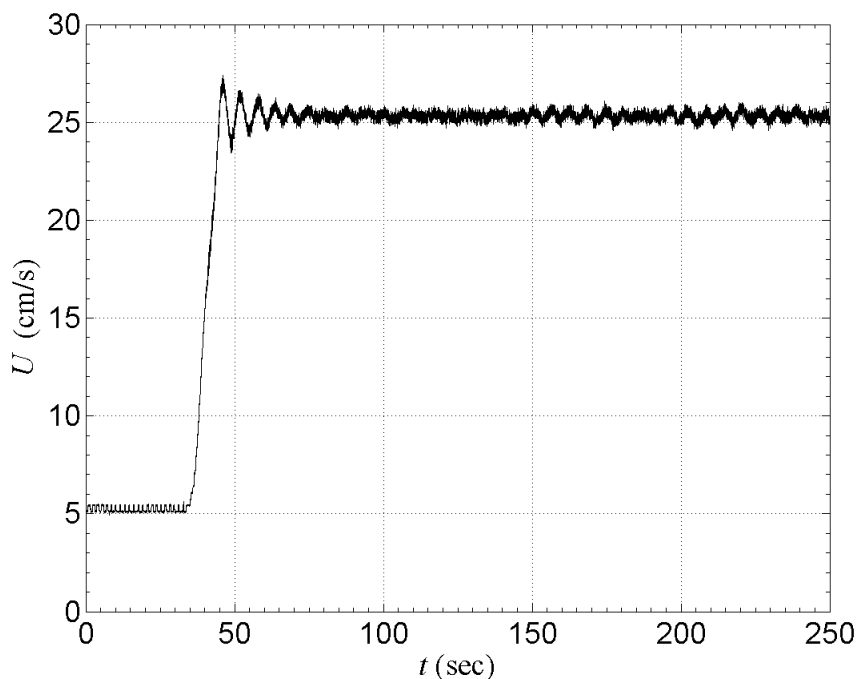


Figure 3.3: Transient response of the tunnel velocity in the test section caused by an extreme “impulsive” tunnel velocity change, from an initial velocity of 3.33 cm/s to a final velocity of 35 cm/s, recorded using a Nixon Streamflo velocity meter.

of the flow in two dimensions.

The transient velocity settling time and the natural frequencies in the test section of the tunnel were explored using a Nixon Streamflow miniature propeller velocity meter. The velocity meter allowed us to measure the instantaneous flow velocity in the test section. In order to determine the settling time for the most extreme transient, the tunnel velocity was increased from its minimum velocity of 3.33 cm/s to its maximum uniform flow operating velocity of 35 cm/s as quickly as the motor allowed. The transient test section velocity was recorded using the miniature propeller situated in the middle of the test section. Figure 3.3 shows the recorded transient behavior of the velocity in the test section. The initial part of the curve represents the tunnel operating at 3.33 cm/s. The steep rise corresponds to the tunnel velocity “impulsively” increasing to 35 cm/s. Of course, the tunnel could not instantaneously make the change so the curve represents the motor’s maximum increase. The final part of the curve shows the final steady velocity of 35 cm/s in the test section. The oscillatory part of the response right after the sharp increase is the transient response

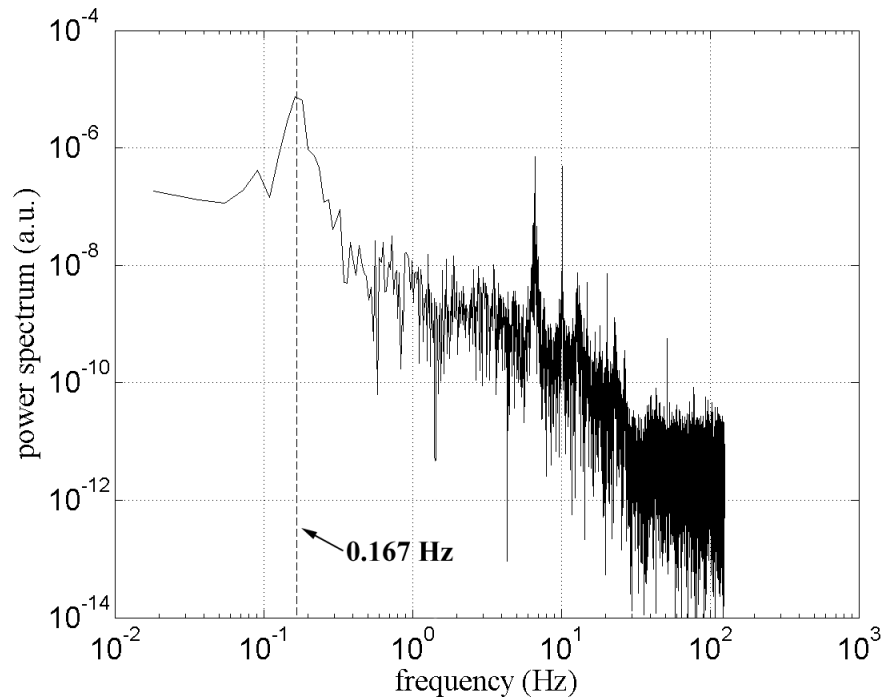


Figure 3.4: Power spectrum of frequencies in the test section caused by an extreme “impulsive” tunnel velocity change.

of the tunnel. One can see the overshoot of the tunnel velocity and then the sinusoidal oscillations as the transients die out. As can be seen in Figure 3.3, the settling time for this large impulsive change is around 60 seconds.

Due to the extreme nature of the tunnel velocity change, we were able to record a fair number of flow velocity oscillations following the overshoot. This oscillating data was analyzed by looking at the power spectrum in Fourier space to determine the dominant frequency of the velocity fluctuations in the test section. The results of this power spectrum can be seen in Figure 3.4. The dominant frequency of velocity fluctuations is approximately 0.167 Hz, which corresponds to a period of about six seconds.

A more appropriate tunnel velocity transient was also investigated. For all of our tests, the tunnel velocity was incremented at either 0.25 cm/s or 0.50 cm/s. Therefore, we looked at the transient velocity response that resulted from an impulsive change of 0.50 cm/s. This was carried out in the same manner as the extreme transient test. The results for the test section velocity can be seen in Figure 3.5, which shows a transient settling time of roughly five seconds for normal operating velocity changes.

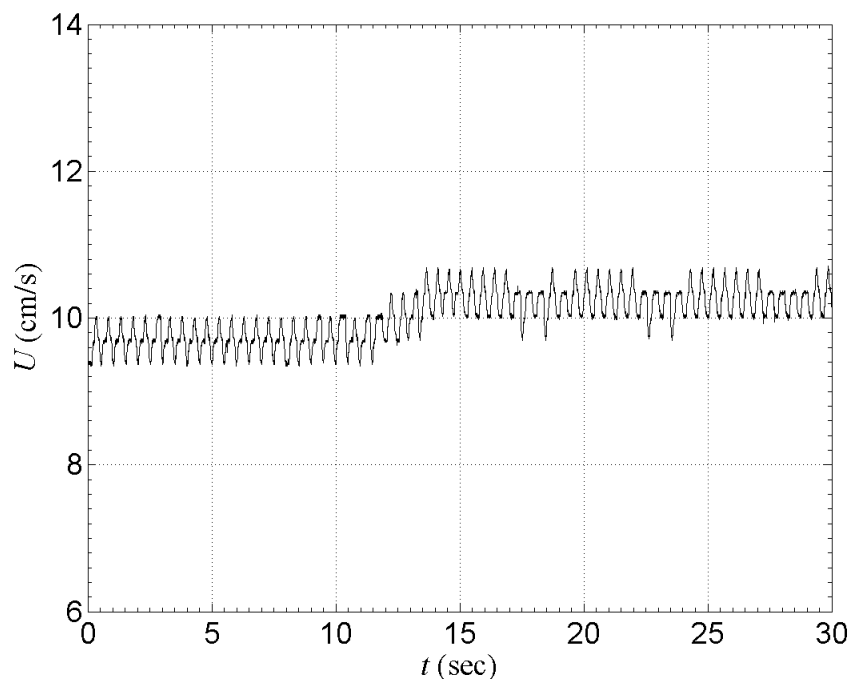


Figure 3.5: Transient settling time for regular operating “impulsive” tunnel velocity changes of 0.50 cm/s

The water tunnel was periodically filtered using an externally connected filter line. This line contained a large filter tank that consisted of six Aqua-Tek filters, 5 cm in diameters and 60 cm in length. A small motor was attached to the filter tank which allowed water to be moved through the system.

3.3 Traversing Plate with Adjustable Mass and Elasticity

A detailed view of the traversing plate with adjustable mass and elasticity can be seen in Figure 3.6. The traversing plate consisted of a Plexiglas plate with various mounting points that rode smoothly on a pair of air bearings. The air bearings served two purposes. First, they restricted any motion in the direction of the flow, thus ensuring purely one-dimensional motion transverse to the flow. Second, they allowed for a very small inherent system damping value. There was a mounting location in the center of the plate that allowed for the cylinder to be attached and suspended downward into the test section. Other mounting points on the plate allowed for various masses and springs to be attached

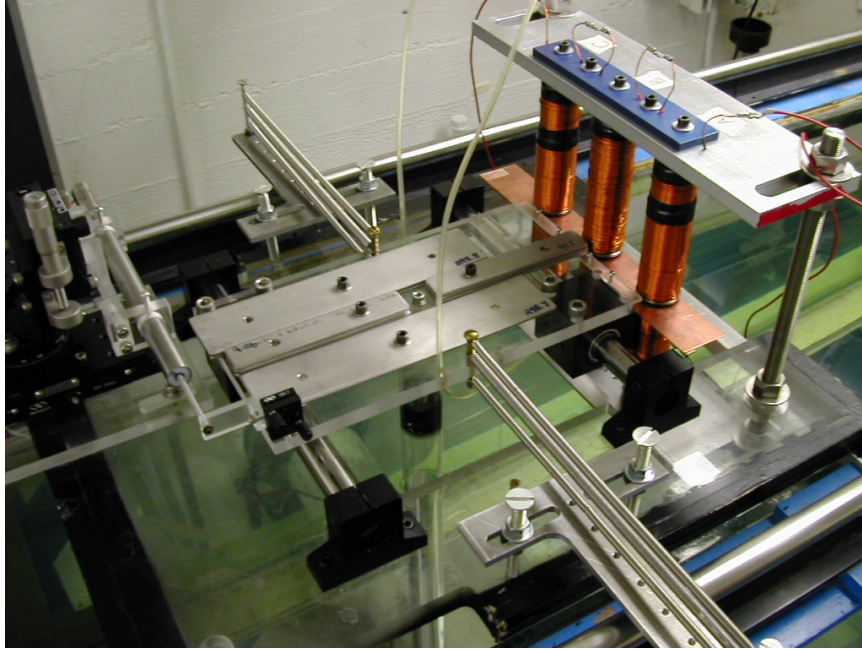


Figure 3.6: General overview of the traversing plate with multiple stainless steel plates attached, for varying the system mass, and multiple springs attached, for varying the system elasticity. Also visible are the LVDT (on the left) and the VMEC damping system (on the right) as well as a test cylinder, suspended downward into the test section.

to it.

The mass of the system was adjusted by stacking various-sized stainless steel plates (which contained enough chromium to be nonmagnetic) onto the traversing plate and securing them using sets of bolts, washers, and nuts. These plates were either “large” plates, with a mass of approximately 310 grams, or “small” plates, with a mass of approximately 90 grams. This can be seen in Figure 3.6 where two large and six small plates are shown attached. For finer mass adjustments than the small plates allowed, the number of bolts and nuts used to secure the plates was varied. For very fine mass adjustments, small bolts and nuts could be attached directly to the traversing plate along with various numbers of washers. This gave us the ability to control the system mass to within approximately three grams.

The elasticity of the system was varied by placing springs in parallel. This can be seen in Figure 3.6 where three springs are attached in parallel to both sides of the traversing plate. By placing the springs in parallel, the total elasticity of the system was simply the sum of the stiffness of each spring used. The springs were custom made from long coils of

metal with diameters between 5 mm and 7 mm obtained from Century Spring Corporation. This allowed for the stiffness and length of each spring could be controlled. It was found that long springs had a smaller inherent damping value than shorter springs of the same stiffness. This is believed to result from the shorter springs being strained more than the longer springs for the same amount of physical displacement. Therefore, extremely long springs were desired. However, there is a certain physical spring length, different for each stiffness, beyond which the spring will sag under the influence of its own weight. Since this first becomes an issue for the softer springs, this critical length was determined by varying the length of the softest spring. The critical length turned out to be approximately 25 cm and then the remaining, more stiff, springs were all made this same length to allow for them to be easily attached in a parallel fashion. The individual springs used in the study varied in stiffness from around 6.5 N/m to 75 N/m.

3.4 Variable Magnetic Eddy-Current Damping System

Controlled damping values for the system were made possible through the use of a variable magnetic eddy-current (VMEC) damping system, inspired by the basic system built by Smith (1962) and used by Feng (1968) in his study of VIV. The system works on the basic physical principal that if a conductor is exposed to a changing magnetic flux, an induced voltage is generated in the conductor. This induced voltage produces eddy currents in the conductor which generate internal resistive heating and oppose the motion.

The VMEC damping system can be seen in detail in Figure 3.7 and consisted of six electromagnets and a copper conducting plate. The six electromagnets were identical with each one made of 1" diameter 1018 steel wrapped in 200 feet of 18 gauge magnet wire. These magnets were attached to aluminum plates to keep them aligned. The system was activated using a Kepco power supply with current control to provide the desired current to the magnet wires. This supplied current, i_{sup} , induced a magnetic field which was amplified by the iron in the steel rods. The conducting plates were copper alloy 110 with thicknesses of 1/8", 1/16", and 1/32". It was found that the thickness of the conductive plate affected the amount of imposed damping, the thicker the conductive plate, the more damping that was achieved. The copper plate was attached to the traversing plate so that it moved in unison with the cylinder and traversing plate. Thus, the conductive plate oscillated between

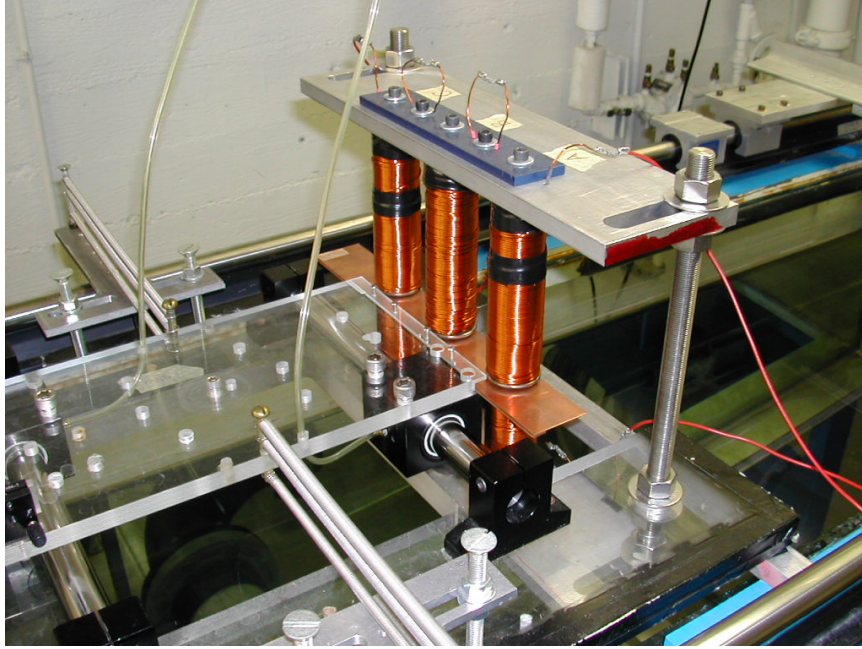


Figure 3.7: General overview of the variable magnetic eddy-current (VMEC) damping system. Shown are the three top electromagnets and the copper conducting plate attached to the traversing plate. The three bottom electromagnets, located underneath the conducting plate, are not visible.

the pairs of electromagnets and created the changes in magnetic flux that the conductive plate felt. The six electromagnets were arranged in vertical pairs of two with opposite polarities facing each other in an attempt to straighten the magnetic field lines and lessen the dependence on the conducting plate's location in the gap between the magnets. In order to generate the higher damping values needed in this study, a strong magnetic field was needed. Since the apparatus was space limited as well as power supply limited, the steel rods could not simply be wrapped with an enormous number of coils (magnetic field strength is proportional to number of coils). Instead, large currents, between one and two amps, were supplied to the electromagnets.

The possible damping values that can be obtained by the system depend on the amount of current supplied to the system and thickness of the copper conducting plate used. The range of values can be seen in Figure 3.8. From the theoretical derivation in Appendix C, the magnetic damping in our system should vary as i_{sup}^2 . This predicted functional relationship is confirmed by the curves in Figure 3.8 which all have the form $b_{mag} = \mathcal{C}i_{sup}^2$ where \mathcal{C} is a constant and depends on numerous parameters.

Linear vibration theory predicts a linear relationship for the free-vibration logarithmic decay of the system amplitude over time for ideal, linear damping (the derivation can be found in Appendix B). We show some selected free-vibration natural decay data in Figure 3.9, which verifies that one gets ideal linear damping from the VMEC damping system. One particular concern was the overheating of the magnets due to the high currents that were sometimes supplied and the duration of test runs, some taking almost two days to complete. This overheating could cause the magnet wires to melt. A series of tests were undertaken to check for changes in the system damping when the VMEC system was supplied with a current of around one amp and left on continuously for two days. The applied damping value was measured multiple times throughout the two days and found to never vary beyond the uncertainty and repeatability of the measurements. Perhaps one reason for resistive heating in the magnet wires not being a problem is even though there is almost a quarter mile of wire in the system, the total system resistance is only 8 ohms, so even currents of the order of 1 amp do not produce that much resistive heating.

3.5 Cylinder Models and Mounting Collars

Two types of circular cylinders of various sizes were used in this study. The most common type were smooth hollow pyrex cylinders that were glass blown at Caltech. They all had a consistent thickness of approximately one millimeter. These cylinders had various diameters with one open end (the top) and one closed end (the bottom). The other type of cylinder, which was seldom used, was a solid plexiglass cylinder. All the cylinders had a smooth rounded bottom, although the curvature slightly changed depending on the actual diameter of the cylinder. The characteristics of all the cylinders used for the study can be found in Table 3.1 and seen in Figure 3.10.

The hollow, pyrex cylinders had various diameters and lengths, although the lengths of all the cylinders were fairly consistent as can be seen in Table 3.1. Attaching the hollow cylinders to the traversing plate was accomplished by using collars that went around the top of the cylinders. These collars had bored internal holes that allowed them to fit over the top of the cylinders. The cylinders were then secured by gluing them into the collar which made a permanent connection. The top center of the collar was drilled and threaded so that a bolt could be used to secure it to the traversing plate. The solid plexiglass cylinder,

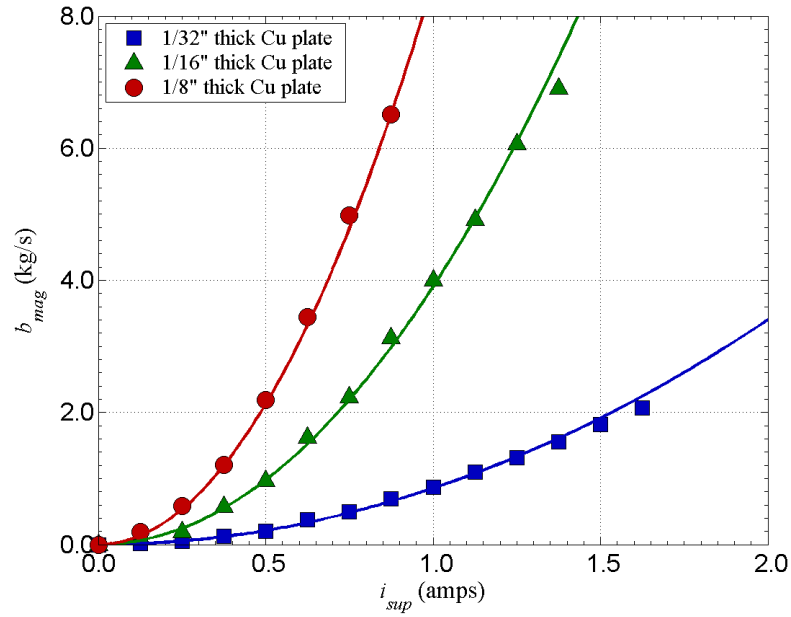


Figure 3.8: Available range of imposed magnetic damping values, b_{mag} , possible using the VMEC damping system as functions of supplied current, i_{sup} , and copper conductive plate thickness.

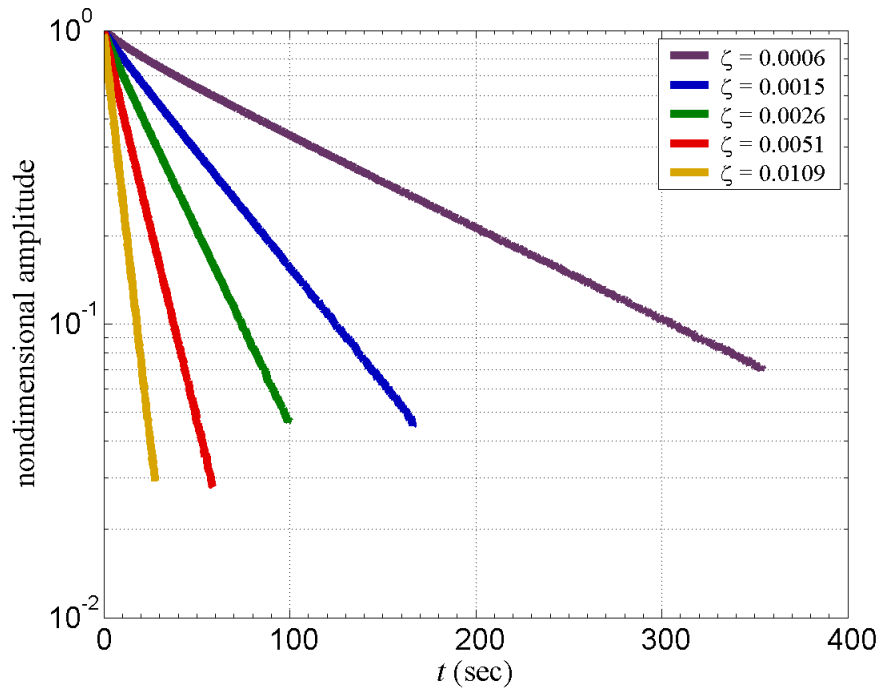


Figure 3.9: Sample of free-vibration decay curves showing the linear relationship between the logarithm of amplitude against time for ideal viscous damping.

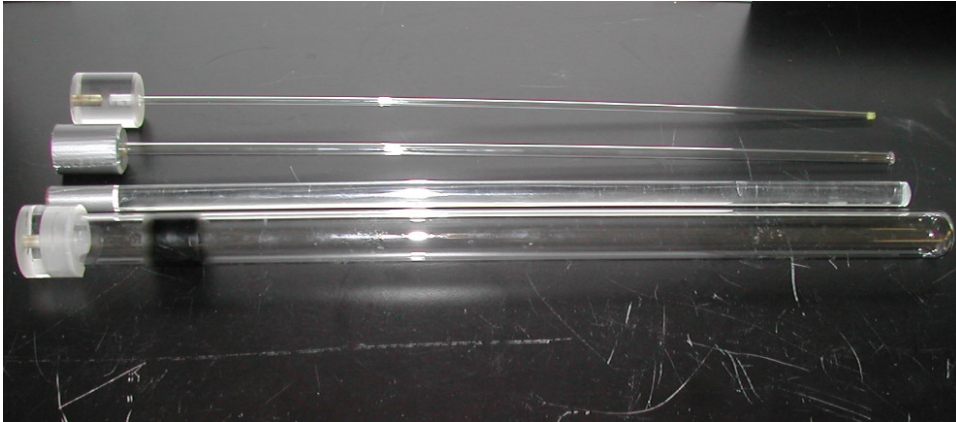


Figure 3.10: View of the four basic circular cylinders used for this study.

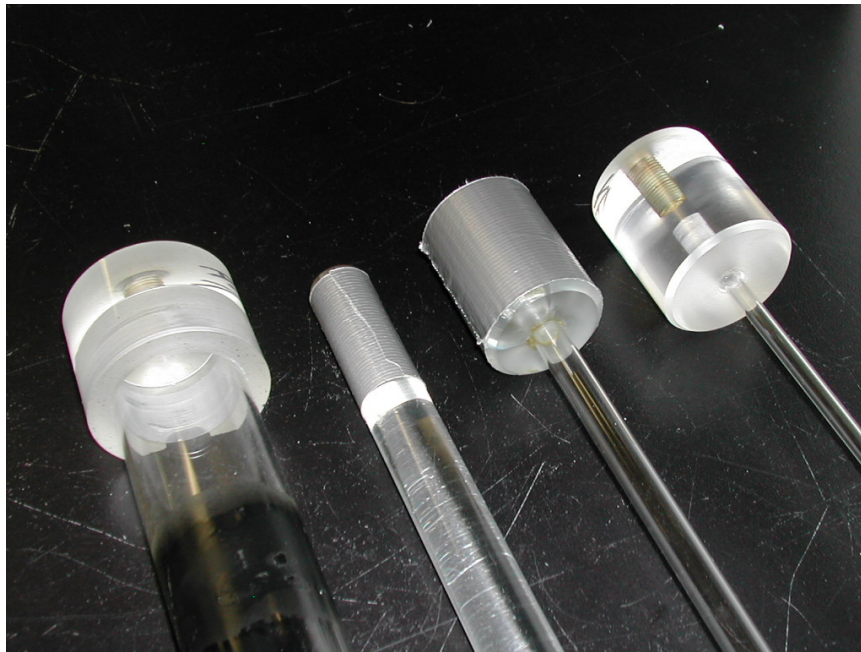


Figure 3.11: View of the three collars for the hollow cylinders, used to attach them to the traversing plate, and the collarless solid cylinder.

D (mm)	L (cm)	L_{total} (cm)	L/D	G/D
hollow pyrex				
6.0	46.95	67.31	78.25	5.33
10.0	46.65	66.99	46.65	3.50
37.8	46.95	67.31	12.42	0.85
solid Plexiglas				
19.3	46.65	66.99	24.17	1.80

Table 3.1: Characteristics of the circular cylinders used in this study.

on the other hand, had a large enough diameter so that an internal hole was drilled and threaded within the cylinder itself. Then it was mounted to the traversing plate directly using this threaded hole without the use of a collar. A detailed view of the hollow cylinders with their collars and the collarless solid cylinder can be seen in Figure 3.11.

3.6 Linear Variable Displacement Transducer

The main data acquisition tool was a DC-750 series linear variable displacement transducer (LVDT) from MacroSensors. This is a non-contact device that measured the instantaneous location of the cylinder while providing frictionless operation. This type of LVDT consists of two cylindrical cylinders, one of which is solid and fits inside the other larger, hollow one. The hollow outer cylinder contains three co-axially wound solenoids, with the middle one called the primary coil and connected to an AC voltage. This causes a magnetic field to be set up in the primary coil, which is linked to the two outer solenoids, called secondary coils, by the ferromagnetic core of the solid inner cylinder. The magnitude of the voltage in each secondary coil depends on the position of the inner cylinder relative to each of them. Both the input (± 15 volts) and output (± 10 volts) voltages of the LVDT were DC with the internal circuitry handling the conversion between AC and DC voltages. Therefore, the output DC voltage was linearly proportional to the location of the inner cylinder. Also, the sign of the output voltage represented which side of the null position the core was on. By attaching the inner cylinder to our traversing plate, we were able to record the instantaneous position of the VIV system.

One major advantage of the LVDT is that it is a non-contact measurement device. However, the solid inner core fits freely, but closely, to the hollow outer core. Therefore, a

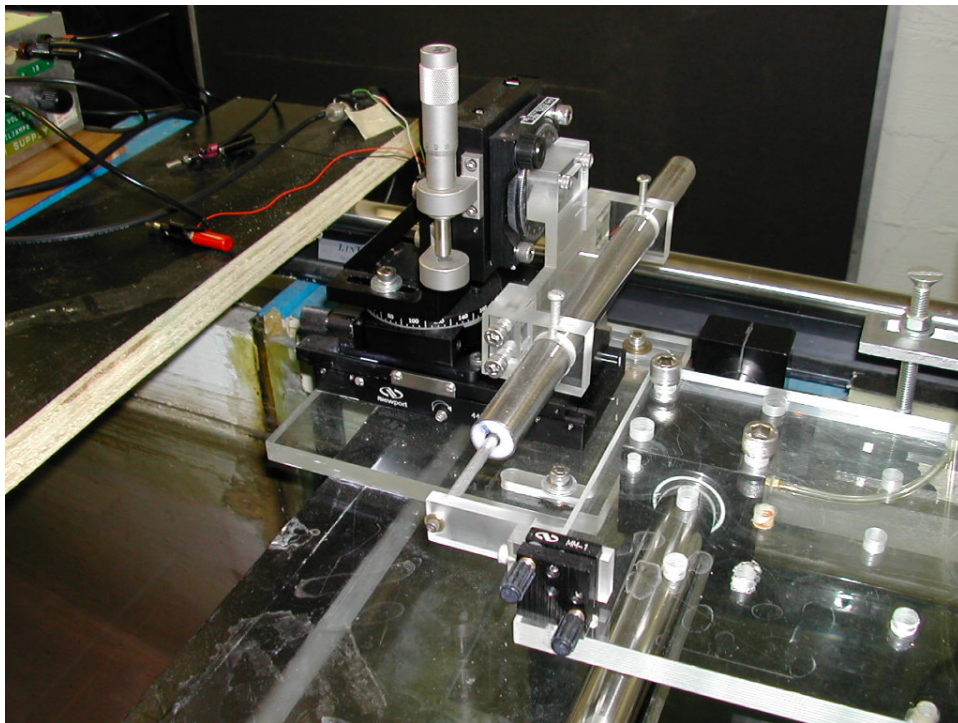


Figure 3.12: View of the setup for the LVDT system showing the six-degree-of-freedom mounting stand along with the attachment point to the traversing plate.

six-degree-of-freedom mounting stand was designed so that the two cylinders could be properly aligned. This mounting stand consisted of optical slides and rotation tables attached orthogonal to each other. The layout and mounting method for the LVDT can be seen in Figure 3.12.

3.7 Digital Particle Image Velocimetry

Digital particle image velocimetry (DPIV) allows the determination of a planar group of velocity vectors by considering the movement of particles in consecutive frames separated by a short time span. When used with bluff-body separated flows, the velocity field can be used to determine other flow quantities, such as vorticity, which allows one to investigate and analyze the wake. For more information regarding DPIV, see Willert and Gharib (1991).

Our DPIV setup involved seeding the tunnel with 40 micron reflective silver particles that were illuminated by a New Wave Class IV laser. The laser emitted a pulse of wavelength 532 nm and a diameter of approximately 5 mm. The laser was passed through a lens that

produced a diverging horizontal sheet that was roughly 20 cm wide and 3 mm thick at the center of the tunnel test section. A timing box, run by the data-logging computer, controlled the laser externally in order to maintain the appropriate spacing and separation of the pulses. A Pulnix analog CCD camera with a 35 mm focal length lens was placed underneath the test section and transferred the images to the data-logging computer. The camera was positioned so that its full-field view captured the laser sheet from the upstream end of the cylinder to four diameters downstream. Particle image pairs were digitally analyzed using a cross-correlation method of subimages (Willert and Gharib, 1991; Westerweel et al., 1997). The image sizes were 480 x 640 pixels with the interrogation boxes being 32 x 32 pixels, and the step size was 16 x 16 pixels. The individual calculated velocity and vorticity fields were then assigned to one of sixteen bins based on the cylinder's position within a cycle. These bins were then averaged to eliminate random noise from individual frames.

Two factors limited the effectiveness of our DPIV method. First, since the actual cylinder diameter used was rather large (37.8 mm), the corresponding laser sheet needed to be quite long, in order to capture the wake four diameters downstream, as well as quite wide, to minimize vortices prematurely exiting through the sides. This caused the intensity of the laser sheet to be at the lower limit of what is acceptable for normal DPIV studies. The second difficulty was in keeping a high particle density in the test section. After a few tunnel recirculation times, the particle density would dramatically drop due to particles getting trapped in the screens and honeycombs. The trapped particles could be freed by increasing the tunnel velocity or manually shaking the screens, however, both of these disrupted the flow and thus could not be done during a test.

3.8 Dye Flow Visualization

Basic dye-injection flow visualization of the wake was also conducted. A red dye was made by mixing 2000 mL of tap water with 80 mL of extra concentrated Red40 food coloring and a blue dye was made by mixing 2000 mL of tap water with 160 mL of Blue1 food coloring. The dye was carried by flexible tubing and injected into the fluid through small holes in specially designed hollow pyrex cylinders, that were identical to the previously discussed cylinders except for the addition of injection holes. These injection holes were located at roughly the vertical midpoint of the cylinders and at about 60° on either side of the front



Figure 3.13: Detailed view of the dye-injection ports on the 38 mm diameter circular cylinder used for flow visualization.

stagnation point. For the 6 mm cylinder, only one injection hole was possible, and this was located at the front stagnation point. The cylinders, tubing, and injection holes can be seen in Figure 3.13. In order to allow for the tubing that carried the dye to pass through the collars and into the cylinders, new collars were used. These new collars were similar to the permanent fit ones but they contained a large axial through hole, near the center, that allowed the flexible tubing to pass through to the interior of the cylinders. These collars were also different due to the fact that the cylinders were secured to them using three or four plastic set screws to pin them in place. The new collars along with this attachment method can be seen in Figure 3.14.

The red and blue dye mixtures were stored in separate glass beakers placed sufficiently high enough above the test section to allow gravity to drive the injection process. The actual dye injection rate was controlled using a flow dial installed along the dye path. The full set up can be seen in Figure 3.15

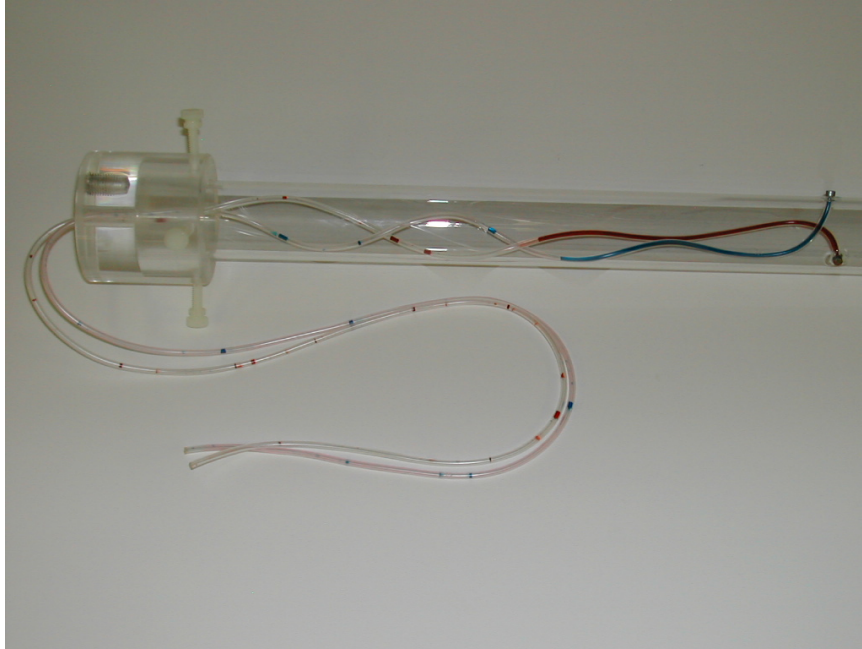


Figure 3.14: General overview of the cylinder component of the flow visualization setup showing the flexible tubing, adjustable collar, and hollow circular cylinder with injection ports.

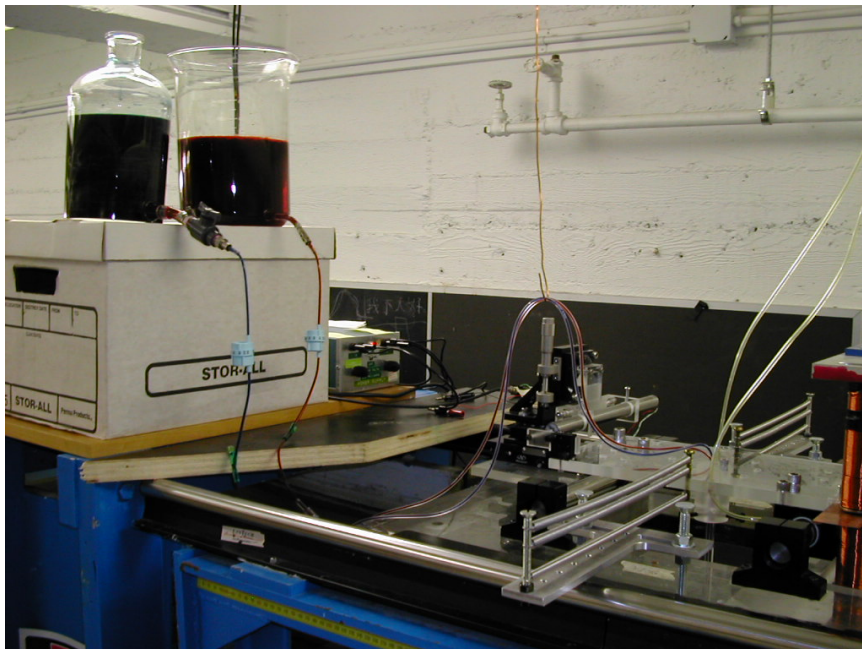


Figure 3.15: Overall view of the complete flow visualization setup. The two large beakers held the food coloring mixtures at a sufficient height to allow gravity to drive the flow of dye. The two dials used to adjust the flow can also be seen (light blue circular knobs).

3.9 General Test Procedure

For a given system with certain m , b , k , and D values, a typical complete test, known as a *Run*, involved spanning the range of tunnel velocities of interest four times, twice in increasing and twice in decreasing increments. This was done to look for hysteresis effects in the behavior as well as to gauge the repeatability of the results. During a run, the tunnel velocity and data recording was remotely controlled by a LabView program. This program first calculated the necessary voltage needed by the motor to produce the correct tunnel velocity of the next test point. Then it output this voltage to the motor, thereby impulsively incrementing the velocity, and held this voltage while the data recording phase occurred. The data recording phase involved waiting a fixed amount of time to allow the structural system to reach steady-state oscillations (typically approximately 250 oscillation cycles), then recorded the position output from the LVDT for a fixed amount of time (typically around 500 oscillation cycles). Finally, once the data recording phase was done, the necessary voltage for the next tunnel velocity was calculated and the entire process was repeated. The success of this strategy lies in the fact that as U is varied over a large enough range, as long as $k > 0$, all values of k_{eff}^* of interest will be spanned.

3.10 Parameter Values

During the course of each experiment, the water temperature was monitored using an Omega DP41-RTD thermometer with Fluke Y2039 probe and was found to be 20 ± 1 °C. This temperature corresponded to a kinematic viscosity of $\nu = 1.004 \times 10^{-6} \pm 0.030 \times 10^{-6}$ m²/s and resulted in variations of Reynolds number during experiments of about 3 percent. Therefore, Reynolds number ranged from $\text{Re} = 200 \pm 6$ at the low end to $\text{Re} = 5050 \pm 150$ at the high end. The circular test cylinders had diameters between 6 mm and 38 mm. The system mass varied between 1.85 kg and 3.70 kg and the total system elasticity between 13.5 N/m and 295 N/m. In this investigation we only considered high aspect ratio cylinders $L/D > 10$. The specific system values for each test configuration can be seen in Table 3.2.

run no.	D (mm)	m (kg)	k (N/m)	m^*	$\text{Re} A_{\text{Max}}^*$
01(a)-(n)	10.0	1.850	65.5	79.3	525
02(a)-(i)	10.0	3.700	135	158.6	525
03(a)-(l)	10.0	1.850	265	79.3	1000
04(a)-(l)	37.8	2.390	13.5	7.1	2600
05(a)-(c)	10.0	1.850	36.5	79.3	400
05(d)	6.0	1.850	295	218.9	400
06(a)-(d)	6.0	1.850	175	218.9	300
06(e)	10.0	1.850	24.0	79.3	300
07(a)-(c)	6.0	1.850	74.5	218.9	200
08(a)-(c)	19.3	1.975	60.5	22.7	1660
09(a)	37.8	2.140	24.0	6.4	3400
10(a)	37.8	2.125	48.5	6.3	5050

Table 3.2: Various fixed system parameters for each test configuration.

3.11 Data Reduction Methodology

The recorded data file was a list of voltages output from the LVDT that corresponded to the instantaneous position of the traversing plate and thus the VIV system, as described in Section 3.6. This data file was then put through a series of MatLab functions which converted, filtered, processed, and output the data. First, the raw data was converted from voltages to physical displacements using the LVDT calibration curve and a corresponding time vector was created using the sampling rate, which was 250 samples/sec for all the experiments. Then the data was filtered using an optimal Wiener filter scheme in Fourier space. The noise signal estimate that is needed for such a scheme was determined by comparing our measured signal power spectrum to the power spectrum of a pure sine wave. The filtered data was then sent through a function that located the positive and negative extrema in the signal. These extrema were then used to calculate cycle-by-cycle amplitude and frequency values. The amplitude for a given cycle was the average of two positive extrema and the negative extrema that occurred between them, with the negative one weighed twice. The frequency was the inverse of the time difference between the two positive extrema. The cycle-by-cycle data was then used to compute statistics on the response, such as the average, minimum, maximum, and standard deviation of the amplitudes and frequencies. Finally, parameters, such as the effective stiffness, were determined along with error values for all relevant parameters. A more detailed explanation of the data reduction

process, particularly the signal filtering, can be found in Appendix A. The determination of the system damping values, which are an integral part of this thesis, can be found in Appendix B.

3.12 Cylinder End Effects and Boundary Layer Effects

In order to ensure that there were no cylinder end effects or boundary layer effects with the bottom of the water tunnel, a series of tests, called gap distance (GD) tests, were performed where the gap distance, G , (the distance between the bottom of the cylinder and the bottom of the test section) was varied. The amplitude and frequency response of these tests were then examined to see if there were any noticeable difference in the system response.

Four different test configurations were used for these tests, which can be seen in Table 3.3. Care must be taken when setting up such a series of tests and comparing the re-

test no.	L/D	G/D	b (kg/s)	m^*	$b^* _{A_{\text{Max}}^*}$	$\text{Re} _{A_{\text{Max}}^*}$
GD01	45	5.5	0.102	86.7	0.504	905
GD02	47	3.5	0.106	82.9	0.513	880
GD03	48	1.8	0.111	80.0	0.509	905
GD04	50	0.4	0.118	77.8	0.521	905

Table 3.3: System configurations used for the gap distance (GD) tests. All GD test configurations had $D = 10$ mm, $m = 1.930$ kg, and $k = 205$ N/m.

sultant amplitudes. It is known that A_{Max}^* is a function of both damping, b^* , and Reynolds number, Re (Klamo et al., 2005). Therefore, one must match these two parameters across all tests or else one would not know if any observed amplitude differences were caused by cylinder end effects and boundary layer effects or damping and Reynolds number effects. Unfortunately, damping was nondimensionalized by the wetted length of the cylinder, L , and this was precisely the parameter we were changing during the gap distance tests. Therefore, we had to apply an external amount of damping, with the VMEC damping system, to compensate for changes in b^* caused by changes to L . As can be seen from Table 3.3, the damping and Reynolds number values were held as constant as the experiment would allow and the nondimensional mass, m^* , although consistent, was allowed to vary freely. The nondimensional mass changed, even though the physical system mass, m , remained constant, due to the changing wetted cylinder length, L , across the tests.

U (cm/s)	Re_x	δ/x	Re_D	δ/D
5	25150	0.0315	498	1.59
10	50300	0.0222	996	1.13
15	75450	0.0182	1494	0.92
20	100600	0.0157	1992	0.80

Table 3.4: Reynolds number and nondimensional laminar boundary layer thickness at various tunnel velocities using two different characteristic lengths, downstream distance from the beginning of the test section to the cylinder, $x = 50.5$ cm, and diameter of cylinder, $D = 10$ mm.

For a laminar, flat-plate boundary layer, the nondimensional boundary layer thickness δ/x is given by

$$\frac{\delta}{x} = \frac{5}{\sqrt{Re_x}}, \quad (3.1)$$

where x is the distance downstream and characteristic length scale used in the Reynolds number. For our setup, the cylinder was located about 50.5 cm downstream from the entrance of the test section. Therefore, for the given fluid properties, at this $x = 50.5$ cm location in the test section we expect to see the range of boundary layer thicknesses given in Table 3.4 for typical tunnel velocities listed.

Due to the inverse relationship between boundary layer thickness and Reynolds number, for a fixed location, as the tunnel velocity is increased the boundary layer thickness decreases. Therefore, if a cylinder is outside the boundary layer at the minimum test velocity, it will remain outside the boundary layer as velocity is increased throughout the test. This was the case for gap distance tests GD01–GD03. They all had a $G/D > 1.8$ while the boundary layer δ/D at the minimum tunnel velocity was smaller than this. Therefore, we did not expect to see any boundary layer effects for this three tests. However, GD04 had a $G/D = 0.4$, which was smaller than the thinnest boundary layer, $\delta/D = 0.8$, at $U = 20$ cm/s. Therefore, this cylinder was submerged in the boundary layer during the entire test. If there were boundary layer effects, we would expect to see them in this test.

The results of the gap distance study can be seen in Figure 3.16 for the amplitude response and Figure 3.17 for the frequency response. There appears to be no effect caused by changing the ratio of gap distance, G , to cylinder diameter, D , by an order of magnitude (from 0.4 to 3.5) on the amplitude or the frequency response profiles. Also, because the amplitude and frequency response of GD04 was consistent with the other three gap tests,

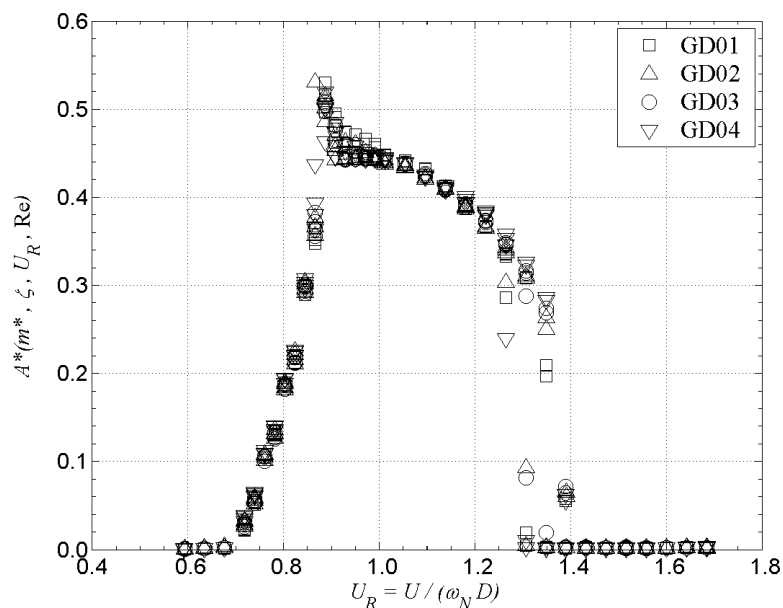


Figure 3.16: Amplitude response profile dependence on the gap distance, G/D , between the end of the cylinder and bottom of the test section.

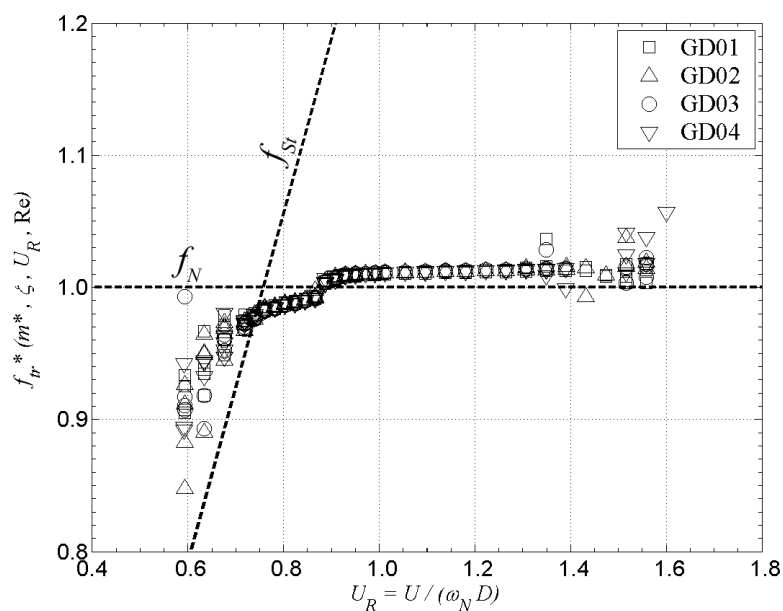


Figure 3.17: Frequency response profile dependence on the gap distance, G/D , between the end of the cylinder and bottom of the test section.

it appears that there was no effect from the boundary layer on the results either.

3.13 Starting Method Dependence

Various researchers have reported a difference in cylinder oscillation behavior depending on how the cylinder motion was started. For instance, Brika and Laneville (1993) reported that the highest amplitude portion of their response curve could only be reached through small incremental increases in the tunnel velocity with the initial conditions of the system at each increment being its previous state. Large increases in velocity increments, starting the cylinder from rest at each velocity increment, or externally imposing a large initial amplitude at each velocity increment did not allow the flexible cylinder to reach the highest amplitude portion of the curve. In another example, Anagnostopoulos and Bearman (1992) reported that they obtained a maximum amplitude of 53 percent of a diameter for cylinder oscillations developing from rest but a maximum amplitude of 60 percent of a diameter for oscillations developing from an already oscillating cylinder.

Due to the results of these studies, we conducted a series of experiments to test the cylinder response dependence on the initial conditions of the system. The two system configurations used for these initial condition, or starting method (SM), tests can be seen in Table 3.5.

test no.	D (mm)	m (kg)	b (kg/s)	k (N/m)	m^*	$b^* _{A_{\text{Max}}^*}$	$\text{Re} _{A_{\text{Max}}^*}$
SM01	10.0	1.880	0.032	295	80.5	0.130	1050
SM02	37.8	2.180	0.024	15.0	6.5	0.038	2700

Table 3.5: System configurations used for the starting method (SM) tests.

Five different initial conditions were investigated. One involved a small incremental increase or decrease in the tunnel velocity with the cylinder still oscillating from its previous steady-state condition. These two test methods were referred to as “up” and “down” tests. The third initial condition involved allowing the tunnel velocity to reach the desired value and then releasing the cylinder from rest. This test was referred to as a “rest” test. The fourth method involved having the cylinder and tunnel at rest, then impulsively starting the tunnel to the desired velocity. This type of test was referred to as a “start” test. The final initial condition involved setting the tunnel to the desired velocity, giving the cylinder

the largest displacement that the air bearings would allow, and then releasing the cylinder from this extreme amplitude. This type of test was referred to as an “impulse” test.

The amplitude response profiles of SM01 and SM02 can be seen in Figure 3.18 and the corresponding frequency response profiles in Figure 3.19 for these various initial conditions. As can be seen in both figures, there appears to be no dependence of the initial conditions of the system on the steady-state, time-averaged amplitude or frequency response profiles. The small variations in the amplitude and frequency responses between the starting method tests is within the experimental repeatability variations. One reason for the lack of initial condition effects in our system compared to the previously cited work could be from the rigidity of our cylinders. Brika and Laneville (1993) used *flexible* circular cylinders. Anagnostopoulos and Bearman (1992) used a rigid cylinder, however, it had an extremely small diameter, approximately 1.6 mm, so that perhaps it behaved as a *slightly flexible* cylinder. This could explain why they saw weaker effects of the initial conditions on the amplitude and frequency response profiles compared to Brika and Laneville. Perhaps a flexible circular cylinder will display initial condition effects and the more a cylinder behaves like a perfectly rigid cylinder, the less important the initial conditions become.

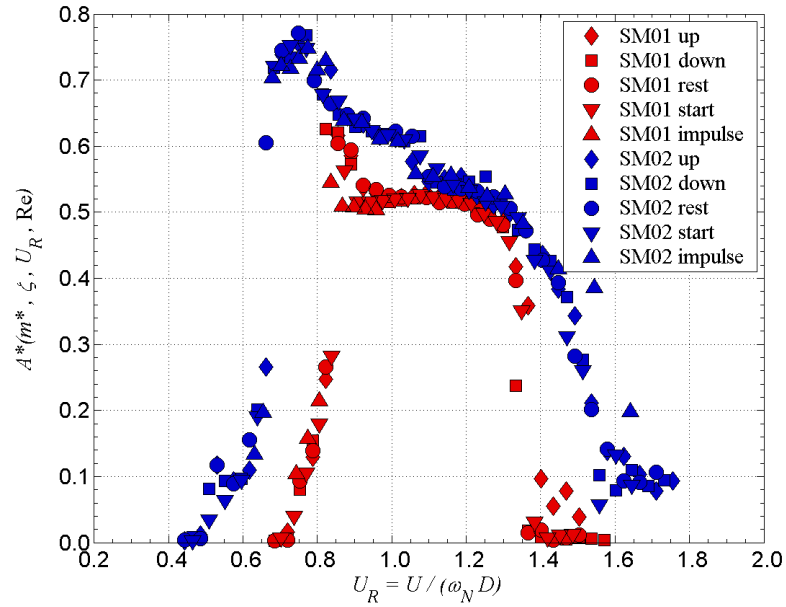


Figure 3.18: Amplitude response profile dependence on various starting method techniques for SM01 and SM02.

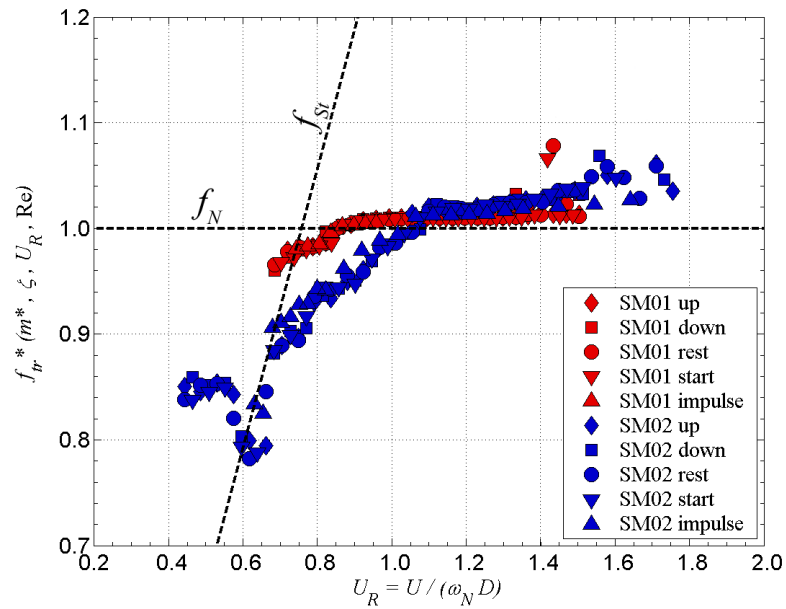


Figure 3.19: Frequency response profile dependence on various starting method techniques for SM01 and SM02.

Chapter 4

Basic Results

4.1 Chapter Overview

The first part of this chapter reviews the different types of behavior that exist in VIV using the traditional formulation and, at the same time, adding new insight to them using the effective stiffness formulation. In the second part, we explore damping and Reynolds number effects on the amplitude and frequency response profiles of an elastically-mounted, rigid, circular cylinder. In Section 4.2 we show some generic amplitude and frequency response profiles allowing us, in Section 4.3, to compare and contrast them in the two different formulations, traditional and effective stiffness. The fluctuations in the time-varying amplitude and frequency responses of the oscillating system are discussed in Section 4.4. Then, in Section 4.5 we discuss common wake structures seen in free-vibrations using a selected system. Next, in Section 4.6 we discuss some particular limiting-parameter cases of VIV. We look at damping effects on the amplitude response profile in Section 4.7 and how a given system transitions from a large-amplitude response profile to a small-amplitude response profile. This process will involve two processes, the scaling down of the lower branch and the “erosion” of the upper branch. Next, the corresponding frequency response changes, as damping changes, are studied in Section 4.8. Then we look at Reynolds number effects on the amplitude response profile in Section 4.9 and the frequency response profile in Section 4.10. This allows us to point out the similarities between damping and Reynolds number effects. Finally, Section 4.11 explains how to use these results to predict when structures are susceptible to large, flow-induced oscillations.

4.2 General Characteristics of Amplitude and Frequency Responses

As will be shown, there is no such thing as a “typical” VIV amplitude or frequency response profile. However, for the sake of comparing and contrasting results in the traditional and effective stiffness formulations, as well as making some general conclusions, we will show two distinct types of response profiles that are commonly seen in the literature. To accomplish this, we will be using two different systems configurations. The parameters for the two configurations can be seen in Table 4.1.

run no.	m (kg)	b (kg/s)	k (N/m)	m^*	ζ	$b^* _{A^*_{\text{Max}}}$	$\text{Re} _{A^*_{\text{Max}}}$
02(a)	3.700	0.023	135	158.6	0.0005	0.194	525
04(a)	2.390	0.016	13.5	7.1	0.0014	0.026	2600

Table 4.1: System configurations used to compare the traditional and effective stiffness formulations.

We begin by looking at the amplitude and frequency response profiles in the traditional formulation, plotted against the reduced velocity, U_R . The amplitude response profiles are shown in Figure 4.1 and the corresponding frequency responses in Figure 4.2. Looking first at the large nondimensional mass, low Reynolds number system, Run02(a), we see the amplitude response profile that was seen in early studies of VIV. The response profile has two distinct “branches” that Khalak and Williamson (1997b) defined and were discussed in Section 1.2. The frequency response of this system shows the classic “lock-in” behavior, meaning that the majority of the frequency response occurs with the system oscillation frequency and wake frequency “locking” into the system natural frequency. Next we look at the response profiles of the small nondimensional mass, high Reynolds number system, Run04(a). We notice that the amplitude response profile shows a different type of behavior that includes a large-amplitude region and thus shows three distinct branches. These three branches were also defined by Khalak and Williamson (1997b) and were also discussed in Section 1.2. The frequency response for this system is also quite different from the previous one. It shows a behavior that violates the common idea that large amplitudes occur only for a system experiencing “lock-in”. More surprising, the system does not “lock” onto any frequency. It appears that its oscillation frequency continues to increase as U_R is increased.

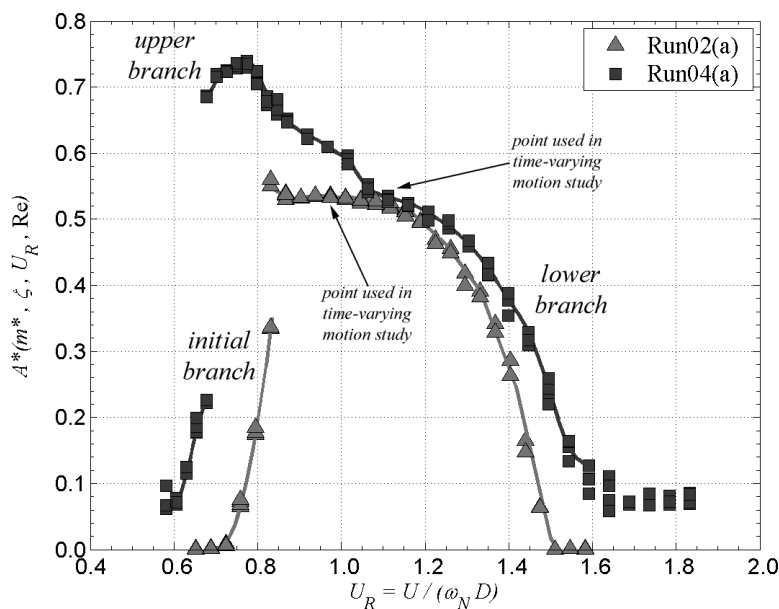


Figure 4.1: Two distinct amplitude response profiles, shown in the traditional formulation plotted against the reduced velocity, U_R , for systems experiencing VIV. Arrows mark a point in each run where time-varying motions will be investigated in Section 4.4.

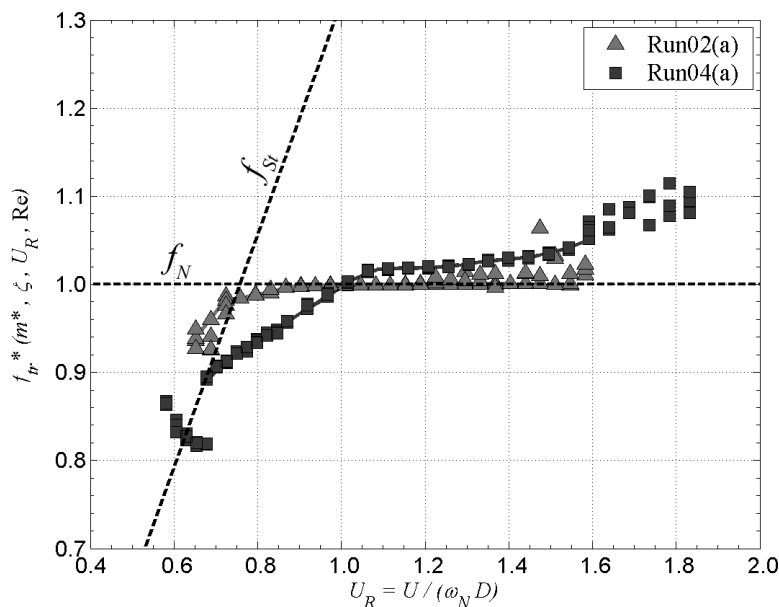


Figure 4.2: Corresponding frequency response profiles for Figure 4.1, shown in the traditional formulation plotted against the reduced velocity, U_R .

Systems that exhibit this lack of “lock-in” behavior have been studied recently by various researchers (Gharib, 1999; Khalak and Williamson, 1997b). Such a system has a frequency response that does not lie on, or “too near,” the natural frequency of the system.

The response profiles of these same two systems are also shown in the effective stiffness formulation. Their amplitude response profiles can be seen in Figure 4.3 and their corresponding frequency response profiles in Figure 4.4, both plotted against negative effective stiffness, $-k_{\text{eff}}^* = \omega^{*2}m^* - k^*$. It is important to note that in general, for a given system, the effective stiffness decreases as flow velocity increases. Therefore, for convenience in comparing with the traditional formulation plots in Figure 4.1 and Figure 4.2, we present plots against negative effective stiffness, $-k_{\text{eff}}^*$, since this increases with increasing U_R .

4.3 Formulation Comparison of Response Profiles

By comparing the system response profiles in the traditional formulation, Figure 4.1 and Figure 4.2 to the same system response profiles in the effective stiffness formulation, Figure 4.3 and Figure 4.4, one can see some of the advantages of using the effective stiffness formulation.

First, in the effective stiffness formulation, there is a collapse of the amplitude response profile and therefore the existence of universal critical values, that represent the beginning, maximum, and ending of the response. In the traditional formulation, the nondimensional mass of the system effects the range of reduced velocity values that one observes a system response. The less massive system, Run04(a), in Figure 4.1 has a much larger range of reduced velocity values over which you see a response than the more massive one, Run02(a). However, this is not the case in the effective stiffness formulation because, by reducing the number of parameters, we have eliminated the effects of mass. Instead, the mass and elasticity of our system are implicitly part of the effective stiffness parameter. For every system, measurable amplitude responses occur over a range of $-1 \lesssim k_{\text{eff}}^* \lesssim 10$ regardless of the actual nondimensional mass.

The reduced velocity is a logical experimental parameter, since most VIV experiments involve spanning tunnel velocities of interest. Nondimensionalizing the tunnel velocity with a characteristic length (cylinder diameter) and time (system natural frequency) appears to be a good idea at first. However, as mentioned above, the reduced velocity parameter is mass

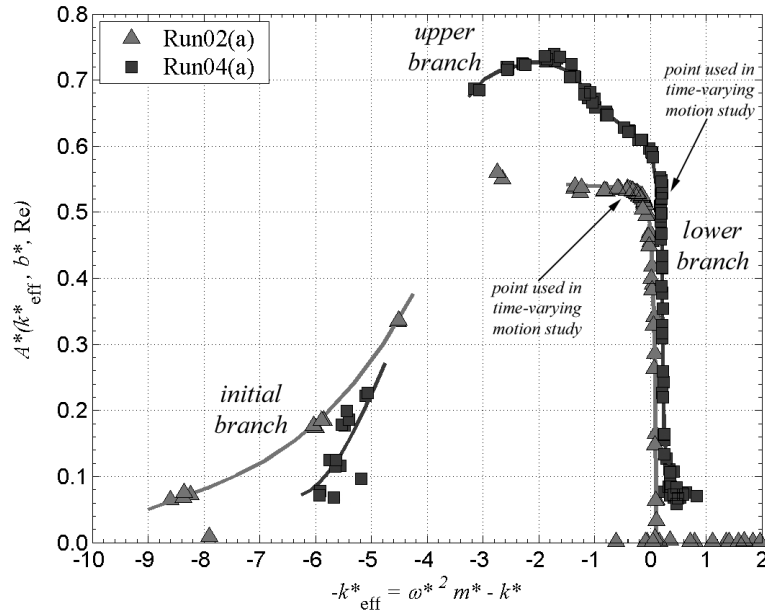


Figure 4.3: Two distinct amplitude responses profiles, shown in the effective stiffness formulation plotted against the negative effective stiffness, $-k_{\text{eff}}^*$, for systems experiencing VIV. Arrows mark a point in each run where time-varying motions will be investigated in Section 4.4.

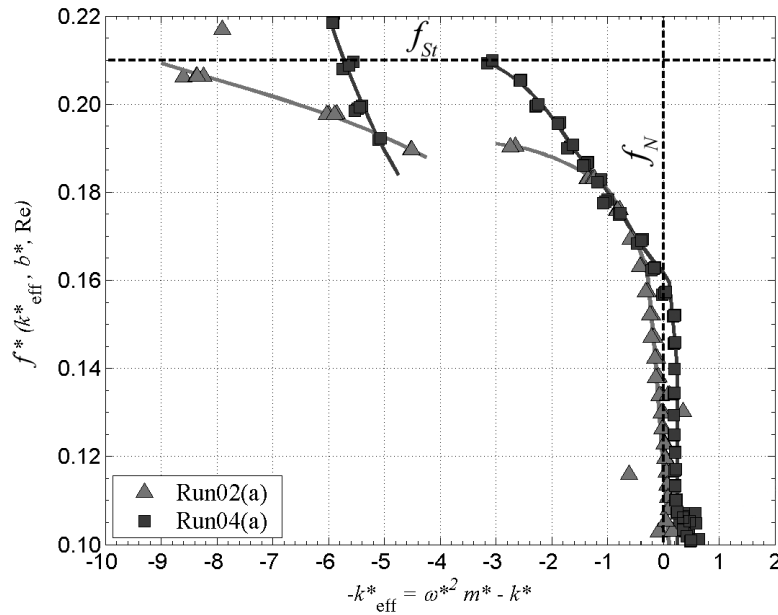


Figure 4.4: Corresponding frequency responses profiles for Figure 4.3, shown in the effective stiffness formulation plotted against the negative effective stiffness, $-k_{\text{eff}}^*$.

dependent, so critical reduced velocity values can only be applied to systems that, at the very least, have identical masses. On the other hand, the effective stiffness parameter, by taking into account the mass, elasticity, fluid velocity, and oscillation frequency of the system, collapses the response profile for all systems, regardless of their actual mass. Therefore, the values that correspond to the beginning, maximum, and end points of the response, are roughly universal ones.

The fact that *all* systems have approximately the same effective stiffness value for their maximum amplitudes is a useful advantage of the effective stiffness formulation. We will take advantage of this fact in Chapter 5 to analyze maximum amplitudes. In the traditional formulation, based on the ideas of “lock-in” and resonance, it followed that the maximum cylinder amplitude would occur when the flow conditions were such that the shedding frequency, f_{shed} , of an equivalent *stationary* cylinder equalled the natural frequency, f_N , of the VIV system. This meant that the maximum cylinder amplitude should occur when $f_{shed} \approx f_N$ and at a reduced velocity value of

$$U_R = \frac{U}{2\pi f_N D} \approx \frac{U}{2\pi f_{shed} D} \approx \frac{1}{2\pi St} \approx 0.758, \quad (4.1)$$

where St is taken to be 0.210 for a stationary circular cylinder. Although the maximum amplitude will indeed occur *near* this reduced velocity value, the actual value will depend on the various systems parameters. Furthermore, the deviation from this value increases as certain system parameters such as mass or Reynolds number approach their extreme limits. However, the effective stiffness formulation allows all maximum amplitudes to occur at approximately the same effective stiffness value. We denote the value of the effective stiffness at peak amplitude as $k_{\text{eff}}^*|_{A_{\text{Max}}^*}$. For a variety of system configurations tested, we find that the peak amplitude in each case occurs around $k_{\text{eff}}^*|_{A_{\text{Max}}^*} \approx 2.5$, with k_{eff}^* varying from 10 to -1. This can be seen in Figure 4.5 where we plot various systems together, including the two previously discussed ones, Run02(a) and Run04(a). The damping and Reynolds number values for all the systems can be found in Table 5.1.

In fact, we find that for lightly to moderately damped systems, the location of the maximum amplitude is invariant to individual system mass and elasticity and always occurs around the same value. We only assign an approximate value to $k_{\text{eff}}^*|_{A_{\text{Max}}^*}$ because we find that the actual value does vary slightly depending on the the specific damping value and

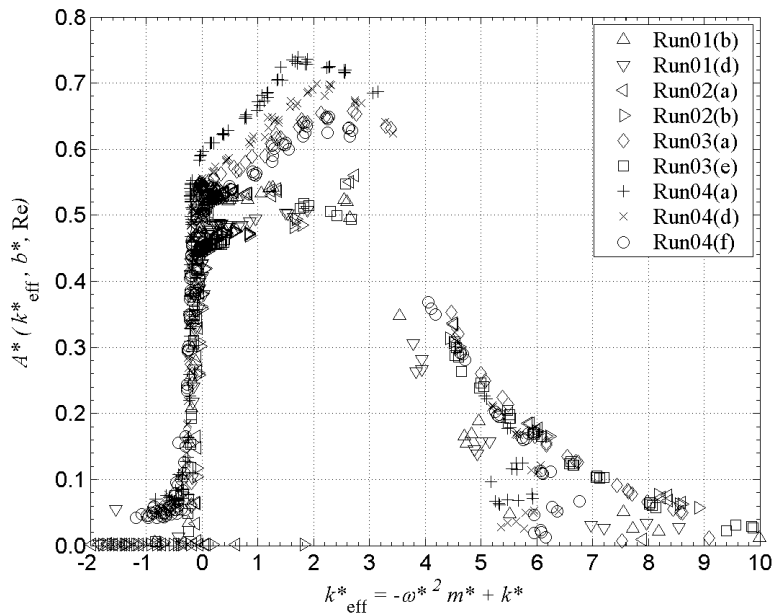


Figure 4.5: Maximum amplitude, A_{Max}^* , of various system configurations plotted against effective stiffness, k_{eff}^* . Note that the maximum amplitude point for each configuration always occurs around $k_{\text{eff}}^*|_{A_{\text{Max}}^*} \approx 2.5$. Damping and Reynolds number values for each run can be found in Table 5.1.

Reynolds number of the system. This is mainly due to the fact that a system with an upper branch will have a slightly different $k_{\text{eff}}^*|_{A_{\text{Max}}^*}$ than one that does not have an upper branch. Also, the large-amplitude portion of a high Reynolds number system has large enough variations in the cycle-by-cycle amplitudes to effect the representative average value and cause $k_{\text{eff}}^*|_{A_{\text{Max}}^*}$ to move slightly, even for consecutive identical runs. It is interesting to note that the maximum amplitude does not occur at $k_{\text{eff}}^* = 0$ (which corresponds to the “lock-in” condition, $\omega^{*2} = \omega_N^{*2} = k^*/m^*$) but at a higher positive value. This highlights the problem with using $U_R = 0.758$ as the maximum amplitude point since it assumed that the maximum amplitude occurred while the system’s shedding and oscillation frequencies were “locked-in” to the system’s natural frequency.

A second advantage of the effective stiffness formulation is that it expands areas of interest (the region of largest amplitudes) and compresses areas of less interest (the nearly constant amplitude portion of the lower branch) on the amplitude and frequency response profiles. The traditional formulation does the opposite; it compresses the largest response region and exaggerates the lower branch response portion. Part of the problem is that the

traditional formulation has an equal spacing in abscissa between all points, assuming a test involved constant incremental changes in fluid velocity. However, the bigger problem is that the largest amplitude region occurs over a relatively small reduced velocity range while the lower branch exists over a large one. This happens even though the system undergoes very dramatic changes through the largest amplitude portion and very little change through the lower branch portion. The effective stiffness parameter captures the dramatic changes as the system passes through the largest amplitude portion of the response curve and its value changes substantially, expanding the largest amplitude portion of the profile curve. This region corresponds to roughly $0 \lesssim k_{\text{eff}}^* \lesssim 3$. On the other hand, the effective stiffness parameter also captures the fact that very little is changing with the system as it goes through the lower branch and consequently, k_{eff}^* changes very little. In fact, it actually reduces the lower branch down to nearly a single point, corresponding to roughly $k_{\text{eff}}^* \approx 0$.

Third, the effective stiffness formulation has an advantage over the traditional formulation with respect to the frequency response profile. In the traditional formulation, the nondimensional frequency is the ratio of oscillation frequency to system natural frequency, $f_{tr}^* = f/f_N$. However, the range that this parameter takes is rather large since the response frequency has contributions from two different sources. At the beginning and end of its response, it roughly follows the Strouhal shedding frequency line, f_{St} . During the middle part of the system response, it lies near the system natural frequency line, f_N . However, these two lines are independent of each other and, in most cases, are far apart from each other at the beginning and end of the response profile. This causes the frequency response to undertake a large range of values. The behavior of the parameter f_{tr}^* is also heavily dependent on the actual nondimensional mass of the system. As can be seen in Figure 4.2, the less massive system has a frequency response that is farther from the “lock-in” condition than the more massive system. The idea of “lock-in” was reinforced by these two unfortunate side effects of the traditional formulation. Since studies of early systems were in air, they had a large nondimensional mass and thus sat very near the natural frequency line. However, it appeared that the system was exactly on the natural frequency line since the range over which the parameter was viewed was large, owing to the effort to capture the natural and Strouhal frequency effects. Khalak and Williamson (1997b) showed that if you had an extremely small nondimensional mass system, you could capture the large range of frequencies and still easily notice the lack of “lock-in.” But this would be nearly impossible

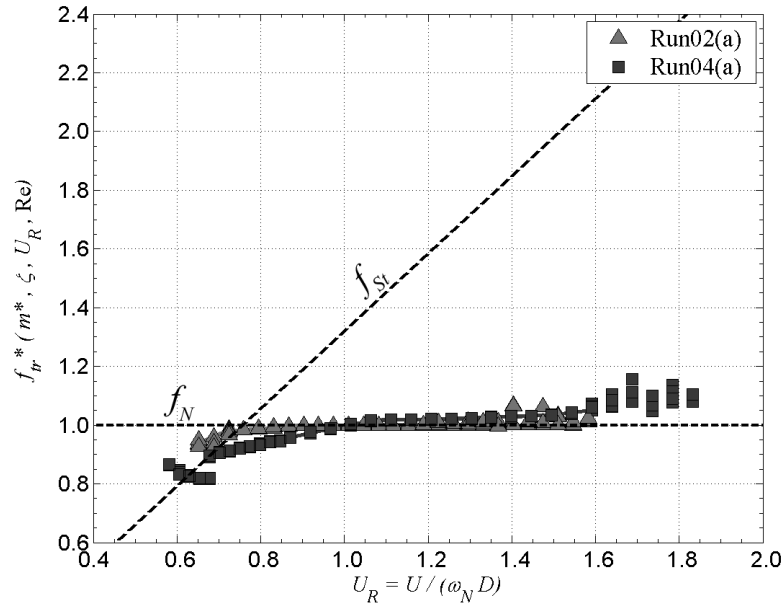


Figure 4.6: Frequency response in the traditional formulation displayed over the entire range of interest which causes the response profile to appear to be “locked-in” to the system natural frequency.

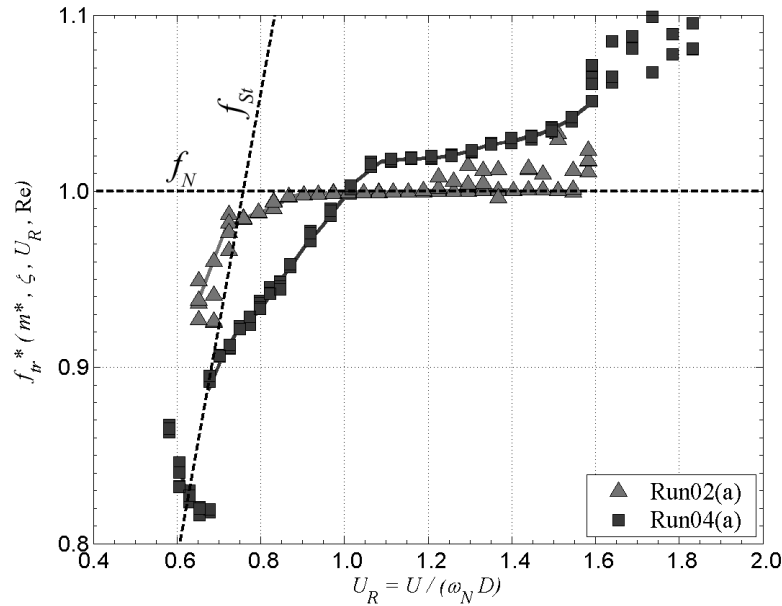


Figure 4.7: Same frequency response as Figure 4.6 but now only displayed over a small range near the system natural frequency.

to do in air; they had an $m_{tr}^* = 2.4$. In Figure 4.6, the traditional method is used to plot the frequency response profiles of the same systems from Figure 4.2 and it appears that both systems are experiencing “lock-in.” However, if *only* the area around the natural frequency line is plotted, as in Figure 4.7, it becomes apparent that the small nondimensional mass system, Run04(a), is not “locked” into the natural frequency and only Run02(a) is, owing to its large nondimensional mass.

In the effective stiffness formulation these problems are not present. The mass dependence is resolved because it is implicitly captured by the effective stiffness parameter, as first mentioned in Section 2.10 and discussed earlier in this chapter. The “lock-in” issue is resolved by not using two different frequency time scales, the fluid shedding frequency and structural natural frequency, in the problem as the traditional frequency does. Instead, only the the natural fluid time scale, D/U , is used. By doing this, the entire frequency response profile can be shown in a compact manner and the frequency contributions from the two independent sources are captured without having to worry about decreasing the parameter viewing range.

It is interesting to note that in the effective stiffness formulation, the Strouhal frequency and natural frequency lines are orthogonal to each other. On the other hand, in the traditional formulation, they cross each other at an angle. The effective stiffness parameter therefore transforms the traditional formulation by stretching the frequency plane out so that those two lines are orthogonal.

4.4 Time-Varying Motion

A major difficulty in representing VIV motion is that it is not a steady-state motion. The amplitude and frequency values of each oscillation cycle are constantly changing in time. Therefore, the data in Figure 4.1 – Figure 4.4 only represents an average behavior over time. As mentioned in Section 3.11, our results are based on an average using every cycle of our time sample, other researchers average various subsets from their entire time sample, but regardless of the method, one must never forget that each data point is only an approximation of the actual behavior. To highlight this difficulty, we look at the time-varying motion of a similar point for the two distinct systems that we have previously compared, Run02(a) and Run04(a). The point in each run that we are comparing is highlighted with

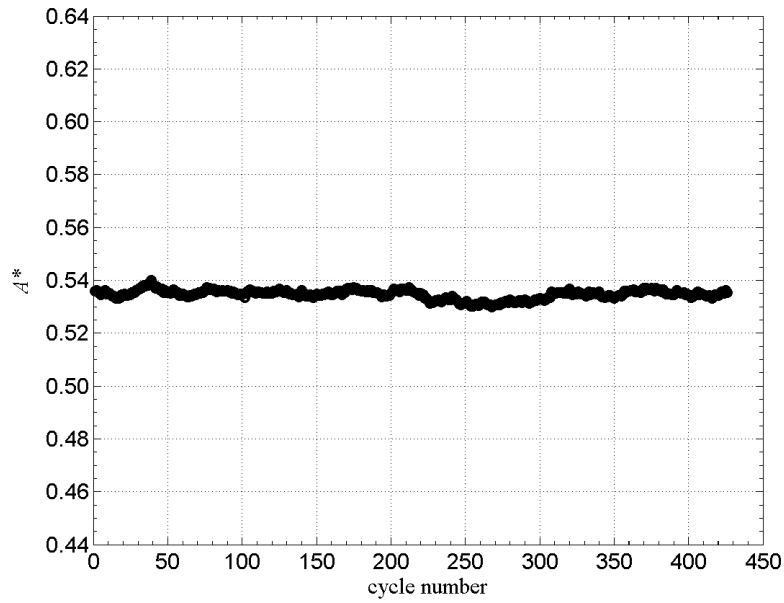


Figure 4.8: Amplitude fluctuations per cycle of a low Reynolds number, high mass system (Run02(a)) viewed over approximately 400 cycles.

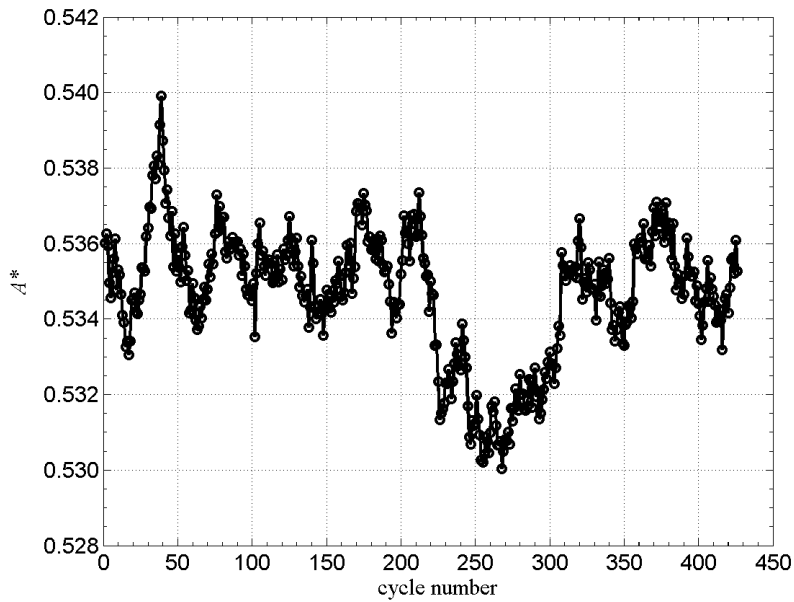


Figure 4.9: Same amplitude fluctuations per cycle as shown in Figure 4.8 but now displayed over a much smaller amplitude range, 0.014 units, in order to show the cycle-by-cycle fluctuations clearly.

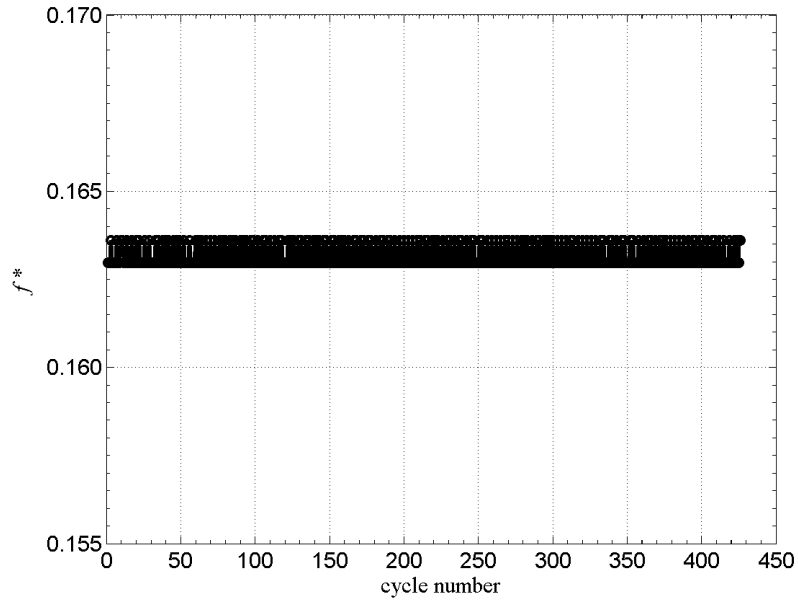


Figure 4.10: Frequency fluctuations per cycle of a low Reynolds number, high mass system (Run02(a)) viewed over approximately 400 cycles. The fluctuations are below our measurement resolution, causing the response to alternate between our two minimum resolved frequencies.

an arrow in Figure 4.1 and Figure 4.3. Both of these points lie in the lower branch region of the response curve and have nearly equal time-averaged amplitudes of $A^* \approx 0.54$.

In some cases, these time variations are small, and representing the amplitude or frequency at a particular response point as a single value is reasonable. We have found that such a situation exists for large nondimensional mass systems at low Reynolds number, such as Run02(a). Our analysis method allows us to keep track of each cycle of motion, therefore, we have cycle-by-cycle amplitude and frequency results. Figure 4.8 shows the time-varying amplitude response of the highlighted point for Run02(a) over a reasonable amplitude range, 0.2 units. By using such a range, the fluctuations between each cycle cannot be seen. In order to see the small fluctuations that occur in each cycle, refer to Figure 4.9. The largest variations, however, are less than 2 percent away from the reported time-averaged value.

The frequency response shows similar behavior, but now, the fluctuations over time are so small, they are at the resolution limit of the data acquisition. Therefore, the time varying fluctuations simply jump between the two smallest values that we can resolve. This can

be seen in Figure 4.10, where the data forms a thin, dense band because the response is jumping between our two minimum resolved frequencies.

These amplitude and frequency response fluctuations can be compared and contrasted against a light mass system in a high Reynolds number flow, such as Run04(a). Our cycle-by-cycle amplitude results, for the highlighted lower branch point, are shown in Figure 4.11 over the same reasonable viewing range, 0.2 units, as Figure 4.8. Our corresponding cycle-by-cycle frequency results are shown in Figure 4.12. For this system, the time variations are much more dramatic. For comparison sake, we roughly match the amplitude response range of Figure 4.11 and Figure 4.8 and the frequency response range of Figure 4.12 and Figure 4.10.

In Figure 4.8, the amplitude response of the large mass, small Reynolds number system is fairly constant, on the other hand, the response for the light mass, high Reynolds number system, Figure 4.11, shows dramatic amplitude fluctuations over time. Run02(a) had roughly 2 percent amplitude fluctuations compared to the roughly 10 percent for Run04(a). This same difference can be seen in the frequency response. Whereas Run02(a) responded at only one frequency (within our ability to resolve), Run04(a) showed a region of response frequencies. In this case, the frequencies varied by about 5 percent.

To see if there were one or two dominant amplitudes or frequencies, histogram plots of the oscillation response of the light mass, high Reynolds number system, Run04(a), were created. This can be seen in Figure 4.13 and in Figure 4.14 respectively. If the system had one or two dominant states, we would expect to see a corresponding number of peaks in our histogram data. Instead, we see a well distributed response suggesting that the system fluctuations are not caused by it moving between two preferred states but rather oscillating within a range of permissible amplitude and frequency values.

4.5 General Wake Structure

The different branches of the response profile have different wake structures associated with them. In order to capture the various wake structures, DPIV was done at several points in the response profile of the large-amplitude system, Run04(a). A total of six different cases will be presented here. The various points that DPIV was performed at can be seen in Figure 4.15.

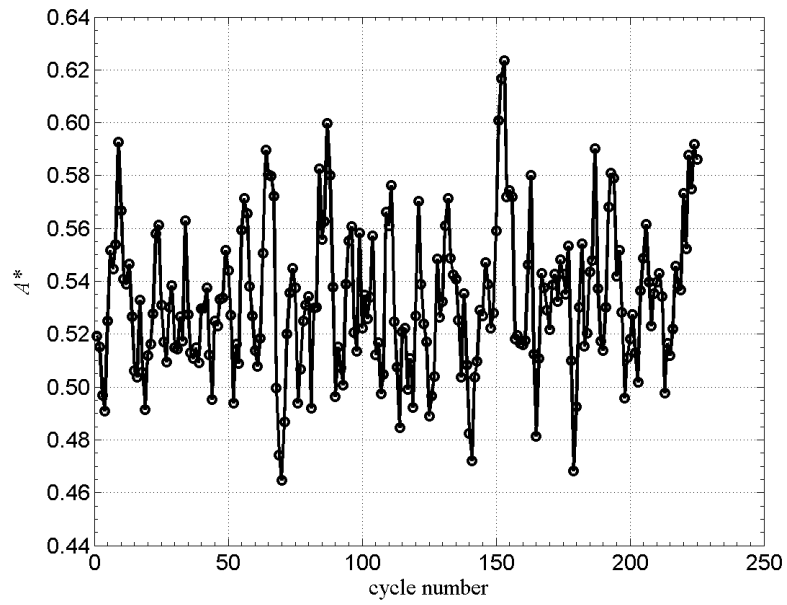


Figure 4.11: Amplitude fluctuations per cycle of a high Reynolds number, light mass system (Run04(a)) viewed over approximately 250 cycles.

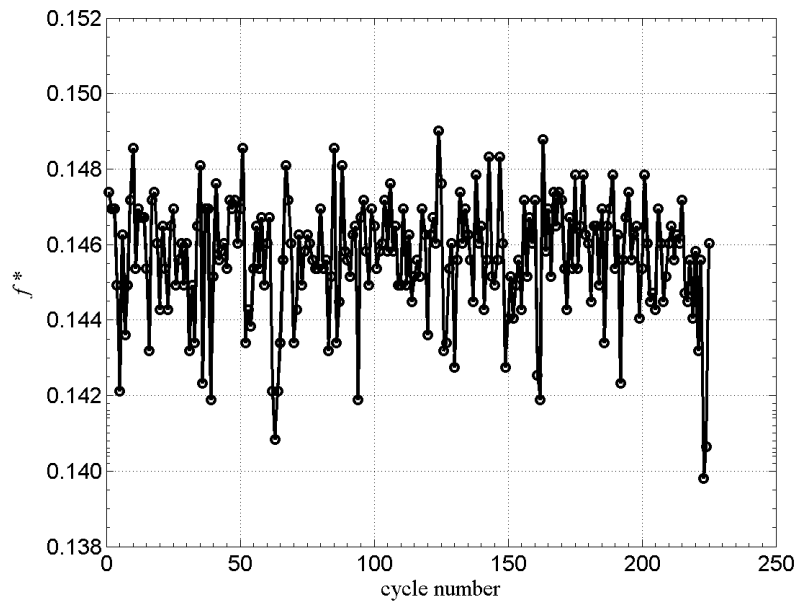


Figure 4.12: Frequency fluctuations per cycle of a high Reynolds number, light mass system (Run04(a)) viewed over approximately 250 cycles.

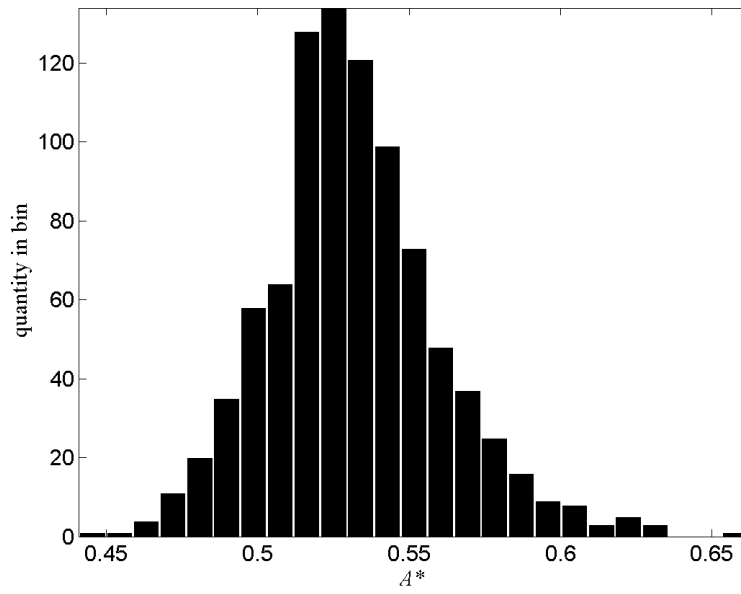


Figure 4.13: Amplitude cycle-by-cycle histogram results for four runs, approx 1000 cycles, of a high Reynolds number, light mass system (Run04(a)).

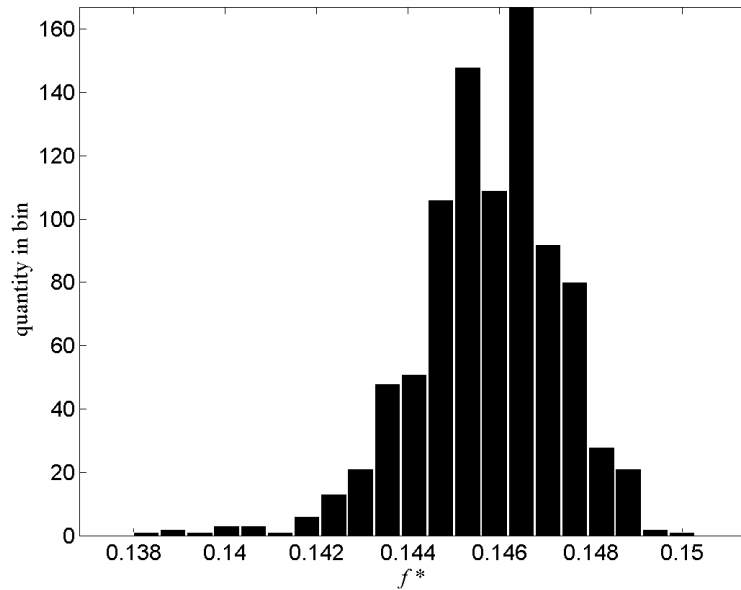


Figure 4.14: Frequency cycle-by-cycle histogram results for four runs, approx 1000 cycles, of a high Reynolds number, light mass system (Run04(a)).

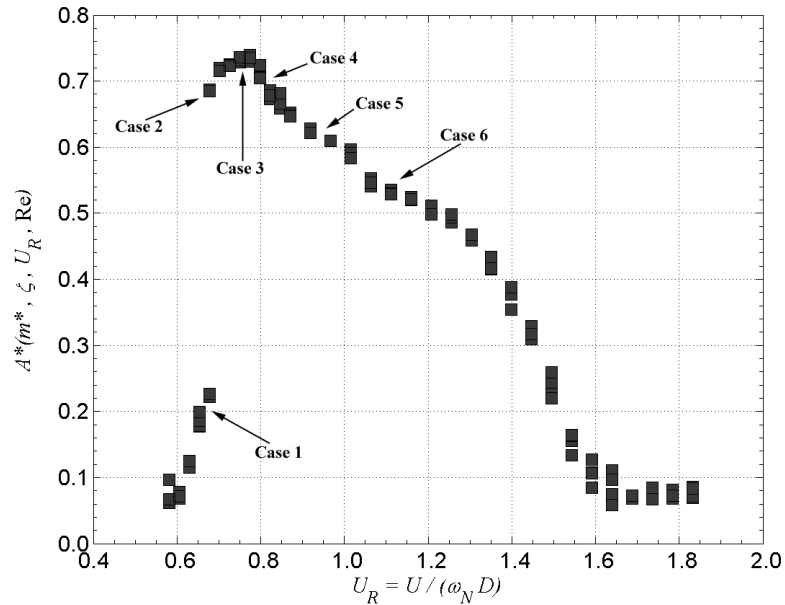


Figure 4.15: Locations in the amplitude response profile where the wake structure was investigated using DPIV.

Previous researchers have shown the various permissible wake structures, depending on the oscillation amplitude and frequency, through forced oscillation experiments (Öngören and Rockwell, 1988a,b; Williamson and Roshko, 1988). The work by Williamson and Roshko (1988) included a “mapping” of such structures. This mapping was discussed in Section 2.4 and shown in Figure 2.3. Based on this work, we can anticipate what the wake structure, for a freely-vibrating system, should be.

Accordingly, the initial branch (case 1) has an amplitude and frequency response that should correspond to a classic 2S wake structure (similar to a von Kármán street). In an early study using a flexible cable, Brika and Laneville (1993) reported that their corresponding initial branch was a classic 2S wake structure, and this is similar to what we find. This wake structure involves the shedding of two single (2S) counterrotating vortices, of opposite sign and approximately equal strength, each cycle. This can be seen in the DPIV images of Figure 4.16 where a cycle is shown over sixteen frames, going from top to bottom, left to right. Also note that the vortices are shed in phase with the motion of the cylinder, the top, clockwise rotating, vortices (blue) are shed when the cylinder is at the top of its motion. The opposite is true for the bottom, counterclockwise rotating, vortices (red), they

are shed at the bottom of the cylinder motion.

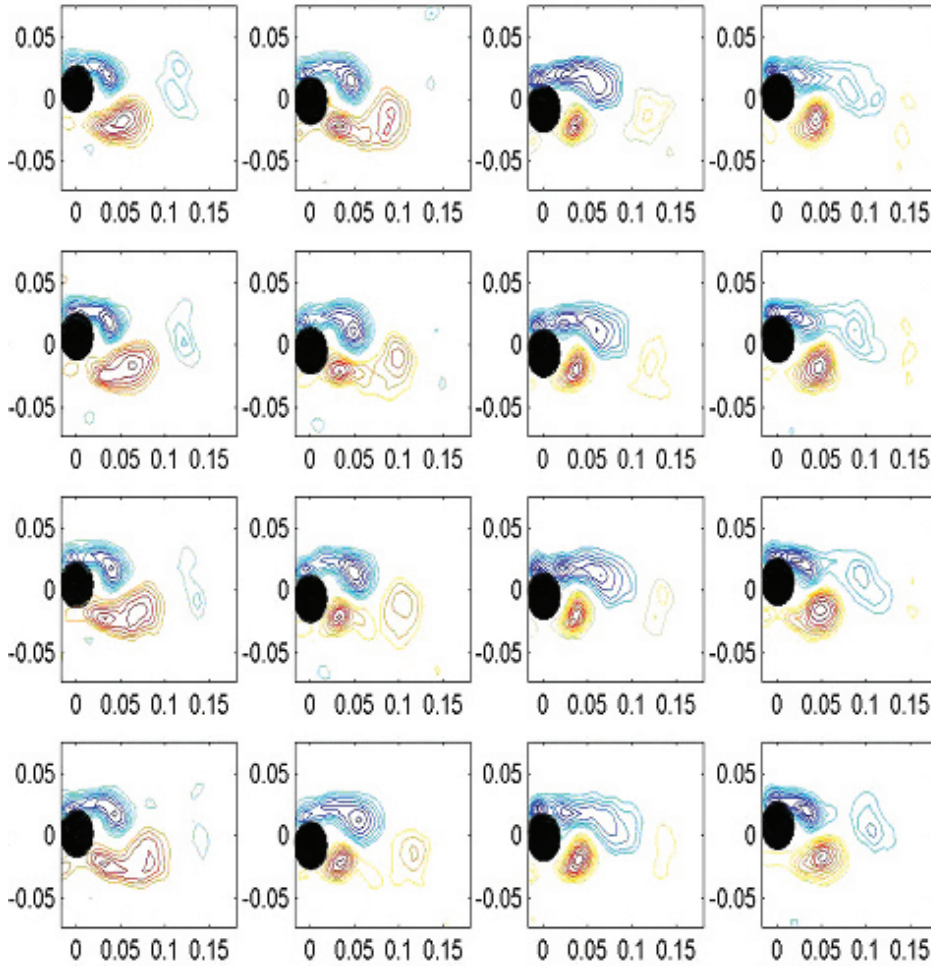


Figure 4.16: Wake structure of the initial branch (case 1).

The upper branch has been reported by various investigators as having a 2P wake structure (Khalak and Williamson, 1999). This structure involves the shedding of two pairs (2P) of counterrotating vortices, of opposite sign and roughly equal strength, each cycle. Recently, Govardhan and Williamson (2000) found that the 2P structure that they observed in the middle of the upper branch was slightly different. They reported seeing an unbalanced vortex pair, with the second vortex in the pair having roughly 20 percent the circulation of the first. By exploring more points in the upper branch, we find that the wake structure of the system immediately after it changes to a large-amplitude state (case 2) is neither a classic 2S nor 2P structure. Instead, we find some characteristics that are typical of each mode. The wakes structure of this point can be seen in Figure 4.17.

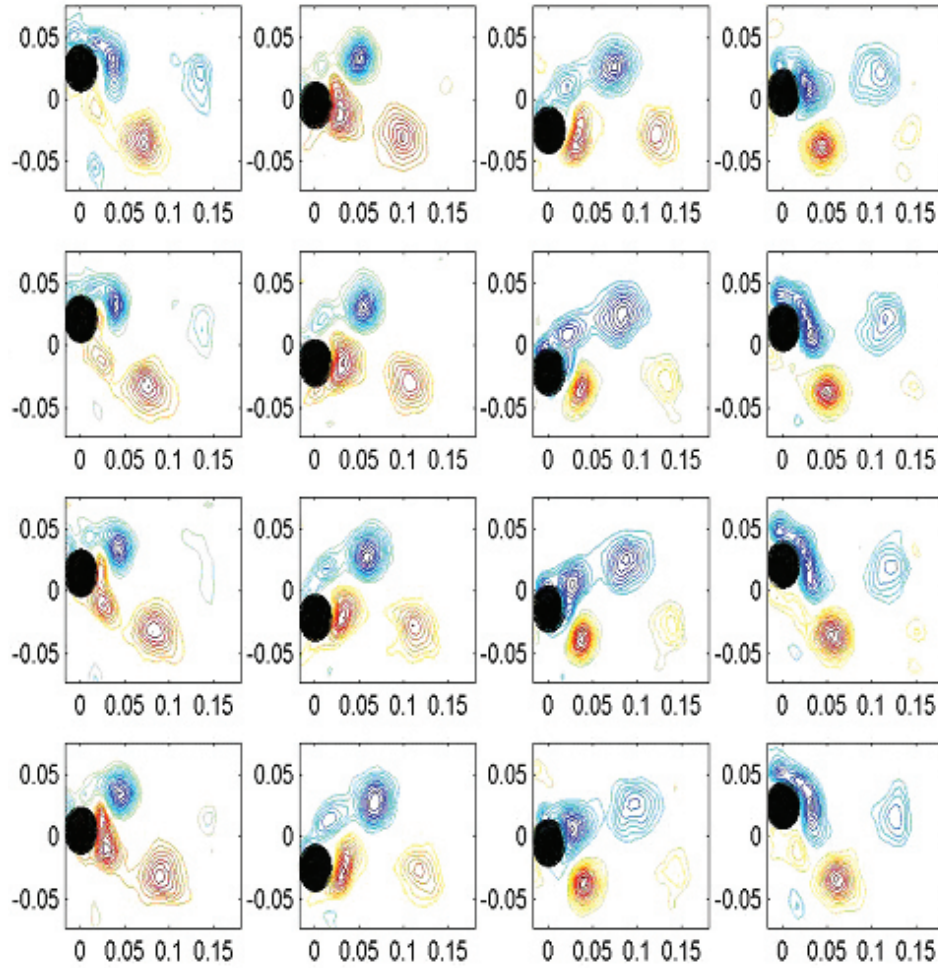


Figure 4.17: Wake structure of the beginning of the upper branch (case 2).

The vortices that are shed are only two single vortices each cycle, this is the 2S contribution. But, due to the large motion of the cylinder, they are shed obliquely, resembling a 2P trajectory. Also, the alternating shear layers that are rolling up cross over the back stagnation point, also consistent with a 2P structure. However, they do not cross over enough to extend beyond the opposite side of the cylinder. It is also interesting to note that it appears that the phase of the shedding has changed. The vortices are now shedding as the cylinder passes through the zero amplitude point.

The middle of the upper branch (case 3) begins to show a definite 2P wake structure, although we find that the second vortex in each pair has almost zero strength. This extremely unbalanced 2P wake state can be seen in Figure 4.18. Since the second vortex in the pair is extremely weak it does not appear in the downstream wake. However, by observing the

near wake, it is possible to see a small, very weak, vortex emerge from the pinch-off of the large shear layer that has wrapped up behind the cylinder.

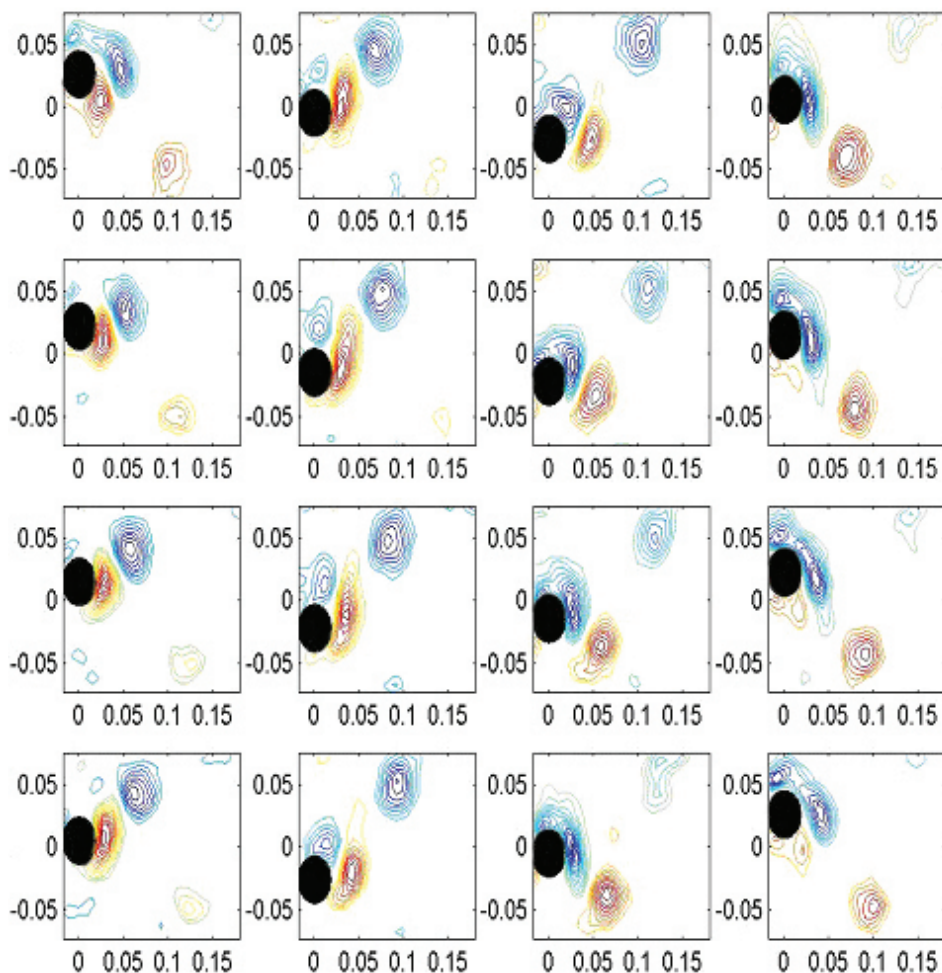


Figure 4.18: Wake structure of the middle of the upper branch (case 3).

At the end of the upper branch (case 4), we begin to see the second vortex of each pair in the downstream wake. It is still extremely weak relative to the first and has decayed below our ability to discern it within two frames after it was pinched off. This can be seen in our DPIV images in Figure 4.19.

Unfortunately, we did not do a quantitative study on the vortices so we are not able to compare our results to the 20 percent strength value that is reported in Govardhan and Williamson (2000). All we can deduce is that as you move through the upper branch, the second vortex in each pair steadily grows in strength.

As we move into the beginning of the lower branch (case 5), we continue to see the trend

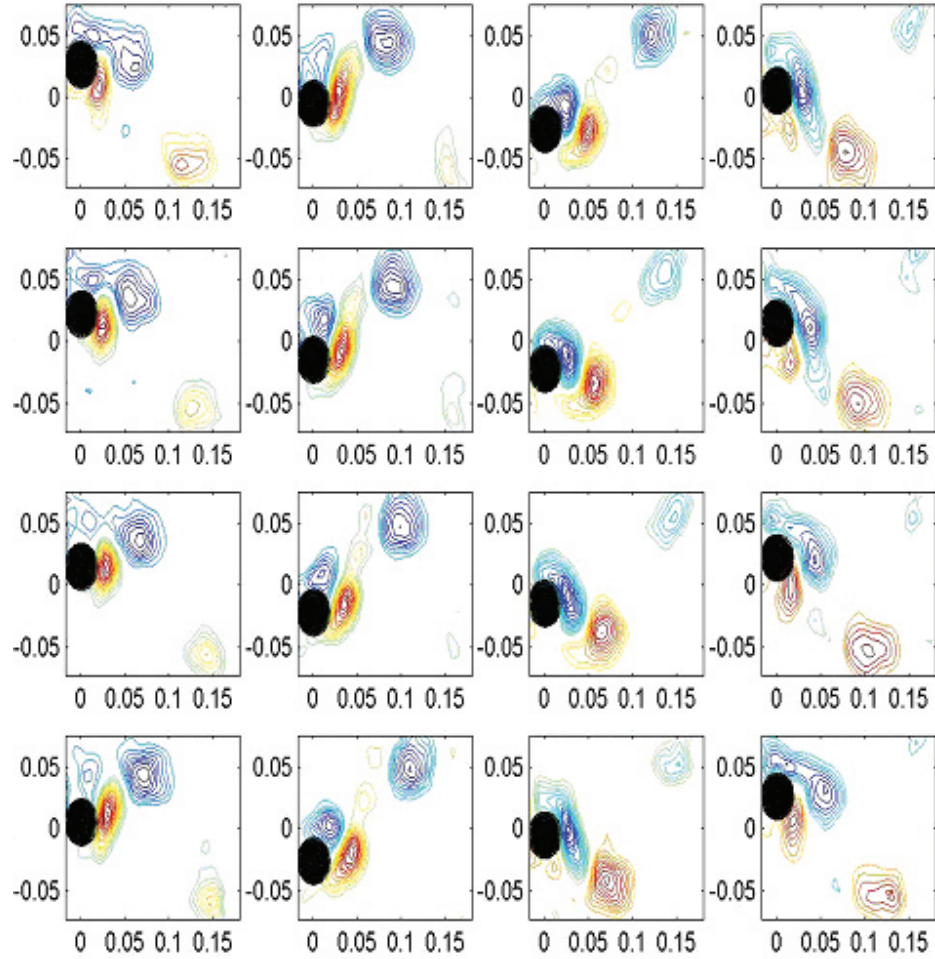


Figure 4.19: Wake structure of the end of the upper branch (case 4).

that we observed while moving through the upper branch: a 2P wake structure that has the second vortex in each pair growing in strength. As can be seen in Figure 4.20, there are two pairs of vortices shed each cycle, and the second vortex in each pair is stronger than in Figure 4.19. However, the second vortices are still not near the strength of the first vortex. In fact, one needs to go into the middle of the lower branch (case 6) in order to find where each vortex in the pair is of nearly the same strength, at least qualitatively. This can be seen in Figure 4.21.

Care must be taken when averaging images from many cycles to produce one representative image. It is the same type of problem that one encounters when averaging the complete oscillation trace to produce a single amplitude value. In the amplitude case, the single, average value could not capture how much variation there was in the complete trace.

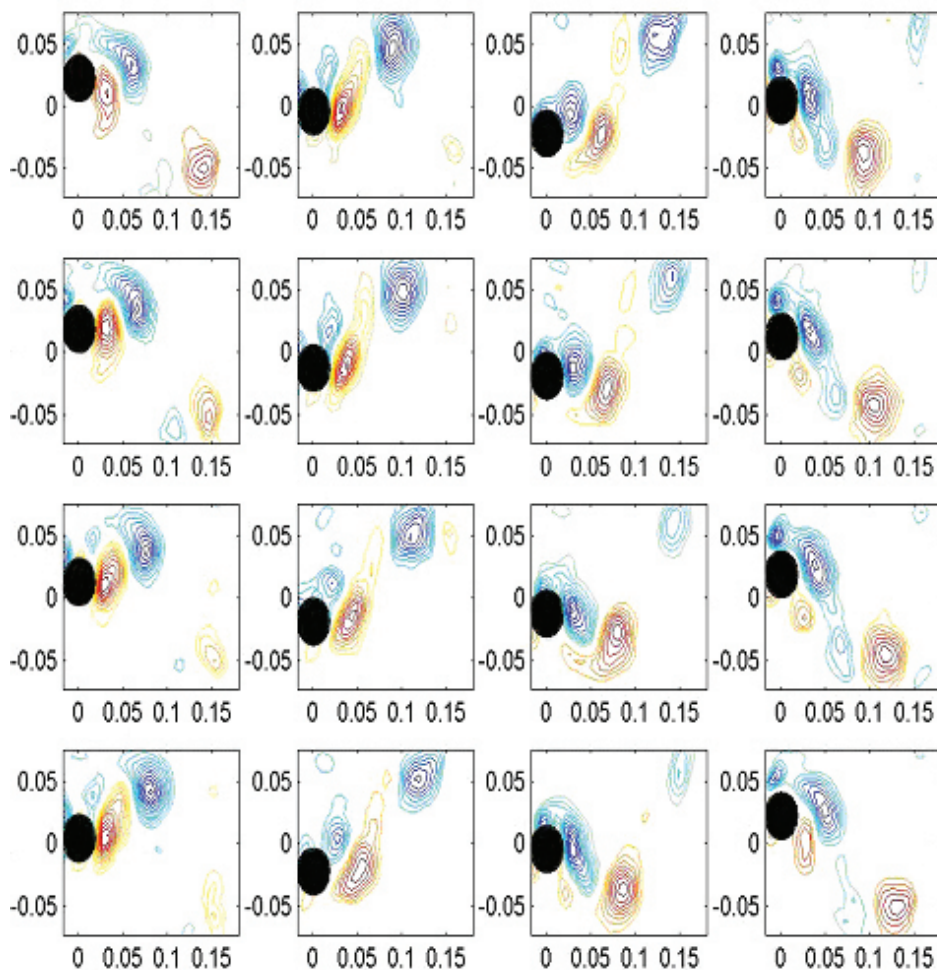


Figure 4.20: Wake structure of the beginning of the lower branch (case 5).

In the flow visualization of the wake state, there is no way to capture how much the wake state is changing, if at all, between cycles. As an example, let us further examine the middle point of the upper branch (case 3) that was shown, through cycle-averaged DPIV, to have a definite 2P wake structure with the second vortex in each pair being very weak. However, by using dye flow visualization and looking at two different instantaneous images of the cylinder wake a few cycles apart, Figure 4.22 and Figure 4.23, we get a very different picture. In the first image, Figure 4.22, we notice that there are not extremely weak second vortices paired with the strong vortices. Instead, the very small amount of opposite color dye near each vortex was caused by entrainment of the near wake. Also, the vortices are shed closer to the centerline than expected (this can be noticed by comparing the vertical

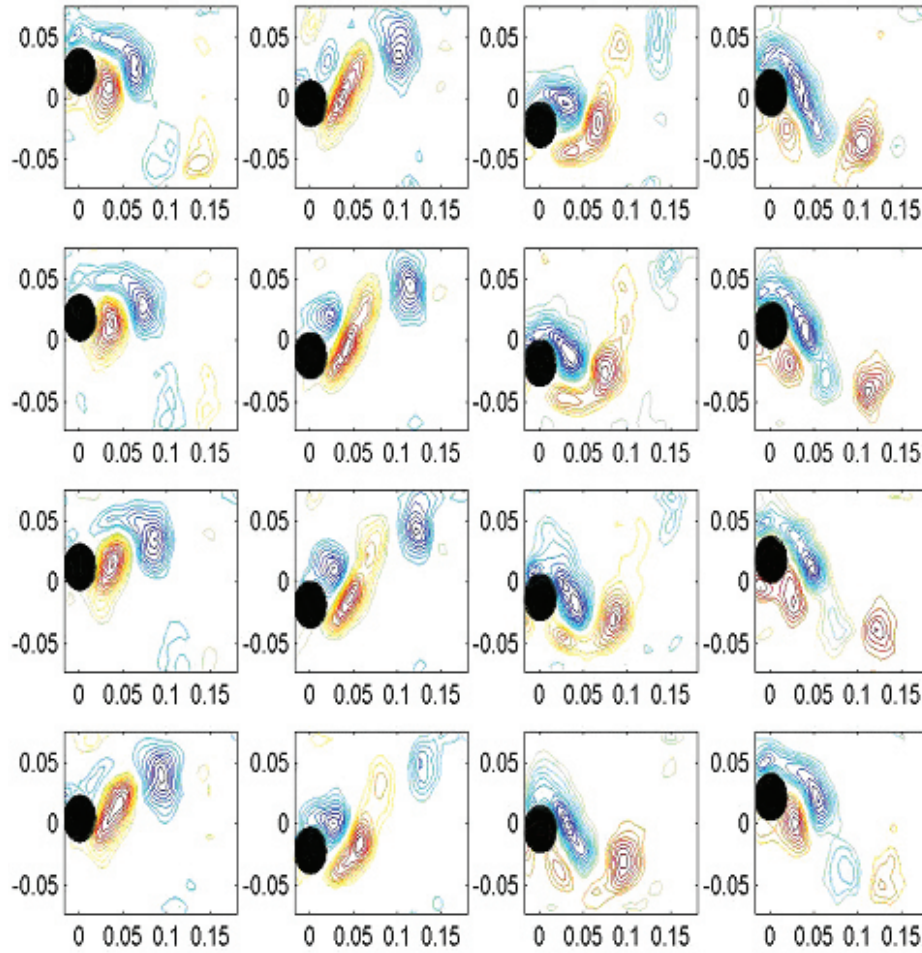


Figure 4.21: Wake structure of the end of the upper branch (case 6).

distance between the red and blue vortices in Figure 4.22 and the two red vortices in Figure 4.23). This wake state is perhaps closer to a 2S state than a 2P state. A completely different wake structure is seen in the second image, Figure 4.23. In this image, two clear and distinct pairs of vortices exist. Although the vortices in each pair are not quite equal in strength, they are much closer in strength, and thus much closer to a classic 2P wake structure, than the DPIV images suggest. Remember that these two flow visualization images came from the *same* test, less than 20 cycles apart. Clearly, the DPIV cycle-averaged images cannot begin to represent the fluctuating and changing wake structure of a system in the upper branch and thus can lead to an insufficient representation of the actual wake dynamics.

According to the WR-plane, the upper and lower branch both lie in the 2P wake struc-



Figure 4.22: Flow visualization of the wake during an individual cycle in the middle part of the upper branch (case 3) showing a structure resembling a 2S wake.



Figure 4.23: Flow visualization of the wake during an individual cycle of the middle of the upper branch (case 3) showing a structure resembling a classic 2P wake.

ture. However, we see changes in the amplitude and frequency responses while moving through those branches. Perhaps the reason for this is that the 2P portion of the plane includes a wide range of wake states that all resemble the classic 2P structure, in a general sense. This wide range of states extends all the way from completely unbalanced (second vortex in pair has zero strength, case 2) to completely balanced (second vortex has equal strength to first, case 6). And during a VIV test, as you move across the WR-plane, you are moving through this region that involves the changing strength of the second vortex in the pair. This changing strength of the second vortex affects the response of the cylinder. The last piece of support for this could be the fact that the lower branch coalesces into a single point in the effective stiffness formulation. This point could correspond to when the second vortex becomes about equal in strength to the first and no further changes can occur, as the tunnel velocity is increased, until a desynchronized wake state is reached.

4.6 System Singularities

The study of limiting structural parameters, such as zero system mass, damping, or elasticity, has the potential to contain interesting behavior. This is another advantage of the effective stiffness formulation: it can handle limiting structural parameters without causing singularities in the formulation. This is because the nondimensionalization does not depend on the system natural frequency. In cases where there is zero mass or elasticity, the natural frequency is undefined, causing problems with the nondimensional parameters in the traditional formulation. This problem is usually side stepped by defining the natural frequency to be zero without addressing such issues as what is the new nondimensional response frequency since $f_{tr}^* = f/f_N$ is either identically zero or infinite for all times and, more importantly, does such a thing as a “natural frequency” even exist in such a system.

One recent example of exploring limiting parameters has been the discussion surrounding the “critical mass” of a system (Govardhan and Williamson, 2002). This concept involves the idea that for any mass-damper-spring system with m^* below a certain critical mass, m_{crit}^* , there is no upper limit on the reduced velocity, U_R , where large-amplitude oscillations disappear and a desynchronized state is reached. In essence, one could keep increasing U_R “forever” with any system that had $m^* < m_{crit}^*$ and never see the large oscillations disappear. They reported that $m_{crit}^* = 0.54$ in the traditional formulation (in the effective

stiffness formulation, $m_{crit}^* = 0.85$) for a circular cylinder allowed to oscillate only normal to the flow direction. To verify that such a light mass system would oscillate “forever,” they removed the springs from a system with $m^* < m_{crit}^*$. They pointed out that $U_R = \infty$, since they defined the natural frequency of this system to be zero, and noted that the *springless* system had appreciable amplitudes.

However, it is more interesting to view a springless system through the viewpoint of the effective stiffness. In fact, by doing so, one can see that this situation corresponds to simply a restricted portion of the response curve. By removing the springs from the system, the effective stiffness parameter is forced to always be negative. This can be seen from Equation (2.39), where it follows that,

$$k_{eff}^* = -m^* \omega^{*2} < 0, \quad (4.2)$$

since $k = 0$ and $m^*, \omega^* > 0$. Thus, the system can only exist on a restricted portion of the amplitude response profile, the part corresponding to $k_{eff}^* < 0$. This is highlighted in the schematic in Figure 4.24, with the solid line corresponding to permissible system states and the dashed line corresponding to system states that are not allowed for this configuration. Most springless systems will have a $k_{eff}^* \ll 0$ and thus the corresponding amplitude $A^* \approx 0$. This is because, under most flow conditions, the vortex shedding frequency will not be near the system natural frequency, and the system will behave in a similar manner to a *stationary* cylinder. This means that

$$k_{eff}^* = -m^* (2\pi St)^2 < -1.74m^* \ll 0, \quad (4.3)$$

since $\omega^* \approx \omega_{shed} D/U = 2\pi St$ and $m^* \approx \mathcal{O}(1)$. However, for systems with small enough nondimensional mass and experiencing the right flow conditions, the system will break from the Strouhal relationship. It will oscillate at a frequency that makes the effective stiffness lie within the range corresponding to measurable amplitude responses. In fact, from examining Figure 4.4, one can see that the nondimensional frequency response of a system in this region is bounded, $0.10 < f^* < 0.16$, and therefore one can obtain the maximum nondimensional mass that will allow for the necessary effective stiffness values. For the springless system, in order for $A^* \gtrsim 0.1$, one needs $-0.3 \lesssim k_{eff}^* < 0$. Using the definition of effective stiffness and these bounds and ranges, we can determine the largest possible nondimensional mass

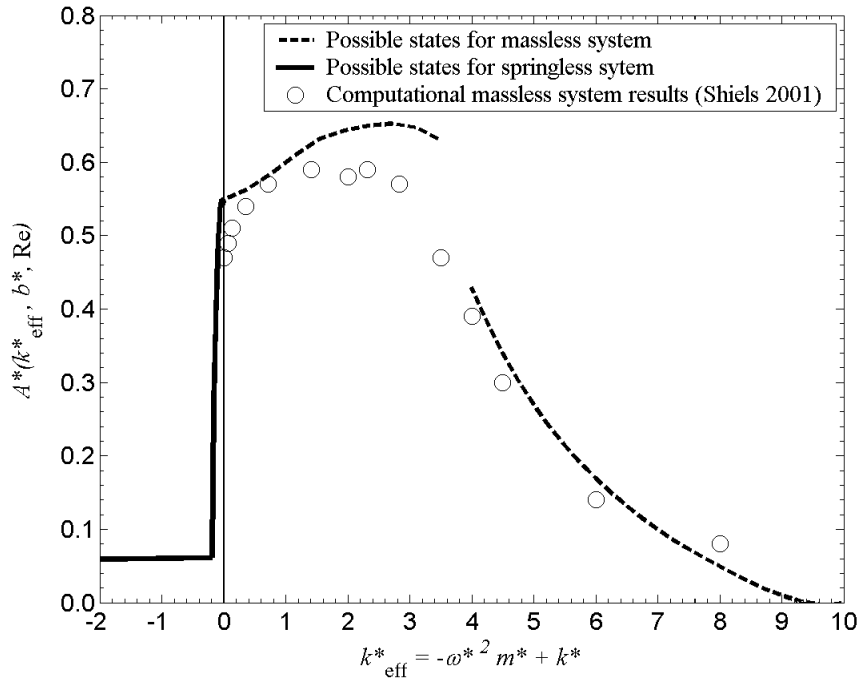


Figure 4.24: Schematic showing allowable system states for two limiting structural parameter cases, a zero mass and zero stiffness system.

as

$$m^* = -\frac{k_{\text{eff}}^*}{(2\pi f^*)^2} \lesssim 0.76, \quad (4.4)$$

where the lower bound was used on k_{eff}^* and f^* . These bounds were used to determine the *largest* mass that a system could have and still experience oscillations. A less massive system will take on values that fall within the specified ranges of k_{eff}^* and f^* while it oscillates.

One other interesting conclusion, realized through the effective stiffness approach, is that all these possible available operating points are lower branch points and are not the maximum amplitude point of the system. The largest amplitude value that one would see for a springless system will depend on the Reynolds number and damping values, which would establish the trajectory line, and the system mass, which would establish how high up the trajectory line the system could move. But one could never see the maximum *possible* amplitude that would occur if the elasticity (springs) were added to the system.

Another possible limiting case would be to remove the mass of the system. Although this cannot be done experimentally, it can be done computationally and was explored by

Shiels et al. (2001). By removing the mass from the system, the effective stiffness parameter is now forced to always be positive. This can be seen from Equation (2.39), where it follows that,

$$k_{\text{eff}}^* = k^* > 0 \quad (4.5)$$

for $m = 0$ and assuming that the elastic components are regular springs such that $k > 0$. Therefore, the system can again only exist on a restricted portion of the amplitude response profile, the part corresponding to $k_{\text{eff}}^* > 0$. This is highlighted in the same schematic as before, Figure 4.24, where this time the dashed line represents permissible system states and the solid line corresponds to system states that are not allowed. Various massless system cases were run by Shiels et al. (2001) and verified that indeed the system can only exist on a partial portion of the response curve. In Figure 4.24 we show that their computational results, for a system with zero mass, only lie on the corresponding restricted response branch.

Since the effective stiffness domain is positive for a massless system, this limiting case is not as interesting as the springless system. Unlike the springless case, where a very limited, and steep, portion of the response profile could be spanned, in the massless case, most of it can be spanned. However, there are still interesting points to be considered. In the springless case, you could not control the effective stiffness value directly because of the implicit relationship on the frequency response. Therefore, it was not possible to know under what flow velocities the Strouhal relationship would be broken and allow appreciable amplitudes. But in the massless case, one can control the value of the effective stiffness directly. It is possible to come up with the relationship to control k_{eff}^* for our system as follows

$$k_{\text{eff}}^* = k^* = \frac{2k}{\rho LU^2} = \frac{k}{235U^2}, \quad (4.6)$$

where k is in N/m and U is m/s and using the typical system parameters, $\rho = 1000 \text{ kg/m}^3$ and $L = 0.47 \text{ m}$. Unlike the *restricted* resonance “forever” situation for a system with $m^* < m_{\text{crit}}^*$, for the massless system, you truly could have resonance “forever.” In the $m^* < m_{\text{crit}}^*$ system, the “forever” only applies to *large* reduced velocity values as you tend toward $U_R \rightarrow \infty$. However, in the massless system, the “forever” includes both *high* and *low* flow velocities. This is because we can control the effective stiffness directly and we only need $k_{\text{eff}}^* \lesssim 7$ for $A^* \gtrsim 0.10$ and, the smaller the effective stiffness value, the larger the

amplitude will be. By looking at Equation (4.6), we can see that for a soft enough elasticity, k , regardless of the flow velocity, the required effective stiffness value can be obtained. Using the effective stiffness value that corresponds to the onset of amplitudes, $k_{\text{eff}}^* \approx 7$, we get the following relationship between elasticity and flow velocity

$$\frac{k}{U^2} = 1645. \quad (4.7)$$

Therefore, for all flow speeds greater than $U \approx 3$ cm/s (the minimum speed of our water tunnel) if you had a spring that was softer than $k \lesssim 1.5$ N/m, the system would oscillate for all our available tunnel speeds.

However, the ultimate resonance forever situation would be a massless and springless system. Such a system would be restricted to one effective stiffness state, $k_{\text{eff}}^* = 0$, and thus would oscillate at *any* tunnel velocity with the amplitude only depending on the system damping and Reynolds number of the flow. Shiels et al. (2001) simulated this situation, showing that the apparent mass force balances the forces from the wake and produces system oscillations with $A^* \approx 0.47$ at $\text{Re} = 100$ with zero damping. Although, similar to the springless system, the maximum *possible* amplitude of this system could never be realized either.

4.7 Damping Effects on the Amplitude Response Profile

The transition undertaken by a system going from a large-amplitude, three-branch response, to a small-amplitude, two-branch response can be seen in Figure 4.25 using the traditional formulation. The damping values for Sequence 03 can be found in Table 5.1. The most lightly damped case, Run03(a), shows the expected low mass-damping, three-branch response. It contains an initial, upper, and lower branch as pointed out by Khalak and Williamson (1997b). The highest damped case, Run03(1), shows the expected high mass-damping, two-branch response. It contains only an initial and lower branch and is similar, although not identical, to the response observed by Feng (1968). The results of Run03(e) – Run03(i) show how the system transitions between these two very different response profiles. The two most dramatic changes are the scaling down of the lower branch portion and the “erosion” and eventual disappearance of the upper branch, or large amplitude, portion

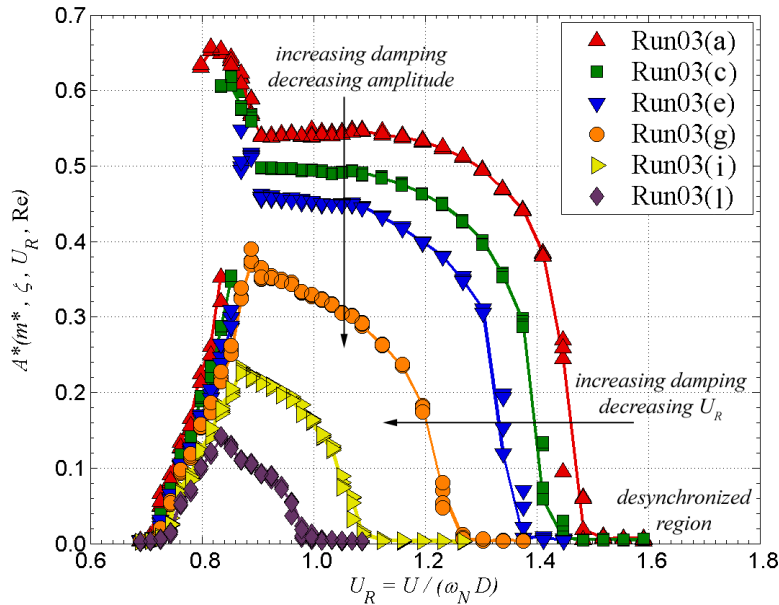


Figure 4.25: Sample of Sequence 03 amplitude response profiles in the traditional formulation showing the two effects that cause the scaling down of the lower branch as damping is increased. Damping values for each run can be found in Table 5.1.

of the response. These same results are also shown in Figure 4.26 using the effective stiffness formulation.

The scaling down of the lower branch is due to two factors, both of which can be seen by looking at the lower branches in Figure 4.25. First, the value of A^* decreases, for a given U_R , as damping is increased. This trend is shown by the vertical arrow in Figure 4.25, notice the diminishing amplitudes of the nearly-constant-amplitude portion of the lower branch for the three most lightly damped cases in the range $0.90 < U_R < 1.10$. For the most lightly damped case, the lower-branch constant-amplitude portion is approximately $A^* \approx 0.54$ and, as damping is increased, it steadily goes down $A^* \approx 0.50$ [Run03(c)] and $A^* \approx 0.46$ [Run03(e)].

Second, as damping is increased, the reduced velocity value that corresponds to the system entering the desynchronized region decreases. This trend is shown by the horizontal arrow in Figure 4.25. For instance, for the most lightly damped case, the desynchronized region is entered at $U_R \approx 1.50$ and as damping is increased, this region is entered sooner, $U_R \approx 1.25$ [Run03(g)] and $U_R \approx 1.00$ [Run03(l)].

The “erosion” of the upper branch is part of the transition from a large-amplitude, three-

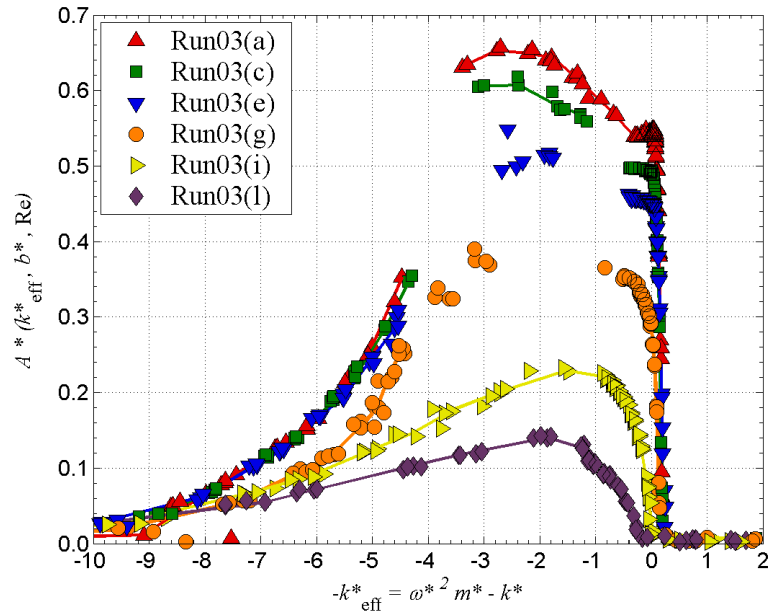


Figure 4.26: Same results as Figure 4.25 showing the effects that damping has on the amplitude response profiles, but now displayed in the effective stiffness formulation plotted against negative effective stiffness, $-k_{\text{eff}}^*$. Damping values for each run can be found in Table 5.1.

branch response to a small-amplitude, two-branch response that involves the disappearance of the upper-branch portion of the profile. It is a gradual process that occurs over a range of damping values. To explore this “erosion,” we use systems which have a low enough damping and sufficiently high enough Reynolds number to allow for an upper branch to exist (Klamo et al., 2006). This “erosion” can be seen in Figure 4.25 and Figure 4.26. Because the upper branch is partially located in a hysteretic region, that has been noted by several investigators (Feng, 1968; Brika and Laneville, 1993; Khalak and Williamson, 1999), the “erosion” of the upper branch is associated with two effects. One occurs for increasing tunnel velocities and one for decreasing tunnel velocities.

To understand the “erosion” of the upper branch, one must first note that the right side of the upper branch ends at a fixed reduced velocity value. This value is different for each particular system, but is independent of damping. For increasing tunnel velocity tests, as damping is increased, the jump from the initial to upper branch is delayed. Each delayed jump causes a smaller upper branch to exist until, for high enough damping values, the jump will be delayed until it occurs at this right side fixed U_R value, in which case, the

system will simply move into a lower branch state. For decreasing tunnel velocity tests, the jump downward is controlled by the system reaching the WR-plane 2S/2P dividing curve. As damping is increased, the decreased amplitudes that result, along with the shape of the dividing curve, cause the system to reach the dividing curve sooner and thus the downward jump to occur sooner, reducing the size of the upper branch as well. The “erosion” of the upper branch will be explored in further detail in Section 6.3 when we explore the various hysteretic regions in detail.

4.8 Damping Effects on the Frequency Response Profile

The corresponding changes in the frequency response profile, as the upper branch amplitude profile is being eroded away, are shown in the effective stiffness formulation in Figure 4.27. Increasing tunnel velocity data is shown using solid lines and decreasing tunnel velocity data is shown using dashed lines. The frequency response for these cases, ones that include an upper branch, exists along three branches. Branch 1 frequencies correspond to initial branch amplitudes, branch 2 frequencies to upper branch amplitudes, and branch 3 frequencies to lower branch amplitudes.

As damping is increased three changes in the frequency response profile take place. First, the jump from branch 1 to branch 2, as tunnel velocity increases, is delayed and occurs at a slightly smaller effective stiffness value. Second, the slope of the roughly linear branch 2 decreases. Lastly, the jump from branch 2 to branch 1, as tunnels velocity is decreased, is expedited and occurs at a slightly smaller effective stiffness value. This, coupled with the first change, makes the size of the hysteresis, the difference between the solid and dashed lines, decrease as damping is increased. These three changes are displayed in simplified form in the schematic of Figure 4.28, which is representative of the general trend of damping effects.

4.9 Reynolds Number Effects on the Amplitude Response Profile

Damping and Reynolds number have the interesting property that they have similar effects on the response behavior of VIV. This means that similar results can be obtained by *either*

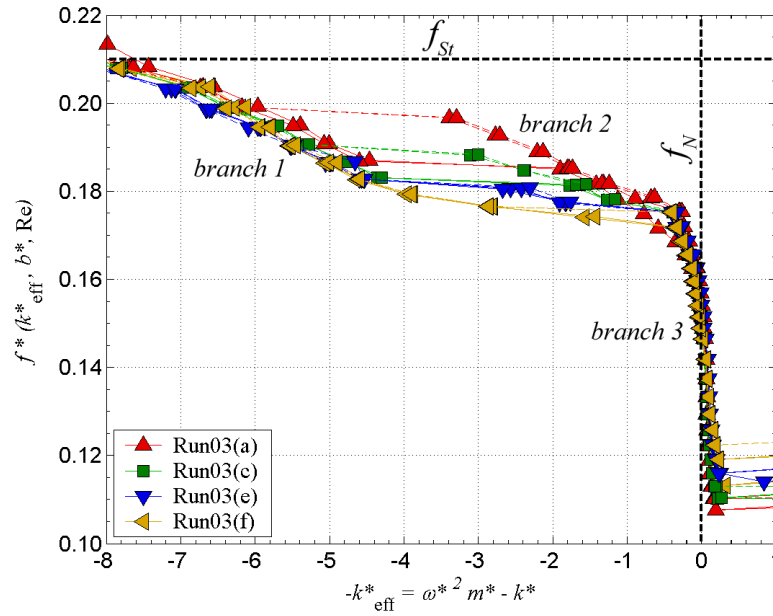


Figure 4.27: Effects of damping on the frequency response profiles of the upper branch systems of Sequence 03 in the effective stiffness formulation. Solid lines represent increasing tunnel velocities; dashed lines represent decreasing tunnel velocities; f_{St} : stationary cylinder Strouhal frequency; f_N : system natural frequency in air. Damping values for each run can be found in Table 5.1.

increasing damping or decreasing the Reynolds number. Because of this, the damping effects on the amplitude and frequency response, discussed previously, can also be caused by Reynolds number changes. As an example, we look at the elimination of the the upper branch from the amplitude response profile. As discussed previously, this is possible by increasing the system damping. Such a situation is shown in Figure 4.29 where the Reynolds number, as well as other relevant parameters, were consistent throughout the two tests. In one test, the damping value is small enough to allow for an upper branch, however, in the second test, the damping value is increased to a large enough value to suppress the upper branch. Contrast that with Figure 4.30 where the damping was the same in the two tests. This time however, the two tests had different Reynolds numbers. The test with the higher Reynolds number shows the existence of the upper branch while the lower Reynolds number test does not. Thus, Reynolds number effects are analogous to damping effects on the amplitude response profile. This means that the existence of an upper branch response is not simply dependent on damping, or the “mass-damping” parameter, as previously

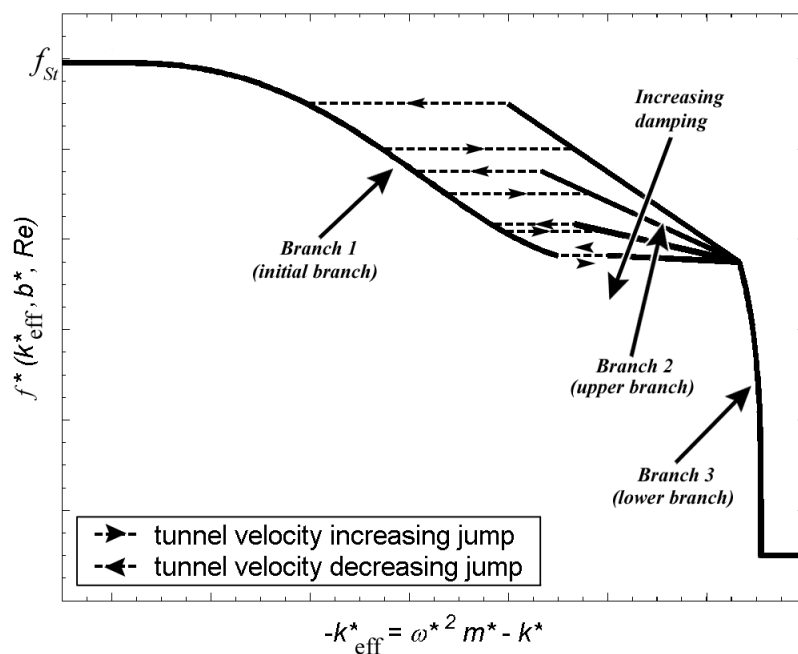


Figure 4.28: Schematic showing the general trends of damping effects on the frequency response profiles for upper branch systems.

thought. In order to have an upper branch response, one needs a low damping value *and* a high enough Reynolds number. The response profile of the system is controlled by the combination of damping and Reynolds number.

This is not to imply that there is a direct coupling between damping and Reynolds number. Something as simple as “a doubling of damping is exactly equivalent to reducing the Reynolds number in half” does not exist. One reason for this is that there appears to be limits for certain behavior. For example, it appears that an upper branch cannot occur at $\text{Re} \lesssim 500$ regardless of how small the damping. However the general effects caused by increases in damping are similar to the effects that one sees by decreasing the Reynolds number. This is highlighted in Figure 4.31, which shows the amplitude response profile for three distinct systems, each with a different combination of damping and Reynolds number. However, the combination of damping and Reynolds number is adjusted for each system such that the amplitude response profile of all three is very similar.

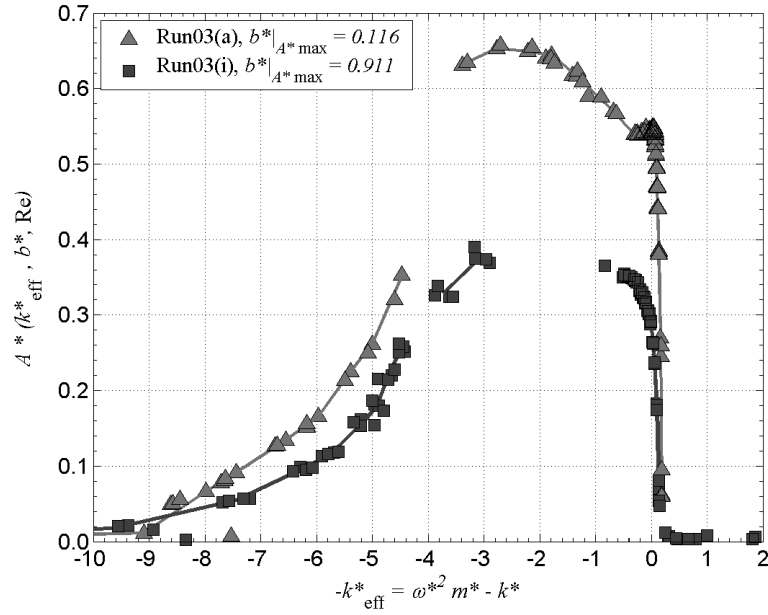


Figure 4.29: Elimination of the upper branch portion of the amplitude response profile through an increase in damping for $\text{Re}|A_{\text{Max}}^* \approx 1000$.

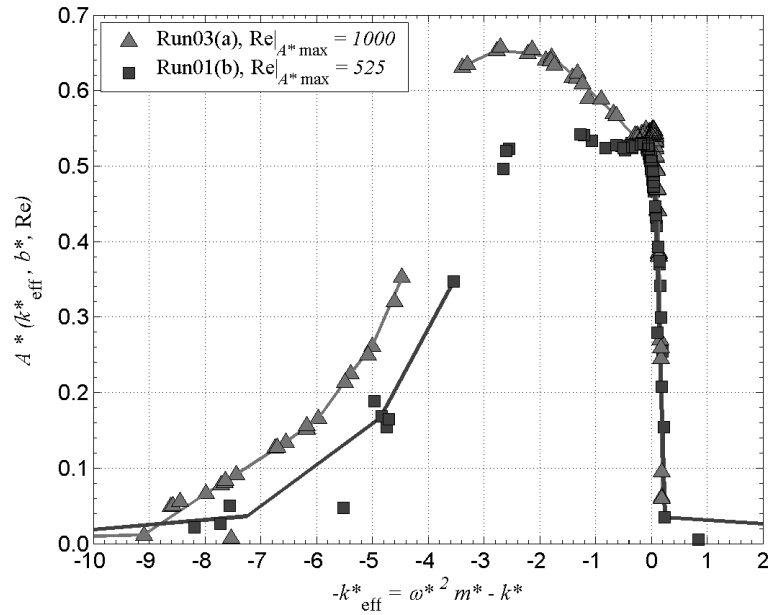


Figure 4.30: Elimination of the upper branch portion of the amplitude response profile through a decrease in Reynolds number for $b^*|A_{\text{Max}}^* \approx 0.13$.

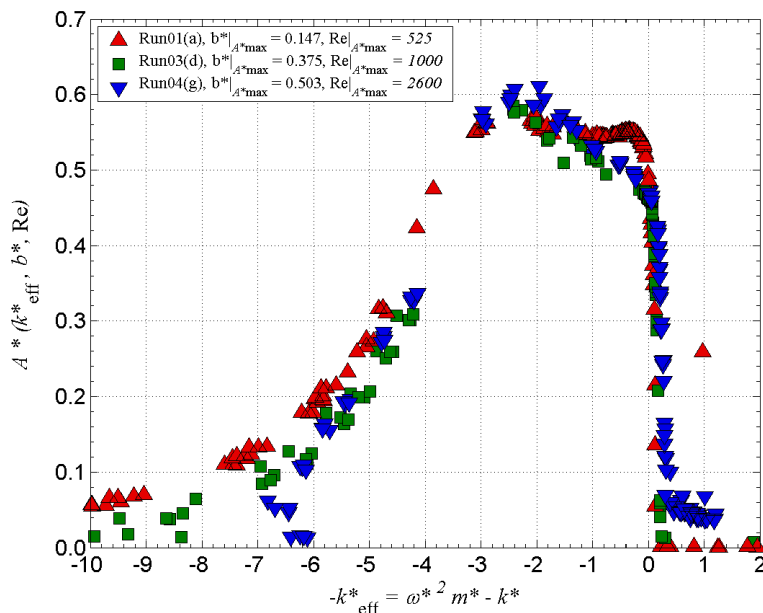


Figure 4.31: Three distinct systems, each with a different damping and Reynolds number value, but by appropriate combinations of them, the amplitude response profiles of the three systems are nearly the same.

4.10 Reynolds Number Effects on the Frequency Response Profile

Damping effects on the frequency response profile for systems with an upper branch were discussed in Section 4.8. Because of the similarities between damping and Reynolds number effects on amplitude responses, as shown in Section 4.9, we expect there to be Reynolds number effects on the frequency response as well. These Reynolds number effects are shown in Figure 4.32 and are similar to the previously discussed damping effects.

The figure shows two systems with different Reynolds numbers but runs with closely matched damping values. By examining a given color, one can see the Reynolds number effects by comparing the two shades of that color (darker shade is $\text{Re}|A_{\text{Max}}^* \approx 1000$, lighter shade is $\text{Re}|A_{\text{Max}}^* \approx 2600$). By doing this, one will notice that decreasing the Reynolds number for a given damping value decreases the slope of the roughly linear Branch 2 of the response profile. This is analogous to what an increase in damping did as discussed in Section 4.8.

There are a few Reynolds number effects on the frequency response profile that do not

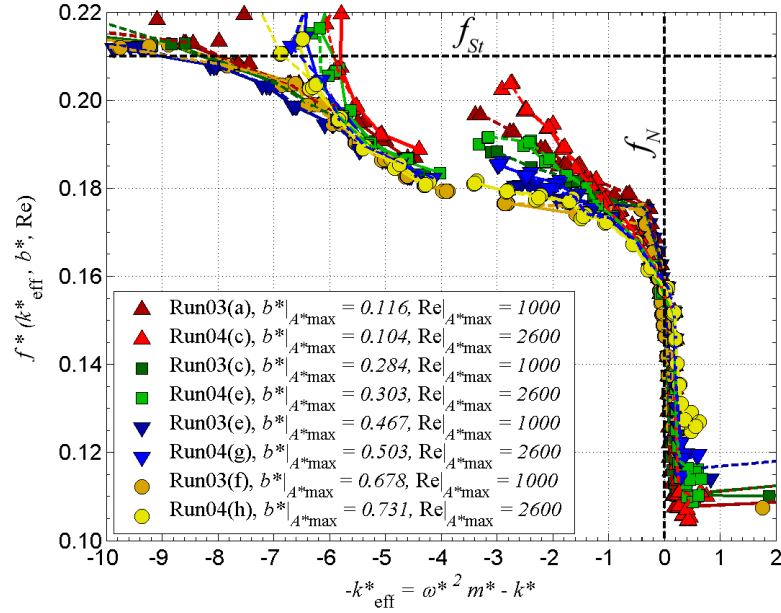


Figure 4.32: Effects of Reynolds number on the frequency response profiles of upper branch systems in the effective stiffness formulation. f_{St} : stationary cylinder Strouhal frequency; f_N : system natural frequency in air.

have analogous damping effects. These unique Reynolds number effects can be seen by comparing Figure 4.27, the previously discussed frequency response for Sequence 03, to Figure 4.33, the frequency response profile for the upper branch cases in Sequence 04. The damping values for Sequence 04 can be found in Table 5.1. Perhaps one of the most obvious differences is the jump between branch 1 and 2. In Figure 4.27 (Sequence 03), the jump has a slightly negative slope whereas in Figure 4.33 (Sequence 4), the jump has a large positive slope. Another difference is the shape of branch 1 as it approaches the Strouhal frequency line (f_{St}).

4.11 Practical Application

In order to accurately predict VIV behavior in structures, one must know the fluid velocity that will cause the maximum amplitude. One approach to estimate the problematic fluid velocity would be to match the system natural frequency to the shedding frequency of an equivalent stationary cylinder,

$$f_{shed} = St \frac{U}{D} = f_N, \quad (4.8)$$

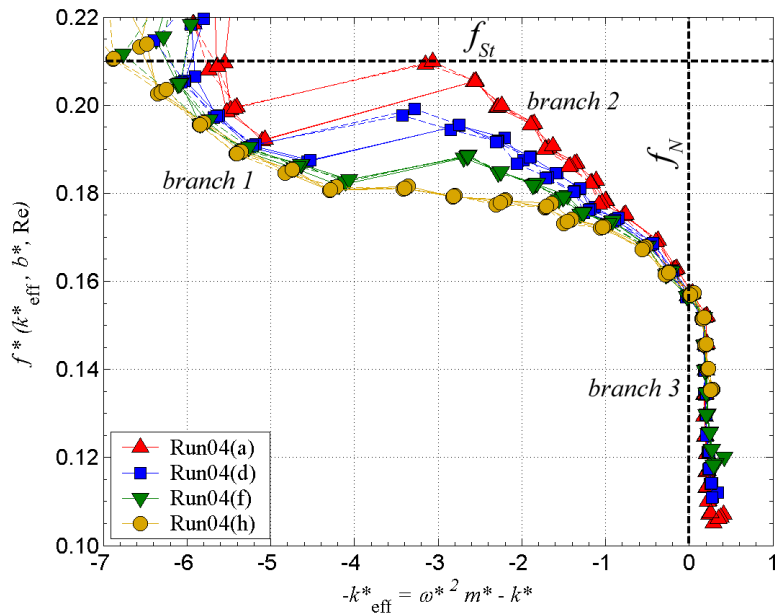


Figure 4.33: Effects of damping on the frequency response profiles of the upper branch systems of Sequence 04 in the effective stiffness formulation. Solid lines represent increasing tunnel velocities; dashed lines represent decreasing tunnel velocities; f_{St} : stationary cylinder Strouhal frequency; f_N : system natural frequency in air. Damping values for each run can be found in Table 5.1.

and obtain the following estimate

$$U = \frac{f_N D}{St} . \quad (4.9)$$

However, we know that the maximum amplitude does not occur at this “lock-in” point (see Section 4.3). Therefore, we know that this approach is fundamentally flawed and as the nondimensional mass of the system increases, the maximum point moves farther away from this point, causing the predicted velocity to have a larger error.

A better approach is to use the effective stiffness formulation since we know that maximum amplitudes occur at $k_{eff}^*|_{A_{Max}^*} \approx 2.5$ for all systems studied. Because the effective stiffness is itself a function of the oscillation frequency, one needs to know the oscillation frequency, ω^* , at the maximum amplitude denoted $\omega^*|_{A_{Max}^*}$. Referring to Figure 4.27 or Figure 4.33 we find that

$$\omega^{*2}|_{A_{Max}^*} \approx \omega^*(k_{eff}^* \approx 2.5, b^*, Re) \approx 1.45 \pm 0.15 , \quad (4.10)$$

run no.	actual $U _{A_{\text{Max}}^*}$	predicted $U _{A_{\text{Max}}^*}$ Equation (4.9)	% diff	predicted $U _{A_{\text{Max}}^*}$ Equation (4.11)	% diff
01(a)	5.04	4.51	-10	4.89	-3
02(a)	5.00	4.55	-9	4.99	0
03(a)	9.73	9.03	-7	9.83	1
04(a)	6.93	6.79	-2	6.69	-3
05(a)	4.35	3.38	-22	3.64	-16
06(a)	5.00	4.39	-12	4.83	-3
07(a)	3.28	2.88	-12	3.15	-4
08(a)	8.22	8.12	-1	8.55	4
09(a)	9.08	9.52	5	9.33	2
10(a)	13.38	13.71	3	13.30	-1

Table 4.2: Comparison between two predictive relationships for $U|_{A_{\text{Max}}^*}$. Note that all $U|_{A_{\text{Max}}^*}$ values are given in cm/s.

for lightly damped systems at the Reynolds numbers tested. From the definition of k^* and k_{eff}^* , we find

$$U^2|_{A_{\text{Max}}^*} = \frac{2k}{\rho L(k_{\text{eff}}^*|_{A_{\text{Max}}^*} + m^* \omega^{*2}|_{A_{\text{Max}}^*})}. \quad (4.11)$$

Therefore, one can use $k_{\text{eff}}^*|_{A_{\text{Max}}^*} \approx 2.50$ and $\omega^{*2}|_{A_{\text{Max}}^*} \approx 1.45$ to determine the fluid velocity using Equation (4.11).

This method, Equation (4.11), is an improvement over the previous method, Equation (4.9). As an example, these two different predictive equations are used to calculate $U|_{A_{\text{Max}}^*}$ in Table 4.2. The effective stiffness method was consistently closer to predicting the fluid velocity at maximum amplitude than the frequency matching method. In fact using the frequency matching method, the relative error in the predicted velocity was approximately 10 percent. The method does appear to give better results at higher Reynolds numbers, $\text{Re}|_{A_{\text{Max}}^*} \gtrsim 1600$, where the relative error was approximately 5 percent. However, with the proposed effective stiffness method, the relative error is less than 4 percent for *all* systems studies except one.

Chapter 5

Maximum and Limiting Amplitudes

5.1 Chapter Overview

In this chapter we investigate the maximum oscillation amplitude that a free-vibration system can obtain and determine the parameters that control it. In Section 5.2 we discuss the difficulties in predicting maximum amplitudes while also looking at recent developments and conclusions. Our theoretical development in Section 5.3 leads to a precise definition of the maximum amplitude and its limit as damping becomes negligible, the limiting amplitude. In Section 5.4 we discuss briefly the experimental test scheme used to obtain the data. Then, in Section 5.5 we show some basic experimental results that display the maximum amplitude dependence on the controlling parameters. Section 5.6 deals with extending those basic results to both lower and higher Reynolds numbers. We use these maximum amplitude results to determine limiting amplitudes in Section 5.7. In Section 5.8 we frame our results with previous work done in this area and comment on the differences that exist. We suggest reasons for the various regions of behavior in the limiting amplitude plot with the aid of flow visualization in Section 5.9. Finally, the phenomena that one sees for a heavily damped system are discussed in Section 5.10.

5.2 Background

One of the most important issues from the design and survivability viewpoint of structural engineering involves being able to predict the maximum amplitude that a freely-vibrating structure would obtain during service. However, since the coupling of the structural and

fluid systems involve nonlinear mechanics, determining that maximum amplitude is not a simple endeavor. It is interesting, though, to see the predicted motion and amplitude if the problem were a simple mass-damper-spring linear vibration system with constant amplitude and frequency sinusoidal fluid forcing function, such as $F_L(t) = F_{L,o} \sin(\omega_d t)$. Assuming constant amplitude and frequency forcing is not exactly correct, but they are not unreasonable assumptions for the traditionally termed “resonant region,” which includes the maximum amplitude location. Experimentally measured lift forces appear to be reasonably approximated by constant amplitude and frequency sine waves (Govardhan and Williamson, 2000; Sarpkaya, 2004).

Under this assumption, the dimensional governing equation, Equation (2.5), first discussed in Section 2.5, would then be given by

$$m\ddot{y} + b\dot{y} + ky = F_{L,o} \sin(\omega_d t) , \quad (5.1)$$

where the dimensional steady-state closed form solution is well-known and can be written in the form

$$y = \frac{F_{L,o}}{\sqrt{(k - \omega_d^2 m)^2 + (\omega_d b)^2}} \sin(\omega_d t - \theta) , \quad (5.2)$$

where

$$\theta = \tan^{-1} \left(\frac{\omega_d b}{k - \omega_d^2 m} \right) , \quad (5.3)$$

is the phase difference between the driving force and the system response. The dimensional maximum amplitude for such a forced system can be written in a form that shows the importance of the difference between the driving and natural frequencies, as well as the damping, as

$$A_{\text{Max}} = \frac{F_{L,o}/(\omega_d m)}{\sqrt{((\omega_N^2 - \omega_d^2)/\omega_d)^2 + (b/m)^2}} . \quad (5.4)$$

This form highlights that at the actual resonance condition ($\omega_d = \omega_N$), the amplitude is limited only by structural damping in the system. It is useful to look at the predicted maximum amplitude in nondimensional terms. In the traditional formulation, the response

from Equation (5.4) can be written as

$$A_{\text{Max}}^* = \frac{C_{L,o}(U_R^2/\pi\omega_{tr}^*)}{\sqrt{((m_{tr}^*/2\omega_{tr}^*)(1-\omega_{tr}^{*2}))^2 + (m_{tr}^*\zeta)^2}}, \quad (5.5)$$

where the system response frequency, ω , is the same as the driving frequency, ω_d , (see Equation (5.2)) so that $\omega_{tr}^* = \omega_d/\omega_N$. In the effective stiffness formulation, the maximum amplitude response is given by

$$A_{\text{Max}}^* = \frac{C_L/\omega^*}{\sqrt{(k_{\text{eff}}^*/\omega^*)^2 + b^{*2}}}. \quad (5.6)$$

The usefulness of this simple derivation and resultant maximum amplitude prediction, using either Equation (5.5) or Equation (5.6), remains an important question to this day. As noted previously, we needed to make the initial assumption of constant amplitude and frequency forcing to solve Equation (5.1). But perhaps a bigger problem for such an assumption is the fact that the lift coefficient amplitude appears to have a *strongly* nonlinear dependence on the motion of the cylinder itself, making the governing equation non-linear (Sarpkaya, 2004).

Since analysis similar to the one we just presented shows a dependence on a parameter that is the product of mass and damping, maximum amplitude data has usually been presented against a mass-damping parameter. Various mass-damping parameters have been used in the past (Vickery and Watkins, 1964; Scruton, 1965) and continue to be used to this day, although in different forms (Khalak and Williamson, 1996; Williamson and Govardhan, 2004). Most are only different by a scale factor, making the trends they convey depend very little on the actual parameter used. Perhaps because Griffin and collaborators did extensive early work collecting and plotting maximum amplitude data, the most common mass-damping parameter is S_G , the parameter they used. This parameter can be written in the traditional formulation as $S_G = 2\pi^3 S_t^2 m_{tr}^* \zeta$ and the effective stiffness formulation as $S_G = 2\pi^2 S_t^2 U_R b^*$. Before leaving this idea, it is important for use in discussion later, that both Equation (5.5) and Equation (5.6) can be written in terms of S_G in a functional form of

$$A_{\text{Max}}^* \propto \frac{A}{\sqrt{B + S_G^2}}, \quad (5.7)$$

where \mathcal{A} and \mathcal{B} capture all the terms other than S_G . It should be noted that the maximum amplitude, A_{Max}^* , goes as $(1 + S_G^2)^{-1/2}$ using this prediction equations.

If one feels uneasy about the assumptions necessary to arrive at either Equation (5.5) or Equation (5.6), then a different approach can be taken. Such a derivation was shown by Sarpkaya (1978) as part of his attempt to explore the reasons for the apparent correlation of maximum amplitude experimental data with S_G . In his derivation, he does not make any assumptions about the lift force amplitude or frequency in Equation (5.1). Instead, he derives a normalized relationship between the amplitude and phase of the system from Equation (5.1). He then makes the assumption that the oscillation frequency to natural frequency ratio is close to one, $f/f_n = 1 - \epsilon$, and substitutes this into his amplitude-phase equation. This assumption is justified for large m^* systems ($m^* \gg 1$) since the cylinder oscillation frequency at resonance will be close to both the stationary cylinder shedding frequency and system natural frequency (Bearman, 1984). After ignoring all third- and higher-order terms of ϵ , Sarpkaya arrives at the expression

$$A_{\text{Max}}^* = \frac{0.5 C_L (f_{\text{St}}/f_N)^2}{\sqrt{(\epsilon/a_o)^2 + S_G^2}}, \quad (5.8)$$

where he concludes that only if C_L and ϵ/a_o remain constant would there be a unique relationship between A_{Max}^* and S_G . It is interesting to note that although different assumptions were made, Equation (5.8) and Equation (5.7) have the same functional dependence on the mass-damping, S_G , of the system.

Because numerous derivations to determine predictive relationships between the maximum amplitude and a mass-damping parameter exist, we present one more extremely common method. This method involves substituting not only a sinusoidal lift force, but a sinusoidal response motion out of phase with the lift, into Equation (5.1). Then the response amplitude and frequency can be derived. This approach has been undertaken by Khalak and Williamson (1999), where they arrive at

$$A_{\text{Max}}^* = \frac{1}{4\pi^3} \frac{C_Y \sin \phi}{(m^* + C_A)\zeta} \left(\frac{U^*}{f^*} \right)^2 f^*, \quad (5.9)$$

as well as Sarpkaya (2004), where he arrives at the expression

$$A_{\text{Max}}^* = \frac{1}{2} C_Y \sin \phi \frac{\text{St}^2}{S_G} \left(\frac{U}{f_{vac} D} \right)^2 \frac{f_{vac}}{f_{com}}, \quad (5.10)$$

with each of the nondimensional parameters being specific to those authors and defined in their papers. The differences between the two expressions mainly arises from the fact that Khalak and Williamson, in an effort to capture low m^* systems, choose to include the added mass term in their nondimensionalization whereas Sarpkaya does not. However, the most important point is that both expressions give the same functional relationship between A_{Max}^* and mass-damping, $m^* \zeta$ or S_G . The maximum amplitude, A_{Max}^* , goes as S_G^{-1} using this methods. This is markedly different than the behavior that was predicted previously and shown in Equation (5.7).

As mentioned previously, the usefulness of Equation (5.7) has been continuously debated for various reasons. One reason involves the disagreement over the idea of combining the mass and the damping into a mass-damping parameter or if the mass and damping act independently on the response. It was pointed out by Sarpkaya (1978) that the governing equation of motion shows that the system response is independently governed by m^* and ζ , and that the governing equation cannot be written in terms of a single mass-damping parameter. On the other hand, Griffin and Ramberg (1982) performed two experiments at a roughly constant S_G but with m^* changing by an order of magnitude and observed about the same maximum amplitude, suggestive of a dependence on the combined mass-damping parameter. The majority of the debate has concentrated around under what conditions would a mass-damping parameter be useful. Much of the debate was exasperated by the traditional formulation and its specific nondimensional parameters. Sarpkaya's point can be understood by looking at Equation (2.17) where m^* and ζ appear separately. Others were driven by the fact that all the maximum amplitude derivations, such as Equation (5.5), contained their product. However, in our formulation this debate does not exist. There is no attempt to combine mass, m^* , and damping, b^* . Instead, mass is combined with elasticity to form the effective stiffness parameter and the maximum amplitude is controlled by both effective stiffness and damping.

It is worth mentioning that some researchers have attempted to represent the complicated fluid forcing function in a variety of ways, including using van der Pol equations and

amplitude dependent lift coefficients. This was discussed briefly in Section 2.6. Perhaps the most extensive model was started in Skop and Griffin (1975) and then further developed by Skop and Balasubramanian (1997). However, no attempt to date has come close to accurately capturing the maximum amplitude response over a full range of system parameters and Reynolds numbers.

It is interesting that the various attempts at predicting the maximum amplitude produce results with different functional forms. Obviously, the predicted responses of the form of Equation (5.9) and Equation (5.10) are troubling because for low mass-damping, the maximum amplitude appears to be unbounded. On the other hand, adopting a response of the form Equation (5.7) and treating the parameters \mathcal{A} and \mathcal{B} as *roughly* constant has dramatic implications for the maximum amplitudes at small damping values. The response of Equation (5.7) is an even function which means that the maximum amplitude function must pass through $b^* = 0$ with zero slope. Therefore, the maximum amplitudes should asymptote to some value and remain constant below a certain mass-damping value. On physical grounds, one would expect the maximum amplitude to smoothly increase through zero damping. One could imagine a system with *slightly* negative damping. Such a system would logically have a slightly larger amplitude than a system with the equivalent positive damping.

Due to the complicated nature of the oscillating structure and the fluid wake, along with the nonlinear mathematics it creates, the most insight gained into understanding the maximum attainable amplitude has been through experimental work. A significant advancement on the subject was made by Griffin and collaborators by collecting various experimental results in air and water and compiling them in a single plot. One of the first plots appeared in Skop and Griffin (1975) with a more detailed plot appearing in Griffin (1980). Due to his early involvement, this type of plot, one where the observed maximum amplitude is plotted against a mass-damping parameter, is now often referred to as a “Griffin plot.” There is however, no consistent axis scaling or damping parameter that is currently universally used. One such Griffin plot is a recent representation by one of the original researchers (Skop and Balasubramanian, 1997), shown in Figure 5.1. In the figure, the curve fit has the form given by Equation (5.7) with $\mathcal{A} = 0.385$ and $\mathcal{B} = 0.12$.

In order to make amplitude predictions using such a plot, researchers would use an equation of the form Equation (5.7) to curve fit the data, as shown in Figure 5.1. However,

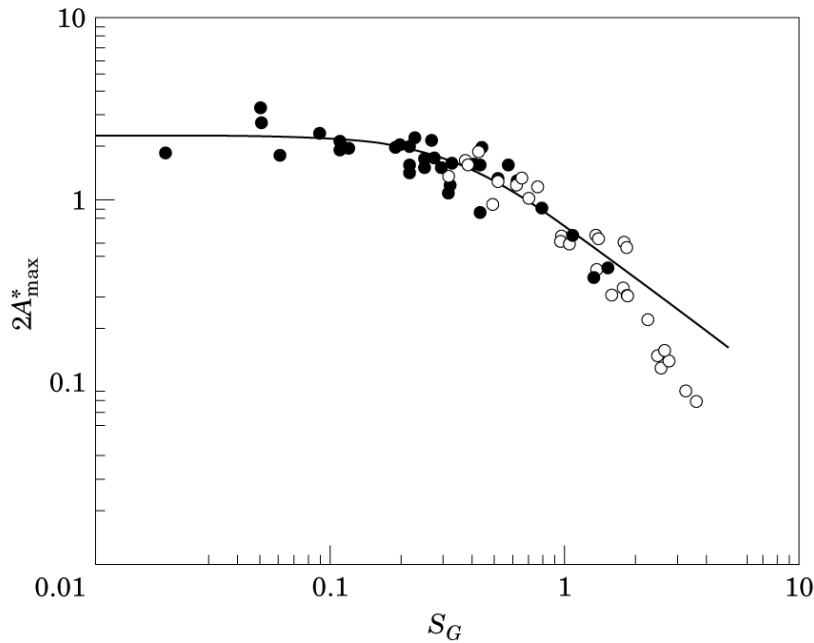


Figure 5.1: A typical “Griffin plot” in log-log form showing the proposed maximum amplitude, A_{Max}^* , dependence on a “mass-damping” parameter, in this case S_G . Curve fit given by Equation (5.7) with $\mathcal{A} = 0.385$ and $\mathcal{B} = 0.12$. Figure from Skop and Balasubramanian (1997).

a major problem was experienced when trying to assign values to the parameters \mathcal{A} and \mathcal{B} that would capture all the experimental data. Consequently, their values have been obtained in different ways. In some cases, these values were based on estimating the parameters that contribute to their values, such as the lift coefficient, from stationary cylinder tests. However, in other cases, the values are obtained by a least-squares curve fit, in the form of Equation (5.7), to all the available data with no inclusive of fluid mechanics principles. Both methods produce less than satisfactory results that do not accurately represent all of the data.

One of the concerns of such a plot is the large amount of data scatter from the best-fit line that is apparent even in a log-log scaling, which compresses much of the scatter. This shortcoming was highlighted by Williamson and Govardhan (2004) where they added more experimental data to Figure 5.1 and changed the scaling to a log-linear plot to accentuate the scatter. Their plot can be seen in Figure 5.2 along with the same curve fit line as in Figure 5.1.

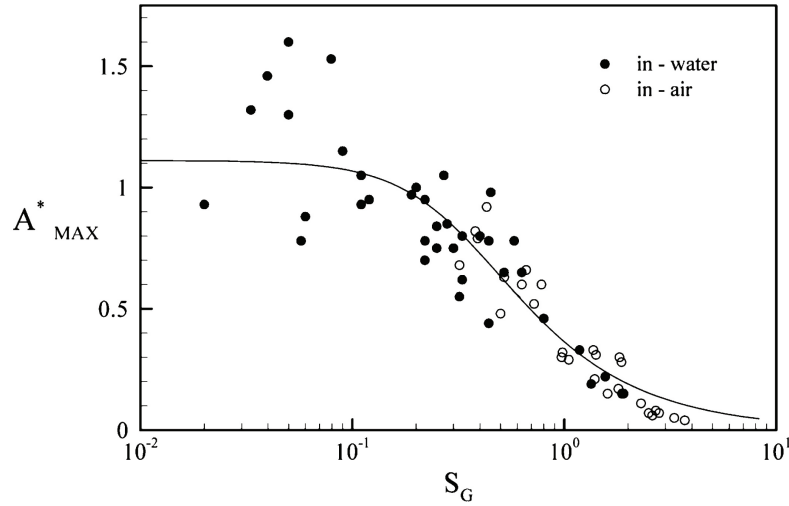


Figure 5.2: A typical “Griffin plot” but in linear-log form to accentuate the large amount of scatter that exists in the compiled data. Curve fit given by Equation (5.7) with $\mathcal{A} = 0.385$ and $\mathcal{B} = 0.12$. Figure from Williamson and Govardhan (2004).

Since one of the original objectives of this work was to determine the maximum attainable amplitude, one must extrapolate the experimental values to $S_G = 0$. We see that a confident extrapolation to zero damping is not possible using such plots. The large amount of scatter that develops as data from various experiments is added has again raised questions as to whether the mass should be lumped together with the damping. This question was addressed, for example in Williamson and Govardhan (2004), where they concluded that perhaps the mass and damping can be lumped together down to a value of $S_G \approx 0.01$, which would be two orders of magnitude lower than the value often cited in the literature.

To improve the utility of the Griffin plot, Williamson and Govardhan (2004) restricted the type of experimental data that is used. Previous researchers had included various geometries in their Griffin plots. For instance, Griffin (1980) produced a plot that included spring-mounted rigid, cantilevered flexible, and pivoted rigid cylinders all on a single plot. In the Williamson and Govardhan rendition, only similar geometries and arrangements were compared, in this case, rigid circular cylinder undergoing one-degree-of-freedom motion. The result of this effort can be seen in Figure 5.3. Even though this is an improvement, there is still an appreciable amount of scatter. It is at this time that we mention that the most important fluid mechanics parameter had not yet been discussed or included. In every

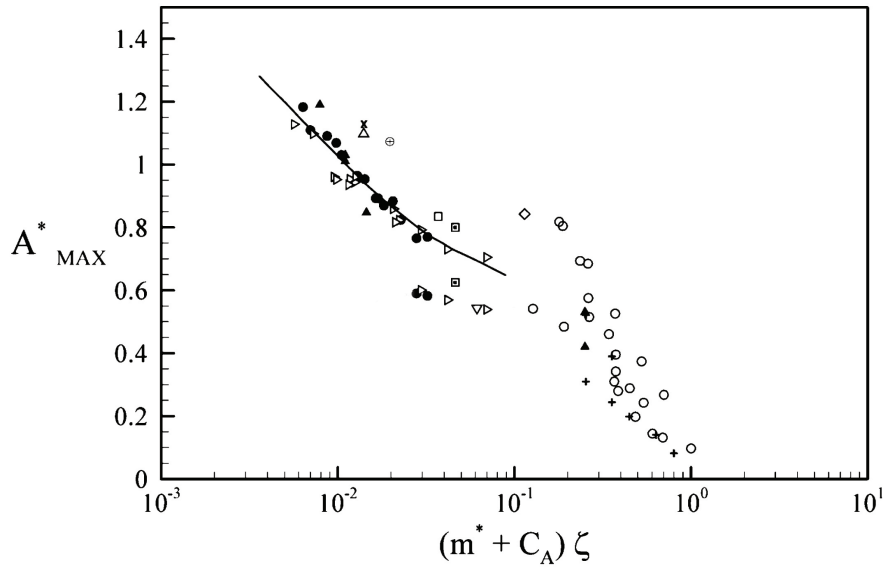


Figure 5.3: A “Griffin plot” modified by Williamson and Govardhan to show only similar geometries in order to reduce the scatter in the reported data. Figure from Williamson and Govardhan (2004). (Note that “lower branch” data has been removed for simplicity.)

variation of the Griffin plot that has been created, the maximum amplitudes are always only a function of the mass-damping parameter. This makes it impossible to represent possible Reynolds number effects. In the next section we present a unified approach that includes Reynolds number as a parameter.

5.3 Theoretical Development

For a stationary cylinder, which has zero-degree-of-freedom motion, one has the simple relationships for the amplitude and frequency responses

$$A^* = 0 , \quad (5.11)$$

$$\omega^* = \omega^*(\text{Re}) = 2\pi\text{St}(\text{Re}) . \quad (5.12)$$

There is no amplitude response since the cylinder is fixed and the frequency response is taken to be the frequency at which vortices are shed into the wake. This nondimensional

frequency is the previously discussed Strouhal number, St (see Section 2.3), and is only a function of the Reynolds number of the flow.

The frequency response in Equation (5.12) is a simple universal relationship, only depending on one parameter, the Reynolds number. One could naturally wonder if a similar relationship exists for a cylinder released from such tight constraints and allowed one-degree-of-freedom motion. One might immediately think that such a simple and universal relationship cannot exist since the new degree of freedom introduces so many new parameters into the problem. However, for maximum and limiting amplitudes, similar universal relationships can be obtained.

For a cylinder that is allowed to only oscillate normal to the flow direction (one-degree-of-freedom motion) and has a large enough aspect ratio so as to minimize end effects, three more parameters must be considered besides the Reynolds number, and we expect

$$A^* = A^*(m^*, b^*, k^*, Re) , \quad (5.13)$$

$$\omega^* = \omega^*(m^*, b^*, k^*, Re) , \quad (5.14)$$

where the frequency response is now the oscillation frequency of the system and the parameters are the same as those defined in Section 2.8.

If we assume sinusoidal motion, then as discussed in Section 2.10 and proposed by Shields et al. (2001), the mass and elasticity of the system can be combined into a single parameter, k_{eff}^* , the effective stiffness of the system. This potentially simplifies the response behavior to be dependent on only three parameters as follows

$$A^* = A^*(k_{\text{eff}}^*, b^*, Re) , \quad (5.15)$$

$$\omega^* = \omega^*(k_{\text{eff}}^*, b^*, Re) , \quad (5.16)$$

where the effective stiffness parameter is defined and discussed in Section 2.10.

For such a system, one expects there to be a maximum amplitude at some point during its full response domain. Previous researchers have used the phrase “maximum amplitude” and the symbol A_{Max}^* imprecisely, sometimes even using it to highlight the maximum amplitude that is observed during only a partial test even though a larger amplitude may exist

in the remainder of the test. We put a strict definition on the term maximum amplitude. We introduced and defined our maximum amplitude, A_{Max}^* , in Klamo et al. (2004), and continue with that definition here so that

$$A_{\text{Max}}^*(b^*, \text{Re}) = \max_{k_{\text{eff}}^*} A^*(k_{\text{eff}}^*, b^*, \text{Re}), \quad (5.17)$$

which shows that maximum amplitudes, A_{Max}^* , are a function of only two parameters and do not depend on the individual mass of the system. One of the main objectives of this chapter is to experimentally determine the function A_{Max}^* for a range of Reynolds numbers. This will result in essentially a generalized version of the traditional Griffin plot and will help explain the reason for the scatter in the compiled data.

As shown by Equation (5.17), maximum amplitudes depend on both the damping and Reynolds number. Since we are interested in the largest maximum amplitudes, we look at cases that have zero damping. We call such points limiting amplitudes, A_{Lim}^* , since they occur in the limit of zero damping at each Reynolds number, and can be written simply as

$$A_{\text{Lim}}^*(\text{Re}) = A_{\text{Max}}^*(b^* \rightarrow 0, \text{Re}), \quad (5.18)$$

which shows that limiting amplitudes, A_{Lim}^* , are only a function of the Reynolds number. Another main objective of this chapter is to experimentally determine the function A_{Lim}^* for a range of Reynolds numbers. Through this derivation, we have obtained a simple and universal relationship between limiting amplitudes and Reynolds number,

$$A_{\text{Lim}}^* = A_{\text{Lim}}^*(\text{Re}). \quad (5.19)$$

Notice that Equation (5.19) mirrors the stationary cylinder frequency case, Equation (5.12), and stresses the importance of Reynolds number in this problem.

5.4 Experimental Procedure

A major problem in previous investigations was that, almost without exception, the mass-damping parameter was not varied systematically. Instead, values of mass and damping were the ad hoc values of the particular experiment. This in itself produces data scatter

even if Reynolds number is considered. To remedy this, we systematically varied the mass-damping parameter, which for us is simply b^* .

For a certain system with m , b , k , and D values, a test *Run* was completed by spanning the range of tunnel velocities of interest four times, twice in increasing and twice in decreasing increments. From such a test run, the maximum amplitude for that specific system was determined. By spanning a large enough velocity range, a maximum amplitude was guaranteed to be observed due to the similarities between spanning U_R and spanning k_{eff}^* , as discussed in Section 2.11. This procedure was then repeated multiple times on the same system (same m , k , and D values) but with different values of damping, b . These repeated test runs at various b values then encompassed a test *Sequence*. Controlled imposed damping values on the system were made possible by the use of our VMEC damping system, described in Section 3.4.

A large portion of the damping plane was explored using four different system configurations and three different Reynolds numbers. Various system damping parameters and the Reynolds numbers for these test runs can be seen in Table 5.1

5.5 Generalized Griffin plot

Four test sequences were carried out in order to experimentally determine Equation (5.17) over a wide range of b^* values. Each of these four sequences are shown in the following manner, Sequence 01 in Figure 5.4, Sequence 02 in Figure 5.5, Sequence 03 in Figure 5.6, and Sequence 04 in Figure 5.7. In all the figures, the independent parameter is the effective stiffness and the damping values for each run can be found in Table 5.1.

We denote the value of the effective stiffness at peak amplitude as $k_{\text{eff}}^*|_{A_{\text{Max}}^*}$. Note that the peak amplitude in each case occurs around $k_{\text{eff}}^*|_{A_{\text{Max}}^*} \approx 2.5$, while k_{eff}^* varies from 10 to -1 in a typical experiment. In fact, we find that for lightly to moderately damped systems, the location of the maximum amplitude, A_{Max}^* , is invariant to individual system mass and elasticity and always occurs near $k_{\text{eff}}^*|_{A_{\text{Max}}^*}$, with the actual specific value depending only on the specific damping and Reynolds number.

Although each point that is part of a given test run, for example Run01(a) in Figure 5.4, corresponds to a different tunnel velocity, and thus a different Reynolds number and b^* value, each value of k_{eff}^* shared within a test sequence (except k_{eff}^* slightly less than 0) corresponds

run no.	b (kg/s)	ζ	$m_{tr}^* \zeta$	$b^* _{A_{Max}^*}$	$\text{Re} _{A_{Max}^*}$
01(a)	0.0172	0.0008	0.039	0.147 ± 0.008	518 ± 23
01(b)	0.0182	0.0008	0.041	0.150 ± 0.030	527 ± 4
01(c)	0.0183	0.0008	0.042	0.157 ± 0.003	516 ± 17
01(d)	0.0363	0.0017	0.083	0.299 ± 0.004	528 ± 5
01(e)	0.0445	0.0020	0.102	0.372 ± 0.007	528 ± 27
01(f)	0.0616	0.0028	0.141	0.486 ± 0.004	540 ± 4
01(g)	0.0742	0.0034	0.169	0.573 ± 0.019	555 ± 3
01(h)	0.0925	0.0042	0.213	0.731 ± 0.004	540 ± 4
01(i)	0.1230	0.0056	0.283	0.972 ± 0.046	540 ± 3
01(j)	0.1533	0.0070	0.353	1.262 ± 0.005	519 ± 4
01(k)	0.1872	0.0085	0.429	1.540 ± 0.003	519 ± 3
01(l)	0.2155	0.0098	0.494	1.773 ± 0.004	519 ± 4
01(m)	0.2385	0.0108	0.547	2.139 ± 0.018	483 ± 2
01(n)	0.2903	0.0132	0.665	2.726 ± 0.019	459 ± 3
02(a)	0.0226	0.0005	0.051	0.194 ± 0.002	517 ± 23
02(b)	0.0470	0.0011	0.111	0.387 ± 0.041	533 ± 3
02(c)	0.0772	0.0017	0.175	0.635 ± 0.004	526 ± 3
02(d)	0.1089	0.0025	0.247	0.896 ± 0.003	530 ± 4
02(e)	0.1358	0.0031	0.309	1.118 ± 0.007	530 ± 2
02(f)	0.1688	0.0038	0.384	1.449 ± 0.003	501 ± 5
02(g)	0.2004	0.0045	0.454	1.720 ± 0.004	505 ± 3
02(h)	0.2313	0.0052	0.526	1.985 ± 0.051	509 ± 5
02(i)	0.2629	0.0059	0.597	2.358 ± 0.006	489 ± 2
03(a)	0.0264	0.0006	0.030	0.116 ± 0.004	995 ± 12
03(b)	0.0465	0.0011	0.053	0.200 ± 0.001	1031 ± 32
03(c)	0.0672	0.0015	0.077	0.284 ± 0.002	1019 ± 13
03(d)	0.0907	0.0021	0.104	0.375 ± 0.001	1045 ± 5
03(e)	0.1129	0.0026	0.129	0.467 ± 0.001	1050 ± 10
03(f)	0.1675	0.0038	0.192	0.678 ± 0.003	1077 ± 24
03(g)	0.2249	0.0051	0.258	0.911 ± 0.004	1083 ± 16
03(h)	0.3139	0.0071	0.360	1.271 ± 0.004	1077 ± 10
03(i)	0.3760	0.0085	0.431	1.554 ± 0.005	1061 ± 10
03(j)	0.4417	0.0100	0.506	1.865 ± 0.021	1032 ± 13
03(k)	0.4778	0.0109	0.548	2.017 ± 0.009	1031 ± 15
03(l)	0.5368	0.0122	0.615	2.315 ± 0.014	1019 ± 10
04(a)	0.0159	0.0014	0.006	0.026 ± 0.001	2635 ± 20
04(b)	0.0172	0.0015	0.007	0.030 ± 0.003	2541 ± 134
04(c)	0.0622	0.0055	0.025	0.104 ± 0.001	2554 ± 45
04(d)	0.1203	0.0106	0.048	0.202 ± 0.001	2534 ± 39
04(e)	0.1803	0.0159	0.072	0.303 ± 0.003	2550 ± 39
04(f)	0.2352	0.0211	0.096	0.382 ± 0.015	2652 ± 14
04(g)	0.3094	0.0274	0.124	0.503 ± 0.002	2639 ± 40
04(h)	0.4637	0.0410	0.186	0.731 ± 0.009	2729 ± 34
04(i)	0.6207	0.0551	0.250	1.009 ± 0.007	2595 ± 34
04(j)	0.7780	0.0688	0.312	1.265 ± 0.013	2619 ± 14
04(k)	0.9366	0.0830	0.376	1.624 ± 0.016	2463 ± 50
04(l)	1.0881	0.0965	0.438	1.887 ± 0.016	2481 ± 31

Table 5.1: Imposed system damping values for sequences with moderate Reynolds number $525 \lesssim \text{Re}|_{A_{Max}^*} \lesssim 2600$.

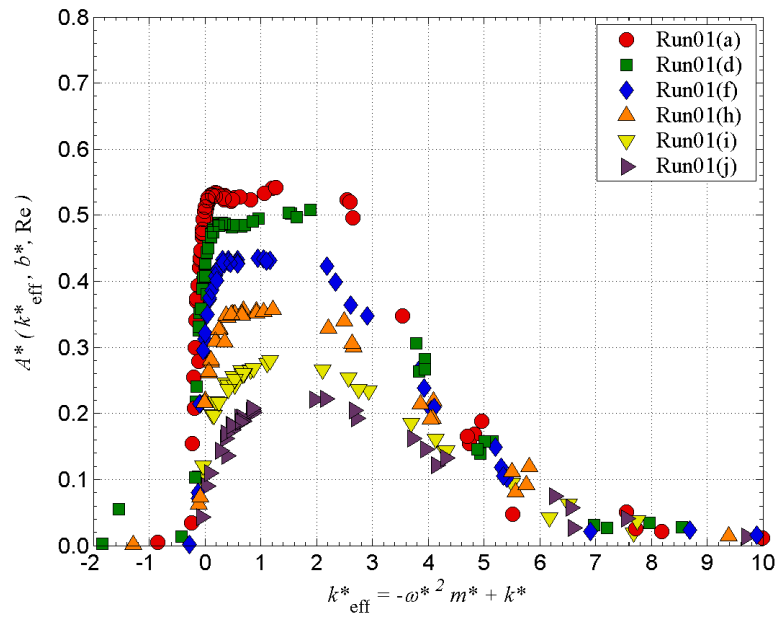


Figure 5.4: Select runs showing Sequence 01 response amplitude, A^* , dependence on the effective stiffness, k_{eff}^* , for various damping values

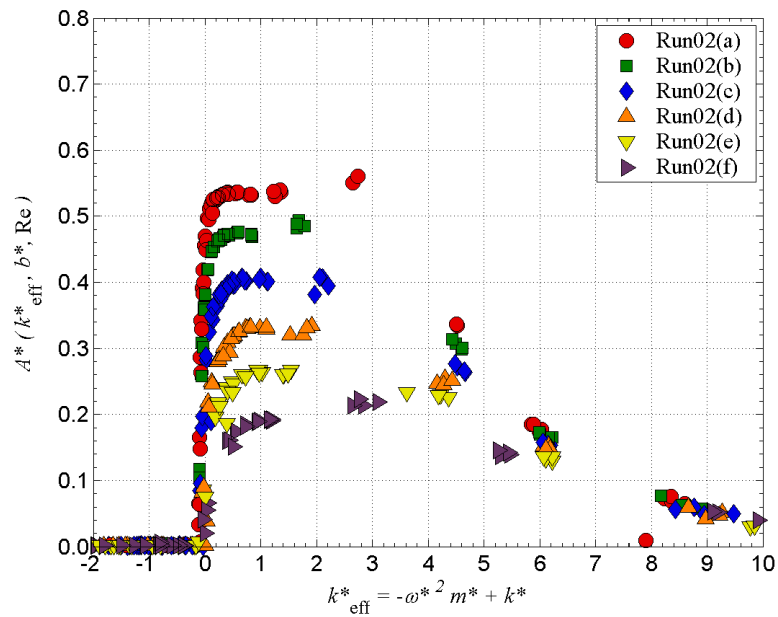


Figure 5.5: Select runs showing Sequence 02 response amplitude, A^* , dependence on the effective stiffness, k_{eff}^* , for various damping values

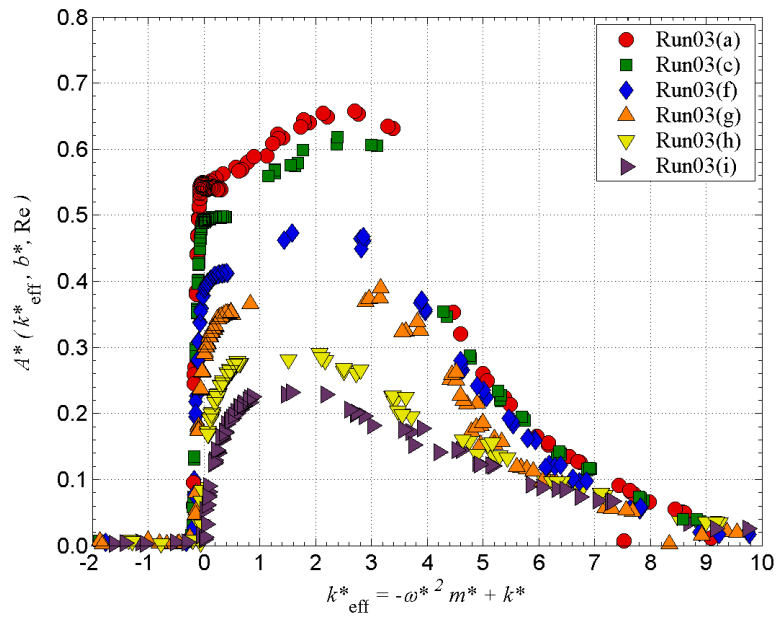


Figure 5.6: Select runs showing Sequence 03 response amplitude, A^* , dependence on the effective stiffness, k_{eff}^* , for various damping values

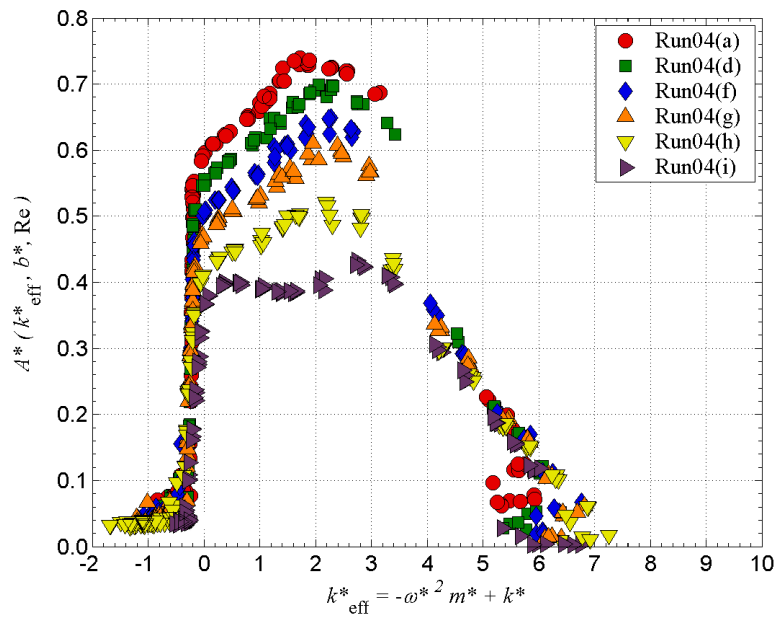


Figure 5.7: Select runs showing Sequence 04 response amplitude, A^* , dependence on the effective stiffness, k_{eff}^* , for various damping values

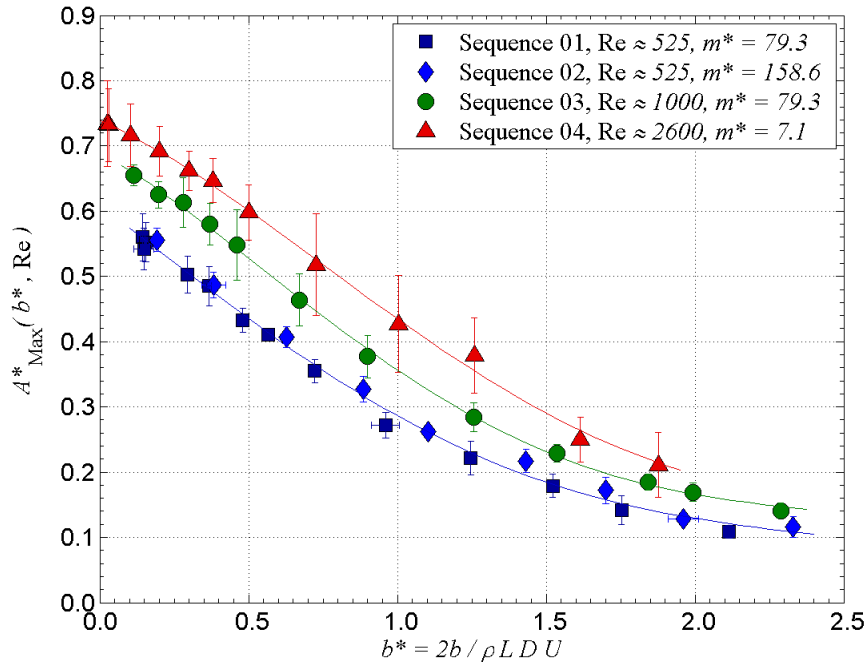


Figure 5.8: New “Generalized” Griffin plot showing maximum amplitude, A_{Max}^* , dependence on damping, b^* , and Reynolds number, Re .

to nearly the same tunnel velocity and Reynolds number for those points. Therefore, the differences in a test sequence at $k_{\text{eff}}^*|_{A_{\text{Max}}^*}$ are essentially only due to damping effects since they share a common Reynolds number. The simplicity of this approach is that now a constant-Reynolds-number curve can be constructed in the amplitude-damping plane by using the points that correspond to $k_{\text{eff}}^*|_{A_{\text{Max}}^*}$ for a given test sequence. This experimental result allows us to determine $A_{\text{Max}}^*(b^*, \text{Re})$ for a fixed Re by varying b^* as described above.

By taking the maximum amplitudes for each test run from Figure 5.4 – Figure 5.7, we can construct a Griffin plot of maximum amplitude against damping. Figure 5.8 shows the results of transferring the data from Figure 5.4 – Figure 5.7 into such a plot. Since not only damping effects but also Reynolds number effects are considered, we refer to Figure 5.8 as a “generalized” Griffin plot since it is a generalization of the concept that Griffin introduced. We present maximum amplitude against *both* damping and Reynolds number. Four test sequences covering three Reynolds numbers ($\text{Re} \approx 525$, $\text{Re} \approx 1000$, and $\text{Re} \approx 2600$) are shown. For most points in the figure, the uncertainty in the damping was less than the size of data point itself. There were a few runs however that had higher uncertainty, and in those

cases, the horizontal bars represent the uncertainty in the measured damping value of the system. As mentioned in Section 4.4, the oscillation amplitude varies in time. Therefore, in order to represent the variation from the plotted average value, we display vertical bars for each individual data point that represents the range necessary to capture 95 percent of the observed time-varying oscillation amplitudes. The trendlines shown are least-squares fourth-order polynomials. The effect of Reynolds number is clearly demonstrated and is the obvious reason why early attempts to compile various data contained so much scatter. Furthermore, this is a graphic representation of A_{Max}^* , which was defined in Equation (5.17), and shows that indeed there is a two parameter dependence.

As discussed in Section 2.10, an important result of the effective stiffness formulation over the traditional formulation is that mass is not an independent parameter but is implicitly contained within the effective stiffness. Therefore, theoretically, only one m^* case, of arbitrary value, needs to be carried out for each constant-Reynolds-number curve in Figure 5.8 because every other value of m^* will still conform to this curve. To validate this assertion, two curves in the damping plane with two different masses, one twice as massive as the first, were generated for the same Reynolds number. As can be seen in Figure 5.8, the two sets of data for $\text{Re} \approx 525$ corresponding to two different mass systems show little dependence on the actual system mass.

5.6 Extending the Reynolds Number Range

The generalized Griffin plot shown in Figure 5.8 contains only three different constant-Reynolds-number curves and therefore cannot show the possible importance of Reynolds number over a larger range. Figure 5.8 is adequate to show the damping and Reynolds number effects on the maximum amplitude, however, it would be advantageous to cover a larger Reynolds number space on the generalized Griffin plot. This would then allow us to locate more than three limiting amplitude points, as defined in Equation (5.18). Therefore, to get a better representation of Reynolds number effects on A_{Max}^* as well as locating more A_{Lim}^* , we also explored three test sequences for Reynolds numbers in the range $200 \lesssim \text{Re}|_{A_{\text{Max}}^*} \lesssim 500$ and three test sequences for Reynolds numbers in the range $\text{Re}|_{A_{\text{Max}}^*} > 10^3$.

The three test sequences for $\text{Re}|_{A_{\text{Max}}^*} < 500$ were numbered Sequence 05 – Sequence 07,

and their relevant system parameters can be seen in Table 5.2. The three test sequences that were carried out with $\text{Re}|_{A_{\text{Max}}^*} > 10^3$ were numbered Sequence 08 – Sequence 10, and their relevant system parameters can be seen in Table 5.3.

run no.	b (kg/s)	ζ	$m_{tr}^*\zeta$	$b^* _{A_{\text{Max}}^*}$	$\text{Re} _{A_{\text{Max}}^*}$
05(a)	0.0158	0.0010	0.049	0.156 ± 0.058	432 ± 1
05(b)	0.0313	0.0019	0.096	0.308 ± 0.003	433 ± 3
05(c)	0.0487	0.0030	0.149	0.479 ± 0.003	430 ± 2
05(d)	0.0538	0.0011	0.155	0.517 ± 0.086	426 ± 2
06(a)	0.0272	0.0008	0.105	0.387 ± 0.014	298 ± 1
06(b)	0.0322	0.0009	0.125	0.458 ± 0.004	297 ± 1
06(c)	0.0350	0.0010	0.136	0.497 ± 0.004	298 ± 2
06(d)	0.0432	0.0012	0.168	0.613 ± 0.003	301 ± 1
06(e)	0.0158	0.0012	0.060	0.221 ± 0.014	305 ± 1
07(a)	0.0179	0.0008	0.107	0.387 ± 0.007	196 ± 2
07(b)	0.0233	0.0010	0.139	0.505 ± 0.004	196 ± 1
07(c)	0.0280	0.0012	0.166	0.607 ± 0.002	195 ± 1

Table 5.2: Imposed system damping values for sequences with $\text{Re}|_{A_{\text{Max}}^*} < 500$

run no.	b (kg/s)	ζ	$m_{ex}^*\zeta$	$b^* _{A_{\text{Max}}^*}$	$\text{Re} _{A_{\text{Max}}^*}$
08(a)	0.0186	0.0008	0.012	0.050 ± 0.001	1582 ± 21
08(b)	0.0954	0.0044	0.063	0.245 ± 0.001	1665 ± 22
08(c)	0.1675	0.0076	0.111	0.430 ± 0.001	1665 ± 22
09(a)	0.0160	0.0011	0.005	0.020 ± 0.001	3422 ± 44
10(a)	0.0158	0.0008	0.003	0.013 ± 0.001	5043 ± 65

Table 5.3: Imposed system damping values for sequences with $\text{Re}|_{A_{\text{Max}}^*} > 10^3$

The general experimental approach for these sequences was the same as for Sequence 01 – Sequence 04, but we did not span the same magnitude of damping values. We did, however, attempt to make sure that for the sequences with $\text{Re}|_{A_{\text{Max}}^*} < 500$, we spanned a large enough damping space to make a reasonable extrapolation back to zero damping. This is an important point, since as a general rule of thumb, as Reynolds number decreases, the minimum possible b^* increases. This is due to the small values of diameter, D , and tunnel velocity, U , contained within b^* for these sequences. Sequence 08 also had a fairly large minimum b^* value so that it was treated like the $\text{Re}|_{A_{\text{Max}}^*} < 500$ sequences. Therefore, Sequence 05 – Sequence 08 were comprised of three runs that were carried out for each

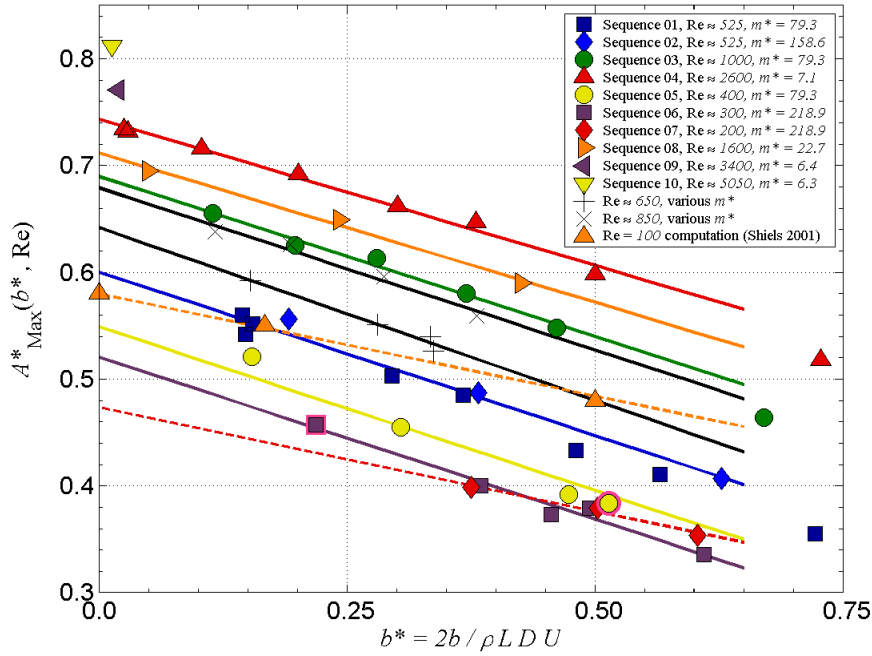


Figure 5.9: Detailed view of the “Generalized” Griffin plot for low damping, $b^* < 0.75$, and various Reynolds numbers, $100 \lesssim \text{Re} \lesssim 5050$.

Reynolds number explored. The first run was the most lightly damped case possible for that configuration (inherent damping only). The remaining two runs were spaced out evenly so that the third run had $b^*|_{A^*_{\text{Max}}} \approx 0.50$. This value was chosen because it was observed from earlier runs, see Figure 5.8, that a linear interpolation to zero damping was a fairly reasonable assumption for this damping range. It should be noted that because some systems had fairly high inherent $b^*|_{A^*_{\text{Max}}}$ values, we relaxed the restraint and allowed up to $b^*|_{A^*_{\text{Max}}} \approx 0.60$. The last two sequences, Sequence 09 and Sequence 10, only involved a single test run since their inherent b^* values were small enough so that their A^*_{Max} values were representative of their extrapolated A^*_{Lim} values.

The results of Sequence 05 – Sequence 10 have been added to the previous generalized Griffin plot, Figure 5.8, and are shown in an updated plot, Figure 5.9. Because a smaller range of b^* values were spanned for these sequences, we restrict ourselves to only focus on the generalized Griffin plot in the area of low damping ($b^* < 0.75$). There are some important things to note about Figure 5.9. First, the least-squares fourth-order polynomial curve fits have been replaced with least-squares linear curve fits for all sequences, except Sequence 09

and Sequence 10 since they only contain a single data point each. All runs in a particular sequence that had a $b^* < 0.60$ were used in the curve fit calculation. These linear curve-fit lines will be used to extrapolate to zero damping and determine A_{Lim}^* in Section 5.7. Second, two new sequences appear that are not discussed previously, these are labeled with a + and x symbol in the figure. These data points were obtained in the traditional ad hoc way where there is not a consistent system configuration used for the test sequence. Third, in order to reaffirm that the difference in the amplitudes of the sequences was a Reynolds number effect and not a cylinder diameter effect, one run in Sequence 05 and Sequence 06 was completed with a different cylinder diameter. These two points are highlighted in Figure 5.9 with a pink colored band around the data point. These points each agree with the rest of the points in their respective sequences, verifying that we are indeed seeing Reynolds number effects. Fourth, the slopes of the linear curve-fit lines for Sequence 01 – Sequence 06, Sequence 08, $Re \approx 650$, and $Re \approx 850$ is surprisingly consistent. There was one exception though. It was noticed that the slope of Sequence 07, the lowest Reynolds number case run, is considerably shallower than the other slopes. However, when this shallow slope is compared with the computational results at $Re = 100$ of Shiels et al. (2001), the two slopes are very closely matched. These two curves are highlighted in Figure 5.9 by dashed lines. Finally, it should be noted that the least-squares linear curve-fit line for Sequence 05 had a steeper slope than the other experimental results. In order to get a better extrapolation to zero damping, we used the slope of a neighboring Reynolds number sequence, $Re = 525$ in this case, and instead only did a least-squares fit on the y-intercept of the linear equation. This modified curve is the one shown in Figure 5.9.

5.7 Limiting Amplitudes

In Figure 5.10 we present limiting amplitudes obtained from extrapolating the maximum amplitude results of the generalized Griffin plot shown in Figure 5.9. We call such a plot, a “limiting amplitudes” plot. For the sequences that contain least-squares linear curve fits, the limiting amplitudes for Figure 5.10 were determined by extrapolating these curves back to zero damping. For the other two sequences (Sequence 09 and Sequence 10), which contain only one damping value, b^* was small enough so that A_{Max}^* was used as A_{Lim}^* .

As can be seen in Figure 5.10, there appears to be a definite dependence of Reynolds

number on limiting amplitudes as predicted by Equation (5.19). Over the Reynolds number range of $200 \lesssim \text{Re} \lesssim 5050$ the limiting amplitude, A_{Lim}^* , increases as Reynolds number increases. There appears to be a possible diminished Reynolds number effect on the limiting amplitude in the range $1000 \lesssim \text{Re} \lesssim 2600$. This can be seen in Figure 5.10 by noting the two dashed lines that represent the general trend of the data below $\text{Re} \lesssim 1000$ and above $\text{Re} \gtrsim 2600$. However, because there is only one point in this range, we cannot say whether the limiting amplitude is independent of Reynolds number or whether there is a weak dependence on Reynolds number. Nevertheless, it appears that there is a relationship change.

It is worth mentioning here that determining A_{Lim}^* for the low Reynolds number cases is more uncertain than the higher Reynolds number cases. As the Reynolds number of the sequences decrease, the minimum possible nondimensional damping value increases. This makes the extrapolation somewhat uncertain because we are not able to get actual points *near* the $b^* = 0$ axis. And while the slopes for Sequence 05 and Sequence 06, being consistent with higher Reynolds numbers slopes, are suggestive of the extrapolation curve being reasonable, the much shallower slope for Sequence 07 has no basis. We noted the similarity to computational results done at $\text{Re} = 100$, however, assuming a slope that is the same as the computational data is dangerous for a few reasons. One, the computational results could be wrong. Two, they may only be valid for that specific Reynolds number. Third, we could have three-dimensional effects that were not present in the purely two-dimensional computational grid of that simulation.

5.8 Comparison with Previous Work

There exists numerous reported maximum amplitudes from experiments at high Reynolds number and computations at low Reynolds numbers. Some of the computations involved zero damping, but most of them, along with all the experiments, involved finite damping. In order to incorporate these reported maximum amplitudes, that cover a much broader range of Reynolds number, in our limiting amplitudes plot, we relaxed the restriction on zero damping. We created an “approximate” limiting amplitudes plot that included reported maximum amplitudes with finite, but *small*, values of damping along with zero damping cases. The results of this can be seen in Figure 5.11, where the figure legend shows the zero

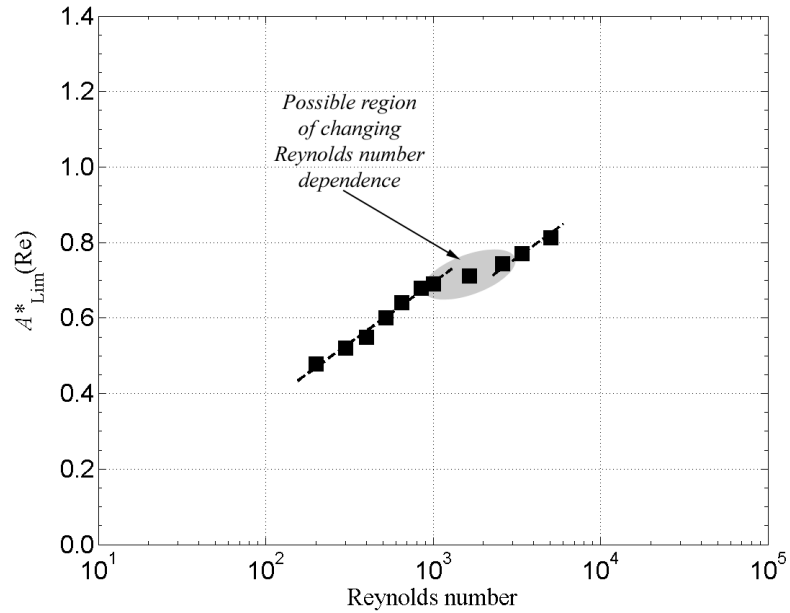


Figure 5.10: Reynolds number effects on limiting amplitudes, A^*_{Lim} , over the range $200 \lesssim \text{Re} \lesssim 5050$ for our data extrapolated to zero damping.

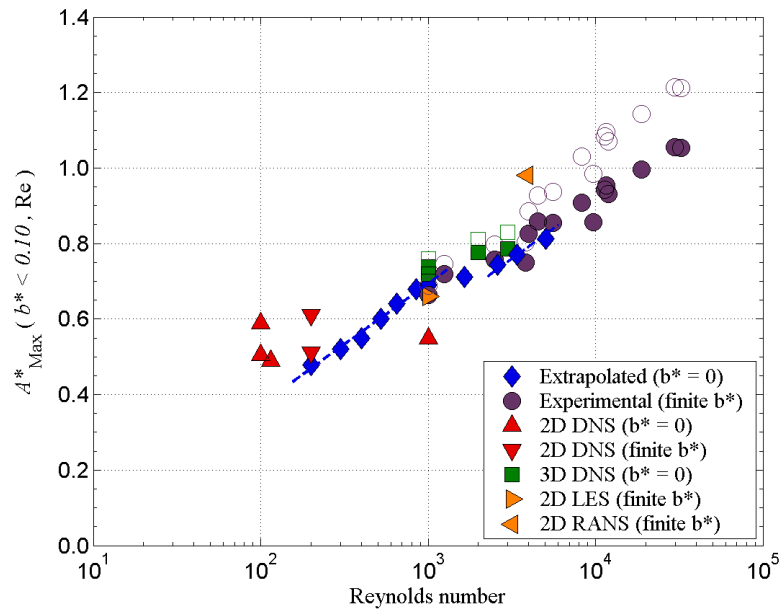


Figure 5.11: Reynolds number effects on maximum amplitudes, A^*_{Max} , with small, but finite, damping values. For these cases, A^*_{Max} should approximate A^*_{Lim} fairly well since $b^* < 0.10$. Experimental data compiled by Williamson and Govardhan (2004).

and finite damping results. Besides our extrapolated A_{Lim}^* values, we also included some computational results at zero damping. These included two 2D DNS codes (Shiels et al., 2001; Willden and Graham, 2006), a 2D and 3D DNS study (Evangelinos and Karniadakis, 1999) and a 3D DNS simulation (Lucor et al., 2005). It should be noted that the 3D DNS codes mentioned here involved using a Fourier expansion in the z-direction so that periodicity of the solution along that axis is implied. For maximum amplitudes that contain a finite amount of damping, we only included results for which we estimated $b^* < 0.10$ so that Figure 5.11 may provide a reasonable representation of what the actual limiting amplitudes plot would look like. The two 2D DNS results with finite damping involved using a vortex-in-cell method (Fujarra et al., 1998; Zhou et al., 1999) with the remaining computational results involving turbulence modeling using LES (Saltara et al., 1998) and RANS (Guilmineau and Queutey, 2004). The numerous experimental results reported by various investigators were tabulated in Williamson and Govardhan (2004).

Many of the reported experimental results, and the simulations by Lucor et al. (2005), calculated the maximum amplitude by averaging only the top 10 percent of recorded amplitudes, compared to our averaging of every recorded amplitude. Therefore, we need to adjust those reported values in order to incorporate them into our figure. In Figure 5.11, the open data points show the reported value while the filled data points show the adjusted value. The adjustment was a simple linear correction based on Reynolds number. From our own results over the Reynolds number range $525 \lesssim \text{Re} \lesssim 5050$, we calculated the maximum amplitudes by averaging both the top 10 percent amplitudes and every amplitude of our data and noted the difference between them. This increasing difference as Reynolds number increased was least-squares fit with a linear curve. This curve was then used to predict what the difference would be for data below $\text{Re} \approx 10^4$. Above this Reynolds number, the extrapolated difference became enormous, and a fixed 15 percent difference was used. This adjustment factor is described in more detail in Appendix D. Even with this adjustment factor and the uncertainty it introduced, there appears to be a strong Reynolds number effect over the entire displayed Reynolds number range.

Looking first at the high Reynolds number results in Figure 5.11, one notices the general agreement with all the experimental data showing a smooth increase in amplitude as Reynolds number increases. It is interesting to note that the top 10 percent amplitude results follow the trend of our $200 \lesssim \text{Re} \lesssim 1000$ data. However, if you adjust the data

to represent every observed amplitude in the set, the data drops slightly and agrees quite closely with our $1650 \lesssim \text{Re} \lesssim 5050$ data. This suggests that using the top 10 percent amplitudes might lead to missing subtle behavior in the data. For $\text{Re} \approx 1000$, there is almost no difference between our extrapolated results, the top 10 percent value, and our adjusted value. However, as Reynolds number increases, the difference between top 10 percent values and our extrapolated values grows. This causes the top 10 percent values to take on artificially high values. This could potentially result in missing the saturating limiting amplitude value. Although more data at higher Reynolds number is necessary, it appears that the top 10 percent data hints at no such saturation value.

Next we turn our attention to the low Reynolds number results in Figure 5.11. The first thing that one notices is the lack of data in this region. One of the reasons for this is that there are many reported maximum amplitudes at low Reynolds number, but most of them are for either rigid cylinders with two-degrees-of-freedom motion (Blackburn and Karniadakis, 1993; Singh and Mittal, 2005), or flexible cables (Newman and Karniadakis, 1996). Another reason is that many of the simulations, and all of the experiments, involve damping values that are too large. It is difficult to maintain a small damping value for low Reynolds number experiments; this is what forced us into our somewhat uncertain extrapolation back to zero. One free-vibration experiment at low Reynolds number was carried out by Anagnostopoulos and Bearman (1992). They explored response behavior at $\text{Re}|_{A_{\text{Max}}^*} \approx 100$. However, due to the low flow velocities and extremely short wetted length (approximately 13 cm) and small diameter (1.6 mm) of the cylinder, their b^* value was quite large, we estimate roughly 0.53, and so their results cannot be used on our approximate limiting amplitudes plot. However, this is not a problem for computations. The problem arises when, instead of exploring zero damping behavior, the computation attempts to *match* a high damping experiment. In order to include more low Reynolds number results, these two-degree-of-freedom motion and flexible-cable results are sometimes included with one-degree-of-freedom motion (Williamson and Govardhan, 2004). However, we take the cautious approach and do not include these results.

The small amount of one-degree-of-freedom data that does exist does not allow many conclusions to be drawn from the low Reynolds number region. One interesting observation is that the 2D DNS simulations at zero damping for $\text{Re} \approx 100$ have much larger amplitudes than our experimental data would suggest for that Reynolds number. This can be seen

in Figure 5.11 by noting that Shiels et al. (2001) predicted $A_{\text{Lim}}^* \approx 0.59$, Evangelinos and Karniadakis (1999) predicted $A_{\text{Lim}}^* \approx 0.50$, and Willden and Graham (2006) predicted $A_{\text{Lim}}^* \approx 0.49$ while our data, *if* it maintained its behavior, predicts an extrapolated value of $A_{\text{Lim}}^* \approx 0.40$. However, our experimental results may not maintain the same behavior down to $\text{Re} = 100$ that they do between $200 \lesssim \text{Re} \lesssim 1000$. The simulations with finite damping at $\text{Re} \approx 200$ also have larger amplitudes than our experimental results. Zhou et al. (1999) predicted an $A_{\text{Max}}^* \approx 0.50$ while Fujarra et al. (1998) predicted an $A_{\text{Max}}^* \approx 0.60$. Since both have very small damping values (we estimate around $b^* \approx 0.05$), it is reasonable to assume that each of these A_{Max}^* values represents their corresponding A_{Lim}^* value reasonably well. The vast amount of two-degree-of-freedom simulations all concentrate around $A_{\text{Lim}}^* \approx 0.50 - 0.60$ for Reynolds numbers between 100 and 300. In fact, Singh and Mittal (2005) conducted a series of computational runs at various Reynolds numbers and report a nearly flat region of maximum amplitudes where there is little, if any, dependence on Reynolds number. The difference between our experimental results and the computations at $\text{Re} = 200$ could be caused by various factors. One could be that the vortex-in-cell computations are not accurate. Another could be that the flow at this Reynolds number has three-dimensional effects that are $\mathcal{O}(1)$ but do not appear that severe in the flow visualizations.

5.9 Flow Visualization

Our results show a smooth, fairly constant, increase in limiting amplitudes, A_{Lim}^* , as Reynolds number increases from at least as low as $\text{Re} \approx 200$ to around $\text{Re} \approx 1000$. That has dramatic ramifications on what effects, if any, the transition from a two-dimensional to a three-dimensional wake structure has on the oscillation amplitude. For a stationary cylinder, the wake transitions to a three-dimensional one around $\text{Re} \approx 180$ (Williamson and Roshko, 1988). For an oscillating cylinder this transition should occur at a higher Reynolds number since it has been observed that cylinder oscillations unify the spanwise flow and would thus delay the transition to a three-dimensional wake. Thus we would expect this transition to occur somewhere between $\text{Re} \approx 180 - \mathcal{O}(10^3)$. Furthermore, we might expect that there should be a change in the limiting amplitude dependence on Reynolds number at this transition point. If this transition occurred at the slightly higher Reynolds number of 200, this might explain why there appears to be such differences between computational

and experimental results at $\text{Re} = 200$. The experiments could have this transitional three-dimensional wake while the computations, being purely two-dimensional simulations, do not. Of course, this difference could be an artifact of the differences between real flows and simulations, and not indicative of a transition point. Unlike simulations, purely two-dimensional flow will never exist in our experiments. Finite aspect ratio effects could be $\mathcal{O}(1)$, for example the drag coefficient for a purely two-dimensional flow over a flat plate is $C_D = 3.6$ while experiments produce $C_D = 2.0$. This could cause experiments and simulations to never agree exactly. With this in mind, we explored the dimensionality of the near wake behind an oscillating cylinder.

We determined the dimensionality of the cylinder near wake, at the maximum amplitude point for different Reynolds numbers, using flow visualization. First, we examined the near wake of a lightly damped system in Sequence 07, which is at $\text{Re}|_{A_{\text{Max}}^*} \approx 200$. A still image of the wake can be seen in Figure 5.12. Although not a pure two-dimensional flow, as can be seen by the slightly three-dimensional vortex being shed from the wake, the scale of the three-dimensional structures appears to be less than a cylinder diameter.

Next we looked at the near wake of a lightly damped system in Sequence 01 for $\text{Re}|_{A_{\text{Max}}^*} \approx 525$. A still image of this wake can be seen in Figure 5.13.

This Reynolds number has a completely different wake structure. The vorticity in the near wake is stretched vertically, as can be seen by the “corkscrew” looking vortices. The scale of this three dimensionality appears to be at least five diameters. Thus, we see a transition from a two-dimensional to a three-dimensional wake between $\text{Re} \approx 200$ and $\text{Re} \approx 525$. However, even though the wake has transitioned in this region, we do not see a change in the limiting amplitude dependence. We feel that $\text{Re} \approx 200$ experiments were two-dimensional enough such that the difference between the experimental and computational results cannot simply be wake dimensionality effects.

There is a difference in our results that occurs around $\text{Re} \approx 200$, the abrupt slope change in the generalized Griffin plot. Due to the time it takes to simulate enough cycles to get good representations of freely-vibrating cylinders, computational results rarely include the dependence of maximum amplitude on damping. If one only cares about limiting amplitudes, the simulations are run with zero damping; they are not burdened with the need to extrapolate back to zero damping. That is unfortunate because then they cannot explore how the maximum amplitude response behaves as it approaches zero damping. However,



Figure 5.12: Flow visualization showing the nearly two-dimensional flow around an oscillating cylinder at its maximum amplitude, $A_{\text{Max}}^* \approx 0.35$, for $\text{Re} \approx 200$.

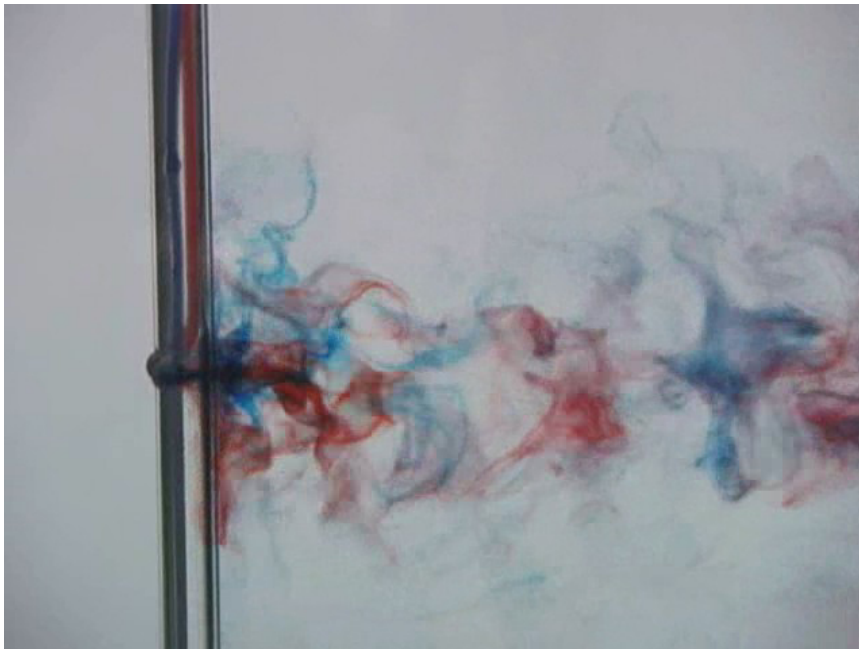


Figure 5.13: Flow visualization showing the three dimensionality of the flow around an oscillating cylinder at its maximum amplitude, $A_{\text{Max}}^* \approx 0.55$, for $\text{Re} \approx 525$.

Shiels et al. (2001) looked at damping effects on the maximum amplitude at $Re = 100$. When Shiels' results and our $Re \approx 200$ results are compared in the generalized Griffin plot, one notices that the slopes of those two constant-Reynolds-number curves are nearly identical and much shallower than all of our other curves, which share an almost equal slope for low damping. This slope agreement is true even though our experimentally determined limiting amplitude trend does not agree with the computational results at $Re = 100$, if extrapolated to such a low Reynolds number. Therefore, we believe that possibly the dimensionality of the wake affects not the limiting amplitude values themselves, but instead the maximum amplitude dependence on damping.

In order to better understand the change in dependence on Reynolds number in the region $1000 \lesssim Re \lesssim 2600$, flow visualization results were examined at the beginning and end of this region to see if some insight could be gained. It has been documented by various researchers that the large-amplitude section (upper branch) of the response curve is an unbalanced 2P wake structure (Govardhan and Williamson, 2000). By unbalanced we mean that one of the two vortices that make up the pair contains significantly lower circulation than the other. Since both of these runs have low enough damping and high enough Reynolds number for an upper branch to exist (Klamo et al., 2005), we expect that they would have the same wake structure, an unbalanced 2P. The wake structure for $Re \approx 1000$ can be seen in Figure 5.14 and for $Re \approx 2600$ in Figure 5.15.

We find that the two runs actually have different wake structures. The beginning of this region ($Re \approx 1000$) appears to have a classic 2S wake structure while at the end ($Re \approx 2600$) it appears to have the expected unbalanced 2P wake structure. Therefore, it seems possible that in this region, the wake structure at the maximum amplitude changes from a 2S to a 2P one. This could account for the slight change in the trend of limiting amplitudes in this region. We suspect that all runs with an A_{Max}^* at $Re \lesssim 1000$ will have a 2S wake structure at its maximum amplitude. On the other hand, all runs with an A_{Max}^* at $Re \gtrsim 2600$ will have a 2P wake structure at its maximum amplitude. To verify this, we examined the wake structure at the maximum amplitude for other systems. For $Re \lesssim 1000$, we examined the wake of the maximum amplitude of a lightly damped system in Sequence 01 at $Re \approx 525$ and the maximum amplitude of a lightly damped system in Sequence 08 at $Re \approx 200$. Both runs showed a 2S wake structure at the maximum amplitude. The $Re \approx 200$ wake structure can be seen in Figure 5.16. For $Re \gtrsim 2600$, we examined the wake of the maximum

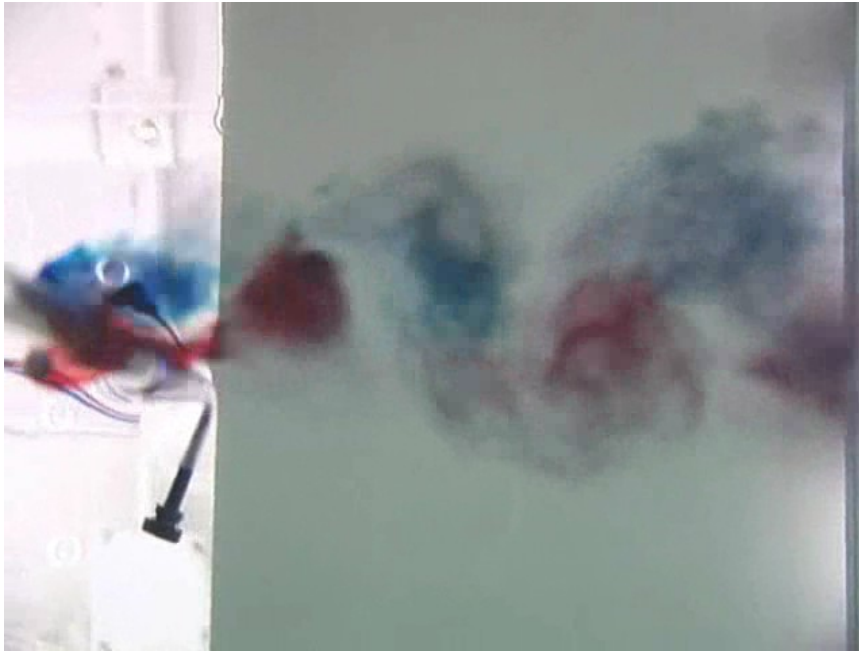


Figure 5.14: Flow visualization showing a 2S wake structure for an oscillating cylinder at its maximum amplitude, $A_{\text{Max}}^* \approx 0.61$, for $\text{Re} \approx 1000$.

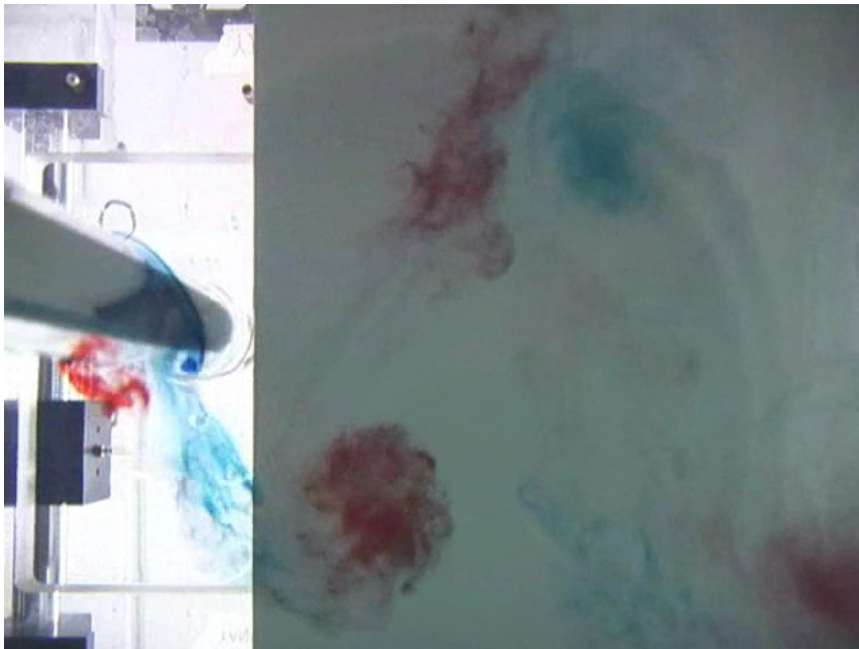


Figure 5.15: Flow visualization showing a 2P wake structure for an oscillating cylinder at its maximum amplitude, $A_{\text{Max}}^* \approx 0.73$, for $\text{Re} = 2600$.

amplitude of a lightly damped system in Sequence 10 at $\text{Re} \approx 5050$ and show the results in Figure 5.17. Both this run, and A_{Max}^* of Sequence 04 at $\text{Re} \approx 2600$, had an unbalanced 2P wake structure at the maximum amplitude point.

5.10 Heavily Damped Systems

It is not a straightforward matter to extend the generalized Griffin plot to higher damping values than are shown in Figure 5.8. We refer to systems with damping values higher than $b^*|_{A_{\text{Max}}^*} > 1.75$ as heavily damped systems. The behavior of such systems is different from lightly and moderately damped systems, which causes problems when attempting to analyze all of them in a consistent manner.

One difference in heavily damped systems is that their A_{Max}^* occurs at a different k_{eff}^* than the lighter damped systems. As first mentioned in Section 4.3, $k_{\text{eff}}^*|_{A_{\text{Max}}^*}$ normally occurs around 2.5, however, for heavily damped systems this value is lower, usually causing $k_{\text{eff}}^*|_{A_{\text{Max}}^*}$ to occur around 1 instead.

The more general fact is that the overall behavior of these heavily damped systems is different. They begin to resemble the response of a forced mass-damping-spring system. In the traditional formulation, the response profile changes to one that only has substantial amplitudes near the resonance condition with the rest of the response being more symmetrical about the maximum peak and decreasing quickly on either side. Due to the fact that the large response regions outside of the resonance condition have been damped away, the amplitude response in the effective stiffness formulation is missing the middle portion of the response profile where the maximum amplitude normally falls. This can be seen by referring to Figure 5.18, which shows results for a heavily damped system of Sequence 02 in the effective stiffness formulation. Notice how there is no response in the domain $1.5 < k_{\text{eff}}^* < 4.5$ since the system simply jumps through those possible effective stiffness values. This is the type of change that we see for all heavily damped lower Reynolds number systems. We see a similar, although slightly different change, for higher Reynolds number systems that are heavily damped.

The changes that occur to a higher Reynolds number system, in this case $\text{Re}|_{A_{\text{Max}}^*} \approx 2600$, can be seen in Figure 5.19. Notice how when the system damping passes through $b^*|_{A_{\text{Max}}^*} \approx 1.75$ the behavior of the response begins to change. First the system seems to



Figure 5.16: Flow visualization showing a 2S wake structure for an oscillating cylinder at its maximum amplitude, $A_{\text{Max}}^* \approx 0.35$, for $\text{Re} = 200$



Figure 5.17: Flow visualization showing a 2P wake structure for an oscillating cylinder at its maximum amplitude, $A_{\text{Max}}^* \approx 0.78$, for $\text{Re} = 5050$

jump between an upper and lower branch state as seen by the large scatter in the data where the upper branch response normally lies. Then, as the system damping is further increased, the amplitude of the system actually increases through the beginning of the lower branch region instead of decreasing as it does for lighter damped systems.

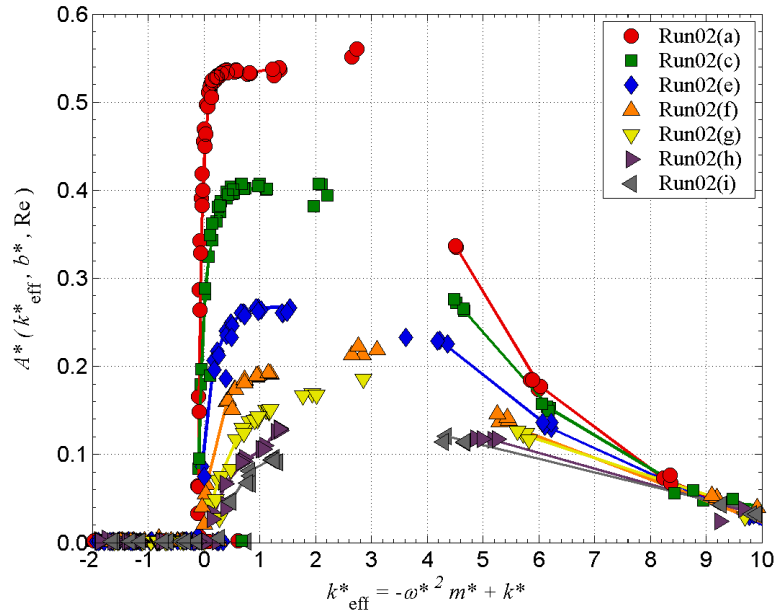


Figure 5.18: Select runs from Sequence 02 showing the changes to the amplitude response profile for heavily damped systems, $b^*|_{A_{\text{Max}}^*} > 1.75$, along with lightly damped systems for reference. Damping values for each run can be found in Table 5.1.

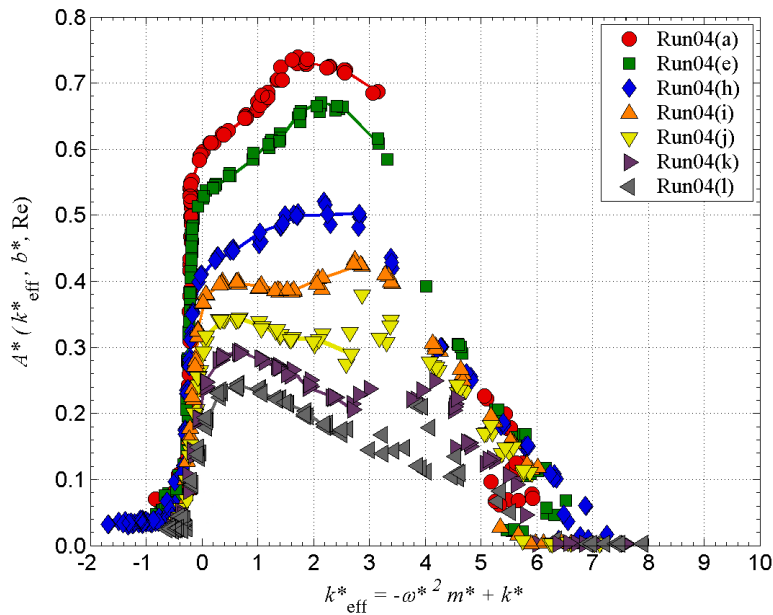


Figure 5.19: Select runs from Sequence 04 showing the changes to the amplitude response profile for heavily damped systems, $b^*|_{A_{\text{Max}}^*} > 1.75$, along with lightly damped systems for reference. Damping values for each run can be found in Table 5.1.

Chapter 6

Discontinuities: Hysteretic Regions and Transient Behavior

6.1 Chapter Overview

We begin by introducing the rationale for exploring the hysteretic regions and transient behavior in Section 6.2. In Section 6.3 we explore the hysteretic region between the initial and upper branch and frame our investigation within the context of the numerous previous studies of this region. We then investigate the region connecting the upper and lower branches and make comparisons to previous conclusions in Section 6.4. Next, in Section 6.5 we describe a newly found hysteretic region between the lower branch and the desynchronized region. Our focus then changes to exploring the transient behavior in the hysteretic region between the initial and upper branch. These transient behaviors are induced two ways, by slight changes in slight tunnel velocity, as discussed in Section 6.6, and by changes in the system damping parameter, covered in Section 6.7. Finally, in Section 6.8 we make comparisons between velocity- and damping-induced transient behavior.

6.2 Background

Most studies of VIV involve recording long time traces of the amplitude and frequency responses, after the transients have died out, while holding the system parameters constant. These time-varying responses are then averaged using a certain method to obtain a single amplitude and frequency value that is supposed to represent the system behavior during that entire test. These time-averaged values are then used to produce the full amplitude and frequency response profiles. In this chapter we break from this tradition and instead

look at hysteretic regions and transient behavior.

There are three known parts of the amplitude response profile that have the potential to exhibit discontinuous behavior due to either hysteretic jumps or intermittent switching. These three regions are (1) the change from the initial branch to the upper branch for large-amplitude systems, or to the lower branch for small-amplitude systems, (2) the change from the upper branch to the lower branch for large-amplitude systems, and (3) the change from the lower branch to the desynchronized region for both systems.

For small-amplitude systems (those lacking an upper branch), region 1 has been investigated by numerous researchers (Feng, 1968; Brika and Laneville, 1993; Khalak and Williamson, 1999). Even though this discontinuous hysteretic region is interesting, we will not explore it here. For large-amplitude response systems, regions 1 and 2 have been investigated and discussed by Khalak and Williamson (1997a, 1999). They found a hysteretic region between the initial and upper branch (region 1), and an intermittent switching region between the upper branch and the lower branch (region 2). We will explore both of these regions in the context of our formulation. The region 3 discontinuity occurs for both large-amplitude and small-amplitude systems, however, as we will show later, only for a small enough Reynolds number. There has been a recent study by Singh and Mittal (2005) for a flexibly mounted cylinder that included region 3, however, in general, there has been very little discussion on the transition from the lower branch to the desynchronization region. This discontinuous region was noticed experimentally and discussed by Klamo et al. (2006).

Although traditional VIV research has involved calculating average values of the system amplitude and frequency response, as well as wake properties, there have been some studies that looked at the transient response of the system. Brika and Laneville (1993) have long time traces of cylinders started from rest and started impulsively, for constant tunnel velocities, showing the displacement and phase changes as the cylinder reaches steady-state conditions. Transient behavior of the wake was investigated by Carberry et al. (2001, 2003) using controlled forced-vibrations. They showed the self-excited change in the wake from a low-frequency, 2P wake structure, to a high-frequency, 2S wake structure, at constant forcing amplitude and frequency. In our experiments, we explore the transient behavior of the system by changing the input parameters in either of two ways, by changing the tunnel velocity or the system damping, and then recording the transient response as the system goes from one response behavior to another.

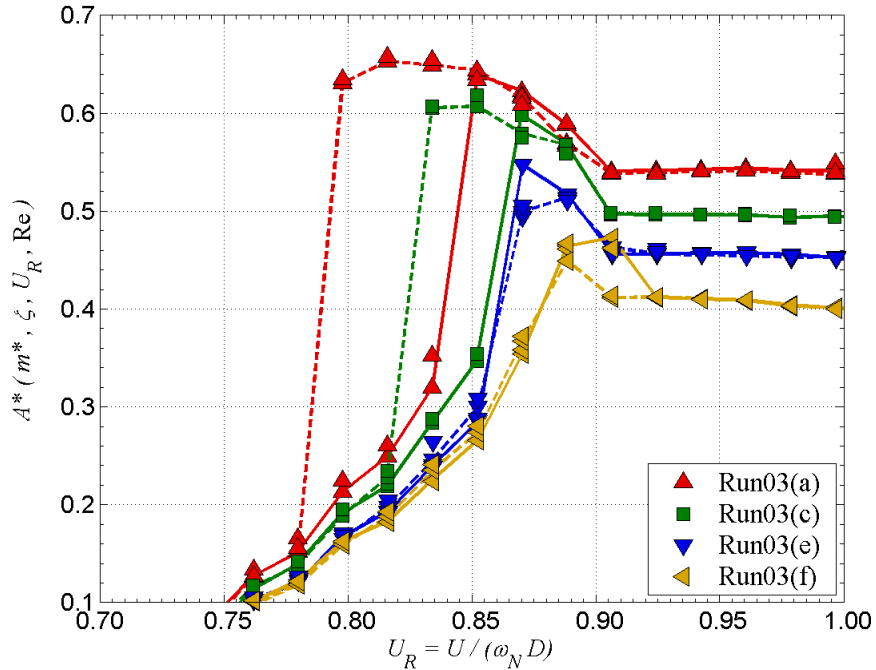


Figure 6.1: Erosion of the upper branch for Sequence 03. Solid lines represent increasing tunnel velocities and dashed lines represent decreasing tunnel velocities. Damping values for each run can be found in Table 5.1.

6.3 Hysteresis Between Initial Branch and Upper Branch

The first hysteretic region that we explore involves the initial and upper branches. Because this region partially lies in the maximum amplitude portion of the response profile, it has been observed and studied by many researchers (Feng, 1968; Brika and Laneville, 1993; Khalak and Williamson, 1999). Our focus is to explore this hysteretic region in terms of its involvement in the “erosion” of the upper branch, as described in Section 4.7. Since the upper branch is partially located in this hysteretic region, the “erosion” of the upper branch is associated with two effects. One occurs for increasing tunnel velocities and one for decreasing tunnel velocities. This “erosion” of the upper branch can be seen in Figure 6.1, in the traditional formulation plotted against reduced velocity, which shows the results for the four most lightly damped cases from Sequence 03 ($\text{Re}|_{A_{\text{Max}}^*} \approx 1000$). The damping values for Sequence 03 can be found in Table 5.1.

The first important point to notice in Figure 6.1 is that the upper branch meets the lower branch at a fixed value of U_R , independent of damping. For this particular system

it occurs at $U_R \approx 0.90$; for other systems the value is different but always independent of damping. The first effect that controls the existence and size of the upper branch is the point at which the jump from the initial to the upper branch occurs for increasing tunnel velocities (solid lines in Figure 6.1). As damping is increased the size of the upper branch decreases due to the fact that this jump to the upper branch is delayed. This can be seen in Figure 6.1 as a higher reduced velocity value at which the amplitude jump discontinuity occurs. For Run03(a), the jump occurs around $U_R \approx 0.84$ while for Run03(f) it occurs around $U_R \approx 0.88$. Since the ending of the upper branch for this system is fixed at $U_R \approx 0.90$, as the jump to the upper branch moves toward higher reduced velocities, the size of the upper branch decreases.

The second effect that controls the existence and size of the upper branch is the point where the jump downward from upper to initial branch occurs (dashed lines in Figure 6.1). As damping is increased, this point occurs at higher values of U_R . In Figure 6.1, for Run03(a), it occurs around $U_R \approx 0.80$, while for Run03(c), the jump downward occurs around $U_R \approx 0.83$. This downward jump from upper to initial branch, as reduced velocity is decreased, is known to be connected to the 2S and 2P regimes of the WR-plane (see Section 2.4). Previous researches have noted that jumps between the initial and upper branches correspond to changes between 2S and 2P wake structures, and thus jumps between the two WR-plane regimes (Khalak and Williamson, 1999). More specifically though, we observe *where* this jump in the WR-plane occurs when reduced velocity is decreased. In Figure 6.2, we show that the jump downward occurs when the response profile *reaches* the boundary between the 2S and 2P regimes. Note that the independent variable is now $1/f^*$. Because of the negative slope of this dividing line and the fact that an increase in damping decreases the overall response amplitude, this line is crossed at higher values of reduced velocity, U_R , as damping is increased. Ultimately, by this process, the upper branch disappears for decreasing tunnel velocity tests. As seen in Figure 6.2, we observe the same phenomenon for Sequence 02 ($\text{Re}|_{A_{\text{Max}}^*} \approx 525$) and Sequence 04 ($\text{Re}|_{A_{\text{Max}}^*} \approx 2600$).

On the other hand, we observe that, as reduced velocity is increased, the system jumps to various locations in the 2P regime which are removed from the 2S/2P dividing boundary curve. We plot the same cases as were shown in Figure 6.2 for decreasing reduced velocity, but this time we plot their corresponding increasing reduced velocity cases. These are shown in Figure 6.3.

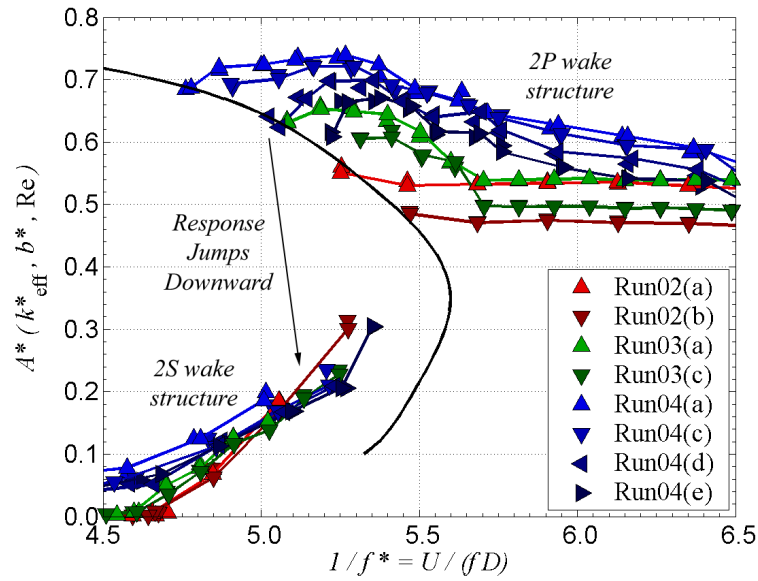


Figure 6.2: Amplitude response downward jump from the upper branch to initial branch for decreasing U_R along with its dependence on the WR-plane 2S/2P dividing curve. Shown are selected runs from Sequence 02 – Sequence 04; the damping values for each run can be found in Table 5.1.

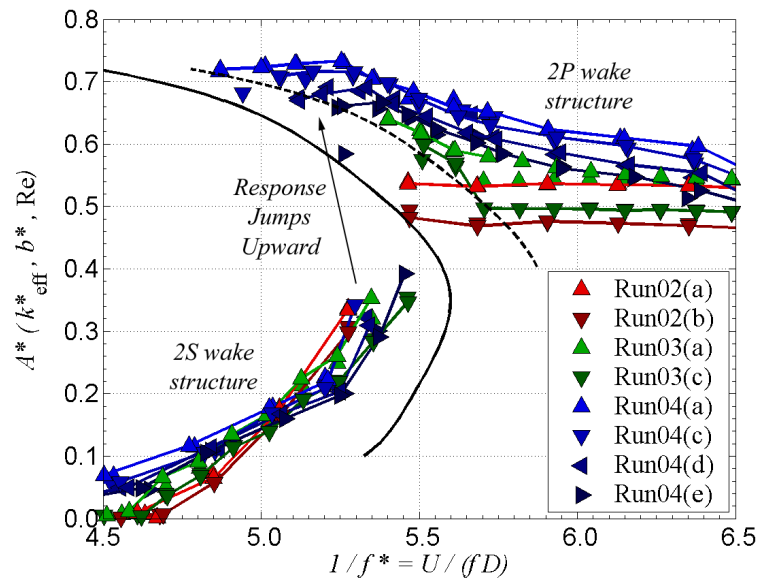


Figure 6.3: Amplitude response upward jump from the initial branch to upper branch for increasing U_R along with the WR-plane 2S/2P dividing curve displayed for reference. Shown are selected runs from Sequence 02 – Sequence 04; the damping values for each run can be found in Table 5.1.

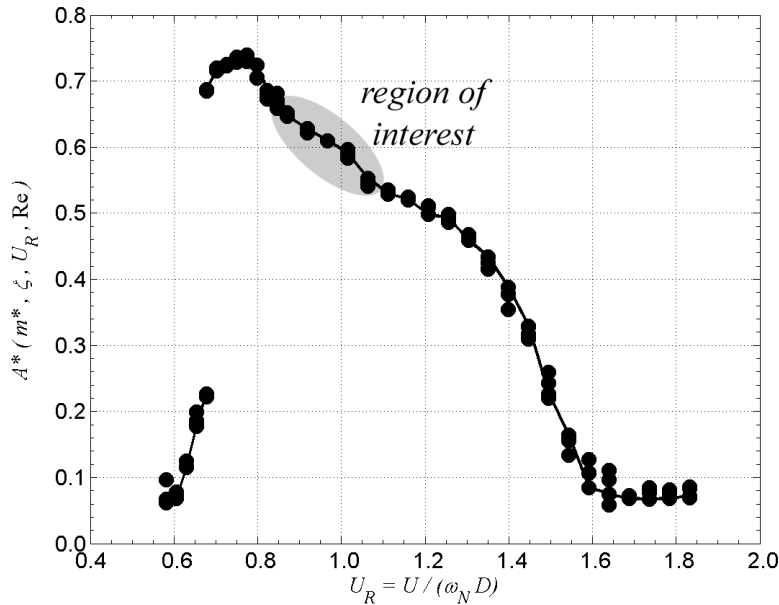


Figure 6.4: Transition region between the upper branch and lower branch, highlighted by the gray ellipse, shown in the traditional formulation.

In order to further highlight the locations where the system jumps to inside the 2P region, we connect these points with a dashed curve. It is interesting to note the relationship between this curve and the traditional location of the WR-plane 2S/2P dividing curve. The curvature of the two lines appears to be close, ultimately however, we are not able to make any statements about whether the 2S/2P dividing curve itself has any hysteretic behavior. For instance, one of the two increasing velocity runs for both Run04(c) and Run04(e) jumped upward to a point near the actual 2S/2P dividing curve, not the dashed curve. Also, for higher damped runs with lower Reynolds numbers, such as Run02(a) and Run02(b), there is not a difference in the jump location between an upward and a downward jumping system.

6.4 Transition Between Upper Branch and Lower Branch

The second part of the amplitude response profile that we examine is the transition area between the upper and lower branches. This area is highlighted in Figure 6.4 using the traditional formulation, and in Figure 6.5 using the effective stiffness formulation.

One reason that this region is interesting is that according to the oscillation amplitudes and frequencies of the upper and lower branches, both lie inside the 2P wake structure regime

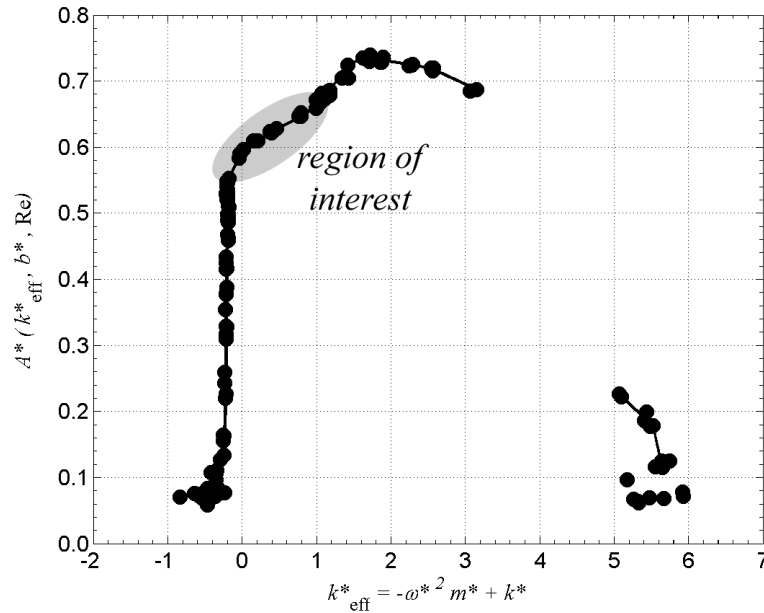


Figure 6.5: Transition region between the upper branch and lower branch, highlighted by the gray ellipse, shown in the effective stiffness formulation.

of the WR-plane. However, even though both branches possess essentially the same general wake structure, they exhibit different amplitude and frequency behavior. Another reason that this region is interesting is that Khalak and Williamson (1997a), and later Govardhan and Williamson (2000), speculated that in this region there is an intermittent switching, where the system jumps between two responses, each distinct to one of the branches. They arrived at this conclusion by first looking at Hilbert space transforms of the phase angle between the lift and displacement. They noticed frequent jumps between two phase angle values, 0° and 180° , signalling changes between upper and lower branch behavior. Looking at the Hilbert transform of the frequency data, they noticed a similar behavior of the data coalescing around two values with rapid jumps between.

We were never able to get useful results from the Hilbert transform of our frequency data because those transform results turned out to be too noisy. However, we examined cycle-by-cycle results and looked for this intermittent switching. Our cycle-by-cycle results for Run04(a) are shown in Figure 6.6 for the amplitude and in Figure 6.7 for the frequency. The four subplots of each figure result from the fact that a *run* involved spanning the velocities of interest four times.

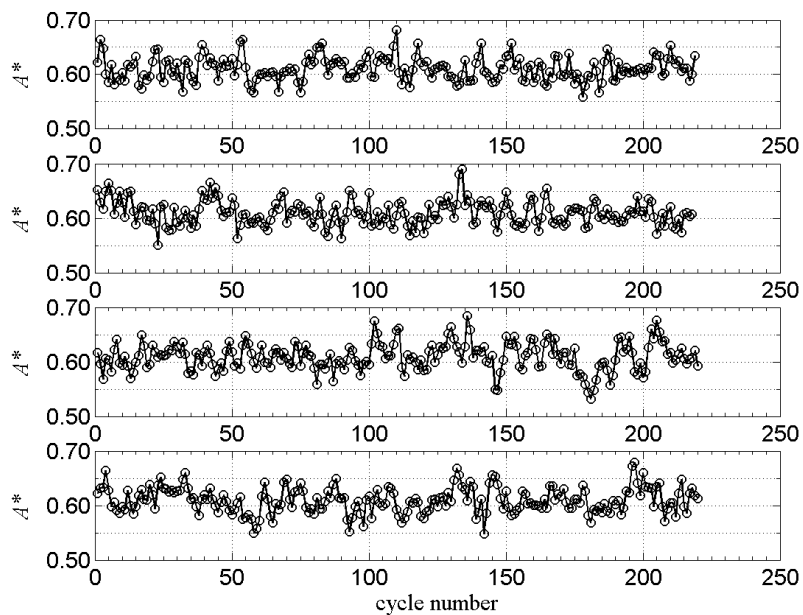


Figure 6.6: Cycle-by-cycle amplitude results from four tests of Run04(a) in the transition region between the upper and lower branch.

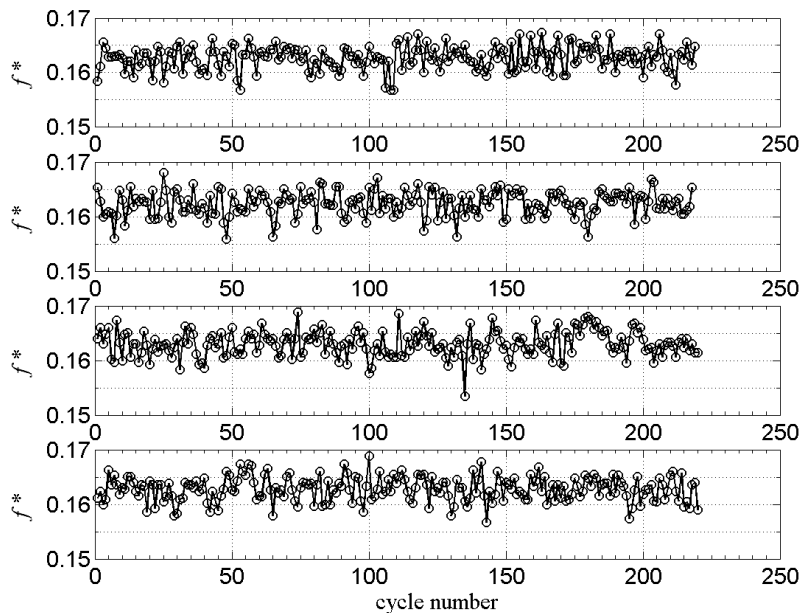


Figure 6.7: The corresponding cycle-by-cycle frequency results from four tests of Run04(a) in the transition region between the upper and lower branch.

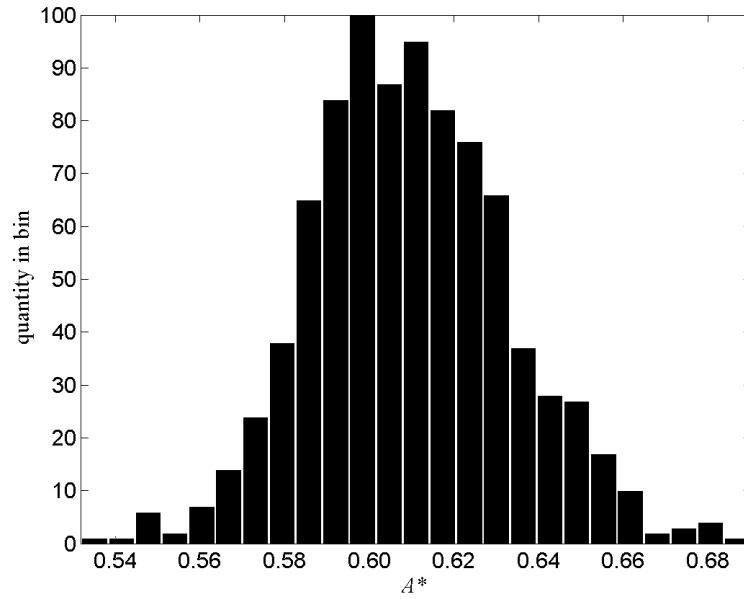


Figure 6.8: Cycle-by-cycle amplitude results from the four tests in Figure 6.6 shown in a single histogram.

Our results show that, although there is not a single dominant amplitude or frequency, there are no two “states” that the system seems to be intermittently switching between. It may indeed be true that the phase angle between the lift and displacement are switching randomly by 180° . This could explain why the system seems to chaotically wander over a range of values. At one phase angle, the system prefers a smaller amplitude, in this case around $A^* \approx 0.56$ and when the wake switches to the other phase angle, the system prefers a larger amplitude states and heads toward amplitudes around $A^* \approx 0.66$. However, it is not obvious to us that the actual amplitude and frequency response should be represented as two distinct responses at the same reduced velocity value. To further look for two distinct system responses at this reduced velocity, we considered histograms of the amplitude and frequency. If the system were indeed jumping between two dominant states, we would expect to see two peaks in our histogram data. Our amplitude histogram results are shown in Figure 6.8 and our frequency histogram results are shown in Figure 6.9. Although the results are not a perfect normal distribution, they suggest a broad response range over which the system operates.

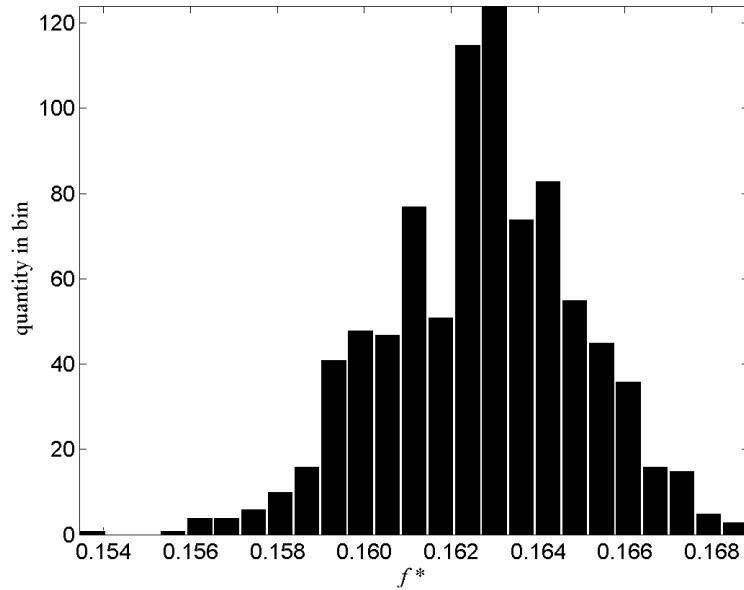


Figure 6.9: Cycle-by-cycle frequency results from the four tests in Figure 6.7 shown in a histogram.

6.5 Hysteresis Between Lower Branch and Desynchronized Region

We have found a hysteretic region between the lower branch and the desynchronized region. We also notice that the size of this hysteresis is damping dependent. This new result can be seen in Figure 6.10 in the traditional formulation. The damping values for Sequence 01 can be found in Table 5.1. In this figure, the solid lines represent the amplitude response for increasing tunnel velocity, and the dashed lines represent the response for decreasing velocity. As can be seen in Figure 6.10, the reduced velocity value at which the system changes between the lower branch and a desynchronized state depends on whether the tunnel velocity is increasing or decreasing. Another interesting result is that, unlike the increasing tunnel velocity case where the amplitude slowly decreases for each response point until the desynchronized region is reached in a fairly smooth manner, for the decreasing velocity case the change from desynchronized state to lower branch is dramatic and takes the form of a jump discontinuity.

The size of this hysteretic region depends on the level of damping in the system. In

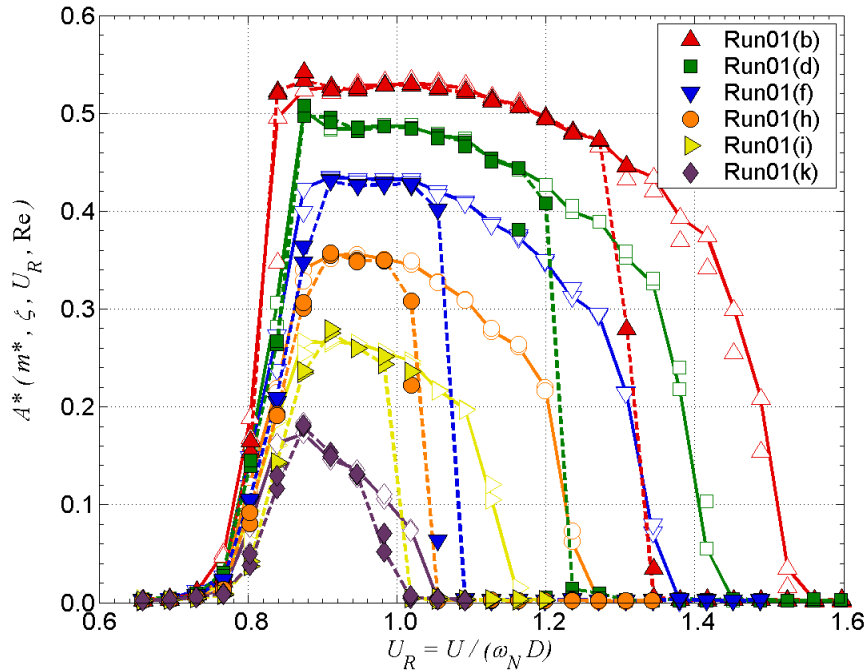


Figure 6.10: Amplitude response profiles for Sequence 01 showing the lower branch to desynchronized state hysteresis. Solid lines and white data points show increasing tunnel velocities and dashed lines and colored data points show decreasing tunnel velocities. Damping values for each run can be found in Table 5.1.

general, as damping is increased, the width, in ΔU_R , of the hysteretic region decreases. This can be seen by noting the large hysteretic zones for the most lightly damped cases, Run01(b) – Run01(f), the smaller width as damping is increased for Run01(i), and finally, in the most heavily damped system, Run01(k), the width of the hysteresis is only a single response point. It is difficult to assign single reduced velocity values for where these hysteretic jumps will occur since they appear to be sensitive to factors such as slight perturbations in the flow. This is not to say that the existence itself is sensitive, for the presence of these hysteretic jumps is always observed in repeated tests. However, the reduced velocity values at which the jumps occur does vary during identical repeated tests.

Perhaps one reason that the lower branch to desynchronized region hysteresis has been missed is the fact that it appears to be a low Reynolds number effect. We found that our $\text{Re}|_{A_{\text{Max}}^*} \approx 2600$ (Sequence 04) amplitude profile displayed no hysteresis of this type and our $\text{Re}|_{A_{\text{Max}}^*} \approx 1000$ (Sequence 03) amplitude profile displayed hysteresis only for the two most lightly damped cases. However both of our $\text{Re}|_{A_{\text{Max}}^*} \approx 525$ amplitude profiles showed this

hysteresis prominently.

6.6 Velocity-Induced Transients

Before showing the transient behavior results, it is important to first establish some terminology. This is necessary because sometimes, as the system moved along its transient path, changing frequency and amplitude values every cycle, it would occasionally settle on a certain frequency-amplitude combination, $(1/f^*, A^*)$, that allowed the system to stay near that particular combination for an extended number of cycles. When the system did this, we called the frequency-amplitude combination that it was operating at, a “marginally stable” one. By our definition then, a “marginally stable” combination means a frequency-amplitude combination, $(1/f^*, A^*)$, where the system oscillates at roughly the same frequency and amplitude values for more than 10 cycles. Finally, there is no attempt to link our terminology to strict mathematical definitions of stability or stable and unstable behavior.

All of the transient behavior results presented here involved exploring the large discontinuity in the amplitude response profile between the initial branch and the upper branch. We investigated velocity-induced and damping-induced transient responses of systems undergoing this jump discontinuity in our transient behavior (TB) tests. Two different system configurations, TB01 and TB02, were used. The major parameters for each of the two configurations can be seen in Table 6.1. In this section involving velocity-induced transients,

test no.	D (mm)	m (kg)	k (N/m)	m^*	$\text{Re} A_{\text{Max}}^*$
TB01	10.0	1.860	260	79.3	1000
TB02	37.8	2.385	13.5	7.1	2600

Table 6.1: System configurations for the transient behavior (TB) tests

these two systems have no external damping applied to them from the VMEC system. The only damping was the inherent damping within the system, hence these tests are designated ID, for inherent damping. This inherent system damping is caused by various things such as the air drag on the moving system and the stretching of the springs. This ID label will distinguish them from tests in the next section using the same system configurations, but with external damping applied to them at two levels, low damping (LD) and high damping

(HD). Both ID systems had a small enough inherent damping and a high enough Reynolds number such that they were large-amplitude (upper branch) systems. The specific damping values used for each configuration can be seen in Table 6.2. Across these two configurations,

configuration no.	b (kg/s)	$b^* _{A^*_{\text{Max}}}$
TB01(ID)	0.0564	0.224
TB01(LD)	0.0597	0.237
TB01(HD)	0.3150	1.327
TB02(ID)	0.0154	0.022
TB02(LD)	0.0185	0.027
TB02(HD)	0.6216	1.082

Table 6.2: Imposed system damping values for damping-induced transient tests

the nondimensional mass changed by an order of magnitude and the Reynolds number by almost a factor of three. It should be noted that the parameters of TB01(ID) are similar to Run03(c) and TB02(ID) to Run04(a).

The location of the jump discontinuity and the test methodology can be seen in Figure 6.11 for TB01 and Figure 6.12 for TB02. Because the amplitude discontinuity that we are exploring occurs in a hysteretic region, as described in Section 6.3, the point at which the jump between the two branches occurs depends on whether the tunnel velocity is increasing or decreasing. Furthermore, for such lightly damped systems, the location of this jump, for each direction of velocity change, is not fixed. It varies slightly from test to test as can be clearly seen in Figure 6.12 where the jump downward occurred at two different reduced velocity values during successive tests. In Figure 6.11 the jump upward, from the initial to the upper branch, occurs in the range of reduced velocities of $0.83 \lesssim U_R \lesssim 0.85$ while the jump downward, from the upper to the initial branch, occurs in the range of $0.81 \lesssim U_R \lesssim 0.83$. In Figure 6.12 the jump upward occurs in the range of reduced velocities of $0.67 \lesssim U_R \lesssim 0.70$ while the jump downward occurs in the range of $0.63 \lesssim U_R \lesssim 0.67$.

Our velocity-induced transient response tests, using TB01(ID) and TB02(ID), involved getting the oscillating system into a steady-state behavior at a reduced velocity value near the edge of one of the jump boundaries. A large number of cycles (between 300 to 500) were then recorded at this steady-state condition. Next, the tunnel velocity was changed by increments of about 2.5 cm/s until the jump upward or downward was observed. During this transient behavior, the system response was recorded. After this transient had occurred, a

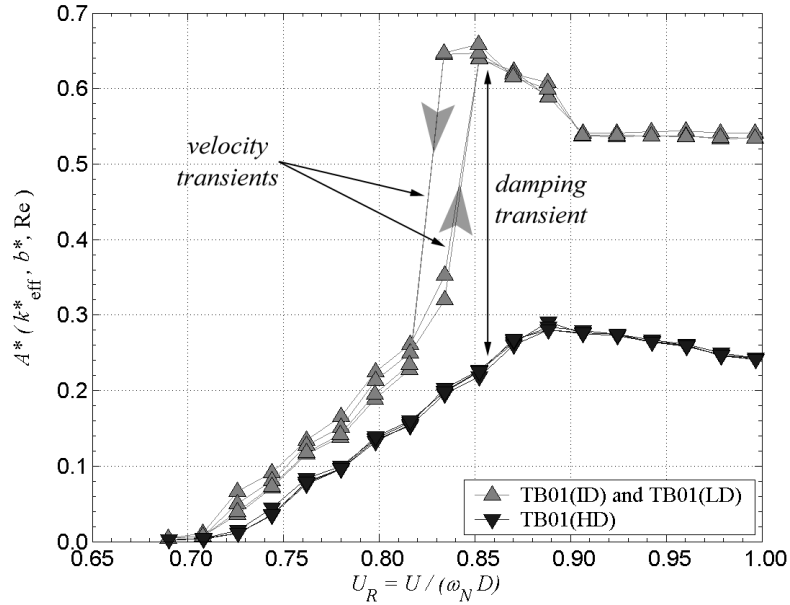


Figure 6.11: Test methodology for transient behavior (TB) tests involving velocity- and damping-induced transients on TB01 configuration.

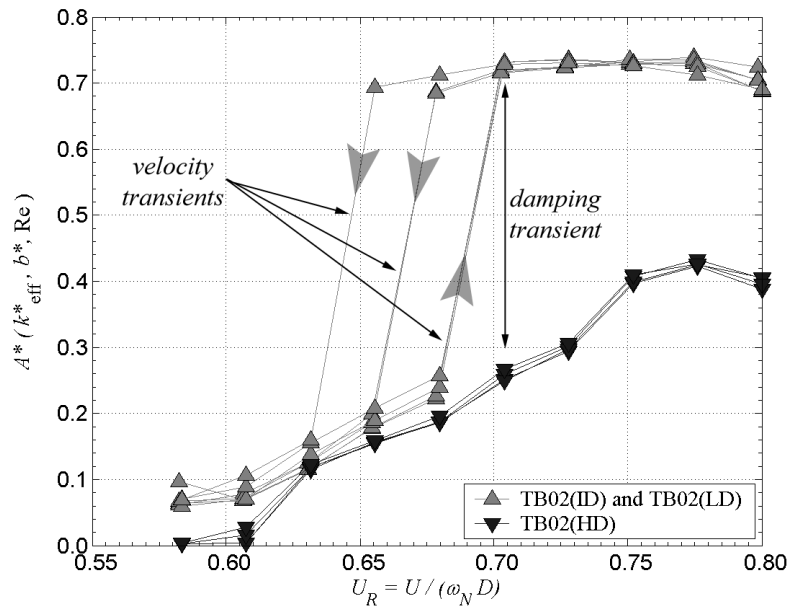


Figure 6.12: Test methodology for transient behavior (TB) tests involving velocity- and damping-induced transient on TB02 configuration.

large number of cycles were again recorded to locate the postjump steady-state condition.

For all three increasing tests of TB01(ID), the system jumped from an initial branch state to an upper branch state when the reduced velocity was increased from 0.834 to 0.852. The jump downward from an upper branch state to an initial branch state occurred when the reduced velocity decreased from 0.834 to 0.816 for all three decreasing tests as well. The amplitude response for all six tests, three upward and three downward jumps, can be seen in Figure 6.13.

Even though all six tests involved undergoing transient behavior from the same reduced velocity, $U_R = 0.834$, the behavior between upward and downward jumps was different. The jump upward occurred over about 100 cycles and the amplitude increase per cycle was fairly consistent. However, for the downward jumping tests, the jump took more than twice the number of cycles to reach an initial branch state. Also, the amplitude decrease per cycle was not as consistent as the upward jumping cases. Instead, the amplitude decreases at a very slow rate per cycle until the amplitude falls below about $A^* \approx 0.50$, then the amplitude decreases at a rate similar to the upward jumping cases.

The frequency-amplitude response of this system can be seen in Figure 6.14 along with the WR-plane 2S/2P dividing curve superimposed. The frequency response of systems with a configuration similar to TB01 does not change much between initial and upper branches. (See Figure 4.27 for the frequency response profile for such a system.) Because of this, the transient response of TB01 does not move much in the horizontal direction in the figure. Instead, the discontinuous jumps involve almost exclusively amplitude changes when moving between the steady-state points. However, one should not conclude that the frequency of the system is not important. For the slight change in tunnel velocity causes the frequency response, $f^* = fD/U$, to change even for a constant frequency, f , since U changed. And this change is enough to force the system into a new state.

Some care must be taken in this transient analysis since the parameter $1/f^*$ contains the tunnel velocity and the response frequency is therefore not nondimensionalized with a constant. Because we induced the transient system behavior through a small increase or decrease in tunnel velocity, we need to take this period of changing velocities into account. Fortunately, the magnitude of the velocity change was small, and the transient time of the tunnel was on the order of five seconds. Since the oscillation period was around 0.5 seconds, the velocity was constant within about ten oscillation cycles. Therefore, only the first ten

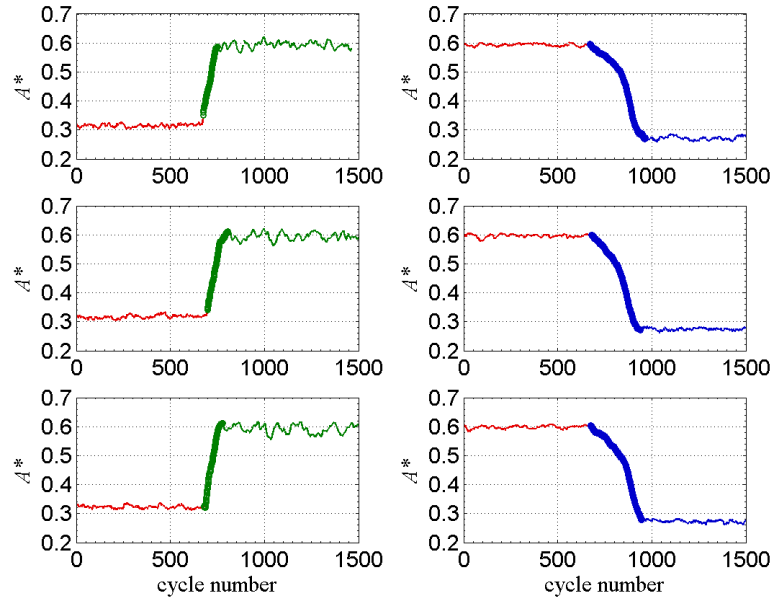


Figure 6.13: Time traces of TB01(ID) amplitudes through the discontinuous region for increasing (left) and decreasing (right) tunnel velocities; blue data: $U_R = 0.816$, red data: $U_R = 0.834$, and green data: $U_R = 0.852$; $-$: steady-state, \circ : transient.

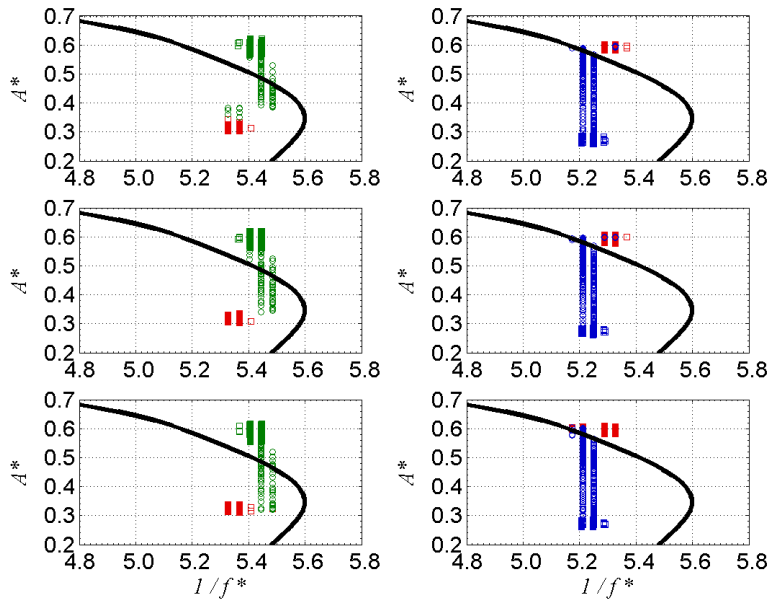


Figure 6.14: Frequency-amplitude mapping of TB01(ID) through the discontinuous region for increasing (left) and decreasing (right) tunnel velocities; blue data: $U_R = 0.816$, red data: $U_R = 0.834$, and green data: $U_R = 0.852$; \square : steady-state, \circ : transient. Also shown is the WR-plane 2S/2P dividing curve.

cycles of the transient nondimensional frequency response need to contain a velocity term that is time dependent. Another important consideration is the effect that the transient behavior of the tunnel itself has on the system response. However, since the transient time of the tunnel, about ten system oscillation cycles, was an order of magnitude smaller than the transient time of the system itself, we feel that the effects due to the transient behavior of the tunnel have been minimized. But, there still could be minor effects from low frequencies embedded in the tunnel test section that could persist for hundreds of cycles.

The same test approach was used for TB02(ID) to observe the transient system response. All four increasing tests of TB02 jumped from an initial branch state to an upper branch state when the reduced velocity was increased from 0.678 to 0.702. However, there was a major difference between the jump downward tests. As can be seen in Figure 6.15, this downward jump had more variability associated with it. Sometimes it occurred when the reduced velocity was decreased from 0.678 to 0.654, however, other times it occurred when the reduced velocity was decreased even further to 0.630. All eight tests, four upward and four downward jumping, can be seen in Figure 6.15

Similar to TB01(ID), there were also dramatic differences between the upward and downward jumps of TB02(ID). The jump upward for this system occurred over about 20 to 40 cycles. The variation in the number of cycles appears to be caused by the system sometimes pausing when it reaches $A^* \approx 0.40$. These pauses can be seen in test 1 (top) and 4 (bottom) while tests 2 (middle top) and 3 (middle bottom) did not show this pause. The downward jumping tests exhibited extremely interesting behavior. When the reduced velocity is changed from $U_R = 0.678$ to $U_R = 0.654$ the system undergoes a quick slight drop in amplitude. However, instead of continuing to decrease down to an amplitude value that corresponds to an initial branch state, the system remains in a marginally stable upper branch state. The number of cycles the system stays in this state varies, in test 2 it existed for roughly 20 cycles; in test 1 it existed for almost 125 cycles, while in test 4 it existed for almost 200 cycles. Also, in tests 1 and 2 the system finally underwent the downward jump. But in tests 3 and 4, the tunnel velocity had to be reduced again, to a value of $U_R = 0.630$, before the system made the downward jump into an initial branch state. In a similar manner to the upward jumps, once the downward jump began, it took between 40 to 60 cycles to complete, with there appearing to be pause that occurred again around $A^* \approx 0.40$.

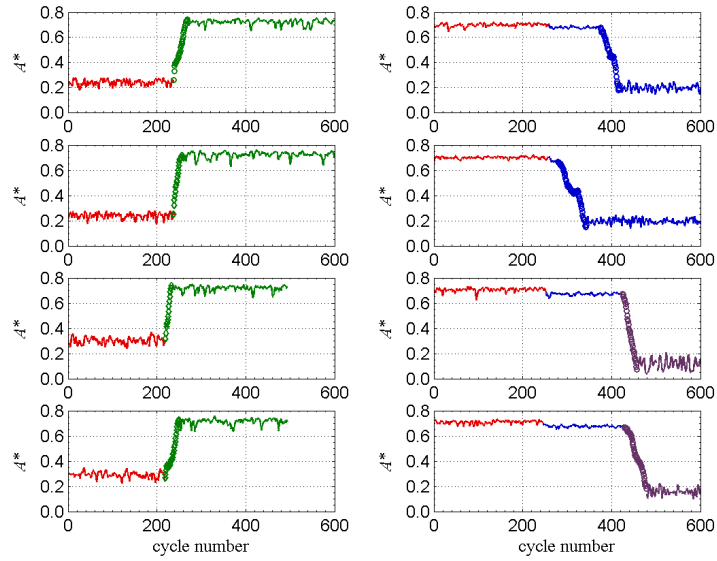


Figure 6.15: Time traces of TB02(ID) amplitudes through the discontinuous region for increasing (left) and decreasing (right) tunnel velocities; purple data: $U_R = 0.630$, blue data: $U_R = 0.654$, red data: $U_R = 0.678$, and green data: $U_R = 0.702$; $-$: steady-state, \circ : transient.

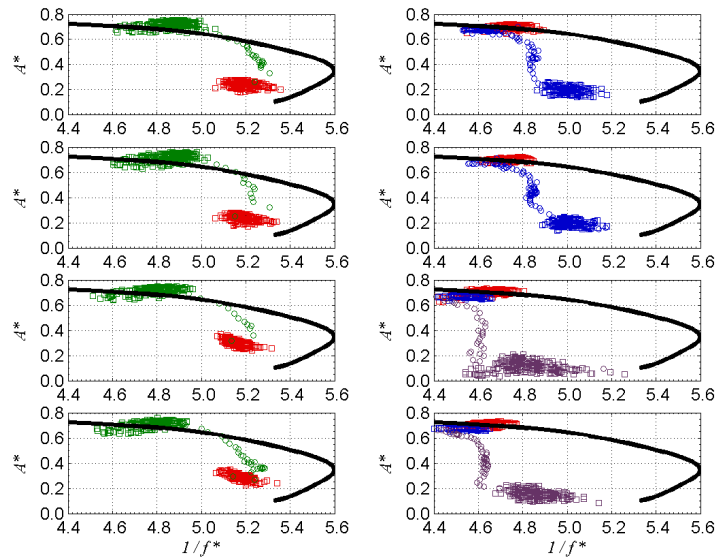


Figure 6.16: Frequency-amplitude mapping of TB02(ID) through the discontinuous region for increasing (left) and decreasing (right) tunnel velocities; purple data: $U_R = 0.630$, blue data: $U_R = 0.654$, red data: $U_R = 0.678$, and green data: $U_R = 0.702$; \square : steady-state, \circ : transient. Also shown is the WR-plane 2S/2P dividing curve.

We again examine the frequency-amplitude response of this system in Figure 6.16 along with the WR-plane 2S/2P dividing curve superimposed. For systems with configurations similar to TB02(ID) there is a substantial change in the frequency response between initial and upper branches. (See Figure 4.33 for the frequency response profile for such a system.) Examining the upward jumping cases first, the slight increase in reduced velocity causes the system to appear to initially move to an operating location roughly centered around $(1/f^*, A^*) = (5.3, 0.4)$, which we estimate as the operating location of the system if it were to stay in the initial branch portion of the response profile. By this we mean that, if you extrapolated the initial branch curve to higher reduced velocities, this point would be on that curve. This might be a possible explanation for why the system pauses there on the upward jump. However, this is an unstable operating point so the system cannot stay there indefinitely and eventually increases in amplitude and decreases in $1/f^*$ until the upper branch operating location is reached. This point lies near, but definitely on the 2P side of, the 2S/2P dividing curve.

The process of the downward jump begins much the same way. This time, the slight decrease in reduced velocity causes the system to appear to initially move to an operating location centered around $(1/f^*, A^*) = (4.6, 0.65)$, which we estimate is the likely operating location of the upper branch corresponding to this reduced velocity value. This operating location appears to be marginally stable and the system can reside there for a very large number of cycles. However, a large enough perturbation would cause it to go to the initial branch state. In runs 1 and 2 this perturbation was internal, in run 3 and 4 this perturbation was a further slight decrease in reduced velocity. It is interesting to note that again the system seems to pause around $A^* \approx 0.40$ although the frequency-amplitude combination appears to not be located near any stable regions.

For TB02(ID), the system oscillation period was around three seconds. This meant that the tunnel velocity's main transient response was finished after only one or two oscillation cycles. Therefore, only the first two cycles of the transient nondimensional frequency response contained a velocity term that was time dependent. Furthermore, because, just like TB01(ID), where the number of oscillation cycles during the tunnel velocity transient is very small compared to the number of oscillation cycles involving the complete system transient response, we feel that the effects of the transient behavior of the tunnel itself on the system response has again been minimized.

6.7 Damping-Induced Transients

An increase in damping causes the system to jump from the initial to the upper branch at a higher reduced velocity, as discussed in Section 6.3. This allowed the transient behavior between these two branches, that we induced using velocity changes in Section 6.6, to be induced using damping changes. Because these damping-induced transients involve a constant tunnel velocity, we do not have to worry about the effects that the transient response of the tunnel has on the system transient response. We used system configurations TB01 and TB02 to explore the damping-induced jump discontinuity region between the initial and upper branches. The location of the jump discontinuity for each system configuration can again be seen in Figure 6.11 for TB01 and Figure 6.12 for TB02 and is designated by the vertical double arrowed lines.

Our damping-induced transient tests were run by getting the system into a steady-state behavior at the appropriate reduced velocity value for either the low damping (LD) or high damping (HD) configuration. A large number of cycles (between 300 to 500) were recorded at this steady-state condition, then the damping was switched to the opposite configuration (LD or HD) until the jump upward or downward was observed. After the transient had occurred, a large number of cycles were again recorded to locate the post jump steady-state condition. Because these tests involved manipulating the damping value of each system, TB01 and TB02 each had two *imposed* damping values. The specific damping values used can be seen in Table 6.2. It should be noted that our two LD configurations had a slightly higher damping value than their corresponding ID configurations did in the velocity-induced transient section. This was because when the HD configuration was switched to a LD configuration, a weak residual magnetic field remained in the VMEC damping system, and caused a slightly increased damping value.

The reduced velocity value that was maintained throughout the test was chosen as one that corresponded to the middle of the upper branch for the LD configuration and not too near the maximum amplitude point of the HD configuration so it would still be in an initial branch state. For TB01, this corresponded to a reduced velocity of $U_R = 0.852$, and for TB02, to a reduced velocity of $U_R = 0.702$.

For all three tests of TB01, the system jumped upward from an initial branch state to an upper branch state when the damping was changed from a high damped to a low

damped state. It also jumped downward from an upper branch to an initial branch state when the damping was changed from a low damped to a high damped state for all three tests. Amplitude data for all six tests, three upward and three downward jumps, can be seen in Figure 6.17.

As the results show, even though the reduced velocity, $U_R = 0.834$, was held fixed, we were still able to induce transients by changing the structural system parameters, in this case, damping. As with the velocity-induced transient tests, we noticed differences in the behavior between upward and downward jumps. The jump upward occurred over about 50 to 100 cycles and the amplitude increase per cycle was fairly consistent. The downward jump occurs much quicker, it took less than half the number of cycles to reach the initial branch. And although the amplitude decrease per cycle was larger, its value appears roughly consistent, as in the upward jumping cases. There is one other thing of interest to note. Once the amplitude decreased below $A^* \approx 0.30$, further decreases in amplitude, down to the steady-state value of $A^* \approx 0.25$, occurred at a much slower rate.

The frequency-amplitude response of TB01 can be seen in Figure 6.18 along with the WR-plane 2S/2P dividing curve superimposed. From the velocity-induced transient results, we do not expect a large frequency change when TB01 jumps between initial and upper branches. However, for our damping-induced transient tests, the steady-state frequency of the system in the LD and HD configurations is the same. This can be seen in Figure 6.18, noting the system oscillating at $1/f^* \approx 5.4$ at the beginnings at ends of the tests. Also note however that the frequency does slightly change during the transient response. The oscillation frequency of the system slightly *decreases*, causing $1/f^* \approx 5.5$, for both upward and downward jumping tests. Since U and D are constants during these tests, the changes in $1/f^*$ are due solely to changes in the oscillation frequency.

We also conducted damping-induced transient tests on TB02. See Figure 6.19 for the specific amplitude responses. All three tests of TB02 jumped downward from an upper branch state to an initial branch state when the system damping went from the LD to the HD configuration. However, the upward jump was sometimes difficult to achieve through a relaxing of the damping. As can be seen in Figure 6.19, for tests 1 and 2 this upward jump had more variability associated with it. In fact, for test 1, the transient run ended before the upward jump was observed. The upper branch response (green data) shown for this test is the expected response using the results from test 2. In order to test the width

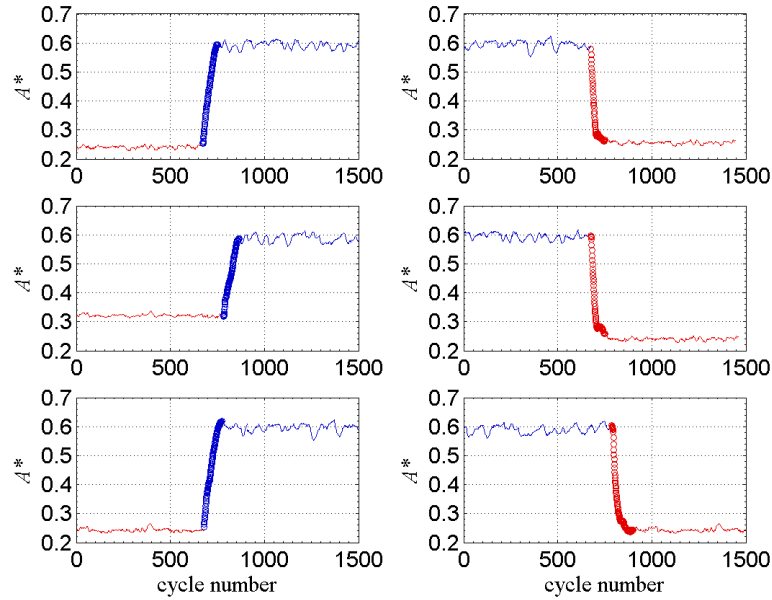


Figure 6.17: Time traces of TB01 amplitudes through the discontinuous region involving damping decreases (left) and increases (right) at $U_R = 0.852$; blue data: low damping (LD) state, red data: high damping (HD) state; $-$: steady-state, \circ : transient.

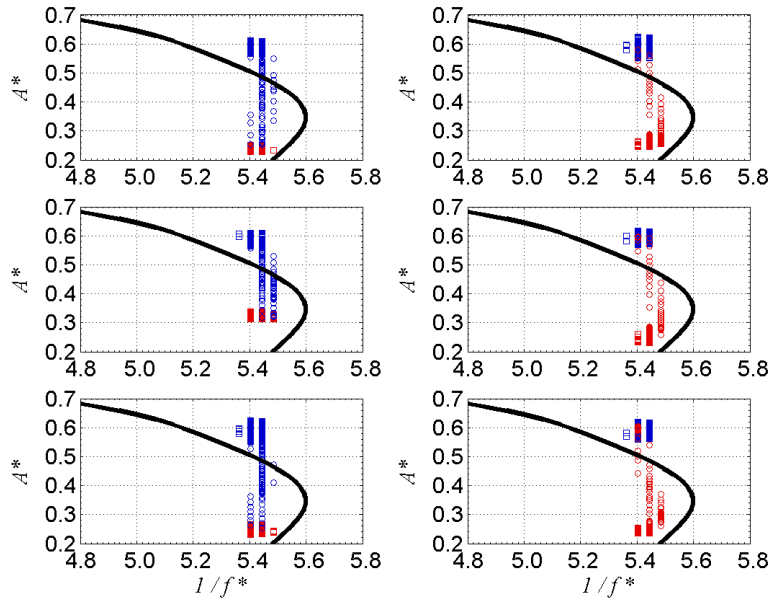


Figure 6.18: Frequency-amplitude mapping of TB01 through the discontinuous region involving damping decreases (left) and increases (right) at $U_R = 0.852$; blue data: low damping (LD) state, red data: high damping (HD) state; \square : steady-state, \circ : transient. Also shown is the WR-plane 2S/2P dividing curve.

of this variability, a third test was undertaken at a higher reduced velocity, $U_R = 0.736$, whereas test 1 and 2 were undertaken at a reduced velocity of $U_R = 0.702$. This slightly higher reduced velocity appears to eliminate the variability and causes the upward jump to occur immediately.

As has been the case for all the transient tests, there were dramatic differences between the upward and downward jumps of TB02. The downward jump was extremely abrupt, it occurred over less than ten cycles once the damping was changed from the LD to the HD configuration. The third test, at the higher reduced velocity, shows no change in the abruptness of the amplitude decrease. The upward jumps exhibit the stability phenomenon again that was first observed with downward jumping velocity-induced transient systems. When the damping is changed from a HD to a LD configuration, the system undergoes a quick increase in amplitude from $A^* \approx 0.225$ to $A^* \approx 0.35$ in about ten cycles. However, instead of continuing to increase to an amplitude value that corresponds to an upper branch state, the system remains in a marginally stable initial branch state. The time the system stays in this state varies, in test 1 it remained in it for around 125 cycles until the test was stopped, while in test 2 it remained in it for almost 100 cycles. In test 2, the system eventually completed the full upward jump. Test 1, however, was stopped after 350 total cycles so it is unknown when, or if, the system would have finished its upward jump. It is surprising that this marginally stable state exists. For if the cylinder is started from rest in the LD configuration, the system amplitude will rapidly increase to its upper branch state in a repeatable fashion. In test 3, the reduced velocity value was larger, and when the damping state went from a HD to a LD configuration, the system immediately started its upward jump and continued until the full jump had been completed. This jump was not nearly as abrupt as all three downward cases, but occurred within about twice the number of cycles, roughly 20.

We once again examined the frequency-amplitude response of this system in Figure 6.20 along with the WR-plane 2S/2P dividing curve superimposed. We observed that for a velocity-induced transient, TB02 underwent a substantial change in the frequency response during the jump between initial and upper branches. In our damping-induced transients, we again noticed a substantial change in the frequency response even though the tunnel velocity has not changed. Examining the downward jumping cases first, the increase in damping, to the HD configuration, causes the system to immediately move toward the initial branch

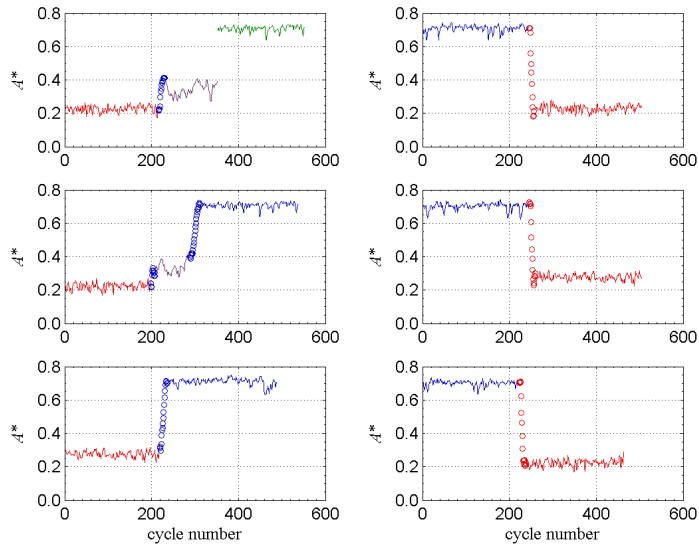


Figure 6.19: Time traces of TB02 amplitudes through the discontinuous region involving damping decreases (left) and increases (right) at either $U_R = 0.702$ (top and middle plots) or $U_R = 0.736$ (bottom plots); blue data: low damping (LD) state, purple data: “marginally stable” low damping state, green data: expected low damping state, red data: high damping (HD) state; \square : steady state, \circ : transient.

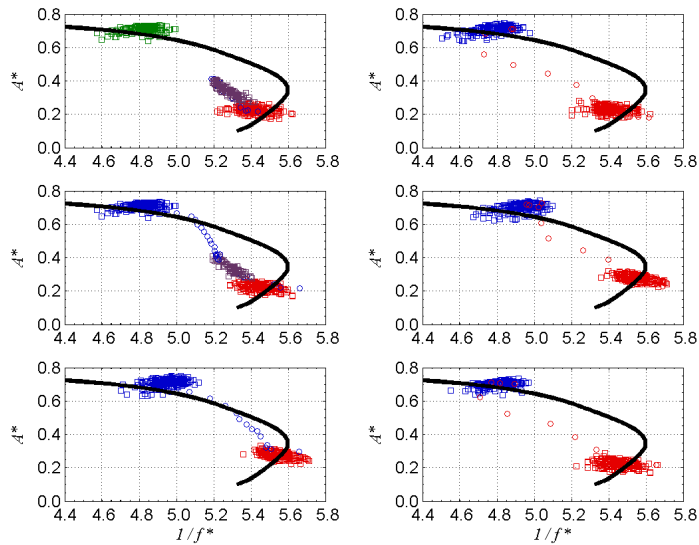


Figure 6.20: Frequency-amplitude mapping of TB02 through the discontinuous region involving damping decreases (left) and increases (right) at $U_R = 0.702$ or $U_R = 0.736$; blue data: low damping (LD) state, purple data: “marginally stable” low damping state, green data: expected low damping state, red data: high damping (HD) state; \square : steady-state, \circ : transient. Also shown is the WR-plane 2S/2P dividing curve.

operating location. The system response takes a nearly straight path between the states. It is interesting to note, although possibly just a coincidence, that the path is roughly parallel to the WR-plane 2S/2P dividing curve. As discussed above, the upward jumping process is much more complicated. This time, the decrease of damping, to a LD configuration, causes the system to move to a new neighboring operating location and into a marginally stable state, since it moves around this location for a large number of cycles. In fact, test 1 ended before the system completed its upward jump. But for test 2, a large enough perturbation caused the system to finish its upward jump and move into an upper branch state. Unlike previous, marginally stable operating areas, which sat along the projected path of the current motion, this operating location is not located near any stable operating areas. For test 3, where the reduced velocity value was slightly larger, we see that the system quickly heads to its upper branch state when the damping is decreased. In this case, the trajectory is slightly higher than the path of the lower reduced velocity value tests and crosses over the 2S/2P dividing curve before reaching its steady state value.

6.8 Comparison of Velocity- and Damping-Induced Transients

By looking at all the TB tests as a whole, we can make some general conclusions about velocity- and damping-induced transients. To pull down the system from a large- to a small-amplitude state, increasing the system damping is much more efficient than decreasing the reduced velocity value. Increasing the damping pulled the system down to a lower amplitude in less than half the number of cycles, and in the case of TB02, it was less than a quarter of the number. It is even more efficient when one considers that a marginally stable region exists when decreasing the amplitude by decreasing tunnel velocity, and the system could reside at that marginally stable region for a large number of cycles. On the other hand, when changing from a small- to large-amplitude state, there is not much difference between decreasing the damping or increasing the tunnel velocity. This holds as long as the system, such as TB02, moves through the other marginally stable region. If the system remains in this region, then increasing reduced velocity is more efficient.

The appearance of marginally stable regions of oscillation are quite interesting and there are some conclusions that can be drawn. First, no marginally stable behavior was observed for TB01, it was only observed for TB02. Whether this means that it is a Reynolds number

or m^* effect, or both, is impossible to say since we do not have enough different configurations. Second, a marginally stable region existed during the downward jump caused by decreasing the reduced velocity and a different such region existed for an upward jump caused by decreasing the damping. This means that one of the marginally stable regions is a large-amplitude, upper branch state and the other is a small-amplitude, initial branch state. The large-amplitude, upper branch marginally stable region could perhaps have been anticipated by looking at the work of Carberry et al. (2001). In their forced-vibration experiments, they noted a self-excited change from a low-frequency, 2P wake, to a high-frequency, 2S wake. This suggests that both wakes can exist for a given operating condition with the 2S wake structure ultimately being the preferred state. However, there is no available information to suggest that a small-amplitude, initial branch state could be marginally stable. In Carberry et al. (2001), they mentioned that they never observed the reverse, a self-excited change from a 2S to a 2P wake. Also, as mentioned before, when TB02 was released from rest in the LD configuration, the system always quickly moved into a large-amplitude, upper branch state. Therefore, seeing a marginally stable region in the initial branch when damping is reduced is quite surprising. Finally, both marginally stable regions can easily be eliminated, by moving to a slightly lower reduced velocity value for the large-amplitude, upper branch region (tests 3 and 4 in Figure 6.17) or a slightly higher reduced velocity value for the small-amplitude, initial branch region (test 3 in Figure 6.19).

Chapter 7

Summary and Future Considerations

In this chapter we summarize our major results and make recommendations for future work. In Section 7.1 we discuss the basic results that includes the advantages of the effective stiffness formulation over the traditional formulation, time-varying motion, general wake structures, system singularities, and the similar effects that damping and Reynolds number have on the response profiles. We summarize all of our findings that relate to the system maximum amplitude in Section 7.2. These include the strict definitions of maximum and limiting amplitudes as well as a creation of a generalized Griffin plot and a limiting amplitudes plot, which shows the importance of Reynolds number in vortex-induced vibrations (VIV). In Section 7.3 we discuss our results that relate to discontinuities in the amplitude response profiles. These arise from two different situations. The first are regions of hysteresis, of which we examine two such regions. And second, transient behavior induced by either a velocity or damping change. Finally, in Section 7.4 we suggest future experiments and simulations that could help in further understanding VIV behavior.

7.1 Summary of Basic Results

Two different system configurations were used to compare and contrast the amplitude and frequency response profiles in the traditional and effective stiffness formulations. The configurations were chosen so that the two distinct types of responses, classified by Khalak and Williamson (1997b), were observed, one type by each configuration. These were the small-amplitude, two-branch response at high mass-damping, for us the large mass, low Reynolds

number system, and the large-amplitude, three-branch response at low mass-damping, for us the small mass, high Reynolds number system. The former shows the classic “lock-in” behavior while the former does not. In fact the small mass, high Reynolds number system does not lock onto any frequency. Instead, the frequency appears to steadily increase as reduced velocity is increased.

There are numerous advantages to using the effective stiffness formulation over the traditional formulation. One is that there is a collapse of the amplitude response profile. Because of this, the response behavior begins and ends at approximately the same effective stiffness values, meaning universal critical values exist. The most important universal value is $k_{\text{eff}}^*|_{A_{\text{Max}}^*}$, the effective stiffness value at which the maximum amplitude occurs. We show this by plotting numerous system configurations together and noting that A_{Max}^* occurs at $k_{\text{eff}}^*|_{A_{\text{Max}}^*} \approx 2.5$ for all of them. A second advantage is that the effective stiffness expands the area of most interest, the large-amplitude, upper branch region, and compresses the region of less interest, the slowly changing lower branch. Third, the frequency response profile does not occur over as wide a range of values. This means that changing the scaling of the frequency axis on which you view the results will not affect how close oscillation frequencies appears to the system natural frequency. A fourth advantage is that the effective stiffness formulation can handle limiting structural parameters while the traditional formulation cannot since it uses these parameters in its nondimensionalization. A final advantage is that when using the effective stiffness parameter, the results are mass independent.

We showed that the motion of VIV is not a steady-state motion. Instead, the amplitude and frequency are changing cycle-by-cycle and we discussed some of the difficulties that this causes. However, sometimes these variations are small and a single time-averaged value is appropriate. We showed that this was the case for a high m^* , low Reynolds number system where the amplitude fluctuations around the mean were less than 2 percent. However, for a low m^* , high Reynolds number system a time-averaged value was not nearly as appropriate and can be misleading since we showed that the amplitude response can vary by 10 percent around the mean at certain locations.

We also showed how the wake structure differs at various locations in the response profile. For the initial branch, we found a 2S-type wake structure. In the large-amplitude, upper branch response portion we initially found a hybrid structure that showed both 2S and 2P characteristics. As we increased the reduced velocity and moved through the upper

branch, we noticed that the wake structure become a 2P one, however, the second vortex in each pair was extremely weak. It was not until we reached the lower branch that the second vortex had any substantial strength, and, not until the middle of that branch, that the second vortex was nearly equal. We noted that care must be taken when using cycle averaged DPIV images since the wake structure can vary dramatically between cycles. As an example, we showed a situation where a given cycle had a classic 2P wake structure, but within a few cycles, the structure had changed to a wake that resembled more of a 2S structure.

We explored the interesting behavior that results from limiting structural parameters using the effective stiffness formulation. For a system with zero elasticity (springless), the response is restricted to only negative effective stiffness values, $k_{\text{eff}}^* < 0$. Furthermore, a small nondimensional mass, smaller than a certain limiting value, is necessary in order for the system to experience oscillations. We calculated this limiting value to be $m^* \approx 0.76$. However, such a system would never be able to obtain A_{Max}^* since $k_{\text{eff}}^*|_{A_{\text{Max}}^*} > 0$. For a system with zero mass, the response profile is restricted to the other portion of the response region, that which effective stiffness is positive, $k_{\text{eff}}^* > 0$. Although not possible experimentally, this result was shown computationally by Shiels et al. (2001). Unlike the springless case, in the massless case, one can control the value of the effective stiffness directly. Therefore, the amplitude response can be dictated through appropriate choices of the elasticity and tunnel velocity. This is important since, for a given damping and Reynolds number, the amplitude is only controlled by the value of the effective stiffness. Finally, a massless and springless system is restricted to only one response point, $k_{\text{eff}}^* = 0$, which corresponds to a system response regardless of tunnel velocity.

We showed how a given system transitions between the two classic response classifications as damping is varied. We observed that a mass-damping parameter was insufficient to define the classification. This is because Reynolds number also has an important effect. We also found that low damping and high Reynolds number were necessary for the large-amplitude, upper branch response to exist. We also studied the frequency response profile and noted three changes that occur in the upper branch as damping is increased. Furthermore, we pointed out that damping and Reynolds number have similar effects on the response profiles. Decreasing the damping has roughly the same effects on the response that increasing the Reynolds number does. As an example, we showed how the upper branch can

be eliminated by either increasing damping or decreasing the Reynolds number. We further made this point by showing three different systems that each had the right damping and Reynolds number combination such that they all had roughly the same amplitude response profile. We also looked at the various effects that Reynolds number has on the frequency response profile as well.

Finally, we showed the advantages of using the effective stiffness parameter in predicting the flow velocity that causes the system maximum amplitude. If one simply matches the oscillation frequency with the natural and predicted Strouhal frequencies then the predicted flow velocity can be off by 10 percent. However, this error is greatly reduced by using the effective stiffness and we showed that the error in our predicted tunnel velocity was less than 4 percent.

7.2 Summary of Maximum and Limiting Amplitudes

We showed various relationships that predicted the maximum amplitude and emphasized how it depended on a mass-damping parameter. However, the most insight came from experimental results. In order to guide our experiments, we showed how, using the effective stiffness formulation, it was possible to reduce your dependence space down to only three parameters, effective stiffness, damping, and Reynolds number. By spanning all k_{eff}^* values of interest, we found A_{Max}^* and showed how maximum amplitudes are only a function of damping and Reynolds number. By taking the limit as damping goes to zero, we concluded that limiting amplitudes are only a function of Reynolds number.

It was demonstrated that maximum amplitudes, A_{Max}^* , depend on damping and Reynolds number and that instead of fitting a universal curve to all VIV data in the Griffin plot, our data segregate onto constant-Reynolds-number curves. Also consistent with the effective stiffness formulation, we showed that there is no dependence on the mass parameter, m^* .

In order to cover a large range of Reynolds numbers, we performed tests at low damping, $b^* < 0.50$, for Reynolds numbers between $200 \lesssim \text{Re} |_{A_{\text{Max}}^*} \lesssim 5050$. These results were extrapolated to zero damping, resulting in limiting amplitudes, A_{Lim}^* . This showed the dependence on, and importance of, Reynolds number for VIV. We also showed that our results are consistent with higher Reynolds number experiments by comparing them to other reported experimental results at small, but finite, damping. However, our results, when

compared to similar low Reynolds number computations, raise some interesting questions.

We performed flow visualization to determine the dimensionality and structure of the wake at the maximum amplitude point. We observed for $Re \approx 200$ flow, the wake was nearly two dimensional, but by the time the Reynolds number was raised to $Re \approx 525$, the wake was highly three dimensional. We also noticed that below $Re \approx 1000$ the wake at the maximum amplitude was a 2S structure. This happens even though an upper branch existed and according to the Williamson-Roshko plane (WR-plane), the wake structure should be 2P. For $Re \gtrsim 2600$ we observe the expected 2P wake structure at the maximum amplitude.

Finally, we recognized the difficulties in extending the generalized Griffin plot to high damping values, $b^* > 1.75$. The main difficulty is that the maximum amplitude point, $k_{\text{eff}}^*|_{A_{\text{Max}}^*}$ begins to move toward a lower value as the system begins to respond more like a traditional linear forced mass-damper-spring system.

7.3 Summary of Discontinuities

We discussed how the nonlinear features of VIV can be missed by representing the response behavior using time-averaged values. These include discontinuities caused by regions of hysteresis and transient behavior.

We examined the disappearance of the large-amplitude, upper branch portion of the response profile as damping and Reynolds number change. This large-amplitude region occurs in a well-known hysteretic region. Therefore, its disappearance depends on which direction it is approached from. We find that for increasing tunnel velocities, the system jumps upward from the initial to the upper branch to a point well inside the WR-plane 2S/2P dividing curve. As damping is increased, this upward jump is delayed, causing a decrease in the size of the upper branch. On the other hand, we find that for decreasing tunnel velocities, the jump downward from the upper to the initial branch is controlled by the WR-plane 2S/2P dividing curve. As damping is increased, this downward jump occurs earlier, also causing a decrease in the size of the upper branch.

We also examined the transition between the upper and lower branches. This region was noted to be an intermittent switching region by Khalak and Williamson (1997a). They observed that their system would switch back and forth between the amplitude, frequency, and phase that was characteristic of each branch. Instead of seeing any switching, we

observe a system that takes on a wide range of amplitudes and frequencies and appears to be randomly moving through all the permissible values of each.

In addition to the well-known hysteresis jump between the initial and upper branches of the three-branch response, we find another hysteresis in the transition from the lower branch to the desynchronized region. We described the effects of damping and Reynolds number on this hysteresis region. This hysteresis exists for low Reynolds numbers and is not observed in $\text{Re}|_{A_{\text{Max}}^*}$ experiments greater than around $\mathcal{O}(10^3)$. Furthermore, as damping is increased, the size of the hysteresis decreases.

We next examined purely transient behavior as the system underwent an amplitude jump discontinuity between the initial and the upper branch. These transients were induced by changing the flow velocity or damping. For transients induced by changing the flow velocity, we noticed that the system always moved quickly from the low-amplitude state to the high-amplitude state. On the other hand, our high nondimensional mass, low Reynolds number system did not jump downward from a large- to a small-amplitude state as quickly. And our low nondimensional mass, high Reynolds number system would sometimes remain in a marginally stable large-amplitude state and only after the tunnel velocity was reduced further would it move to the low-amplitude state.

For transients induced by changing the system damping, we noticed some interesting trends. This time, the system would always go from a large-amplitude to a small-amplitude response by increasing the damping. However, jumps upward, induced by decreasing the damping on the system, were much slower to occur. And just like the velocity-induced transient cases, the amount of delay depended on the system. Our large nondimensional mass, low Reynolds number system always went to the large-amplitude response but at a much slower rate than it jumped downward. On the other hand, our small nondimensional mass, high Reynolds number system sometimes got stuck in another marginally stable response for a large number of cycles before finally moving to a large-amplitude response.

7.4 Future Considerations

A fundamental question that remains in VIV is to what extent the canonical situation of a rigid, elastically-mounted, circular cylinder with only one-degree-of-freedom motion can be generalized to more practical real world situations. There have been many studies

that used more realistic system arrangements. Some of these systems not only had two-degree-of-freedom motion, but some even used flexible circular cylinders, or cables. Other systems explored not only elastically-mounted but cantilevered, pinned, pivoted, and even tethered cylinders. Due to this work, there is a much better understanding of the conditions necessary for a realistic system to behave in a similar manner to a canonical system, such as ours. However, another important aspect of the system has received much less attention; the shape of the bluff body. For the most part, all investigations of VIV has involved the circular cylinder. This is with good reason, since an enormous amount of previous work on stationary bluff bodies involved circular cylinders. While a few previous studies have used different cross-section shapes, such as D-shaped (Feng, 1968) and dodecagonal (Scruton, 1965), there is still a number of unique shapes to investigate. The shapes of most interest would be ones that have *fixed* separation points, such a D-shaped and triangular-shaped cross sections. This thesis pointed out many Reynolds number effects experienced by a circular cylinder. For a circular cylinder, the location of its separation points are not fixed and will move depending on the Reynolds number of the flow. How would these Reynolds number effects be altered, if at all, for a geometry that had fixed separation points.

Since Reynolds number and m^* are both dependent on the cylinder diameter, in general, the higher the Reynolds number, the lower the m^* , in VIV experiments. This has made it very difficult to sort out what are Reynolds number and what are m^* effects in certain situations. In the effective stiffness formulation, there are no individual m^* effects when using time-averaged amplitude and frequency values obtained from roughly steady-state behavior. However, when dealing with the instantaneous cycle-by-cycle, time-varying motion, m^* effects *could* be present in the formulation. For example, the cycle-by-cycle amplitude values of high Reynolds number, small m^* systems have a larger scatter around their time-averaged mean values than do low Reynolds number, large m^* systems. Therefore, it would be very helpful to have high Reynolds number, large m^* tests and low Reynolds number, small m^* tests. These could then be compared to the large amount of previous and current work at high Reynolds number, small m^* and low Reynolds number, large m^* to determine the relative effects of Reynolds number and m^* .

In regards to limiting amplitudes, it would be interesting to extend experimental work into both extreme ends of the Reynolds number range. It would be extremely helpful to perform experiments at $\text{Re}|_{A^*_{\text{Max}}} < 200$ with reasonably low damping. If a sufficiently small

damping value cannot be obtained, then numerous tests at various damping values should be undertaken such that a reasonable extrapolation to zero damping can be accomplished. This would allow one to determine if the amplitude eventually increases to around the $A^* \approx 0.60$ value that many simulations predict at $\text{Re} = 100$ or the $A^* \approx 0.40$ value that our experimental results predict when extrapolate down to that Reynolds number. It would also be insightful to perform tests at Reynolds numbers that are an order of magnitude higher than what have been previously done. All results for $\text{Re}|_{A^*_{\text{Max}}} < \mathcal{O}(10^5)$ appear to show the limiting amplitudes increasing with Reynolds number. It would seem that the amplitudes should eventually saturate. For stationary cylinders, the drag crisis, and then the roughly constant drag coefficient, occurs around $\text{Re} \approx \mathcal{O}(10^6)$. VIV studies must be performed in this range to see if unexpected behavior occurs, as well as amplitude saturation.

Finally, due to the time-varying visual features that wake structures can take, especially a 2P one, it would be advantageous to attempt to describe the state on more quantitative qualities of the wake instead of visual ones. For instance, the amount of opposite-signed vorticity that crosses the rear stagnation point of the cylinder could be used for the 2P wake structure. This would allow for there to be less interpretation of what type of wake structure is present.

Appendix A: Detailed Overview of the Data Reduction Process and Filtering Scheme

The measured signal is recorded as a data file that contains a vector of voltages output from the LVDT at every sample time. This vector is analyzed by sending it through a series of MatLab functions.

The first function takes the recorded data of voltages, V , and converts it into physical position, y , using the conversion factor

$$y(\text{mm}) = 5.0 V(\text{volts}) . \quad (\text{A.1})$$

The mean value of the vector is then subtracted away so that the converted data is centered about zero. The time vector, corresponding to each displacement point, is calculated by making the first data point occur at time zero seconds and then the corresponding time for each point after that is determined using the sampling rate. Since the sampling rate was 250 samples per second, the time separation for each point was $1/250 = 0.004$ seconds. Finally, both position and time are nondimensionalized according to the effective stiffness formulation although both nondimensional and dimensional quantities are carried throughout the code.

The second function performs an optimal Wiener filter on the data. Since we do this filtering in Fourier space, we first make the data periodic by finding the first and last zero crossing, going in the same direction, and remove the points before and after them. Then the data is converted into Fourier space using MatLab's fast Fourier transform (FFT). In order to use the Wiener filter, we need an estimate of the noise in the measured signal. Luckily, even a rough estimate of the noise will produce sufficient filtering. To accomplish

the noise estimation, we determine the power of the Fourier coefficients for a pure sine wave. For

$$A_o \sin(2\pi ft) , 0 < t < T \quad (\text{A.2})$$

the power of the Fourier coefficients are given by

$$|c_k|^2 = \left(\frac{A_o \sin^2(\pi fT)}{\pi(k+fT)(k-fT)} \right)^2 (k^2 \cos^2(\pi fT) + (fT)^2 \sin^2(\pi fT)) \quad (\text{A.3})$$

where A_o , f , and T need to be assigned values. We determine f , the oscillation frequency, by looking at the power spectrum of our recorded data and finding the frequency corresponding to the maximum power. We then perform a least-squares fit on the Fourier power coefficients of the pure sine wave to the power spectrum of the recorded data, using A_o and T as the fitting parameters. While it is true that we could have also determined the value of T from our recorded data, in order to make the Fourier power coefficients of the pure sine wave better match the recorded data power spectrum, we do not do this. For example, in the unfortunate situation that the product fT , determined from our recorded data, was *exactly* an integer, our pure sine wave Fourier coefficients would be zero for all values of k except two, $k = \pm fT$. This resultant set of coefficients would be worthless in helping estimate the noise. Instead, we allow T to be a free fitting parameter with the one condition that T cannot take on a value that makes fT equal to an integer. By doing this, we force the power of the $k = 0$ pure sine wave Fourier coefficient into a nonzero value as well as make the power spectrum of the rest of the Fourier coefficients better match the shape of the recorded data power spectrum. When performing the least-squares fit, we only consider the Fourier coefficients corresponding to frequencies greater than f to minimize the error against. Furthermore, this minimized error is only based off considering the bottom edge of the high frequency portion of the recorded data. We iterate to the values of A_o and T that minimize the distance between the Fourier power coefficients of the pure sine wave and the bottom edge of the recorded data power spectrum, for high frequencies. A sample plot showing the results of “fitting” these coefficients to our recorded data is shown in Figure A.1.

By looking at the difference between the actual recorded data and the least-squares fitted coefficients, we can obtain a rough noise estimate. Once we have this noise estimate in Fourier space, constructing the filter is a straightforward task. The optimal Wiener filter

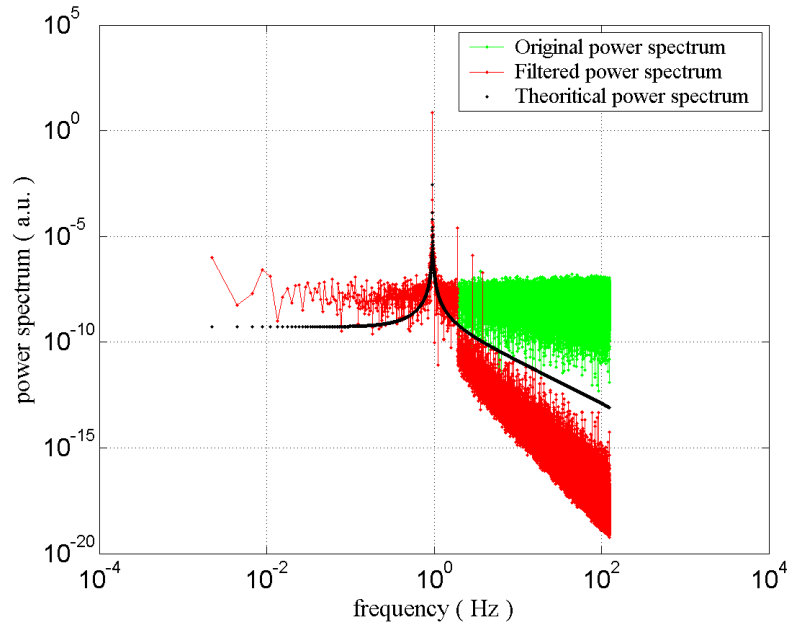


Figure A.1: Noisy measured signal data (green data) along with the “fitted” ideal power spectrum (black data) and the Wiener filtered results (red data). Note that for frequencies below about 1 Hz, the measured noisy signal and the filtered results coincide.

is given by

$$\Phi(f) = \frac{|C(f)|^2 - |N(f)|^2}{|C(f)|^2} \quad (\text{A.4})$$

where $\Phi(f)$ is the optimal filter, $C(f)$ is the recorded, noisy data, and $N(f)$ is the noise estimate, all of which are in Fourier space. Then we simply arrive at our filtered recorded data, in Fourier space, through the relationship $S(f) = C(f)\Phi(f)$ where $S(f)$ is the optimal filtered data. The filtered power spectrum $|S(f)|^2$ can be seen in Figure A.1 as the red data. It is important to note that when we arrive at our noise estimation, we do not consider power spectrum spikes that occur at harmonics in the Fourier space of the recorded data as noise. Instead, we allow them to be included in the filtered results. This is accomplished by assigning the harmonic frequencies a value of zero in our noise estimation. The harmonics for the case shown in Figure A.1 are the three decreasing magnitude spikes in the power spectrum. The filtered recorded data is then transformed back into time space using the inverse fast Fourier transfer (IFFT) and the results are past to the next function.

This next function locates the extrema points of the time series. This is accomplished by looking for a sign change in the slope between consecutive points. Since the points are

sampled at a constant interval, only the actual value of each point is necessary to determine the sign of the slope. By subtracting the values of the points on either side of our point of interest from the value of that point of interest and then multiplying these two differences, we can tell if our point of interest is a local extrema. If the multiplication produces a negative signed term, the point of interest is a local extrema. If the multiplication produces a positive signed term, the point of interest is not a local extrema and we move on to the next point in the data vector. A second test is done on the local extrema points that passed the first criteria to eliminate any artificial extrema that results from residual high frequency noise. All the extrema are put in a bin with their corresponding time values. Then we move through this bin and look at the time difference between consecutive extrema. We know that the time difference between the extrema should be the same order of magnitude as the average oscillation period, $1/f$, determined previously. Therefore, if we see any time difference that is an order of magnitude less than this, we know that one of the two extrema involved in that time difference is an artificial extreme point. Of the two, the one that has a time difference closer to the oscillation period, when compared to the time value of the last known actual extreme point, is kept and the other is eliminated. After making sure that all the local extrema occur at the right time scale, we pass these extrema values on to the next function. Our optimal Wiener filter worked so well however, that our resultant filtered curve was sufficiently smooth so that we observed no artificial extrema. A typical result can be seen in Figure A.2. Note that even for displacements as small as 0.5 mm, which are about the minimum displacement we consider for cylinder movement, the Wiener filter produces a smooth curve. On the other hand, a simple high frequency truncation filter produces occasional artificial extrema, as seen in Figure A.2 for $t \approx 297$ or $t \approx 299$. Therefore, this extra step of checking the time difference between extrema turned out to be redundant.

The next function took the extrema data and turned it into cycle-by-cycle results. First, the function found the first and last positive extrema and threw away the negative extrema on the ends, if ones existed. This was done so that we would not be left with any half cycles at the end of the data and would always have a positive-negative-positive oriented cycle (although negative-positive-negative would have worked just as well). The amplitude of each cycle was calculated by averaging the value of the three consecutive extrema, P1, N1, and P2, with the negative one, N1, weighted twice. Then the function moved to the next

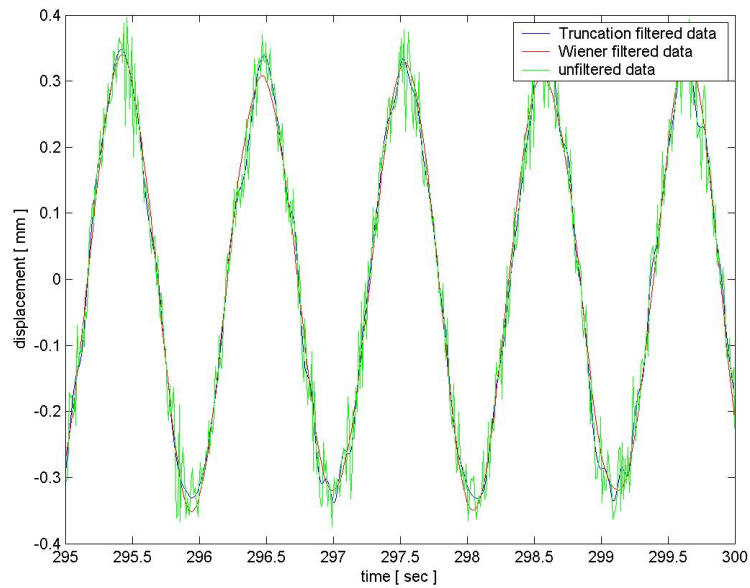


Figure A.2: Comparison of the optimal Wiener filter to a simple high frequency truncation filter. The measured noisy signal (green data) is shown along with the truncation filter results (blue data) and Wiener filter results (red data).

cycle, P2, N2, P3, and repeated the process. The frequency of the cycle was determined by looking at the time difference between successive positive points. For instance, the first cycle period involved the time difference between P1 and P2; the next cycle period involved P2 and P3. The frequency was simply the inverse of the time difference.

The last function determined the statistics of the cycle-by-cycle results. These included the minimum, maximum, mean, and standard deviation of the amplitude and frequency. The standard deviation was calculated using the built-in MatLab function STDEV. The effective stiffness parameter was also computed at this time using Equation (2.43).

Appendix B: Damping Theory and System Damping Determination for Free-Vibration Natural Decay

The governing equation for a mass-damper-spring system undergoing free vibration natural decay is

$$m\ddot{y} + b\dot{y} + ky = 0, \quad (\text{B.1})$$

where m , b , and k , are the system mass, damping, and elasticity respectively. The time eigenvalues of this equation are

$$\lambda = \lambda_A \pm \lambda_B = -\frac{b}{2m} \pm \sqrt{\left(\frac{b}{2m}\right)^2 - \left(\frac{k}{m}\right)}. \quad (\text{B.2})$$

For lightly damped systems, $b < 2\sqrt{mk}$, λ_B will be imaginary and the system will undergo oscillatory motion. For heavily damped systems, $b > 2\sqrt{mk}$, λ_B will be real and the behavior of the system will not be oscillatory. This “critical” value of damping, $b = 2\sqrt{mk}$ which causes λ_B to change from imaginary to real is termed the “critical damping” value.

For a lightly damped system governed by Equation (B.1) and released from initial position $y(0) = Y_o$ and zero initial velocity $\dot{y}(0) = 0$, the time decaying motion is given by

$$y(t) = Y_o \sqrt{1 + \left(\frac{b}{2m\omega_o}\right)^2} e^{-\frac{b}{2m}t} \cos(\omega_o t - \alpha), \quad (\text{B.3})$$

where ω_o is the damping altered natural frequency given by

$$\omega_o = \sqrt{\omega_N^2 - \left(\frac{b}{2m}\right)^2}, \quad (\text{B.4})$$

and α is the phase shift given by

$$\alpha = \tan^{-1} \left(\frac{b}{2m\omega_o} \right). \quad (\text{B.5})$$

The system damping, b , was determined in two different ways, depending on the number of cycles that the decaying system experienced. For a system that went through a large number of oscillations, the damping value was obtained by examining the decaying amplitudes. The time decaying amplitudes, $A(t)$, from Equation (B.3) are given by

$$A(t) = Y_o \sqrt{1 + \left(\frac{b}{2m\omega_o} \right)^2} e^{-\frac{b}{2m}t}. \quad (\text{B.6})$$

We can then use properties of logarithms to write the amplitudes as

$$\ln(A(t)) = \ln \left(Y_o \sqrt{1 + \left(\frac{b}{2m\omega_o} \right)^2} \right) - \frac{b}{2m}t. \quad (\text{B.7})$$

This shows that the logarithm of the decay amplitudes is a linear function of time

$$\underbrace{\ln(A(t))}_y = \underbrace{-\frac{b}{2m}}_{\eta} t + \underbrace{\ln \left(Y_o \sqrt{1 + \left(\frac{b}{2m\omega_o} \right)^2} \right)}_{y\text{-intercept}}, \quad (\text{B.8})$$

with the slope being related to the system damping, b . Therefore, we simply use a least-squares linear curve fit to the logarithm amplitudes to determine the slope η . This process can be seen in Figure B.1. The strongly linear nature of the actual data reaffirms the linear nature of our setup and points to the validity of this approach to determine the damping value.

This method to determine the slope, η , could not be used for systems that only went through a few oscillations before coming to rest. This was because such systems could only provide a few amplitude points with which to use in the curve fit. This limited number of points caused a large amount of error in the value of η . Instead, the full time trace of the decay was used to determine η . Going back to Equation (B.3), one can see that the decay

response can be represented by

$$y(t) = e^{\eta t} (\mathcal{A} \sin(\omega_o t) + \mathcal{B} \cos(\omega_o t)) , \quad (\text{B.9})$$

where we used two trigonometric functions instead of a single one with a phase angle. Representing the response with this functional form, we performed a least-squares fit on the full time series decay data with the fitting parameters being A , B , ω_o , and η . Due to the non-linear nature of the curve fitting function, in order to determine the four fitting parameters, a simple Newton iteration method for matrices was used. This method can be written as

$$x^{(n+1)} = x^{(n)} - \left[F'(x^{(n)}) \right]^{-1} F(x^{(n)}) , \quad (\text{B.10})$$

where n is the current iteration number and $(n + 1)$ is the next step. F is composed of the four functions that minimize the error expression with respect to each fitting parameter. A typical result of the Newton iteration method to determine the fitting parameters for our functional representation can be seen in Figure B.2. Fitting a curve to the entire time trace is a straightforward way to determine the value of η when a limited number of amplitude cycles exist.

Regardless of which of the two methods was used, once the parameter η is determined, the system damping b was given by

$$b = -2m\eta . \quad (\text{B.11})$$

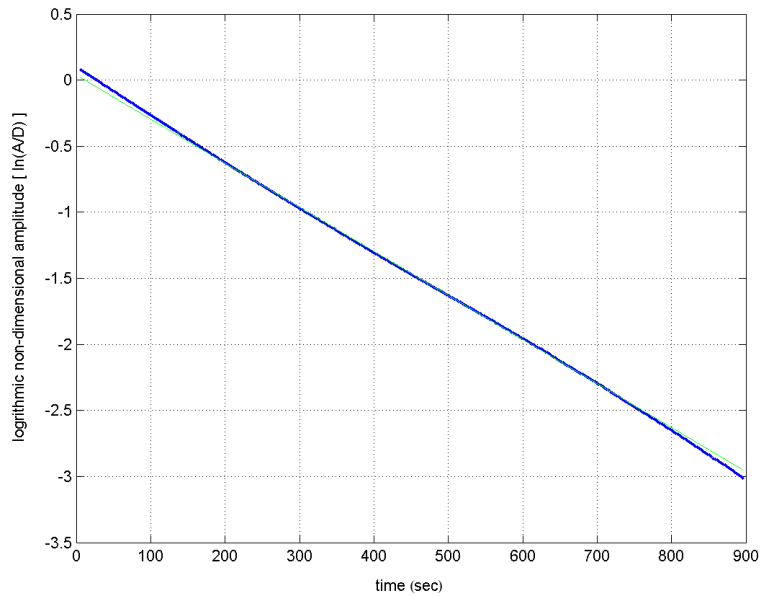


Figure B.1: Least-squares linear curve fit to the amplitudes of a free-vibration natural decay test undergoing a large number of oscillations. The actual amplitude (blue data) deviates very little from the linear curve fit (green line) and only noticeably at the beginning and end of the time trace.

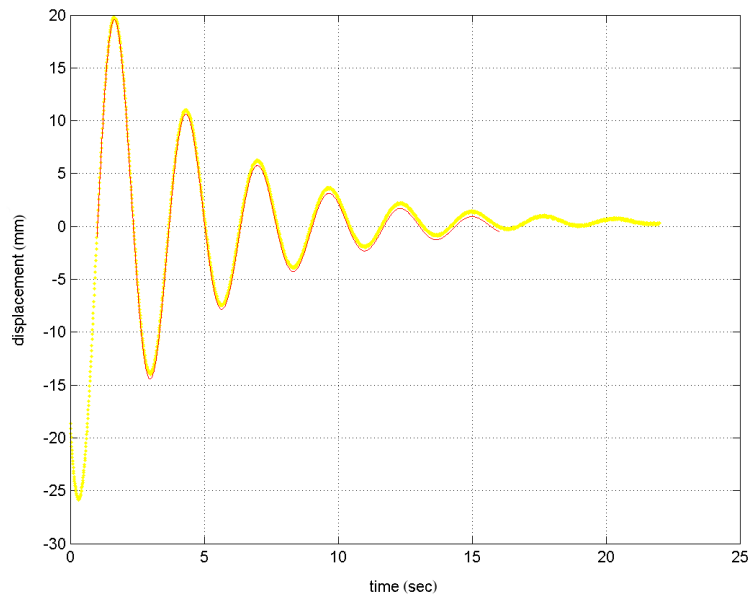


Figure B.2: Least-squares exponentially decaying sine wave curve fit to the full displacement time trace of a free-vibration natural decay test undergoing a limited number of oscillations. The actual displacement (yellow data) deviates very little from the curve fit (red data).

Appendix C: Variable Magnetic Eddy-Current Damping System Theory

We can arrive at an approximation for how the system damping, b , will depend on the VMEC input parameter, supplied current, i_{sup} , by making some simplifying assumptions and focusing our attention locally around the edge of one of the electromagnets. The local induced voltage, $V_{induced}$, in the conductor plate can be estimated, using Faraday's Law and assuming that our electromagnet has roughly constant magnetic field, B , as

$$V_{induced} = \frac{d}{dt} \left(\int \mathbf{B} \cdot d\mathbf{a} \right) = Bwv, \quad (\text{C.1})$$

where w is the width (non-oscillating direction) of the conducting plate and v is the oscillation velocity of the plate. Next, we make the simplifying assumption that the induced voltage, and resultant eddy current, i_{eddy} , will behave approximately according to ohm's law,

$$V_{induced} = i_{eddy}R, \quad (\text{C.2})$$

where R is the local resistance of the conductive plate. Then, one can combine Equation (C.1) and Equation (C.2) to create an expression for the eddy current generated in the conductive plate

$$i_{eddy} = \frac{Bwv}{R}. \quad (\text{C.3})$$

The force, F , experienced by a current carrying material, in this case the conductive plate with eddy currents, through a magnetic field is given by

$$F = |i_{eddy}\mathbf{L} \times \mathbf{B}| = i_{eddy}wB. \quad (\text{C.4})$$

In this approximation, we assumed that the eddy current flows uniformly in an approximate rectangular path within the plate so that two portions of the current flow path produce equal and opposite forces and a third portion is outside the magnetic field and experiences no force.

The result from Equation (C.3) can then be combined with Equation (C.4) to arrive at

$$F = \frac{w^2 B^2 v}{R} . \quad (\text{C.5})$$

Linear viscous damping is modeled as a force proportional to velocity, with the constant of proportionality being the damping, such that

$$F = bv . \quad (\text{C.6})$$

By noting the form of the linear viscous damping model in Equation (C.6), we can determine the parameters that make up the magnetic damping term, b_{mag} , in Equation (C.5)

$$F = b_{mag}v = fn(w, R, \dots)B^2v , \quad (\text{C.7})$$

meaning that the magnetic damping term is composed of

$$b_{mag} = fn(w, R, \dots)B^2 . \quad (\text{C.8})$$

For a simple electromagnet, such as those being used in this apparatus, we know that

$$B = k_{rel} \mu_o n i_{sup} , \quad (\text{C.9})$$

where k_{rel} is the relative permeability, $\mu_o = 4\pi \times 10^{-7}$ T/amp/m, and n is the turn density (loops per unit length). Therefore, we expect to see a functional relationship between magnetic damping and supplied current of the form

$$b_{mag} = fn(w, R, k, \mu_o, n, \dots)i_{sup}^2 , \quad (\text{C.10})$$

for our VMEC system. The exact form of the leading term is not a trivial calculation. First, the nature of eddy current behavior is not well understood. Also, other parameters

that were excluded due to our assumptions, such as distance between the conducting plate and magnets, play a role in system performance and must be included in a more thorough analysis. However, the magnetic damping dependence on i_{sup}^2 , that this derivation predicts, is clearly seen in the experimental validation tests on the system.

Appendix D: Top 10% Average Amplitude Adjustment Factor Calculations

In the literature, the time-averaged amplitudes of free-vibration systems are determined in various ways. Two of the most common methods are the full average value, obtained by averaging every recorded cycle's amplitude, and the top 10% average value, obtained by averaging only the largest 10% of recorded cycle's amplitudes. Unfortunately, in certain cases, the different averaging methods can result in identical tests giving substantively different A_{Max}^* values. Throughout this thesis we have used the full average value method and, in order to compare our results to the numerous higher Reynolds number results that used the top 10% average value method, we determined an adjustment factor in order to relate the two methods.

We determined the maximum amplitude, A_{Max}^* , of all our lightly damped systems ($b^* \lesssim 0.50$), for each of our numerous test sequences using both of these popular averaging methods. These test sequences covered a substantial range of Reynolds numbers ($200 \lesssim \text{Re}|_{A_{\text{Max}}^*} \lesssim 5050$). To highlight the difference between the two averaging methods, we show in Figure D.1, using the most lightly damped case in each sequence, two calculated maximum amplitudes, one for each of the two methods. The difference between the two methods at low Reynolds number ($\text{Re} \lesssim 1000$) is less than three percent and therefore insignificant. However, for higher Reynolds numbers, the difference is significant. Using the two sets of calculated maximum amplitudes for all lightly damped systems tests, we can determine an average percentage difference between the two methods for each Reynolds number. This can be seen in Figure D.2, which shows the average percent difference between the top 10% average value method, $A_{\text{top10\%}}^*$, and the full average value method, A^* , for various Reynolds numbers.

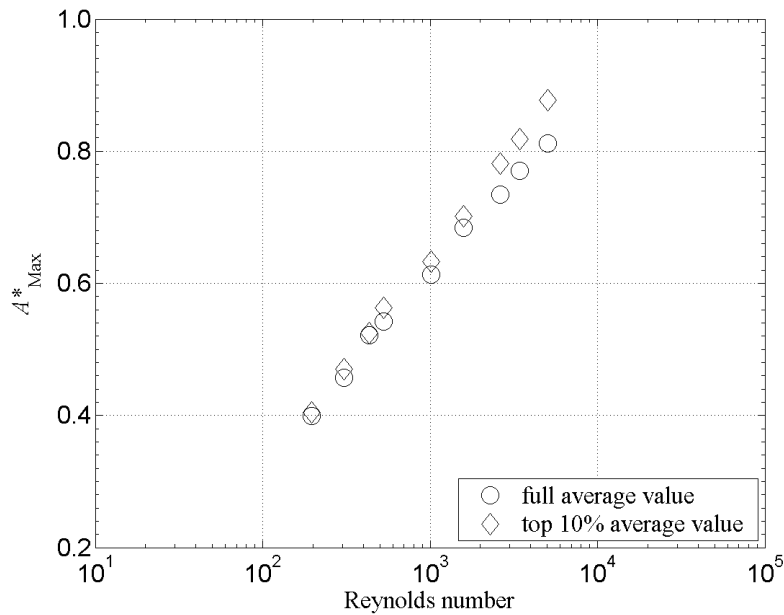


Figure D.1: Differences in maximum amplitudes, A^*_{Max} , determined by averaging every cycle (full average value) and by averaging the largest 10% amplitude cycles (top 10% average value).

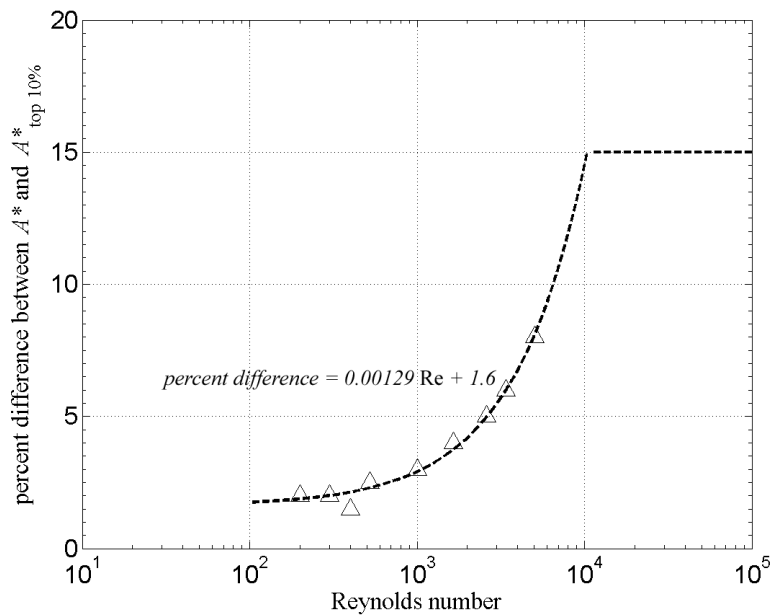


Figure D.2: Increasing percent difference between the top 10% average value and full average value methods as a function of Reynolds number. Dashed line is least-squares linear curve fit, for $Re < 10^4$, and constant value approximation, for $Re > 10^4$.

We determined the least-squares linear fit to our average percent difference data, which is also shown in Figure D.2. By using this curve fit, we could adjust the top 10% average values reported in the literature so that they would be consistent with our method. The adjustment factor was

$$A_{\text{full ave}}^* = PA_{\text{top 10\%}}^* , \quad (\text{D.1})$$

where P is the percent difference between the two methods and is determined using the curve-fit parameters such that

$$P = 1 - \frac{1}{100}(0.00129 \text{ Re} + 1.6) \text{ for } \text{Re} < 10^4 \quad (\text{D.2})$$

$$P = 1 - \frac{1}{100}(15) \text{ for } \text{Re} > 10^4 . \quad (\text{D.3})$$

One cannot extrapolate the percent difference value P to an infinitely large Reynolds number using the curve-fit parameters. The curve-fit parameters were obtained over a Reynolds number range of $10^2 < \text{Re} < 10^4$. Predicting the percentage difference using these parameters at $\text{Re} > 10^4$ gives an incorrectly large percent difference value. Therefore, for a correction factor above $\text{Re} > 10^4$, a constant percent difference of 15% was used.

Bibliography

- Al-Jamal, H., Dalton, C., 2004. Vortex-induced vibrations using Large Eddy Simulation at a moderate Reynolds number. *Journal of Fluids and Structures* 19, 73–92.
- Anagnostopoulos, P., Bearman, P. W., 1992. Response characteristics of a vortex-excited cylinder at low Reynolds numbers. *Journal of Fluids and Structures* 6, 39–50.
- Apelt, C., West, G., Szewczyk, A., 1973. The effects of wake splitter plates on the flow past a circular cylinder in the range $10^4 < \text{Re} < 10^5$. *Journal of Fluid Mechanics* 61, 187–198.
- Bearman, P. W., 1984. Vortex shedding from oscillating bluff bodies. *Annual Review of Fluid Mechanics* 16, 195–222.
- Bishop, R. E. D., Hassan, A. Y., 1964. The lift and drag forces on a circular cylinder oscillating in a flowing fluid. *Proceedings of the Royal Society of London, Series A* 277, 51–75.
- Blackburn, H. M., Henderson, R., 1996. Lock-in behavior in simulated vortex-induced vibration. *Experimental Thermal and Fluid Science* 12, 184–189.
- Blackburn, H. M., Karniadakis, G. E., 1993. Two- and three-dimensional simulations of vortex-induced vibration of a circular cylinder. In: *Proceedings of the Third International Offshore and Polar Engineering Conference*. Golden, CA: ISOPE, pp. 715–720.
- Blevins, R. D., 1994. *Flow Induced Vibration*, 2nd Edition. Krieger Publishing, Malabar, FL.
- Branković, M., 2004. Vortex-induced vibration attenuation of circular cylinders with low mass and damping. Ph.D. thesis, Imperial College.
- Brika, D., Laneville, A., 1993. Vortex-induced vibrations of a long flexible circular cylinder. *Journal of Fluid Mechanics* 250, 481–508.

- Carberry, J., Sheridan, J., Rockwell, D., 2001. Forces and wake modes of an oscillating cylinder. *Journal of Fluids and Structures* 15, 523–532.
- Carberry, J., Sheridan, J., Rockwell, D., 2003. Controlled oscillations of a cylinder: a new wake state. *Journal of Fluids and Structures* 17, 337–343.
- Carberry, J., Sheridan, J., Rockwell, D., 2005. Controlled oscillations of a cylinder: forces and wake modes. *Journal of Fluid Mechanics* 538, 31–69.
- Chyu, C., Rockwell, D., 2002. Near-wake flow structure of a cylinder with a helical surface perturbation. *Journal of Fluids and Structures* 16, 263–269.
- Cowdrey, C., Lawes, J., 1959. Drag measurements at high Reynolds numbers of a circular cylinder fitted with three helical strakes. Technical Report Aero Rep. 384, National Physics Lab.
- Evangelinos, C., Karniadakis, G., 1999. Dynamics and flow structures in the turbulent wake of rigid and flexible cylinders subject to vortex-induced vibrations. *Journal of Fluid Mechanics* 400, 91–124.
- Feng, C. C., 1968. The measurement of vortex induced effects in flow past stationary and oscillating circular and D-section cylinders. Master's thesis, University of British Columbia.
- Fujarra, A. L. C., Meneghini, J. R., Pesce, C. P., Parra, P. H. C. C., 1998. An investigation of vortex-induced vibration of a circular cylinder in water. In: *Proceedings of 1998 Conference on Bluff Body Wakes and Vortex-Induced Vibrations*. Ithaca, NY: Cornell University, paper No. 25.
- Gharib, M. R., 1999. Vortex-induced vibration, absence of lock-in, and fluid force deduction. Ph.D. thesis, California Institute of Technology.
- Govardhan, R., Williamson, C. H. K., 2000. Modes of vortex formation and frequency response of a freely vibrating cylinder. *Journal of Fluid Mechanics* 420, 85–130.
- Govardhan, R., Williamson, C. H. K., 2002. Resonance forever: existence of a critical mass and an infinite regime of resonance in vortex-induced vibration. *Journal of Fluid Mechanics* 473, 147–166.

- Griffin, O. M., 1971. The unsteady wake of an oscillating cylinder at low Reynolds number. *ASME Journal of Applied Mechanics* 38, 729–738.
- Griffin, O. M., 1972. Flow near self-excited and forced vibrating circular cylinders. *ASME Journal of Engineering for Industry* 94, 539–547.
- Griffin, O. M., 1980. Vortex-excited cross-flow vibrations of a single cylindrical tube. *ASME Journal of Pressure Vessel Technology* 120, 158–166.
- Griffin, O. M., Ramberg, S. E., 1982. Some recent studies of vortex shedding with application to marine tubulars and risers. *ASME Journal of Energy Resources Technology* 104, 2–13.
- Griffin, O. M., Skop, R. A., Koopman, G. H., 1973. The vortex-excited resonant vibrations of circular cylinders. *Journal of Sound and Vibration* 31, 235–249.
- Guilmineau, E., Queutey, P., 2004. Numerical simulations of vortex-induced vibration of a circular cylinder with low mass-damping in turbulent flow. *Journal of Fluids and Structures* 19, 449–466.
- Hover, F. S., Miller, S. N., Triantafyllou, M. S., 1997. Vortex-induced vibration of marine cables: Experiments using force feedback. *Journal of Fluids and Structures* 11, 307–326.
- Hover, F. S., Techet, A. H., Triantafyllou, M. S., 1998. Forces on oscillating uniform and tapered cylinders in crossflow. *Journal of Fluid Mechanics* 363, 97–114.
- Hover, F. S., Tvedt, H., Triantafyllou, M. S., 2001. Vortex-induced vibrations of a cylinder with tripping wires. *Journal of Fluid Mechanics* 448, 175–195.
- Jauvtis, N., Williamson, C. H. K., 2003. Vortex-induced vibration of a cylinder with two degrees of freedom. *Journal of Fluids and Structures* 17, 1035–1042.
- Jauvtis, N., Williamson, C. H. K., 2004. The effect of two degrees of freedom on vortex-induced vibration at low mass and damping. *Journal of Fluid Mechanics* 509, 23–62.
- Jeon, D., Gharib, M., 2001. On circular cylinders undergoing two-degree-of-freedom forced motions. *Journal of Fluids and Structures* 15, 533–541.
- Jones, G., Lamb, W., 1992. The use of helical strakes to suppress vortex induced vibrations. *Proceedings 6th International Conference on Behavior of Offshore Structures* 2, 804–831.

- Khalak, A., Williamson, C. H. K., 1996. Dynamics of a hydroelastic cylinder with very low mass and damping. *Journal of Fluids and Structures* 10, 455–472.
- Khalak, A., Williamson, C. H. K., 1997a. Fluid forces and dynamics of a hydroelastic structure with very low mass and damping. *Journal of Fluids and Structures* 11, 973–982.
- Khalak, A., Williamson, C. H. K., 1997b. Investigation of relative effects of mass and damping in vortex-induced vibration of a circular cylinder. *Journal of Wind Engineering and Industrial Aerodynamics* 69-71, 341–350.
- Khalak, A., Williamson, C. H. K., 1999. Motions, forces and mode transitions in vortex-induced vibrations at low mass-damping. *Journal of Fluids and Structures* 13, 813–851.
- Klamo, J. T., Leonard, A., Roshko, A., 2004. On the maximum amplitude in vortex-induced vibrations. *Bulletin of the American Physical Society* 49, 36.
- Klamo, J. T., Leonard, A., Roshko, A., 2005. On the maximum amplitude for a freely vibrating cylinder in cross-flow. *Journal of Fluids and Structures* 21, 429–434.
- Klamo, J. T., Leonard, A., Roshko, A., 2006. The effects of damping on the amplitude and frequency responses of a freely vibrating cylinder in cross-flow. *Journal of Fluids and Structures* 22, 845–856.
- Koopmann, G. H., 1967. The vortex wakes of vibrating cylinders at low Reynolds numbers. *Journal of Fluid Mechanics* 28, 501–512.
- Lucor, D., Foo, J., Karniadakis, G. E., 2005. Vortex mode selection of a rigid cylinder subject to VIV at low mass-damping. *Journal of Fluids and Structures* 20, 483–503.
- Marcollo, H., Hinwood, J. B., 2006. On shear flow single mode lock-in with both cross-flow and in-line lock-in mechanisms. *Journal of Fluids and Structures* 22, 197–211.
- Mittal, S., Kumar, V., 1999. Finite element study of vortex-induced cross-flow and in-line oscillations of a circular cylinder at low Reynolds numbers. *International Journal for Numerical Methods in Fluids* 31, 1087–1120.
- Moe, G., Wu, Z. J., 1990. The lift force on a cylinder vibrating in a current. *ASME Journal of Offshore Mechanics and Arctic Engineering* 112, 297–303.

- Morse, T. L., Williamson, C. H. K., 2006. Employing controlled vibrations to predict fluid forces on a cylinder undergoing vortex-induced vibration. *Journal of Fluids and Structures* 22, 877–884.
- Newman, D., Karniadakis, G., 1996. Simulations of flow over a flexible cable: a comparison of forced and flow-induced vibration. *Journal of Fluids and Structures* 10, 439–453.
- Newman, D., Karniadakis, G., 1997. A direct numerical simulation study of flow past a freely vibrating cable. *Journal of Fluid Mechanics* 344, 95–136.
- Norberg, C., 1994. An experimental investigation of the flow around a circular cylinder: influence of aspect ratio. *Journal of Fluid Mechanics* 258, 287–316.
- Norberg, C., 2001. Flow around a circular cylinder: aspects of fluctuating lift. *Journal of Fluids and Structures* 15, 459–469.
- Öngören, A., Rockwell, D., 1988a. Flow structure from an oscillating cylinder. Part 1: Mechanisms of phase shift recovery in the near wake. *Journal of Fluid Mechanics* 191, 197–223.
- Öngören, A., Rockwell, D., 1988b. Flow structure from an oscillating cylinder. Part 2: Mode competition in the near wake. *Journal of Fluid Mechanics* 191, 225–245.
- Parkinson, G. V., 1989. Phenomena and modeling of flow-induced vibrations of bluff bodies. *Progress in Aerospace Science* 26, 169–224.
- Protos, A., Goldschmidt, V. W., Toebe, G. H., 1968. Hydroelastic forces on bluff cylinders. *ASME Journal of Basic Engineering* 90, 378–386.
- Roshko, A., 1954. On the drag and shedding frequency of two-dimensional bluff bodies. Technical Report TN-3169, NACA.
- Ryan, K., Thompson, M., Hourigan, K., 2005. Variation in the critical mass ratio of a freely oscillating cylinder as a function of Reynolds number. *Physics of Fluids* 17, Article No. 038106.
- Sallet, D., 1970. A method of stabilizing cylinders in fluid flow. *Journal of Hydraulics* 4, 40–45.

- Saltara, F., Meneghini, J. R., Siqueira, C. R., Bearman, P. W., 1998. The simulation of vortex shedding from an oscillating circular cylinder with turbulence modeling. In: Proceedings of 1998 Conference on Bluff Body Wakes and Vortex-Induced Vibrations. Ithaca, NY: Cornell University, paper No. 13.
- Sarpkaya, T., 1977. In-line and transverse forces on cylinders in oscillatory flow at high Reynolds numbers. *Journal of Ship Research* 21, 200–216.
- Sarpkaya, T., 1978. Fluid forces on oscillating cylinders. *ASCE Journal of Waterway Port Coastal Ocean Division* 104, 275–290.
- Sarpkaya, T., 1979. Vortex-induced oscillations. A selective review. *ASME Journal of Applied Mechanics* 46, 241–258.
- Sarpkaya, T., 1995. Hydrodynamic damping, flow-induced oscillations, and biharmonic response. *ASME Journal of Offshore Mechanics and Arctic Engineering* 117, 232–238.
- Sarpkaya, T., 2004. A critical review of the intrinsic nature of vortex-induced vibrations. *Journal of Fluids and Structures* 19, 389–447.
- Scruton, C., 1965. On the wind-excited oscillations of stacks, towers and masts. In: Proceedings Symposium on Wind Effects on Buildings and Structures. London: HMSO, pp. 798–836.
- Scruton, C., Walshe, D., 1957. A means of avoiding wind-excited oscillations of structures with circular or nearly circular cross section. Technical Report Aero Rep. 335, National Physics Lab.
- Shiels, D., 1998. Simulation of controlled bluff body flow with a viscous vortex method. Ph.D. thesis, California Institute of Technology.
- Shiels, D., Leonard, A., Roshko, A., 2001. Flow-induced vibrations of a circular cylinder at limiting structural parameters. *Journal of Fluids and Structures* 15, 3–21.
- Singh, S. P., Mittal, S., 2005. Vortex-induced oscillations at low Reynolds numbers: hysteresis and vortex-shedding modes. *Journal of Fluids and Structures* 20, 1085–1104.
- Skop, R. A., Balasubramanian, S., 1997. A new twist on an old model for vortex-excited vibrations. *Journal of Fluids and Structures* 11, 395–412.

- Skop, R. A., Griffin, O. M., 1975. On a theory for the vortex-excited oscillations of flexible cylindrical structures. *Journal of Sound and Vibration* 41, 263–274.
- Smith, J. D., 1962. An experimental study of the aeroelastic instability of rectangular cylinders. Master's thesis, University of British Columbia.
- Stansby, P. K., 1976. The locking-on of vortex shedding due to the cross-stream vibration of circular cylinders in uniform and shear flows. *Journal of Fluid Mechanics* 74, 641–665.
- Stansby, P. K., Pinchbeck, J., 1986. Spoilers for the suppression of vortex-induced oscillations. *Applied Ocean Research* 8, 169–173.
- Staubli, T., 1983. Calculation of the vibration of an elastically mounted cylinder using experimental data from forced oscillation. *ASME Journal of Fluids Engineering* 74, 225–229.
- Sumer, B. M., Fredsoe, J., 1997. *Hydrodynamics around cylindrical structures*, 2nd Edition. World Scientific, Singapore.
- Taneda, S., 1956. Experimental investigation of the wakes behind cylinders and plates at low Reynolds numbers. *Journal of Physical Society of Japan* 11, 302–307.
- Toebe, G. H., 1969. The unsteady flow and wake near an oscillating cylinder. *ASME Journal of Basic Engineering* 91, 493–502.
- Triantafyllou, M. S., Techet, A. H., Hover, F. S., Yue, D. K. P., 2003. VIV of slender structures in shear flow. *IUTAM Symposium on Flow-Structure Interactions*, Rutgers State University, USA.
- Vandiver, J. K., 1993. Dimensionless parameters important to the prediction of vortex-induced vibration of long flexible cylinders in ocean currents. *Journal of Fluids and Structures* 7, 423–455.
- Vandiver, J. K., Jong, J., 1987. The relationship between in-line and cross-flow vortex-induced vibration of cylinders. *Journal of Fluids and Structures* 1, 381–399.
- Vickery, B. J., Watkins, R. D., 1964. Flow-induced vibrations of cylindrical structures. In: *Proceedings 1st Australian Conference on Hydraulics and Fluid Mechanics*. New York: Pergamon, pp. 213–241.

- Westerweel, J., Dabiri, D., Gharib, M., 1997. The effect of a discrete window offset on the accuracy of cross-correlation analysis of digital PIV recordings. *Experiments in Fluids* 23, 20–28.
- Willden, R. H. J., Graham, J. M. R., 2006. Three distinct response regimes for the transverse vortex-induced vibrations of circular cylinders at low Reynolds numbers. *Journal of Fluids and Structures* 22, 885–895.
- Willert, C. E., Gharib, M., 1991. Digital particle image velocimetry. *Experiments in Fluids* 10, 181–193.
- Williamson, C. H. K., Govardhan, R., 2004. Vortex-induced vibrations. *Annual Review of Fluid Mechanics* 36, 413–455.
- Williamson, C. H. K., Roshko, A., 1988. Vortex formation in the wake of an oscillating cylinder. *Journal of Fluids and Structures* 2, 355–381.
- Woodgate, L., Maybrey, J., 1959. Further experiments on the use of helical strakes for avoiding wind excited oscillations of structures of circular or nearly circular section. Technical Report Aero Rep. 381, National Physics Lab.
- Zdravkovich, M. M., 1981. Review and classification of various aerodynamic and hydrodynamic means for suppressing vortex shedding. *Journal of Wind Engineering and Industrial Aerodynamics* 7, 145–189.
- Zhang, J. F., Dalton, C., 1996. Interactions of vortex-induced vibrations of a circular cylinder and a steady approach flow at a Reynolds number of 13,000. *Computers and Fluids* 25, 283–294.
- Zhou, C. Y., So, R. M. C., Lam, K., 1999. Vortex-induced vibrations of an elastic circular cylinder. *Journal of Fluids and Structures* 13, 165–189.